Tailoring Molecular Magnetism

Von der Fakultät für Mathematik, Informatik und Naturwissenschaften der RWTH Aachen University zur Erlangung des akademischen Grades eines Doktors der Naturwissenschaften genehmigte Dissertation

vorgelegt von

Master of Science

Taner Esat

aus Pirmasens

Berichter: Univ.-Prof. Dr. Frank Stefan Tautz
apl.-Prof. Dr. Maarten Rolf Wegewijs
Univ.-Prof. Dr. Markus Morgenstern

Tag der mündlichen Prüfung: 4. April 2017

Diese Dissertation ist auf den Internetseiten der Universitätsbibliothek online verfügbar.

There is nothing impossible to him who will try.
– Alexander the Great

This work is dedicated to my mother, father and sister.

Acknowledgments

This thesis is the result of a joint PhD program between the institutes of Prof. Dr. F. Stefan Tautz and Prof. Dr. Claus M. Schneider at the Peter Grünberg Institute (PGI) of the Forschungszentrum Jülich.

At this point I would like to take the opportunity to thank the people who supported me during my PhD thesis and in parts my whole life and made this work possible in the first place – many thanks!

- I sincerely thank **Prof. Dr. F. Stefan Tautz** for giving me the opportunity to work in his research group and institute (PGI-3) within the joint PhD program. Furthermore I really appreciate his open ear for all kinds of problems, the fruitful discussions about physics, the great support regarding paper writing and everything else and all the inspirations which contributed to the success of this work. In the end I believe that at least a bit of his academic precision and enthusiasm rubbed off on me.

- I also warmly thank **Prof. Dr. Claus M. Schneider** for giving me the opportunity to carry out part of my work in his research group and institute (PGI-6) within the joint PhD program. Moreover, I highly value not only his advices and encouragements during my struggle with the spin-polarized measurements, but also all his support which made this work a success.

- I am indebted to **Dr. Ruslan Temirov** who was more than just a supervisor for me. He did not only share his knowledge about physics with me, but rather infected me with his enthusiasm and curiosity for physics. Without his knowledge, advice and encouragement this work would have not been possible. Moreover, I would like to thank him for his endless support and advice regarding work and everything else.

- I am also grateful to **Dr. Daniel E. Bürgler** for always having an open ear for all my grumblings about the spin-polarized measurements, his encouragements and endless believe in the success of the measurements which in the end paid off. Furthermore, I would like to thank him for all his advice and support during the last years.

- Many thanks to **Dr. Christian Wagner** and **Dr. Frank Matthes** for all their support in the labs and for not leaving me alone with the typical problems of an experimentalist. Also many thanks for the fruitful discussions about physics and the anecdotes which made the daily lab life more fun.

- My special thanks go to our collaborators who contributed substantially the success of this work: **Dr. Thorsten Deilmann**, **apl. Prof. Dr. Peter Krüger** and **Prof. Dr. Michael Rohlfing** from the University of Münster; **Dr. Benedikt Lechtenberg** and **Prof. Dr. Frithjof B. Anders** from the TU Dortmund University; **Dr. Rico Friedrich**, **Dr. Vasile Caciuc**, **Dr. Nicolae Atodiresei** and **Prof. Dr. Stefan Blügel** from the Forschungszentrum Jülich.

- I also would like to thank all members of the PGI-3 and PGI-6 for the pleasant atmosphere in the institutes, the good conservations and the funny moments which made working a great joy. In particular I would like to thank **Dr. Caroline Henneke**, **Dr. Sonja Schröder**, **Markus Franke**, **Simon Weiß**, **Dr. Volkmar Hess**, **Matthew Green**, **Dr. Martin Willenbockel**, **Dr. Giuseppe Mercurio**, **Dr. Benjamin Stadtmüller**, **Philipp Leinen**, **Janina Felter**, **Aizhan Sabitova**, **Dr. Francois Bocquet**, **Dr. Marcus Blab**, **Prof. Dr. Bert Voigtländer** and **Prof. Dr. Christian Kumpf**.

- Especially I thank **my parents** and **my lovely sister** for their infinite love, patience and tireless support in all situations of my life – basically for everything!

Contents

CHAPTER 1

Introduction

The invention of the modern computer in the 20th century has significantly changed our way of living and ushered in a new epoch of information technology – the Information age. When Konrad Zuse completed the first programmable, fully automatic and digital computer, the Z3, in Berlin in 1941 [1] it would have been impossible to imagine how computers would become part of our daily lives. Although the computational power of the first computers back then is actually comparable with modern pocket calculators, they were enormous and consumed a lot of power. For example the Z3, which was based on 2000 electromechanical relays, operated at a clock frequency of only $5 - 10\,\mathrm{Hz}$ and had a power consumption of $4000\,\mathrm{W}$ [1]. The first electronic programmable computer, the ENIAC, was presented in the USA in 1946 and used vacuum tubes instead of electromechanical relays. It was one thousand times faster than the electromechanical computers at that time, but it also had a power consumption of $150\,\mathrm{kW}$ and needed a space of approximately $170\,\mathrm{m}^2$ [2]. Nowadays personal computers have typically clock frequencies of about $2 - 3\,\mathrm{GHz}$, fit easily in a backpack and have a power consumption of only several hundreds of Watts in spite of much larger computational power. These values impressively show the rapid development of the computer technology within the last decades.

The corner stone for this rapid development was laid by the American physicists John Bardeen, Walter Brattain and William Shockley when they built the first transistor in 1947. The transistor rolled up the field of electronics and paved the way to smaller, more powerful, less power consuming and cheaper electronic devices. For their achievement they were awarded the Nobel Prize in Physics in 1956. The transistor found its way into computer design already a few years after its invention and replaced vacuum tubes. The first fully transistorized computer was built in the group of Kilburn at Manchester University in 1953 [3]. Ultimately, the invention of the integrated circuit (IC) by Jack Kilby in 1958 led to a breakthrough in the commercial and personal use of computers. The fabrication of ICs by photolithography allowed a huge number of tiny electronic circuits and components, e.g. transistors, to be embedded on a small plate. This offered the possibility of an easy and low cost mass production of personal computers

based on ICs. For his achievements Jack Kilby was awarded the Nobel Prize in Physics in 2000.

With the technological advance the conducting lines and integrated components in an IC have become smaller and smaller in the last few decades. State-of-the-art computer chips are fabricated by the so-called 14 nm technology, i.e. that the smallest distance between repeated features in an IC is about 14 nm. However, with further miniaturization the current transistor technology is reaching its physical limits. The reason for this is the quantum mechanical nature of matter at the atomic length scale. At distances smaller than 10 nm already quantum tunneling becomes a non-negligible phenomenon and leads to leak currents between source and drain in a transistor. Hence, the properties of transistors and ICs are not well-defined anymore. Consequently, new approaches are necessary in order to meet the demands on more computational power and storage capacity while continuously reducing the power consumption and the size of the electronic devices.

On the way to new solid-state devices one promising approach is to utilize the spin of an electron and thus its magnetic moment in addition to its charge. The main idea is to tailor nanostructures with well-defined magnetic properties which can be manipulated and detected in a controlled manner in order to store information or to carry out spin-based logic operations [4, 5, 6]. The most famous spin-based device is the hard disk drive (HDD) which can be found in almost every personal computer. It is based on the giant magnetoresistance (GMR) [7, 8] or tunnel magnetoresistance (TMR) [9] and makes use of the fact that the electrical resistance depends on the magnetization of two adjacent ferromagnetic layers to store information. For the discovery of the GMR effect Albert Fert and Peter Grünberg were awarded the Nobel Prize in Physics in 2007. The success of the HDD demonstrates impressively the capability of spin-based devices in future information technology.

Thus, the magnetic properties of nanostructures and in particular of quantum impurities, i.e. of nanostructures with well-defined charge and spin degrees of freedom that are coupled to one or more conduction bands, are currently in the focus of research [10, 11]. Quantum impurities, e.g. quantum dots, molecules or even single atoms, might be also used as qubits for quantum computers [12, 13, 14, 15, 16]. A quantum computer has the advantage that some operations can be carried out much faster in comparison to classical computers. The most famous examples are integer factorization using Shor's algorithm [17] or the inversion of a function using Grover's algorithm [18]. In general one hopes to solve certain problems, e.g. the simulation of quantum many-body systems, in much shorter time and more efficiently than with any classical computer. However, on the way towards the realization of quantum computers or spin-based devices based on quantum impurities it is crucial to gain better understanding of the physics of quantum impurities – in particular of their interaction with each other and with their environment.

The versatility of the scanning tunneling microscope (STM) [19, 20] makes it the ideal experimental tool in order to investigate the properties of quantum impurities and their interactions on the atomic length scale. In addition to its capability of imaging nanostructures with an unmatched resolution it also allows for the measurement of the local electronic and magnetic properties of nanostructures. Furthermore, the capability of the STM to manipulate single atoms and molecules offers the possibility to tailor artificial nanostructures and thus to study systematically their properties.

Indeed, some outstanding achievements have been accomplished by means of STM in recent years. The most important achievements are based on single magnetic atoms and single molecular magnets adsorbed on metal surfaces. For example it has been shown that both atoms and molecular magnets with uncompensated spins can undergo a Kondo effect with the itinerant electrons of the metal substrate [21, 22, 11, 23, 24, 25]. The Kondo effect is a fingerprint for magnetic impurities which interact via spin-flip scattering with the conduction band [26] and manifests itself in the density of states (DOS) as a sharp resonance at the Fermi level [11]. Since the Kondo resonance represents the spin degree of freedom of a quantum impurity it is often used to detect the interaction between quantum impurities. This is possible because the magnetic properties, i.e. the spin, of the quantum impurity is unavoidably coupled to the shape of the Kondo resonance. Already tiny changes in the properties of a quantum impurity – be it due to the coupling to the environment or due to interactions with other impurities – are reflected in the Kondo resonance. Therefore, the Kondo effect can be used as a probe for the magnetic properties of quantum impurities. In addition, or when the Kondo effect is absent, one can make use of spin-polarized scanning tunneling microscopy (SP-STM) [27] in conjunction with an external magnetic field to gain further insight into the magnetic properties of quantum impurities. Both approaches, i.e. investigations based on the Kondo effect or by means of SP-STM, lead to interesting findings and achievements. To name some prominent achievements:

- measurement of the spin excitation spectrum of magnetic atoms [28]
- demonstration of spin coupling in artificially tailored atomic chains [29]
- determination of the magnetic anisotropy of single magnetic atoms [30]
- showing the role of magnetic anisotropy in the Kondo effect [31]
- visualization of the spin of molecular magnets [32]
- revealing the effect of magnetic coupling between a Kondo-screened atom and a magnetic atom [33]

- controlling the quantum spin state of magnetic atoms with electric currents [34]
- measuring the spin relaxation times of single magnetic atoms by pump-probe spectroscopy [35]
- mapping the strength of the RKKY interaction on the atomic scale [36]
- formation of a $2D$ Kondo lattice via RKKY coupling of single molecular magnets [37]
- realization of spin-based logic operations with single atoms connected to spin leads [38]
- assembly of a stable magnetic byte of 96 single atoms [39]
- observation of spin-split molecular orbitals of adsorbed molecular magnets [40]
- measurement of the spin dynamics of quantum magnets [41]
- atom-by-atom engineering of complex nanomagnets [42]
- controlling quantum magnets by atomic exchange bias [43]
- demonstration of magnetic coupling between molecules mediated by a nanoskyrmion lattice [44]
- measurement of spin resonances in single molecules and atoms by resonant radio-frequency current [45, 46]
- showing magnetic remanence in single atoms up to 30 K [47]

However, as one can see, all this work is based on quantum impurities with localized spins, i.e. the spin resides in a d or f orbital of a metal or rare earth metal atom. Even in the case of single molecular magnets the spin is carried by a metal ion that is shielded by organic ligands and hence again localized in a d or f orbital. The use of localized spins has the advantage that they are only barely effected by the environment and consequently have well-defined magnetic properties – this applies in particular for single molecular magnets where the spin is even shielded by the organic ligands from the environment. But at the same time this advantage results also in a shortcoming regarding the tunability and the coupling of quantum impurities: the magnetic properties can only be influenced weakly by the environment or by other quantum impurities. In order to couple such quantum impurities one has typically to rely on the indirect Ruderman-Kittel-Kasuya-Yosida (RKKY) interaction [48, 49, 50] that is mediated by

the conduction band electrons. The nature and strength of the RKKY interaction strongly depends on the distance between the quantum impurities. It oscillates between ferromagnetic and antiferromagnetic coupling and its coupling strength decreases exponentially with increasing distance. For tailoring complex nanostructures from single magnetic atoms this approach is quite sufficient, as seen by the above mentioned results. But if one wants to use more complex building blocks, i.e. single molecules, one is confronted with several problems. The reason for this is on the one hand the larger size of the single molecules and thus the larger distance between the quantum impurities and on the other hand the shielding of the spin by the organic ligands in common molecular magnets. Hence, with exception of Ref. [37], there is very little work on the successful coupling of common molecular magnets to each other, which indicates how difficult this task is.

But since molecules can be synthesized in a large number with identical properties and have the tendency to self-assemble on metal surfaces it is only natural to want to make use of molecules as quantum impurities in order to design nanostructures with different functionalities. One solution to overcome the problem regarding the coupling of common molecular magnets would be to disengage oneself from localized spins and to switch to delocalized spins, e.g. to molecules which carry an unpaired spin in an extended orbital. The advantage of such delocalized spins lies in their propensity to interact more easily with the environment or other quantum impurities. Furthermore they might offer the possibility to tune the magnetic properties by chemical interactions instead of magnetic exchange interactions. This could lead to a new avenue in crafting spin-based devices or quantum computers. But, due to the delocalized nature of the spin it is also more difficult to prepare quantum impurities with well-defined electronic and magnetic properties. In particular if one wants to study systematically the interaction of delocalized spins it is indispensable to have full control of the geometry of the impurities with respect to each other, since already tiny changes in the wavefunction overlap, i.e. in the chemical interaction, could lead to drastic changes in the system.

However, quantum impurities with delocalized spins have only recently moved into the focus of research [51, 52, 53] and thus the understanding of their properties and in particular their interaction with the environment and other quantum impurities is poor. With the work presented here I will fill this gap and improve the understanding of such systems. In particular I will concentrate on the question how quantum impurities with delocalized spins and well-defined electronic, magnetic and geometric properties can be tailored and how the properties of such impurities can be tuned by interactions with the environment or other quantum impurities. In this context I will unveil several astonishing properties and physical effects which are related to the delocalized nature of the spin and cannot be observed in quantum impurities with localized spins. All studies presented in this thesis are based on

the versatility of the STM and a close collaboration with theoretical groups.

The thesis itself is organized as follows: After this introduction I describe in chapter 2 the theoretical concepts which are necessary in order to understand the experiments and findings that are presented in this work. In chapter 3 I demonstrate how a single quantum impurity with a delocalized spin and well-defined electronic, magnetic and geometric properties can be tailored by adsorption of single metal atoms onto molecules which are embedded into a molecular layer. Afterwards I investigate in chapter 4 its interaction with another quantum impurity of the same type and unveil several unusual features which are related to their delocalized spins. In chapter 5 I present an alternative approach in order to tailor a quantum impurity with a delocalized spin, namely by charge transfer from a metal surface into a π orbital of an organic molecule, and demonstrate that already tiny changes in the environment can alter its magnetic properties and could lead to unexpected phenomena. Finally, in chapter 6 I study the spin-dependent hybridization of an organic molecule on a ferromagnetic substrate and show that the newly formed hybrid molecular magnet exhibits some interesting features.

CHAPTER 2

Theoretical background

Nature isn't classical, dammit, and if you want to make a simulation of nature, you'd better make it quantum mechanical, and by golly it's a wonderful problem, because it doesn't look so easy. – Richard Feynman

In this chapter I will describe the theoretical concepts that are essential for understanding the experiments and their results which are presented in this thesis. However, it is not the goal to describe all theory in detail, but rather to explain the most important basics which are relevant for this work, since more complete and detailed descriptions can be found elsewhere.

In the first part of this chapter I will explain the working principle and the theoretical background of the scanning tunneling microscope (STM), its capabilities of doing spectroscopy and even measuring magnetic properties on the scale of nanostructures. In the second part I will concentrate on Kondo physics. Based on the single impurity Anderson model (SIAM) I will explain the properties of a spin-$1/2$ quantum impurity (QI) which is coupled to a metal host. Since the SIAM cannot be treated analytically due to its complexity, I also describe the numerical renormalization group (NRG) approach which represents a numerical method for solving QI models like the SIAM. Furthermore, I comment on the interaction between two QIs based on the two impurity Anderson model (TIAM). In the last part of this chapter I give a brief introduction to the terminology and different types of quantum phase transitions.

2.1 Scanning tunneling microscopy and spectroscopy

The invention of the scanning tunneling microscope (STM) by Binnig and Rohrer [54, 55] at the laboratories of IBM Zürich in 1981 opened a new pathway for investigating the physical properties of nanostructures, molecules and even single atoms on surfaces. The STM offers not only the capability to image nanostructures with sub-angstrom spatial resolution but also allows to gain local information about their electronic and magnetic properties [27]. Furthermore it affords the capability to manipulate single atoms [56] and molecules in a controlled manner [57]. This versatility makes the STM an invaluable tool to investigate the properties of nanostructures, the interaction within and between nanostructures and also with their environment. A detailed and extensive description of STM theory and its application can be found in numerous textbooks [19, 20].

A typical STM consists of an atomically sharp metallic tip and a conducting sample. The principle of operation is based on the quantum mechanical tunneling effect. For this purpose the STM tip is brought into close vicinity of the conducting sample by using piezoelectric elements which allow a precise control on atomic length scales. When the distance between tip and sample is of the order of several Ångströms, tunneling of electrons between the tip and sample takes place. Applying a bias voltage V across the junction, i.e. between tip and sample, then results in a net tunneling current I which usually ranges from a few picoamperes up to several nanoamperes. In Fig. 2.1 a schematic illustration of a typical STM setup is shown. The STM

tip is scanned over the surface with the x and y piezo elements, typically line by line, while the vertical position of the tip is adjusted via a feedback loop to maintain a constant current between tip and sample. From the variations of the vertical tip position a topographical image is then constructed. This operation mode is known as constant current mode and as shown in the following it yields maps of the isosurface of the local density of states (LDOS). If the surface is very flat the STM can be also operated in the so-called constant height mode. In this mode the feedback loop is switched off and the tip is scanned over the surface while the vertical tip position is kept constant. In this mode the tunneling current is recorded and used to reconstruct a topographic image. Normally the STM is operated in the constant current mode, since the feedback loop allows a safer operation of the STM, e.g. avoiding crashes due to roughnesses or tilt of the surface.

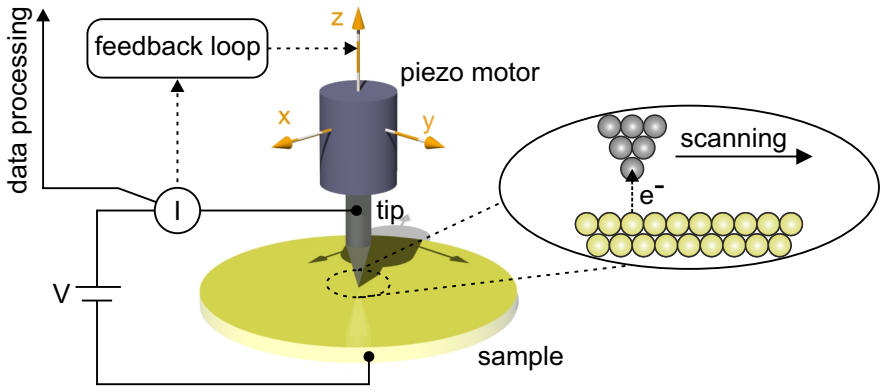

Figure 2.1: Schematic illustration of a typical STM setup. An atomically sharp metallic tip is mounted on a piezoelectric element with the capability to move the tip in x, y and z direction with atomic precision. Applying a bias voltage V between the tip and the conducting sample leads to a net tunneling current I when the distance between tip and sample is in the order of several Ångström. The STM tip is scanned over the surface of the sample while the detected tunneling current I is used to regulate the distance between tip and sample. The inset illustrates the distances in the junction on an atomic scale.

After having described the basic operating principle of the STM, we have a closer look at the working principle behind it. Already twenty years before the invention of the STM Bardeen calculated the tunneling current for two planar electrodes separated by a thin oxide layer based on time-dependent perturbation theory [58]. Bardeen showed that in the case of weak interaction between the two electrodes the tunneling probability between the two unperturbed electronic states Ψ_μ and Ψ_ν is given by their wave function overlap. In our case Ψ_μ and Ψ_ν correspond to the states of the tip

and sample, respectively. The tunnel matrix element is then according to Bardeen given by

$$M_{\mu\nu} = -\frac{\hbar^2}{2m} \int (\Psi_\mu^* \vec{\nabla} \Psi_\nu - \Psi_\nu^* \vec{\nabla} \Psi_\mu) \cdot d\vec{S} \tag{2.1}$$

where the integration has to be carried out over any surface which separates the two electrodes. In general the tunneling current can be calculated by the summation over all possible initial and final states, multiplied by the transition probability. In the limit of low temperatures and small bias voltages the tunneling current then can be expressed by

$$I = \frac{2\pi}{\hbar} e^2 V \sum_{\mu\nu} |M_{\mu\nu}|^2 \delta(E_\mu - E_F) \delta(E_\nu - E_F) \tag{2.2}$$

where E_μ and E_ν are the energies of the states Ψ_μ and Ψ_ν, respectively. As seen from eq. (2.2) the tunneling current I strongly depends on the exact knowledge of the wave functions Ψ_μ and Ψ_ν of both electrodes and therefore also on the atomic structure of those. However, the exact atomic structure of the tip and sample are generally unknown.

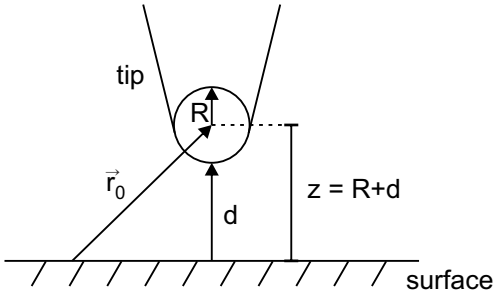

Figure 2.2: Illustration of the STM junction in the Tersoff and Hamann model. It is assumed that the apex of tip has a spherical shape where the radius of the curvature is given by R. The distance between tip and sample is given by d. The vector $\vec{r_0}$ denotes the center of the tip apex. Adapted from Ref. [59].

Nevertheless, a good approximation for the tunneling current can be achieved when Bardeen's theory is adopted to the peculiarities of the STM junction. This has been done by Tersoff and Hamann in 1983 [59, 60]. They assumed that the tip has a spherical shape at the apex and that the curvature is given by the radius R. For calculating the tunnel matrix elements they considered only s-like wave functions for the tip and also neglected contributions from wave functions with angular dependence. The geometry of the model STM junction as proposed by Tersoff and Hamann is shown in Fig. 2.2 where $\vec{r_0}$ describes the tip position and d the distance

between tip and sample. Under these assumptions the tunneling current is given by

$$I \propto \frac{2\pi}{\hbar} e^2 V \rho_t(E_F) e^{2\kappa R} \sum_\nu |\Psi_\nu(\vec{r_0})|^2 \delta(E_\nu - E_F) \tag{2.3}$$

in the limit of low temperatures and small bias voltages, where $\rho_t(E_F)$ denotes the DOS of the tip at the Fermi energy, $\kappa = \sqrt{2m\Phi}/\hbar$ the decay constant and Φ the effective barrier height between tip and sample. The last term

$$\rho_s(E_F, \vec{r_0}) = \sum_\nu |\Psi_\nu(\vec{r_0})|^2 \delta(E_\nu - E_F) \tag{2.4}$$

in eq. (2.3) can be identified as the LDOS $\rho_s(E_F, \vec{r_0})$ of the sample at the Fermi energy E_F, evaluated at the tip position $\vec{r_0}$. An exponential dependence of the tunneling current on the distance d is found if we consider that the wave functions of the sample decay exponentially into the vacuum, i.e. $\Psi_\nu \propto e^{-\kappa z}$. Thus, we obtain $\rho_s(E_F, \vec{r_0}) \approx \rho_s(E_F) e^{-2\kappa(d+R)}$, with $z = d + R$, for the LDOS of the sample (see also Fig. 2.2) and consequently

$$I \propto \frac{2\pi}{\hbar} e^2 V \rho_t(E_F) \rho_s(E_F) e^{-2\kappa d} \tag{2.5}$$

for the tunneling current. This exponential dependence of the tunneling current on the distance d is the main reason for the attainable atomic resolution in STM. As a rule of thumb one can say that the tunneling current increases by an order of magnitude if the distance between tip and sample is decreased by 1 Å.

But it is important to note that the tunneling current does not only depend exponentially on the distance d between tip and sample, but is also proportional to the LDOS $\rho_s(E_F, \vec{r_0})$ of the sample. This must be kept in mind when interpreting the constant current images. They can only be interpreted as topographic images when the geometrical structures dominate the tunneling current. However, this is rarely the case on the atomic length scale and thus the constant current images have to be considered to reflect both, the apparent height and the LDOS of the sample. Thus, the constant current images can be considered to reflect the isosurface of the LDOS of the sample at low bias voltages as mentioned before. Therefore, it is possible that e.g. adsorbates on a metallic surface appear as depressions instead of elevations due to differences in the LDOS and potential barrier height compared to the surface.

Up to now we have only considered vanishing bias voltages, but to describe a more realistic scenario we have to account for finite bias voltages. Generalizing the Tersoff and Hamann formula in eq. (2.5) to a finite bias window eV under the assumption that the wave functions and thus the energy eigenvalues are undistorted at finite bias voltages leads to [61]

$$I \propto \frac{2\pi}{\hbar} e \int_0^{eV} \rho_t(-eV + E) \rho_s(E) \underbrace{e^{-2\kappa_{\text{eff}}(E,V)d}}_{T(E,V)} dE \tag{2.6}$$

with $\kappa_{\text{eff}} = \sqrt{2m\Phi_{\text{eff}}(E,V)}/\hbar$ and $\Phi_{\text{eff}}(E,U) = \frac{\Phi_t+\Phi_s+eV}{2} - E$. Hence, the tunneling current is in the more general case not directly proportional to the LDOS but rather to the convolution of the LDOS of the tip and sample over the energy interval eV. Note that also the decay constant and the effective barrier height have now an energy and bias voltage dependence. The exponential term in eq. (2.6) is often labeled as transmission coefficient $T(E,V)$ [62]. In Fig. 2.3 the tunneling process at finite bias voltages is shown schematically. It is also important to note that due to the energy and bias voltage dependence of the transmission coefficient $T(E,V)$ electrons close to the Fermi level of the negatively polarized electrode have higher probability for tunneling, since they feel a smaller effective barrier height. Therefore the strongest contribution to the tunneling current stems from those electrons. This is indicated by the arrows in Fig. 2.3.

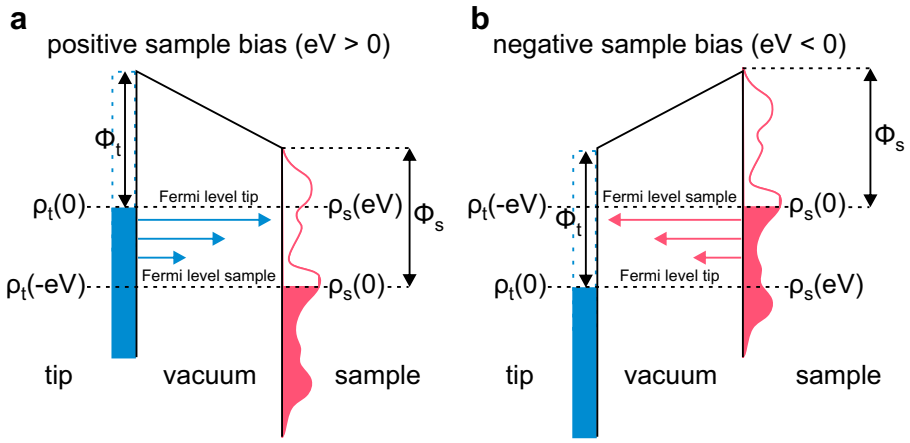

Figure 2.3: **a** Illustration of the tunneling process at a finite bias voltage V. The sample is positively biased. Thus, the electrons from the occupied states of the tip tunnel into the unoccupied states of the sample. **b** As panel a, but for a negatively biased sample. In this case the electrons from the occupied states of the sample tunnel into the unoccupied states of the tip. The arrows indicate that the tunneling process is enhanced at higher energies.

Although the tunneling current I depends on the energy-integrated LDOS of the sample in the case of finite bias voltages, it is possible to measure the energy dependence of the LDOS of the sample. This is done by scanning tunneling spectroscopy (STS). STS is based on the bias dependence of the tunneling current. For this purpose the STM tip is placed at the location of interest, then the feedback loop of the STM is switched off and the bias voltage is swept while the differential conductance $dI/dV(V)$ is recorded. Whenever the Fermi level of the tip passes through a resonance in $\rho_s(E)$ the tunneling current will show a rapid increase according to eq. (2.6). This

change is then visible as a peak in the differential conductance $dI/dV(V)$ signal. Formally this can be seen by differentiating eq. (2.6):

$$\frac{dI}{dV}(V) \propto \rho_t(0)\rho_s(eV)T(E,V) + \int_0^{eV} \rho_t(-eV+E)\rho_s(E)\frac{d(T(E,V))}{dV}dE. \tag{2.7}$$

Note that we assumed a flat DOS of the tip here, i.e. $d\rho_t/dV \approx 0$. As seen, the differential conductance $dI/dV(V)$ is proportional to the LDOS $\rho_s(eV)$ of the sample at the energy eV in first approximation. Since the transmission coefficient $T(E,V)$ is monotonic with applied bias voltage V, the second term in eq. (2.7) will only give a smoothly varying background signal. Thus, the observed structures in the differential conductance signal $dI/dV(V)$ can be attributed to LDOS of the sample and therefore sweeping the bias voltage V allows to probe the energy dependence of the LDOS of the sample. Note that STS allows to probe occupied and unoccupied states of the sample depending on the polarity of the applied bias voltage (see also Fig. 2.3).

2.1.1 Spin-polarized tunneling

In our considerations so far we have completely neglected the spin of the electrons and thus only focused on the electronic properties of the sample. If we want to address also the magnetic properties of a sample, we have to take the electron spin into account when we calculate the tunneling current. The principle of spin-polarized tunneling is based on the fact that in a ferromagnetic material the density of states differs for both spin orientations, namely for spin-up ($\uparrow$) and spin-down ($\downarrow$). According to the Stoner model for band ferromagnetism this is caused by the exchange interaction which shifts the spin-up and spin-down DOS with respect to each other in energy. Thus, resulting in a difference for the spin-up ($\uparrow$) and spin-down ($\downarrow$) DOS. A measure for this difference is given by the spin polarization

$$P = \frac{\rho_\uparrow - \rho_\downarrow}{\rho_\uparrow + \rho_\downarrow} \tag{2.8}$$

where $\rho_\uparrow$ and $\rho_\downarrow$ correspond to the DOS of the spin-up and spin-down channel, respectively.

Slonczewski has shown that the tunneling current between two ferromagnetic electrodes exhibits a $\cos\theta$ dependence with θ being the angle between the magnetization directions of the two electrodes [63]. In the limit of low temperatures, vanishing bias voltages and under the assumption of free electrons the spin-polarized tunneling current then can be expressed by

$$I_{\mathrm{sp}} = I_0(1 + P_t P_s \cos\theta). \tag{2.9}$$

Here I_0 denotes the tunneling current for the corresponding nonmagnetic case and $P_{t,s}$ the spin polarizations of the two electrodes (in our case tip and sample), respectively. According to eq. (2.9) the most extreme cases for the tunneling current occur for parallel ($\theta = 0°$) and anti-parallel ($\theta = 180°$) alignment of the two magnetizations:

$$I_{\uparrow\uparrow} = I_0(1 + P_t P_s), \text{ for } \theta = 0° \tag{2.10}$$

$$I_{\uparrow\downarrow} = I_0(1 - P_t P_s), \text{ for } \theta = 180° \tag{2.11}$$

The physical origin of the dependence of the tunneling current on the relative alignment of the magnetization directions can be easily understood if we consider the situation in Fig. 2.4 where the tunneling process between two identical ferromagnetic materials (tip and sample) is sketched for parallel and anti-parallel alignment of their magnetizations. If spin-flip processes are excluded, then the spin-up (spin-down) electrons of the tip will always tunnel into the spin-up (spin-down) states of the sample when a small bias voltage is applied between tip and sample. Since the tunneling current depends on the DOS of the electrodes, a high tunneling current will be observed in the case of parallel alignment of the magnetization directions, because of the high spin-down DOS at the Fermi energy in tip and sample (Fig. 2.4a). For anti-parallel alignment of the magnetization directions no tunneling current will be detected in our scenario, because in this case the spin-down DOS at Fermi energy is diminished for the sample due to the magnetization reversal (Fig. 2.4b). This phenomena is also known as the tunnel magnetoresistance (TMR) effect [9].

Although, the considerations so far explain the basic mechanism behind the spin-polarized tunneling between two ferromagnetic materials, it is necessary to extend the model to the peculiarities of the STM junction to gain additional information on the dependence of the tunneling current on the local properties like the LDOS of the sample. This has been done by Wortmann et al. in 2001 [64] when they described the spin-polarized STM on the basis of the Tersoff and Hamann model. According to Wortmann et al. the tunneling current is then given by the expression

$$\begin{aligned} I(\vec{r_0}, V, \theta) = I_0(\vec{r_0}, V) + I_{sp}(\vec{r_0}, V, \theta) &\propto \rho_t \tilde{\rho}_s(\vec{r_0}, V) + \vec{m}_t \tilde{\vec{m}}_s(\vec{r_0}, V) \\ &= \rho_t \tilde{\rho}_s(\vec{r_0}, V) + m_t \tilde{m}_s(\vec{r_0}, V) \cos\theta \\ &= \rho_t \tilde{\rho}_s(\vec{r_0}, V)(1 + P_t P_s(\vec{r_0}, V) \cos\theta) \end{aligned} \tag{2.12}$$

in the case of finite bias and low temperatures [64]. Here $\rho_t = \rho_t^{\uparrow} + \rho_t^{\downarrow}$ denotes the constant unpolarized DOS of the tip with $\rho_t^{\uparrow}$, $\rho_t^{\downarrow}$ = constant, but $\rho_t^{\uparrow} \neq \rho_t^{\downarrow}$ to account for the magnetization $\vec{m}_t = (\rho_t^{\uparrow} - \rho_t^{\downarrow})\vec{e}_M$ of the tip. The quantity $\tilde{\rho}_s(\vec{r_0}, V)$ is the energy integrated LDOS of the sample and $\tilde{\vec{m}}_s(\vec{r_0}, V)$ the energy integrated local magnetization of the sample, respectively. As seen from eq. (2.12) the tunneling current can be divided

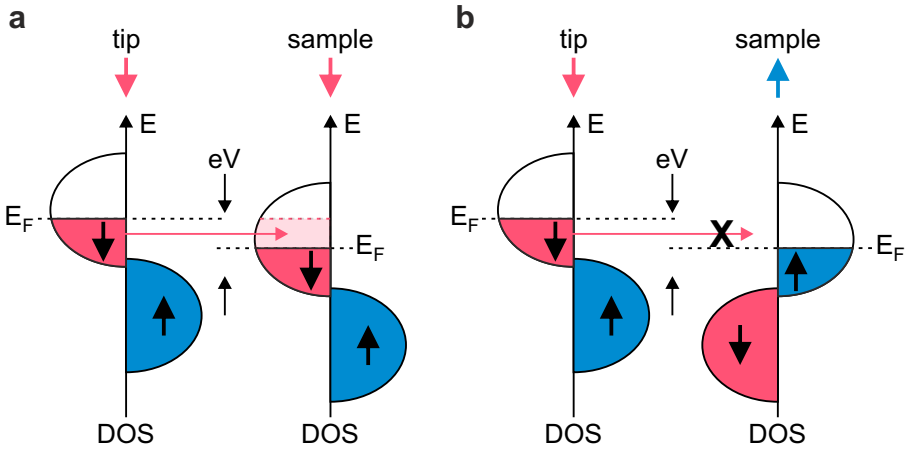

Figure 2.4: **a** Schematic representation of the spin-polarized tunneling between a magnetic tip and a magnetic sample for parallel alignment of the magnetization directions. Applying a bias voltage V between tip and sample leads to a spin-polarized current: the spin-down electrons from the tip tunnel into the unoccupied spin-down states of the sample. There is no tunneling for the spin-up electrons since the tip has no spin-up DOS in the energy interval from E_F to $E_F - eV$. Note that spin-flip processes are neglected in these considerations. **b** As panel b, but for anti-parallel alignment of the magnetization directions. In this scenario no tunneling current is observed since the sample has no unoccupied spin-down states in the energy interval from E_F to $E_F - eV$. The situation for the spin-up electrons is like in panel a.

into an unpolarized part $I_0(\vec{r_0}, V)$ and a spin-dependent part $I_{sp}(\vec{r_0}, V, \theta)$, where the spin-dependent part depends on the projection of $\tilde{\vec{m}}_s(\vec{r_0}, V)$ onto $\vec{m}_t$ and thus on the angle θ between the magnetization directions of the tip and sample. The dependence on the angle θ is again in the form of $\cos\theta$. Note that eq. (2.12) is an extension of eq. (2.9) and that it reduces to the result of the Tersoff and Hamann model when either the tip or the sample is non-magnetic. Compared to the non-magnetic case, which contains information about the topography and the electronic structure of the sample, the tunneling current in the spin-polarized case is superimposed with additional information of the magnetization of the sample.

However, since the spin-polarized tunneling current depends on the energy integrated local magnetization of the sample, it is a quite challenging task to extract magnetic information directly from the tunneling current, e.g. from constant current images. The reason stems from the fact that the unpolarized part I_0 always increases when the bias voltage V is increased, whereas the spin-dependent part I_{sp} can stay constant or even diminish due to an inversion of the spin polarization in the considered energy interval.

Thus, the tunneling current I is usually dominated by I_0. Nevertheless, these difficulties can be overcome if we consider again the differential conductance which is given by

$$\frac{dI}{dV}(\vec{r_0}, V) \propto \rho_t \rho_s(\vec{r_0}, E_F + eV) + \vec{m}_t \vec{m}_s(\vec{r_0}, E_F + eV) \tag{2.13}$$

in the case of spin-polarized tunneling. The equation shows that the differential conductance is directly proportional to the spin-averaged LDOS $\rho_s(\vec{r_0}, E_F + eV)$ and the local magnetization $\vec{m}_s(\vec{r_0}, E_F + eV)$ of the sample at the chosen energy $E_F + eV$. Thus, an appropriate choice of the bias voltage V can maximize the quantity $\vec{m}_s(\vec{r_0}, E_F + eV)$ over $\rho_s(\vec{r_0}, E_F + eV)$, leading to a highly spin-polarized signal. Therefore, it is more convenient to measure spectroscopic images, i.e. $dI/dV(V)$ images, instead of mere constant current images when magnetic samples are investigated, since they provide a higher contrast regarding the magnetic information. A further advantage of measuring the differential conductance is that it allows to probe the magnetization at a well-chosen energy, i.e. of a state of particular interest.

An experimentally important quantity is the so called spin asymmetry A which is defined by

$$A(V) = \frac{(dI/dV(V))_{\uparrow\downarrow} - (dI/dV(V))_{\uparrow\uparrow}}{(dI/dV(V))_{\uparrow\downarrow} + (dI/dV(V))_{\uparrow\uparrow}}. \tag{2.14}$$

$A(V)$ is a measure for the degree of magnetization of the sample at a chosen energy. Note that A does not give the absolute value of the magnetization but rather the effective magnetization (or spin polarization) of the junction, since differential conductance also depends on the magnetization of the tip. Furthermore eq. (2.14) is only applicable when the differential conductance is measured at the same location and at the same tip-sample distance d for parallel ($\uparrow\uparrow$) and anti-parallel ($\uparrow\downarrow$) alignment of the magnetization directions of tip and sample. A different tip-distance can falsify the value of $A(V)$, since it has strong effect on the tunneling current and thus on the differential conductance. Therefore, it is important to stabilize the tip-sample distance at a bias voltage V where the spin-dependent contribution I_{sp} vanishes before measuring the differential conductance at this fixed distance for parallel ($\uparrow\uparrow$) and anti-parallel ($\uparrow\downarrow$) configurations. Hence, the constant height mode is the proper choice for measuring spectroscopic images, even though the constant current mode can be also used if the obtained data is analyzed with reasonable care.

The capability of spin-polarized tunneling will be used in chapter 6 to determine the spatial spin polarization of organic molecules which are adsorbed on a ferromagnetic surface.

2.2 Kondo physics

As mentioned in the introduction of this thesis, the Kondo effect will be used as a probe for the magnetic properties of quantum impurities, namely in the chapters 3, 4 and 5. Hence, it is important to understand the origin of the Kondo effect, and also which parameters have an influence on the properties of the Kondo effect.

The story of the Kondo physics started in 1934 in Leiden, when De Haas et al. measured an anomalous electrical resistivity minimum in a gold sample at very low temperatures [65]. Surprisingly, they observed that the electric resistivity increases again below certain temperatures. Since the contributions from electron-phonon and electron-electron scattering decrease with lowering temperature, neither a minimum nor an increase of the resistivity was expected for temperatures $T \to 0\,\mathrm{K}$. Although, the De Haas et al. suspected that the renewed increase might be related to impurities in the gold sample, it took 30 years until Jun Kondo unraveled the mystery of the origin of the anomalous behavior in the resistivity [26].

In 1964 Kondo showed that the minimum in the electric resistivity is linked to the presence of magnetic impurities which couple via magnetic exchange interaction to the electron spins of the conduction band in the non-magnetic host metal using perturbation theory [26]. In the framework of Kondo the simplest Hamiltonian which describes the coupling of an impurity via an effective Heisenberg interaction J to the conduction electrons can be expressed by

$$\begin{aligned} H_{\mathrm{K}} = & \underbrace{\sum_{\vec{k},\sigma} \epsilon_{\vec{k}} c^{\dagger}_{\vec{k},\sigma} c_{\vec{k},\sigma}}_{\text{conduction electrons}} \underbrace{- J \sum_{\vec{k},\vec{k'}} (c^{\dagger}_{\vec{k'},\uparrow} c_{\vec{k},\uparrow} - c^{\dagger}_{\vec{k'},\downarrow} c_{\vec{k},\downarrow}) S_z}_{\text{spin-conserving scattering}} \\ & \underbrace{- J \sum_{\vec{k},\vec{k'}} c^{\dagger}_{\vec{k'},\uparrow} c_{\vec{k},\downarrow} S^{-} + c^{\dagger}_{\vec{k'},\downarrow} c_{\vec{k},\uparrow} S^{+}}_{\text{spin-flip scattering}} . \end{aligned} \tag{2.15}$$

Here $\epsilon_{\vec{k}}$ denotes the one-electron energies of the conduction band and $c^{(\dagger)}_{\vec{k},\sigma}$ is the annihilation (creation) operator for an electron with the momentum $\vec{k}$ and spin $\sigma = \uparrow, \downarrow$. The spin operator of the impurity is given by S with the z-component S_z and $S^{\pm} = S_x \pm i S_y$. Based on this Hamiltonian Kondo showed that the spin-flip scatterings give rise to a temperature dependent term in the electric resistivity which is proportional to $J \log(T)$ and from comparison with experimental data he concluded that the exchange interaction must be antiferromagnetic ($J < 0$). Thus, the temperature dependence of the resistivity of a metal with embedded magnetic impurities is generally given by

$$\rho(T) = \rho_0 + a T^5 + c J \log(T) \tag{2.16}$$

with $J < 0$ and ρ_0 describing the residual resistance due to non-magnetic imperfections of the metal sample. As seen, at high temperatures the resistivity is dominated by the electron-phonon scattering term aT^5 and at low temperatures by the spin-flip scattering term $cJ\log(T)$. Although, the spin-flip scattering term explains the minimum in the electric resistivity for $J < 0$ it has one shortcoming: since the term $cJ\log(T)$ diverges for $T \to 0\,\mathrm{K}$ the Kondo model leads to unphysical results for low temperatures. An extension of the perturbative approach by Abrikosov in 1965 [66] that involved higher order scattering processes showed that the perturbative approach breaks down in the case of antiferromagnetic coupling for $T \leq T_\mathrm{K}$ with

$$T_\mathrm{K} \sim \exp^{-\frac{1}{\rho|J|}} . \tag{2.17}$$

Thus, the Kondo model is only valid for temperatures higher than the so-called Kondo temperature T_K. The search for a proper description of the $T \leq T_\mathrm{K}$ regime was called the *Kondo problem* and attracted the attention of various theoretical physicists around the 1970s [67, 68, 69, 70, 71, 72]. It was Wilson in 1975 who solved this problem by applying the non-perturbative numerical renormalization group (NRG) method to the Kondo Hamiltonian with a single spin-1/2 impurity (eq. (2.15)) [73]. Wilson showed that for a strong antiferromagnetic coupling the impurity spin combines with a conduction electron spin to form a non-magnetic singlet state at $T = 0\,\mathrm{K}$. Note that this new ground state is a many-body phenomenon, since it includes the interaction with many electrons of the host metal. The process of increased spin-flip scattering at low temperatures and the formation of the new many-body singlet ground state is nowadays termed the *Kondo effect*.

In the following section the details of the Kondo physics will be discussed within the framework of the single impurity Anderson model (SIAM), which is a more general form of the Kondo model, since it also includes charge fluctuations in addition to the spin fluctuations. Here it is important to note that SIAM can be directly related to the Kondo Hamiltonian under certain conditions. For more details we refer the reader to the next section.

2.2.1 Single impurity Anderson model

As mentioned in the previous section we will discuss in the following the basics of the Kondo physics based on the single impurity Anderson model (SIAM) [74]. First we will introduce the SIAM itself and then we will extend our discussion to the different regimes of the model which occur for different parameters, with the main focus lying on the regime where the Kondo effect emerges.

The SIAM describes a zero-dimensional impurity, e.g. single atom or molecule, which is coupled to a bath of non-interacting electrons. In the SIAM the QI consists of only one spin-degenerate energy level ϵ_d which can

host up to two electrons with opposite spin $\sigma =\uparrow,\downarrow$. In the case of double occupancy the on-site Coulomb repulsion U has to be overcome. The coupling between the QI and the conduction band is characterized by the hybridization strength V_k. These properties and interactions are summarized in the SIAM Hamiltonian which is given by

$$\begin{aligned} H_{\text{SIAM}} =& \sum_{\sigma} \epsilon_d d_\sigma^\dagger d_\sigma + U d_\uparrow^\dagger d_\uparrow d_\downarrow^\dagger d_\downarrow \\ &+ \sum_{k,\sigma} \epsilon_k c_{k,\sigma}^\dagger c_{k,\sigma} + \sum_{k,\sigma} V_k (d_\sigma^\dagger c_{k,\sigma} + c_{k,\sigma}^\dagger d_\sigma). \end{aligned} \tag{2.18}$$

For a more detailed description on the effect of the single terms and the fermionic annihilation (creation) operators $d_\sigma^{(\dagger)}$ and $c_{k,\sigma}^{(\dagger)}$ we refer the reader to section 2.2.2.

The SIAM, and also the Kondo model, are usually solved by NRG approach, since it yields an accurate description of the low energy physics. A detailed description of NRG method and its application to the SIAM is presented in section 2.2.2. In the following we will discuss the main properties of the SIAM based on the analysis of Krishna-murthy et al. obtained by using the NRG method [75, 76]. Note that the approach of Krishna-murthy et al. is just the same as the one presented section 2.2.2. For simplicity a constant hybridization function

$$\Gamma(\omega) = \pi\rho|V_k|^2 \tag{2.19}$$

has been used.

Before we analyze the properties of the SIAM in detail, let us survey the properties of the QI in the SIAM itself. In the simplest case, namely when the QI is decoupled from the conduction band ($\Gamma = 0$), the QI orbital is empty ($n_f = 0$) for $\epsilon_d > 0$, occupied by one electron ($n_f = 1$) when $\epsilon_d < 0$ and $\epsilon_d + U > 0$ or doubly occupied ($n_f = 2$) for $\epsilon_d + U < 0$. A finite Γ leads to a mixing of the QI states and the conduction band states. However, if the coupling of the QI to the conduction band is weak, or, to put it another way, if Γ is small compared to the separation of $|\epsilon_d|$ and $\epsilon_d + U$, then the picture described above still remains valid in first approximation and helps in understanding the SIAM.

In the following sections we limit our discussion to the most interesting case with the QI being in the state $n_f = 1$, i.e. to $\epsilon_d < 0$ and $\epsilon_d + U > 0$. This state corresponds to the spin-1/2, i.e. magnetic, state of the QI. Both other cases, $n_f = 0$ and $n_f = 2$, result in a $S = 0$, i.e. non-magnetic, state of the QI and thus are non-relevant in the context of spin Kondo physics. The properties of the SIAM in this regime will be discussed as a function of all relevant physical parameters, i.e. U, Γ, ϵ_d and T. First we consider the so-called symmetric SIAM and later extend our discussion to the asymmetric SIAM. The term of symmetry here refers to the energies of the electrons

in the QI. While the first electron in the QI has the energy ϵ_d the second electron has the energy $\epsilon_d + U$ due to the Coulomb repulsion U. Thus, the symmetric case occurs if $\epsilon_d = -U/2$ and $\epsilon_d + U = +U/2$. Note that the Hamiltonian of the symmetric SIAM is invariant under a particle-hole transformation. Since ϵ_d is completely defined by U in this scenario, we can exclude it from our considerations for now. Therefore, the parameter space is restricted to U, Γ and T, easing the first analysis. Note that in the case of the asymmetric SIAM, i.e. for $\epsilon_d \neq -U/2$, all four parameters have to be taken into account.

2.2.1.1 Symmetric SIAM

First of all we look at the scenario with a large temperature T, so that $T \gg \max(U, \Gamma)$. In this case all states of the QI are equally populated and the interactions, i.e. Γ and U, on the QI are negligible at these high energy scales of T. Hence, the QI can be considered as if it is non-interacting and therefore the situation can be compared to the one where U and Γ are equal to zero. Thus, this regime is refereed to as the *free-orbital regime* and results in an effective local magnetic moment of $\mu^2_{\text{eff}} = 1/8$ [1] in the QI orbital.

If we now assume that $\Gamma \ll U$, then a *local moment regime* is formed as the temperature T decreases below U, so that $k_B T \lesssim U/10$. In this regime the QI states with $n_f = 0$ and $n_f = 2$ can be ignored and thus the QI looks like an effective spin-1/2 object. For $\Gamma = 0$ the magnetic moment would be therefore given by $\mu^2_{\text{eff}} = 1/4$. However, a small but finite Γ leads to a spin-spin interaction between the QI spin and the conduction band electrons (Kondo effect). As it turns out, the SIAM can be mapped onto the Kondo Hamiltonian in this regime via a Schrieffer-Wolf transformation [77] where the effective coupling in the Kondo Hamiltonian is given by $\rho J = -(8\Gamma)/(\pi U)$. Hence, the effect due to further reduction of the temperature T is clear: the effective local magnetic moment diminishes with decreasing T and vanishes for $T \to 0\,\text{K}$, i.e. $\mu^2_{\text{eff}} = 0$, due to the Kondo effect and the formation of a many-body singlet state. The scenario at $T = 0\,\text{K}$ corresponds to the situation where the QI degree of freedom is frozen out and is refereed to as the *strong coupling regime* (see also section 2.2.1.3). The smooth transition between the local moment and strong coupling regimes can be separated by the Kondo temperature

$$T_{\text{K}}(\Gamma, U) = 0.182\sqrt{\Gamma U}\exp\left(-\frac{\pi U}{8\Gamma}\right). \tag{2.20}$$

One can say that the local moment regime occurs for roughly $0.5T_{\text{K}} < T < 16T_{\text{K}}$ and is followed by a strong coupling regime for $T \ll T_{\text{K}}$ (say

[1] The values for the magnetic moments in the different regimes are all obtained from NRG calculations [75, 76].

approximately $T < \frac{1}{10}T_{\mathrm{K}}$). A pictorial description of the Kondo effect and its manifestation in the DOS is given in section 2.2.1.3.

An increasing Γ, while U is kept fixed, leads to an increase of the effective coupling $|J|$ and thus to an increase of the Kondo temperature $T_{\mathrm{K}}(\Gamma, U)$. This results in a shrinking of the local moment regime and in a growing of the strong coupling regime, until $\pi\Gamma \approx U$. For $\pi\Gamma \approx U$ the two transition regions, free-orbital to local moment and local moment to strong coupling, start to merge. Therefore, there is direct transition from the free-orbital regime ($T \gg \Gamma$) to the strong coupling regime ($T \ll \Gamma$) when $\Gamma \gg U$.

For purposes of illustration the various regimes of the symmetric SIAM are schematically sketched in Fig. 2.5 as a function of U, Γ and T.

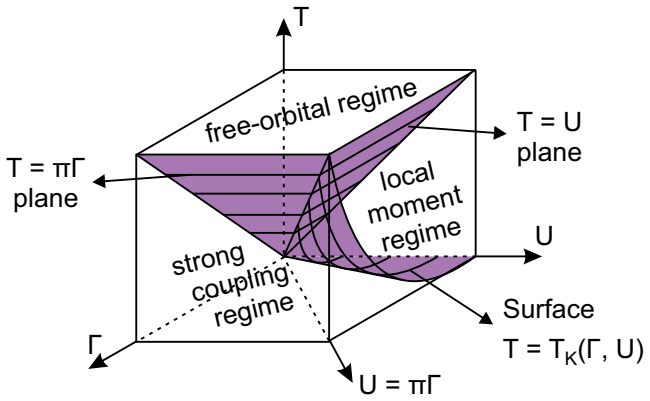

Figure 2.5: Schematic illustration of the different regimes for the symmetric SIAM. Note that the separation of the different regimes is actually very fuzzy and not so sharp as illustrated in the drawing. Illustration adapted from Ref. [75].

2.2.1.2 Asymmetric SIAM

Now, we extend our considerations to the asymmetric case, i.e. $\epsilon_d \neq -U/2$. In this scenario we have four parameters (U, Γ, ϵ_d and T) which we have to take into account. However, we can restrict ourselves to the parameter region with $\epsilon_d > -U/2$, because the SIAM Hamiltonian transforms to itself for a particle-hole symmetric conduction band when ϵ_d is replaced by $-(\epsilon_d + U)$. In the following we will discuss again the interesting cases with $\Gamma \ll U$ and $\Gamma \gg U$ and will consider what happens as ϵ_d is swept from $-U/2$ through zero to positive values.

First we look at the case where $\Gamma \ll U$ and steadily decrease $-\epsilon_d$ from $U/2$. The first characteristic case is then given for $\Gamma \ll -\epsilon_d \ll U$, so that Γ is still small compared to the separation of the QI states. For $T \gg U$ the situation is similar to the symmetric SIAM, i.e. we get again the *free-orbital regime*. But now if the temperature T drops below U, we end up in

a whole new regime which is referred to as the *valence-fluctuation regime*. This regime corresponds to the situation where the QI states with $n_f = 0$ and $n_f = 1$ are equally thermally populated, whereas the $n_f = 2$ state is thermally depopulated and can be removed from the considerations. In the valence-fluctuation regime the effective local magnetic moment is given by $\mu^2_{\text{eff}} = 1/6$ [2]. A further reduction of T leads to thermal depopulation of the $n_f = 0$ subspace, so that only the $n_f = 1$ state is present. Thus, a *local moment regime* is formed as in the symmetric SIAM, in which the spin-spin interaction between the QI spin and the conduction band electrons again gives rise to the Kondo effect. A further reduction of the temperature T leads then as in the symmetric case to a gradual transition into the *strong coupling regime* where the QI degree of freedom is again frozen out, so that $\mu^2_{\text{eff}} = 0$. The effect of a decreasing $-\epsilon_d$ leads to a hybridization of the $n_f = 0$ and $n_f = 1$ states which results in a diminishing local moment regime. As soon as $-\epsilon_d \ll \Gamma$, the local moment regime vanishes and we get a direct transition from the valence fluctuation into the strong coupling regime when the temperature is decreased from $T \gg U$ to $T \ll U$. Note that this transition is much steeper than the usual transition from the local moment to the strong coupling regime. The $-\epsilon_d = 0$ case is only special when $\Gamma = 0$, because then the valence fluctuation regime is also stable for $T \to 0\,\text{K}$.

For $\Gamma \gg U$, which implies $|\epsilon_d| \ll \Gamma$, the physics is dominated by Γ and similar to that of the symmetric SIAM: we have direct transition from the free-orbital regime ($T \gg \Gamma$) to the strong coupling regime ($T \ll \Gamma$).

Note that the asymmetric SIAM can be also mapped onto the Kondo Hamiltonian but now an additional potential scattering term [3] must be included in the Kondo Hamiltonian. Then the Kondo Hamiltonian has the form

$$H'_{\text{K}} = H_{\text{K}} + \sum_{k,k',\sigma} K c^\dagger_{\vec{k},\sigma} c_{\vec{k}',\sigma} \tag{2.21}$$

where the exchange coupling and potential scattering are given by

$$\rho J = -\frac{2\Gamma}{\pi}\left(\frac{1}{|E^*_0|} + \frac{1}{\epsilon_d + U}\right), \tag{2.22}$$

$$\rho K = \frac{\Gamma}{2\pi}\left(\frac{1}{|E^*_0|} - \frac{1}{\epsilon_d + U}\right). \tag{2.23}$$

Here E^*_0 describes the renormalization of the bare level due to high energy charge fluctuations, given by the self-consistent solution of $E^*_0 = \epsilon_d +$

[2] The values for the magnetic moments in the different regimes are all obtained from NRG calculations [75, 76].

[3] This potential scattering term makes the Kondo Hamiltonian particle-hole asymmetric. Physically, it describes the collision of an electron with the QI: an electron with the momentum $\vec{k}$ is scattered into the state with the momentum $\vec{k}'$. The spin of the scattered electron is conserved.

$(\Gamma/\pi)\ln(-U/E_0^*)$. The potential scattering has only little effect on the effective local magnetic moment. In the asymmetric case the Kondo temperature can be expressed by

$$T_{\mathrm{K}}(\Gamma,\epsilon_d,U) = 0.182|E_0^*|\sqrt{|\rho J_{\mathrm{eff}}|}\exp\left(-\frac{1}{|\rho J_{\mathrm{eff}}|}\right) \tag{2.24}$$

where $\rho J_{\mathrm{eff}} = \rho J[1+(\pi\rho K)^2]^{-1}$.

2.2.1.3 Kondo effect

In order to get a better idea of the physics behind the spin-flip processes which lead to the Kondo effect we will survey the different possibilities that result in a flip of the spin in the QI from $\uparrow$ to $\downarrow$, or vice versa, within the framework of the SIAM. The following presentation is based on Ref. [11]. For the sake of convenience we will restrict our considerations to the symmetric SIAM that is occupied by one electron ($n_f = 1$).

In this case there are two different possibilities to flip the spin of the QI:

1. first the orbital of the QI is emptied and then subsequently filled by a new electron from the conduction band

2. or alternatively first the QI is filled by an additional (second) electron from the conduction band and then subsequently one electron is again removed from the QI.

Both processes can result in a opposite spin of the QI in comparison to the initial state as schematically sketched in Fig. 2.6.

Since both events require an energy of at least $U/2$ they are forbidden classically, but allowed in the world of quantum physics due to the Heisenberg uncertainty principle. For a short time scale of $\tau \sim \hbar/(U/2)$ these excitations are permitted as a *virtual process* [10]. Hence, another electron has to reverse this virtual process within this timescale by tunneling to (from) the QI from (to) the conduction band in order to end up again with a singly occupied QI (energy conservation). Obviously, this processes most likely happen at the Fermi level of the bath and occur on time scales of some femtoseconds for typical values of U.

This *dynamic* process of spin exchange lowers the total energy of the system and leads to a formation of new many-body ground state which manifests itself as a sharp resonance at the Fermi level, the so-called Kondo resonance (see Fig. 2.6) and has a Lorentzian line shape with a logarithmic correction for $1 < |\omega/T_{\mathrm{K}}|$. At zero temperature the interaction results in a non-magnetic many-body singlet ground state ($|S\rangle = 1/\sqrt{2}(|\uparrow\downarrow\rangle - |\downarrow\uparrow\rangle)$) where the QI spin is paired with the many electrons of the bath. One says the QI spin is screened by the conduction band electrons.

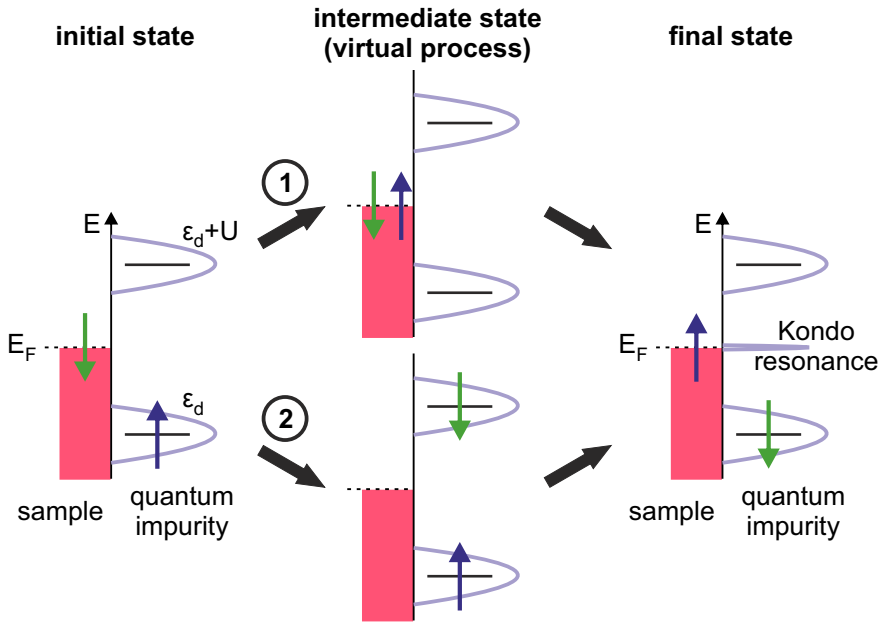

Figure 2.6: Schematic illustration of the processes which can lead to a flip of the QI spin. Within the framework of the SIAM the QI spin can be exchanged by an electron with opposite spin from the host metal via the processes 1 or 2. The virtual processes lead to an empty (process 1) or a doubly occupied (process 2) intermediate state of the QI. In the final state the QI is again singly occupied, but now with an electron of opposite spin. Many of these processes lead to the formation of a new many-body ground state which manifests itself as the Kondo resonance at the Fermi energy. Illustration adapted from Ref. [11].

The full width at half maximum (FWHM) Δ of the Kondo resonance at $T = 0\,\mathrm{K}$ is related by

$$\Delta = 2k_\mathrm{B}T_\mathrm{K} \tag{2.25}$$

to the Kondo temperature T_K [78]. With increasing temperature the Kondo resonance broadens and decreases in intensity. The effect of broadening is related to the smearing of the Fermi level with increasing temperature and can be approximately described by [78]

$$\Delta = \sqrt{(\alpha k_\mathrm{B}T)^2 + (2k_\mathrm{B}T_\mathrm{K})^2} \tag{2.26}$$

with $\alpha = 5.4$. The height of the Kondo resonance decays slowly with $1 - c(T/T_\mathrm{K})^2$ in the limit of $T \ll T_\mathrm{K}$ [72] and logarithmically in the case of $T \gtrsim T_\mathrm{K}$ [79]. In the case of a spin-$1/2$ object and for $T \lesssim T_\mathrm{K}$, i.e. in the local moment and strong coupling regime, the resonance height can be described

by the empirical formula

$$\rho(E=0) = \frac{\rho_0}{\left[1 + (2^{1/s} - 1)(\frac{T}{T_K})^2\right]^s} \tag{2.27}$$

with $s = 0.22$ [80].

However, in STS measurements the line shape of the Kondo resonance can show strong deviations from the Lorentzian shape. The reason for this stems from the fact that in STS measurements different tunneling path can contribute to the current and thus to the $dI/dV(V) \propto \rho(V)$ signal. To understand this behavior let us consider Fig. 2.7a. In this schematic illustration the electrons of the STM tip have three possibilities to tunnel into the states of the QI:

(i) by tunneling into an empty state of the substrate metal and then by hopping into the Kondo resonance,

(ii) by tunneling directly into the Kondo resonance,

(iii) or by tunneling into the localized state of the QI via a spin-flip process.

The shape of the Kondo resonance is then determined by the quantum interference effect between the two spin conserving channels [81], namely (i) and (ii). The third channel (iii) does not contribute to the quantum interference effect, since it results in a different final state of the QI (see Fig. 2.7a).

This quantum interference effects leads to a so-called Fano line shape of the Kondo resonance and can be described by [82, 83]

$$\rho(E) \propto \rho_0 + \frac{(q+\epsilon)^2}{1+\epsilon^2} \tag{2.28}$$

with the normalized energy

$$\epsilon = \frac{E - E_K}{(\Delta/2)} \tag{2.29}$$

where E_K specifies the position of the Kondo resonance. The form factor q is given by [81]

$$q = \frac{t_2}{\pi\rho_0 V t_1} \tag{2.30}$$

where t_1 and t_2 correspond to the tunneling probabilities of the two channels (i) and (ii), respectively. V accounts for the hybridization between the localized QI state and the conduction band. The term $\pi\rho_0 V$ in the denominator describes the probability of the hopping process from the substrate into the Kondo resonance in the channel (i). In the limit of $q \to \infty$, i.e. when the electrons mainly tunnel through the Kondo resonance, we obtain a Lorentzian line shape whereas for $q = 0$, i.e. when the electrons tunnel

mainly into the host metal and then into the Kondo resonance, a dip-like shape is observed in the energy spectrum. Some line shapes for different values of the form factor q are shown in Fig. 2.7b.

As demonstrated in chapter 5, quantum interference effects can also lead to spatial variations of the Kondo resonance on the same QI if the spin resides in a π orbital and thus is spatially delocalized.

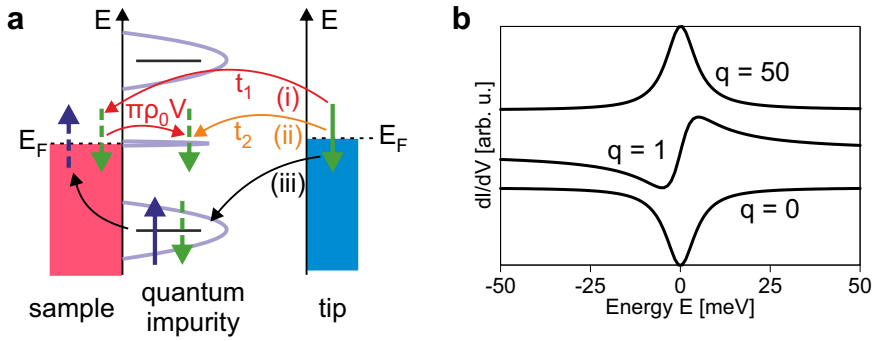

Figure 2.7: **a** Visualization of the different tunneling paths that electrons from the STM tip can use to tunnel into the sample. A quantum interference effect between the spin conserving tunneling paths (i) and (ii) results in a Fano line shape of the Kondo resonance. The indirect transition through the tunneling path (iii) via a spin-flip process does not contribute to the quantum interference effect because of the different final state. Adapted from Ref. [11]. **b** Illustration of the Fano line shape for different values of the form factor q.

2.2.2 Numerical renormalization group method

Ab initio methods such as the density functional theory (DFT) which are often used to describe the physical properties of systems on the atomic length scale have one shortcoming, namely that they fail to describe the correlation effects in a quantum impurity (QI) system which is coupled to a bath (fermionic or bosonic) that has a continuous excitation spectrum with arbitrarily small energies. The most famous example for these difficulties is the Kondo problem. Nevertheless, the correlation effects of a QI system can be studied by using the so-called numerical renormalization group (NRG) method. The NRG method, as its name already portends, is a numerical method which was originally developed by Wilson in order to solve the Kondo problem [73]. Its main advantage is that it allows to investigate QI systems in a systematic and a non-perturbative way and thus to treat quantum many-body systems that interact with a continuum of excitations. Nowadays, the NRG method has become a standard tool to investigate many different QI systems [84], e.g. the symmetric [75] and asymmetric [76] single-

impurity Anderson model (SIAM) and many others. The NRG method has been also used in this work in order to the describe the properties of a single QI based on the SIAM in chapter 3 and to investigate the interaction of two QIs based on the two impurity Anderson model in chapter 4. The following discussion is mainly based on the presentation of Ref. [84].

Before we look into the details of the NRG method, we briefly introduce the general strategy that is applied in basically all NRG approaches:

1. The bath is discretized logarithmically, i.e. the continuous bath spectrum is reduced to a discrete set of states. The bath spectrum is divided into a set of logarithmic intervals for this purpose.

2. The logarithmically discretized model is mapped onto a semi-infinite chain.

3. The semi-infinite chain is solved by iterative diagonalization.

Note that the NRG method can only be applied to a QI which is coupled to a bath of fermions or bosons that do not interact, because otherwise the strategy described above (and in more detail in the following) cannot be applied. A further precondition for the NRG method is that the Hamiltonian of the QI can be diagonalized exactly, i.e. that it has only a small number of degrees of freedom and that the Hilbert space is finite.

The general form of the Hamiltonian H of a QI system is given by

$$H = H_{\text{imp}} + H_{\text{bath}} + H_{\text{int}}. \tag{2.31}$$

The three parts correspond to the Hamiltonians of the QI (H_{imp}), the bath (H_{bath}) and impurity-bath interaction (H_{int}), respectively. For simplicity we will explain the NRG method and its main strategy using the Hamiltonian of the SIAM [74] (see also section 2.2.1). The SIAM describes a QI with a single localized energy level that is coupled to a bath of spin-$1/2$ fermions (electrons) which are non-interacting and thus fulfilling the requirements from above.

Hence, the Hamiltonian of the bath in the SIAM is given by

$$H_{\text{bath}} = \sum_{k,\sigma} \epsilon_k c^\dagger_{k,\sigma} c_{k,\sigma} \tag{2.32}$$

and the Hamiltonian describing the interaction between bath and QI by

$$H_{\text{int}} = \sum_{k,\sigma} V_k (d^\dagger_\sigma c_{k,\sigma} + c^\dagger_{k,\sigma} d_\sigma) \tag{2.33}$$

where the fermionic operator $c^\dagger_{k,\sigma}$ ($c_{k,\sigma}$) creates (annihilates) an electron with the spin $\sigma =\uparrow,\downarrow$ and momentum k in the conduction band. ϵ_k are the

one-electron energies of the conduction band states. The fermionic operators $d_\sigma^\dagger$ (d_σ) correspond to the QI whose Hamiltonian is given by

$$H_{\text{imp}} = \sum_\sigma \epsilon_d d_\sigma^\dagger d_\sigma + U d_\uparrow^\dagger d_\uparrow d_\downarrow^\dagger d_\downarrow. \tag{2.34}$$

Here U parametrizes the Coulomb repulsion between two electrons on the impurity. The coupling of the bath and the impurity is given by the k-dependent hybridization V_k.

The effect of the conduction band on the QI is completely determined by the so-called hybridization function

$$\Gamma(\omega) = \pi \sum_k V_k^2 \delta(\omega - \epsilon_k). \tag{2.35}$$

In order to treat the SIAM numerically it is more convenient to formulate the Hamiltonian H in an integral representation. Bulla et al. [85] have shown that a possible reformulation of the whole Hamiltonian in a one-dimensional energy representation is given by

$$H = H_{\text{imp}} + \sum_\sigma \int_{-D}^{D} d\epsilon\; g(\epsilon) a_{\epsilon,\sigma}^\dagger a_{\epsilon,\sigma} + \sum_\sigma \int_{-D}^{D} d\epsilon\; h(\epsilon)(d_\sigma^\dagger a_{\epsilon,\sigma} + d_\sigma a_{\epsilon,\sigma}^\dagger) \tag{2.36}$$

with a dispersion $g(\epsilon)$ and a hybridization $h(\epsilon)$. Here, without loss of generality, it is assumed that $\Gamma(\omega)$ lies completely within the energy interval $[-D, D]$, with $D > 0$. Henceforth, the energy cutoff D is set to $D = 1$ and used as the energy unit. The new introduced fermionic operators $a_{\epsilon,\sigma}^\dagger$ and $a_{\epsilon,\sigma}$ satisfy the standard anticommutation relation $\{a_{\epsilon,\sigma}^\dagger, a_{\epsilon',\sigma'}\} = \delta(\epsilon - \epsilon')\delta_{\sigma,\sigma'}$. Note that the Hamiltonian in this integral representation (eq. (2.36)) is equal to original Hamiltonian if the relation

$$\Gamma(\omega) = \pi \frac{d\epsilon(\omega)}{d\omega} h[\epsilon(\omega)]^2 \tag{2.37}$$

is fulfilled [85]. Here $\epsilon(\omega)$ is the inverse function to $g(\epsilon)$, i.e. $g[\epsilon(\omega)] = \omega$. For a given hybridization function $\Gamma(\omega)$ the functions $\epsilon(\omega)$ and $g(\epsilon)$ are not exactly predetermined, i.e. there are different possibilities to split the energy dependence ω between $\epsilon(\omega)$ and $h[\epsilon(\omega)]$. In the simplest case, namely for a constant hybridization function $\Gamma(\omega) = \Gamma_0$, this relation can be satisfied by $\epsilon(\omega) = \omega$, i.e. $g(\epsilon) = \epsilon$, and $h^2(\epsilon) = \Gamma_0/\pi$.

2.2.2.1 Logarithmic discretization

Solving the integral representation of the Hamiltonian presented in eq. (2.36) is numerically an unfeasible task, because of the infinite number of eigenstates of the bath. Therefore, it is necessary to determine the most essential eigenstates of the bath which contribute to the physics of interest and to

discretize the bath based on this knowledge. As it turns out, QI systems are usually shaped by the low energy eigenstates of the bath. Thus, to ensure a high resolution in the low energy scale of the bath a logarithmic mesh can be used. A set of intervals with the discretization points

$$x_n^{\pm} = \pm\Lambda^{-n},\ n = 0, 1, 2, \ldots \tag{2.38}$$

is then defined by the so-called discretization parameter $\Lambda > 1$. The width of each interval is given by

$$d_n = \Lambda^{-n} - \Lambda^{-n-1} = \Lambda^{-n}(1 - \Lambda^{-1}) \tag{2.39}$$

and as sketched in Fig. 2.8 the intervals get finer approaching the Fermi level.

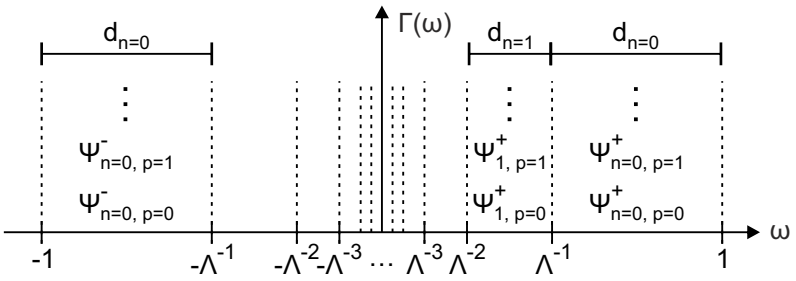

Figure 2.8: A logarithmic set of intervals is defined by introducing the discretization parameter Λ with the discretization points $x_n^{\pm} = \pm\Lambda^{-n}$. Here the logarithmic mesh is illustrated for $\Lambda = 2$. Around the Fermi level the logarithmic mesh gets finer and finer. Illustration adapted from Ref. [84]. In each interval a complete set of orthonormal functions $\Psi_{n,p}^{\pm}$ is defined (see eq. (2.40).

In the next step a complete set of orthonormal functions (Fourier series)

$$\Psi_{n,p}^{\pm} = \begin{cases} \frac{1}{\sqrt{d_n}} \exp^{\pm i(\omega_n p)\epsilon} & \text{for } x_{n+1}^{\pm} < \pm\epsilon < x_n^{\pm} \\ 0 & \epsilon \text{ outside the interval} \end{cases} \tag{2.40}$$

is defined within each interval (see also Fig. 2.8). Here the Fourier index p ranges from $-\infty$ to ∞ (only integer values) and the fundamental Fourier frequency is given by $\omega_n = 2\pi/d_n$. Now the Hamiltonian in eq. (2.36) is expressed in terms of discrete operators by expanding the creation and annihilation operators in eq. (2.36) in this basis, i.e.

$$a_{\epsilon,\sigma} = \sum_{n,p} [a_{n,p,\sigma}\Psi_{n,p}^{+}(\epsilon) + b_{n,p,\sigma}\Psi_{n,p}^{-}(\epsilon)] \tag{2.41}$$

with

$$a_{n,p,\sigma} = \int_{-1}^{1} d\epsilon\ [\Psi_{n,p}^{+}(\epsilon)]^* a_{\epsilon,\sigma} \tag{2.42}$$

and

$$b_{n,p,\sigma} = \int_{-1}^{1} d\epsilon \; [\Psi^{-}_{n,p}(\epsilon)]^* a_{\epsilon,\sigma}. \tag{2.43}$$

Note that so far no approximations have been made. Thus, the Hamiltonian H is still exact in the new basis and recovers the whole continuum of the bath. The actual discretization of the Hamiltonian is achieved by dropping all $p \neq 0$ terms. Although this seems to be a crude approximation it turns out that the results obtained by this manner yield astonishingly good results for values of Λ as large as $\Lambda = 2$. Physically this can be understood by considering the operators $a_{n,p,\sigma}$ and $b_{n,p,\sigma}$: the terms with $p \neq 0$ are eigenstates with large eigenenergies and exhibit a larger distance to the impurity in the phase space. Therefore, one can argue that the couplings of the $p \neq 0$ states to the impurity are small. Then the discretized Hamiltonian, after dropping the $p \neq 0$ states and renaming the operators $a_{n,0,\sigma} \equiv a_{n,\sigma}$ etc, reads

$$\begin{aligned} H =& H_{\text{imp}} + \sum_{n,\sigma} (\xi^{+}_{n} a^{\dagger}_{n,\sigma} a_{n,\sigma} + \xi^{-}_{n} b^{\dagger}_{n,\sigma} b_{n,\sigma}) \\ &+ \frac{1}{\sqrt{\pi}} \sum_{n,\sigma} (d^{\dagger}_{\sigma} (\gamma^{+}_{n} a_{n,\sigma} + \gamma^{-}_{n} b_{n,\sigma}) + (\gamma^{+}_{n} a^{\dagger}_{n,\sigma} + \gamma^{-}_{n} b^{\dagger}_{n,\sigma}) d_{\sigma}) \end{aligned} \tag{2.44}$$

in the new basis with $\gamma^{\pm 2}_{n} = \int^{\pm,n} d\epsilon \; \Gamma(\epsilon)$ and a discrete set of energies [85]

$$\xi^{\pm}_{n} = \frac{\int^{\pm,n} d\epsilon \; \Gamma(\epsilon)\epsilon}{\int^{\pm,n} d\epsilon \; \Gamma(\epsilon)} \tag{2.45}$$

and the convention

$$\int^{+,n} d\epsilon \equiv \int_{x^{+}_{n+1}}^{x^{+}_{n}} d\epsilon, \;\; \int^{-,n} d\epsilon \equiv \int_{x^{-}_{n}}^{x^{-}_{n+1}} d\epsilon. \tag{2.46}$$

2.2.2.2 Mapping on a semi-infinite chain

The next step in the NRG approach is to transform the discretized Hamiltonian (eq. (2.44)) into a semi-infinite chain form, since it is more convenient to solve a chain Hamiltonian by an iterative procedure. In the chain Hamiltonian the first site of the chain will represent the degrees of freedom of the impurity that will be only directly coupled to one conduction electron degree of freedom with the operator $c^{(\dagger)}_{0,\sigma}$. Hence, the form of the operator $c^{(\dagger)}_{0,\sigma}$ can be directly read off from the second line in eq. (2.44):

$$c_{0,\sigma} = \frac{1}{\sqrt{\xi_0}} \sum_{n} (\gamma^{+}_{n} a_{n,\sigma} + \gamma^{-}_{n} b_{n,\sigma}) \tag{2.47}$$

with the normalization constant

$$\xi_0 = \sum_{n} ((\gamma^{+}_{n})^2 + (\gamma^{-}_{n})^2) = \int_{-1}^{+1} d\epsilon \; \Gamma\epsilon. \tag{2.48}$$

The new defined operator $c^{(\dagger)}_{0,\sigma}$ is of course not orthogonal to the operators $a^{(\dagger)}_{n,\sigma}$ and $b^{(\dagger)}_{n,\sigma}$ in eq. (2.44). However, the desired chain Hamiltonian is obtained by constructing a new set of orthogonal operators $c^{(\dagger)}_{n,\sigma}$ from $c^{(\dagger)}_{0,\sigma}$ and $a^{(\dagger)}_{n,\sigma}$, $b^{(\dagger)}_{n,\sigma}$. This is done by standard tridiagonalization procedure and gives the chain Hamiltonian

$$\begin{aligned} H =& H_{\text{imp}} + \sqrt{\frac{\xi_0}{\pi}} \sum_{\sigma} (d^{\dagger}_{\sigma} c_{0,\sigma} + c^{\dagger}_{0,\sigma} d_{\sigma}) \\ &+ \sum_{\sigma,n=0}^{\infty} \left[\epsilon_n c^{\dagger}_{n,\sigma} c_{n,\sigma} + t_n (c^{\dagger}_{n,\sigma} c_{n+1,\sigma} + c^{\dagger}_{n+1,\sigma} c_{n,\sigma}) \right] \end{aligned} \tag{2.49}$$

with

$$c^{(\dagger)}_{n,\sigma} = \sum_{m=0}^{\infty} (u^{(*)}_{n,m} a^{(\dagger)}_{m,\sigma} + v^{(*)}_{n,m} b^{(\dagger)}_{m,\sigma}) \tag{2.50}$$

which annihilates (creates) an electron on the n-th site of the semi-infinite chain, which is often called Wilson chain. The recursion relations of the parameters of the Wilson chain, namely the on-site energies ϵ_n, the hopping matrix elements t_n and the coefficients $u_{n,m}$ and $u_{n,m}$, can be derived by equating the coefficients in eq. (2.44) and eq. (2.49). The general form of these parameters can be found in [84]. For the sake of convenience we only focus on the results for a constant hybridization function $\Gamma(\omega) = \Gamma_0$ where the parameters can be calculated analytically. In this case ϵ_n is zero for all n, i.e. $\epsilon_n = 0$, and t_n is given by

$$t_n = \frac{(1+\Lambda^{-1})(1-\Lambda^{-n-1})}{2\sqrt{1-\Lambda^{-2n-1}}\sqrt{1-\Lambda^{-2n-3}}} \Lambda^{-n/2}. \tag{2.51}$$

For large n it reduces to

$$t_n \to \frac{1}{2}(1+\Lambda^{-1})\Lambda^{-n/2}. \tag{2.52}$$

As seen, the hopping parameter t_n decreases exponentially with the distance from the QI. This finding is essential for the discussion of the final step of the NRG method, namely the iterative diagonalization, because this *separation of energy scales* allows us to evaluate the terms in the sum in the chain Hamiltonian one after another as described in the next section. A schematic sketch of the Wilson chain is shown in Fig. 2.9.

The wave functions of the conduction electron sites of the Wilson chain can be considered as a sequence of shells which are peaked at the QI site, i.e. the maximum of their wave functions are located at the position of the QI, and extend in space as $\propto \Lambda^{n/2}$. The first site of the Wilson chain represents the shell which is maximally localized around the QI.

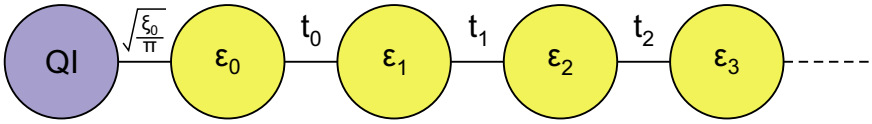

Figure 2.9: Illustration of the semi-infinite chain (Wilson chain) where the QI only couples directly to the first site of chain. The strength of the coupling of the QI is given by $\sqrt{\frac{\xi_0}{\pi}}$. The hopping parameter t_n decreases exponentially with increasing n. Adapted from Ref. [84].

2.2.2.3 Iterative diagonalization

In the last step of the NRG method finally the renormalization group (RG) character of the approach enters by defining an iterative RG procedure for the semi-infinite chain. The chain Hamiltonian in eq. (2.49) can be considered as a series of Hamiltonians H_N which reaches H in the limit of $N \to \infty$ ($N = 0, 1, 2, \ldots$):

$$H = \lim_{N\to\infty} \Lambda^{-(N-1)/2} H_N \tag{2.53}$$

with

$$\begin{aligned} H_N =& \Lambda^{(N-1)/2}\Bigg(H_{\text{imp}} + \sqrt{\frac{\xi_0}{\pi}} \sum_\sigma (d_\sigma^\dagger c_{0,\sigma} + c_{0,\sigma}^\dagger d_\sigma) \\ &+ \sum_{\sigma,n=0}^{N} \epsilon_n c_{n,\sigma}^\dagger c_{n,\sigma} + \sum_{\sigma,n=0}^{N-1} t_n (c_{n,\sigma}^\dagger c_{n+1,\sigma} + c_{n+1,\sigma}^\dagger c_{n,\sigma}) \Bigg). \end{aligned} \tag{2.54}$$

Here, the scaling factor $\Lambda^{(N-1)/2}$ and consequently $\Lambda^{-(N-1)/2}$ have been introduced to remove the N dependence of the hopping matrix element t_n for large N.

Based on eq. (2.54) two adjacent Hamiltonians are connected by the relation

$$\begin{aligned} H_{N+1} =& \sqrt{\Lambda} H_N + \Lambda^{N/2} \sum_\sigma \epsilon_{N+1} c_{N+1,\sigma}^\dagger c_{N+1,\sigma} \\ &+ \Lambda^{N/2} \sum_\sigma t_N (c_{N,\sigma}^\dagger c_{N+1,\sigma} + c_{N+1,\sigma}^\dagger c_{N,\sigma}) \end{aligned} \tag{2.55}$$

with the Hamiltonian

$$H_0 = \Lambda^{-1/2} \left(H_{\text{imp}} + \sum_\sigma \epsilon_0 c_{0,\sigma}^\dagger c_{0,\sigma} + \sqrt{\frac{\xi_0}{\pi}} \sum_\sigma (d_\sigma^\dagger c_{0,\sigma} + c_{0,\sigma}^\dagger d_\sigma) \right) \tag{2.56}$$

describing the starting point, i.e. the first Hamiltonian of the sequence of Hamiltonians H_N. This starting Hamiltonian specifies a two-site cluster that

is formed by the QI and the first site of the Wilson chain. The recursive relation in eq. (2.55) can be recognized as a RG transformation R:

$$H_{N+1} = R(H_N). \tag{2.57}$$

In the NRG approach the Hamiltonians H_N and thus the RG flow are characterized by the eigenenergies $E_N(r)$ of the Hamiltonian H_N:

$$H_N|r\rangle_N = E(r)_N|r\rangle_N,\ r = 1, \ldots, N_S. \tag{2.58}$$

Here $|r\rangle_N$ denotes the eigenstates and N_S the dimension of the Hamiltonian H_N. In order so set up an iterative procedure for the diagonalization of the Hamiltonian H_N and to discuss the flow of the eigenenergies $E_N(r)$, let us assume that for a given N the Hamiltonian H_N has already been diagonalized, i.e. that the eq. (2.58) has been solved so that all eigenstates $|r\rangle_N$ and eigenenergies $E_N(r)$ are known. The basis of H_{N+1} is then constructed by product states which consist of the eigenbasis of H_N and a suitable basis $|s(N+1)\rangle$ of the new added site of the Wilson chain:

$$|r;s\rangle_{N+1} = |r\rangle_N \otimes |s(N+1)\rangle \tag{2.59}$$

The matrix of the Hamiltonian H_{N+1}, which describes the enlarged Wilson chain, is then given by:

$$H_{N+1}(rs, r's') = {}_{N+1}\langle r;s|H_{N+1}|r';s'\rangle_{N+1}. \tag{2.60}$$

A further diagonalization of this matrix results in the new eigenenergies $E_{N+1}(w)$ and the eigenstates $|w\rangle_{N+1}$ of the extended Hamiltonian H_{N+1}. The new eigenstates are related by

$$|w\rangle_{N+1} = \sum_{rs} U(w, rs)|r;s\rangle_{N+1} \tag{2.61}$$

via the unitary matrix U to the basis $|r;s\rangle_{N+1}$. After each diagonalization step the ground-state energy is extracted and all energies are measured relative to the ground state energy.

However, simply using the iterative procedure described above is insufficient for long Wilson chains. The reason is not related to the theoretical approach but to the numerical diagonalization: adding a new site to the Wilson chain increases exponentially the dimension of H_{N+1} with N. Thus, the dimension of the matrix becomes already very large after a few iteration cycles and makes an numerical diagonalization unfeasible. This problem can be overcome by introducing a simple truncation scheme: after each iteration (diagonalization) cycle only the N_l eigenstates with the lowest eigenenergy are kept. This truncation of high-energy eigenstates leads to a fixed dimension N_l of the Hilbert space and ensures that the computational time only increases linearly with length of the Wilson chain. The value of N_l strongly

depends on the model and has to be determined by carrying out calculations with different (increasing) N_l till the eigenenergies converge. Although, this truncation scheme seems to be crude, it is justified by the separation of energy scales as mentioned before. Simultaneously, the temperature is reduced after each step of iteration, in order to ensure that the discarded high energy states do not contribute to the thermodynamic expectation values.

The iteration procedure itself is usually stopped when the desired temperature is reached, or the desired stable low temperature fixed point. Here a stable fixed point is characterized by a set of eigenenergies that do not change with further increasing iteration number N.

2.2.3 Two impurity Anderson model

The simplest models which describe the interaction between two QIs are the two impurity Kondo model (TIKM) [86, 87, 88, 89, 90, 91, 92, 93, 94, 95] and the two impurity Anderson model (TIAM) [96, 91, 97, 98, 99, 100, 101, 102, 103]. Both models are extensions of the previously described single QI models, namely of the Kondo model and the SIAM, respectively. Although, the TIKM and the TIAM have been both studied intensively in the past, their physical properties are far from being completely and well understood. The reason for this is the competition between various interactions which can lead to different physical properties of the system, depending sensitively on the relative strength of the various interactions. For this reason we will consider separately the most relevant interactions in order to describe qualitatively the physical effects of those on the QIs in the following sections. Our considerations are in analogy to the SIAM based on the TIAM.

A general form of the TIAM Hamiltonian is given by $H = H_0 + H_{\mathrm{QIS}} + H_{\mathrm{hyb}}$ where H_0 describes the conduction band, H_{QIS} the two interacting QIs and H_{hyb} the hybridization between the conduction band and the QIs. The conduction band Hamiltonian H_0 is in detail given by

$$H_0 = \sum_{\vec{k},\sigma} \epsilon_{\vec{k},\sigma} c^\dagger_{\vec{k},\sigma} c_{\vec{k},\sigma} \tag{2.62}$$

where $c^\dagger_{\vec{k},\sigma}$ ($c_{\vec{k},\sigma}$) creates (annihilates) an electron with the spin σ and momentum $\vec{k}$ in the conduction band with the dispersion $\epsilon_{\vec{k},\sigma}$. The Hamiltonian which describes the two interacting QIs can be expressed by

$$\begin{aligned} H_{\mathrm{QIS}} = & \sum_{j,\sigma} E_j d^\dagger_{j,\sigma} d_{j,\sigma} + U \sum_j n_{j,\uparrow} n_{j,\downarrow} + \frac{2U' - J_{\mathrm{ex}}}{2} \sum_{\sigma,\sigma'} n_{1,\sigma} n_{2,\sigma'} \\ & - 2J_{\mathrm{ex}} \vec{S}_1 \vec{S}_2 + J_{\mathrm{ex}} (d^\dagger_{1,\uparrow} d^\dagger_{1,\downarrow} d_{2,\downarrow} d_{2,\uparrow} + \mathrm{h.c.}) \\ & + \frac{t}{2} \sum_\sigma \left(d^\dagger_{1,\sigma} d_{2,\sigma} + d^\dagger_{2,\sigma} d_{1,\sigma} \right) \end{aligned} \tag{2.63}$$

where $d^\dagger_{j,\sigma}$ ($d_{j,\sigma}$) creates (annihilates) an electron with spin σ in a local level of the QI j with the energy E_j. J_{ex} is a (Heisenberg) exchange coupling, $\vec{S}_j$ denotes the spin of the QI j and t is the tunneling (hopping) strength between the two QIs. Furthermore, the intra- and interorbital Coulomb repulsions are denoted by U and U', respectively. To ensure rotational invariance of the spin, a pair-hopping term (second term in the second line of eq. (2.63)) proportional to J_{ex}, is included. The hybridization between the conduction band and the QIs is described by

$$H_{\mathrm{hyb}} = \sum_{j\in\{1,2\},\vec{k},\sigma} V_{j,\vec{k}} c^\dagger_{\vec{k},\sigma} e^{\mathrm{i}\vec{k}\vec{R}_j} d_{j,\sigma} + \mathrm{h.c.}\,, \tag{2.64}$$

where $V_{j,\vec{k}}$ describes the hybridization strength with the bath and $\vec{R}_j$ the location of the QI j. Note that this model is also used in chapter 4 in order to investigate the interaction of two QIs with delocalized spins.

In summary, the interactions between the two QIs which are covered by the here presented TIAM and which will be discussed qualitatively in the following sections are:

1. a direct exchange coupling between the two QIs,
2. an indirect exchange interaction which does not appear explicitly in the Hamiltonian, but is encoded implicitly in it and
3. single-particle hopping due to direct chemical hybridization between the two QIs.

Furthermore it is important to note that the Kondo physics, i.e. the antiferromagnetic exchange interaction between the conduction band electrons and the QIs, is also encoded in the TIAM (compare with SIAM in section 2.2.1).

2.2.3.1 Direct exchange coupling

First we will discuss the effect of the direct exchange coupling J_{ex} between the two QIs according to Ref. [103], i.e. for now we neglect the indirect exchange interaction and the direct hopping term t. Thus, we have only a competition between the Kondo effect and the direct exchange coupling J_{ex}. Remember that the Kondo effect itself results from an antiferromagnetic coupling J between the particular single impurity and the conduction band electrons (see also section 2.2.1) and is characterized by the energy scale $k_B T_{\mathrm{K}}$.

In the case of a large ferromagnetic exchange coupling between the two impurities, i.e. $J_{\mathrm{ex}} > 0$ and $J_{\mathrm{ex}} > k_B T_{\mathrm{K}}$, the spins of the two QIs get aligned parallel. Thus, they can be considered as one object with spin $S = 1$. The physics is similar to what happens in a multi-orbital SIAM, i.e.

the direct exchange coupling leads to a narrowing of the Kondo resonance [103, 104, 105]. Hence, also the Kondo temperature of the two directly coupled QIs is reduced in comparison to a single QI ($T_{\mathrm{K}}^{\mathrm{TIAM}} < T_{\mathrm{K}}$).

Furthermore, at excitation energies in the order of $\omega \approx \pm J_{\mathrm{ex}}$ small humps next to the narrow Kondo resonance are visible in the DOS. These humps indicate the break down of the weak correlations between the two QIs, i.e. the two impurities behave like two uncoupled and isolated single QIs for energies larger than $|\omega| > J_{\mathrm{ex}}$. This is schematically sketched in Fig. 2.10.

The same behavior is also reproduced in the temperature dependency. For temperatures T larger than the direct ferromagnetic coupling J_{ex}, i.e. $k_B T > J_{\mathrm{ex}}$, the two QIs behave like two uncoupled impurities and thus the Kondo resonance is described by the SIAM. Only for temperatures $k_B T \lesssim J_{\mathrm{ex}}$ the direct exchange interaction plays a dominant role and causes the narrowing of the Kondo resonance and the appearance of the above mentioned humps in the DOS.

In contrast, a large antiferromagnetic coupling, i.e. $J_{\mathrm{ex}} < 0$ and $|J_{\mathrm{ex}}| > k_B T_{\mathrm{K}}$, favors the locking of the two QI spins into a singlet state ($S = 0$). This leads to a suppression of the Kondo effect and opens up a gap at the Fermi level. The formation of the gap is simply related to the fact that the singlet state does not give rise to the Kondo effect. Side peaks in the DOS at the excitation energies $\omega = \pm J_{\mathrm{ex}}$ in this case indicate the excitation into the triplet state which again undergoes a Kondo effect (see Fig. 2.10). The gap formation happens only at temperatures $k_B T \lesssim |J_{\mathrm{ex}}|$.

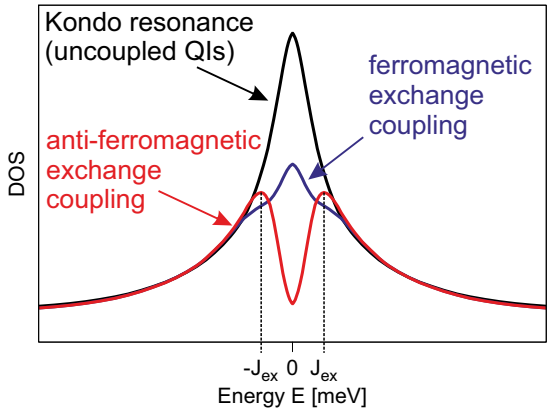

Figure 2.10: Illustration of the effect of direct exchange coupling J_{ex} on the Kondo resonance of the two interacting QIs with spin-1/2. An antiferromagnetic exchange coupling leads to a formation of molecular singlet state and thus to a suppression of the Kondo resonance. For a ferromagnetic exchange coupling the two QIs form a $S = 1$ state which leads to a reduction of the Kondo temperature and thus to a narrowing of the Kondo resonance.

2.2.3.2 Indirect exchange coupling

In the case of the indirect exchange coupling the interaction is mediated by the non-interacting conduction band electrons and is known as the Ruderman-Kittel-Kasuya-Yosida (RKKY) interaction [48, 49, 50]. Like for direct exchange coupling (see section 2.2.3.1) the RKKY interaction can lead to ferromagnetic or anti-ferromagnetic coupling between the two QIs. The main difference stems from the fact that the RKKY interaction has a spatial dependence, i.e. depending on the distance R between the two impurities it can lead to ferromagnetic or anti-ferromagnetic coupling. Since it does not rely on the direct overlap of the wave functions like the direct exchange coupling, it produces a long-ranged magnetic interaction.

The RKKY interaction is usually derived by mapping the TIAM onto a TIKM via a Schrieffer-Wolf transformation. Then, by using second-order perturbation theory in J one can show that the RKKY interaction between two localized spins in a free electron gas in three-dimensions (3D) is given by [48]

$$J_{\mathrm{RKKY}}(R) = 9\pi \frac{J}{E_F}\left(\frac{\cos(2k_F R)}{(2k_F R)^3} - \frac{\sin(2k_F R)}{(2k_F R)^4}\right) \tag{2.65}$$

with k_F being the Fermi momentum and J the Kondo coupling.

According to eq. (2.65) the RKKY interaction J_{RKKY} is ferromagnetic for small $k_{\mathrm{F}}R$ and starts to oscillate between ferromagnetic and antiferromagnetic with increasing $k_{\mathrm{F}}R$. The envelope of J_{RKKY} decays with $(k_{\mathrm{F}}R)^{-3}$ in first approximation. As in the case of the direct exchange coupling the physics of the two impurities are governed by the competition [91, 94, 95] between the Kondo effect and, in this case, the indirect RKKY interaction J_{RKKY}.

If the indirect exchange interaction J_{RKKY} is much larger than the Kondo scale T_{K}, i.e. $J_{\mathrm{RKKY}} \gg k_B T_{\mathrm{K}}$, and ferromagnetic, then the spins of the two QIs get locked to a $S = 1$ state. In this scenario the two coupled impurities undergo a so-called two-stage Kondo effect. At high temperatures the $S = 1$ spin is partially screened, i.e. the conduction band electrons only screen a $1/2$ unit of the total $S = 1$ spin. If the temperature is decreased further the residual $1/2$-spin of the two coupled QIs gets also screened by the conduction band electrons. Thus, the coupled system exhibits two characteristic Kondo temperatures T_{K1} and T_{K2} which define the partial screening of a spin-$1/2$ unit [95]. Note that the new Kondo temperatures are much smaller than the Kondo temperature of a single QI, i.e. $T_{\mathrm{K2}} < T_{\mathrm{K1}} < T_{\mathrm{K}}$. In the DOS this characteristics are reflected by the observation of two different Kondo resonances, i.e. with different widths, for temperatures T in the order of T_{K1} and T_{K2}.

In contrast, if the interactions are dominated by a antiferromagnetic J_{RKKY}, i.e. $J_{\mathrm{RKKY}} < 0$ and $|J_{\mathrm{RKKY}}| \gg k_B T_{\mathrm{K}}$, then the impurity spins are

a locked into a singlet state ($S = 0$). Hence, the Kondo effect plays no role. Like for the direct exchange coupling this leads to a suppression of the Kondo resonance in the DOS.

For $k_B T_K \gg |J_{RKKY}|$, i.e. when the interaction is dominated by the antiferromagnetic coupling of the impurities to the conduction band, the two QIs are independently screened by the electrons of the bath. Thus, the physics of the impurities is described separately by a SIAM, respectively.

2.2.3.3 Single-particle hopping

The effect of single-particle hopping due to direct chemical hybridization between two QIs received only little attention [99, 103] in comparison to the direct or indirect exchange interaction. In most studies of the TIAM the term due to single-particle hopping is actually neglected. Hence, there is no well-established description of the physical properties which arise due to direct chemical hybridization. One reason for the less efforts in understanding the effect of single particle hopping might be related to the fact that no such a system has been realized experimentally up to now. However, within this work we succeeded in tailoring a system where the magnetic properties of the system are defined by the competition of the direct non-magnetic chemical hybridization between the two QIs and the Kondo effect. Thus, we refer the reader to chapter 4 where the unusual features due to this competition are described extensively.

2.3 Quantum phase transitions

The study of the interaction of two QIs with delocalized spins in chapter 4 revealed that the system undergoes a quantum phase transition. Hence, in the following section the terminology and different types of quantum phase transitions will be briefly introduced in order to give the reader an idea of the difference between classical and quantum phase transitions. For more details we refer the reader to Ref. [106, 107, 108].

In classical physics a phase transition describes the qualitative change of the properties of a system, as a result of the change of an external control parameter, e.g. temperature or pressure. An everyday example is the vaporization of water upon heating to the boiling point, i.e. a transition between the liquid and gaseous state of matter. The driving force in classical phase transitions is a competition between the entropy and energy of the system. But since the entropy of classical systems is equal to zero at absolute zero temperature, no classical phase transitions can occur.

However, at zero temperature also phase transitions can take place – the so-called quantum phase transitions (QPT). A QPT is a result of the competition between different ground states at absolute zero temperature and can only be accessed upon variation of a non-thermal control parameter[106,

107]. In contrast to classical phase transitions, the QPT describes a abrupt change in the many-body ground state of the system due to quantum fluctuations [106, 107], which result from the Heisenberg uncertainty principle. As classical phase transitions, also QPTs can be classified into first-order and continuous transitions according to Ehrenfest's classification. The transition point in a QPT between the two stable phases is called quantum critical point (QCP).

QI systems, as considered in the previous sections, belong to the class of so-called impurity transitions, i.e. to QPTs where only the degrees of freedom of a subsystem, i.e. of the QI, become quantum critical [108]. The impurity QPT is completely independent of possible phase transitions of the bath. Depending on the type (order) of the QPT the interplay between thermal and quantum fluctuations leads to different finite temperature crossovers in the vicinity of the QCP as depicted in Fig. 2.11.

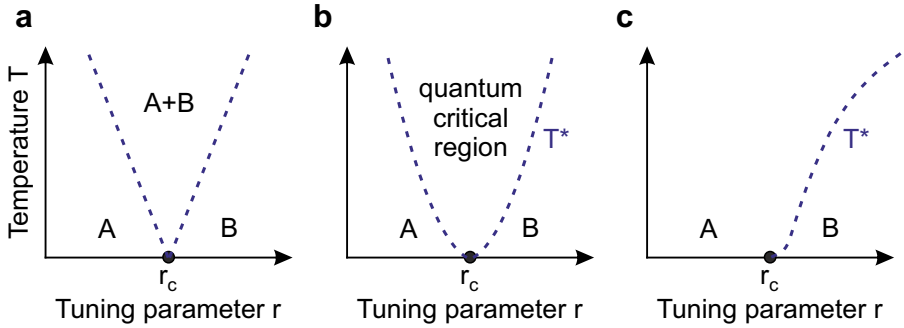

Figure 2.11: **a** Finite temperature phase diagram of an impurity QPT of first-order. A and B are the two stable phases of the QI system and r_c the QCP, which defines the transition point between the two stable phases. The region $A + B$ at finite temperature is simply a thermodynamic mixture of the two stable phases A and B. **b** As panel a, but an impurity QPT of second-order. The boundary T^* of the quantum critical region follows a power law (for more details see main text). In this quantum critical region the physics of the system are determined by thermal and quantum fluctuations. **c** As panel a, but a QPT of Kosterlitz-Thouless type (infinite-order QPT). At finite temperature the two stable phases are separated by only one crossover line. At the QCP T^* vanishes exponentially. Figures adapted from Ref. [108].

A first-order QPT, as shown in Fig. 2.11a, is a simple level crossing in the many-body ground state of the system with A and B being the two distinct stable phases. The parameter r is the non-thermal tuning parameter and r_c the position of the QCP at zero temperature. The region $A + B$ at finite temperature T is simply a thermodynamic mixture of A and B. A quantum critical region at finite temperature is only present for second-

order QPTs as depicted in Fig. 2.11b. The boundaries of the quantum critical region are described by $T^* \propto |d^\nu| = |(r - r_c)/r_c|^\nu$ [108], where $d = (r - r_c)/r_c$ is a dimensionless measure for the distance to the QCP r_c and ν the correlation length critical exponent. The physics in the quantum critical region are governed by quantum and thermal fluctuations and can show unexpected physical behavior, e.g. non-Fermi liquid behavior. In an infinite-order QPT of Kosterlitz-Thouless type, as illustrated in Fig. 2.11c, the system shows only one crossover line T^* at finite temperature and T^* vanishes exponentially at the QCP in this scenario [108].

In chapter 4 the two stable phases of the two interacting QIs correspond to a partially Kondo-screened triplet and a singlet ground state. The QPT is driven by the chemical hybridization between the two QIs, i.e. by the non-thermal tuning parameter t – the tunneling term between the two QIs (see also section 2.2.3). However, we did not determine the exact type of QPT for the system in chapter 4, but according to previous studies of similar systems [109, 110], where the singlet-triplet transition in quantum dots has been investigated, the QPT of the system in chapter 4 should be of Kosterlitz-Thouless type (Fig. 2.11c). According to Ref. [109], it is expected that T^* depends exponentially on the distance $\Delta t = t - t_c$ from the QCP t_c as long as $\Delta t < T_\mathrm{K}$:

$$T^* \sim \exp(-T_\mathrm{K}/\Delta t). \tag{2.66}$$

For $\Delta t > T_\mathrm{K}$ a linear dependence of T^* on Δt is expected [109]:

$$T^* \approx \Delta t. \tag{2.67}$$

The Kondo temperature T_K of the partially Kondo-screened triplet state ($t < t_c$, for more details see chapter 4) remains constant for different t in this many-body ground state.

CHAPTER 3

Transfering spin into an extended π orbital of a large molecule

Atoms are very special: they like certain particular partners, certain particular directions, and so on. It is the job of physics to analyze why each one wants what it wants. –
Richard P. Feynman

3.1 Introduction

In order to investigate spin-dependent phenomena and specially the interaction of QIs with a net spin in a systematic way it is important to obtain full control of the properties and the geometric structure of these QIs on the metal surface. However, it is not possible to control precisely the adsorption geometry of two single complex structures, like metal-molecule complexes, on the surface with respect to each other, but this is essential if one wants to study the interaction between two QIs. The most intuitive way to avoid this problem and to achieve full control of the geometry of the QIs is to embed them in well-ordered structures, e.g. in self-assembled molecular layers.

In the following article in section 3.2 we demonstrate the formation of a spin-1/2 metal-molecule complex that is embedded in a self-assembled molecular layer. The metal-molecule complex is formed by adsorption of single Au atoms on a 3,4,9,10-perylene-tetracarboxylic dianhydride (PTCDA) monolayer physisorbed on the Au(111) surface. Consequently, the newly formed complex is integrated into the monolayer and its geometry with respect to its neighbors and the substrate is fixed. Furthermore the chemical reaction between the Au atom and the PTCDA molecule leads to an unpaired electron in the highest occupied molecular orbital of the Au-PTCDA complex. Since this orbital has a π orbital character and thus extends over the whole Au-PTCDA complex also the spin is delocalized over the whole complex.

The spin-1/2 nature of the Au-PTCDA complex we demonstrate by proving that the sharp zero-bias differential conductance peak originates from the Kondo effect using low-temperature scanning tunneling microscopy (STM) and spectroscopy (STS). By temperature dependent measurements we show that zero-bias differential conductance peak exhibits the characteristics of a Kondo spin-1/2 system and determine the Kondo temperature to be $T_K = (38 \pm 8)$ K. By means of density functional theory (DFT) and many-body perturbation theory (MBPT) we calculate the geometric and electronic structure of the Au-PTCDA complex and obtain excellent agreement between theory and experiment. We find out that the Au atom has four equivalent adsorptions sites on the PTCDA molecules and that the $6s$ orbital of the Au atom and the lowest unoccupied molecular orbital (LUMO) of the PTCDA molecule hybridize strongly, forming a bonding (LUMO+Au) and an antibonding (LUMO-Au) combination. It turns out that the LUMO+Au orbital is delocalized over the whole complex, half-filled and thus giving rise to the Kondo effect. Furthermore, we describe the low-energy excitation spectrum of the spin degree of freedom, i.e. the Kondo effect, by using the numerical renormalization group (NRG) approach based on the SIAM. Taking into account the full energy dependence of the coupling function the NRG provides an accurate description of the Kondo resonance and yields a Kondo temperature that is very close to the experimental value.

This quantitative description of the Au-PTCDA complex forms the basis

for our investigation of the interaction between two Au-PTCDA complexes, i.e. between two delocalized spins, in chapter 4.

3.2 Transfering spin into an extended π orbital of a large molecule

The following article has been published in the journal **Physical Review B**:

- **T. Esat**, T. Deilmann, B. Lechtenberg, C. Wagner, P. Krüger, R. Temirov, F. B. Anders, M. Rohlfing, and F. S. Tautz, "Transfering spin into an extended π orbital of a large molecule," *Physical Review B*, vol. 91, no. 14, p. 144415, 2015.

Author contributions:
R.T., C.W., **T.E.** and F.S.T. conceived the experiments. **T.E.** conducted the experiments under the supervision of R.T. **T.E.** analysed the experimental data. T.D., P.K. and M.R. performed density functional and many-body perturbation calculations and analysed the resultant data. B.L. and F.B.A. carried out the numerical renormalization group calculations and analysed the resultant data. **T.E.** and T.D. have prepared the figures. **T.E.**, T.D., B.L., F.B.A., M.R. and F.S.T. wrote the paper.

PHYSICAL REVIEW B **91**, 144415 (2015)

Transfering spin into an extended π orbital of a large molecule

Taner Esat,[1,2,*] Thorsten Deilmann,[3] Benedikt Lechtenberg,[4] Christian Wagner,[1,2] Peter Krüger,[3] Ruslan Temirov,[1,2] Frithjof B. Anders,[4] Michael Rohlfing,[3] and F. Stefan Tautz[1,2]

[1]*Peter Grünberg Institute (PGI-3), Forschungszentrum Jülich, 52425 Jülich, Germany*

[2]*Jülich Aachen Research Alliance (JARA), Fundamentals of Future Information Technology, 52425 Jülich, Germany*

[3]*Institut für Festkörpertheorie, Westfälische Wilhelms-Universität Münster, 48149 Münster, Germany.*

[4]*Lehrstuhl für Theoretische Physik II, Technische Universität Dortmund, Otto-Hahn-Str. 4, 44221 Dortmund, Germany*

(Received 22 December 2014; revised manuscript received 12 March 2015; published 20 April 2015)

By means of low-temperature scanning tunneling microscopy (STM) and spectroscopy (STS), we have investigated the adsorption of single Au atoms on a PTCDA monolayer physisorbed on the Au(111) surface. A chemical reaction between the Au atom and the PTCDA molecule leads to the formation of a radical that has an unpaired electron in its highest occupied orbital. This orbital is a π orbital that extends over the whole Au-PTCDA complex. Because of the large Coulomb repulsion in this orbital, the unpaired electron generates a local moment when the molecule is adsorbed on the Au(111) surface. We demonstrate the formation of the radical and the existence of the local moment after adsorption by observing a zero-bias differential conductance peak that originates from the Kondo effect. By temperature dependent measurements of the zero-bias differential conductance, we determine the Kondo temperature to be $T_K = (38 \pm 8)$ K. For the theoretical description of the properties of the Au-PTCDA complex we use a hierarchy of methods, ranging from density functional theory (DFT) including a van der Waals correction to many-body perturbation theory (MBPT) and the numerical renormalization group (NRG) approach. Regarding the high-energy orbital spectrum, we obtain an excellent agreement with experiments by both spin-polarized DFT/MBPT and NRG. Moreover, the NRG provides an accurate description of the low-energy excitation spectrum of the spin degree of freedom, predicting a Kondo temperature very close to the experimental value. This is achieved by a detailed analysis of the universality of various definitions of T_K and by taking into account the full energy dependence of the coupling function between the molecule-metal complex and the metallic substrate.

DOI: 10.1103/PhysRevB.91.144415 PACS number(s): 75.20.Hr, 68.37.Ef, 73.20.Hb, 75.50.Xx

I. INTRODUCTION

Interest in magnetic properties of nanoscale structures has been growing rapidly for the last few years. Understanding and gaining control over their properties might open a route to nanospintronics and quantum computing [1]. Since molecular compounds demonstrate a remarkable tendency to self-assemble, the idea of combining the molecular pathway with magnetism is now attracting more attention [2,3]. Therefore it is crucial to obtain a better understanding of spin and charge transfer processes between molecules, surfaces, and even single atoms.

One of the interesting possibilities to tune the magnetic properties of molecules is by controlled charge transfer from other molecules or metal surfaces. For example, it has been shown that the electron-acceptor molecule TCNQ on a gold surface can be manipulated reversibly between two integer charge states by gating the local electric field with the tip of a scanning tunneling microscope and therefore inducing charge transfer from the adjacent donor molecule TMTFF [4]. A further example is provided by our previous work, in which we have demonstrated that the controlled cleavage of the π-conjugated molecule PTCDA from a Ag(111) surface gradually de-hybridizes the molecule from the metal substrate and tunes the molecule into a magnetic state, which then undergoes the Kondo effect with itinerant electrons in the metal [5–8].

Another interesting approach to adjust the magnetic properties of molecules is the on-surface chemical modification of individual molecules. Here, the reversible on- and off-switching of the Kondo resonance of a MnPc molecule through attachment and detachment of a single hydrogen atom [9] can be cited as an illustrative example. Also, a temperature-induced stepwise intramolecular ligand reaction of a gold adsorbed porphyrin molecule which induces changes in its magnetic fingerprint [10] falls in this category. Finally, it has been shown that the ligand and metal orbitals of metal phthalocyanines on a metal substrate can be selectively charged by site-dependent doping with one or more Li dopants [11].

In this work, we construct a metal-molecule complex that is a paramagnetic radical and in which, unlike in common molecular magnets where the spin usually resides in a d or f orbital of a metal ion that is shielded by organic ligands, the spin is carried by a π orbital that extends over the whole molecule. The advantage of such an extended radical lies in its propensity to interact magnetically with its neighbours, offering the potential to harness this coupling. In our experiments, we form chemically bonded metal-molecule complexes by reacting 3,4,9,10-perylene-tetracarboxylic dianhydride (PTCDA) molecules, adsorbed on the inert Au(111) surface, with single Au atoms. We investigate these Au-PTCDA complexes by means of scanning tunneling microscopy (STM). While the reversible bond formation of a single PTCDA molecule and an Au atom on a thin insulating film has been demonstrated before [12], we here investigate the Au-PTCDA complex on a metal substrate by scanning tunneling spectroscopy (STS). By demonstrating the Kondo effect, we prove that this metal-molecule complex indeed has an unpaired electron, which generates a local moment in the π orbital due to the

*Corresponding author: t.esat@fz-juelich.de

large Coulomb interaction compared to the electron-substracte coupling energy.

Complementary to our experimental investigation of this magnetic metal-molecule complex, we use density functional theory (DFT) including a van der Waals correction to calculate the structure of the Au-PTCDA complex, in excellent agreement with experiment, as revealed, for example, by calculated STM images. Furthermore, we use a spin-polarized DFT calculation plus many-body perturbation theory (MBPT) to obtain the high-energy charge excitation spectrum of Au-PTCDA complexes in the gas phase and adsorbed on Au(111). A correct physical description of the local moment formation and the Kondo effect, however, is not possible in a mean-field approach. Therefore, on top of these calculations, we finally perform numerical renormalization group (NRG) calculations to obtain the excitation spectrum of the metal-molecule complex on Au(111) also at low energies. Importantly, we use the full energy dependence of the coupling function between Au-PTCDA complex and the metal substrate as provided by the DFT/MBPT approach. This enables us to achieve a quantitatively correct description of its electronic properties, predicting a Kondo temperature within 1 K of the measured value and reaching a 0.25 eV accuracy of the high-energy spectrum.

II. METHODS

A. Experiment

An atomically clean Au(111) surface was prepared in ultrahigh-vacuum (UHV) by repeated cycles of Ar^+ sputtering and annealing at 430 °C, followed by a final annealing step at 180 °C for 30 minutes. Using a home-built Knudsen cell, we deposited a submonolayer film of PTCDA molecules onto a clean Au(111) surface held at room temperature. The sample was then transferred into a low-temperature CREATEC STM with a base temperature of $T = 9.5$ K. By heating a thin gold wire, we evaporated gold atoms onto the PTCDA submonolayer *in situ* at $T = 12$ K. The low sample temperature prevents clustering and single Au atoms are found on the sample after this processing step.

The electrochemically etched tungsten tip was treated in UHV by field emission and afterwards *in situ* by applying controlled voltage pulses and indentations into the clean gold surface until the spectroscopic signature of the Au(111) surface appeared. Differential conductance $dI/dV(V)$ spectra were recorded via the conventional lock-in technique with the feedback loop switched off.

The analysis of the Kondo effect requires recording differential conductance spectra at varying temperatures. After each temperature increase of the STM, we waited 20 h to obtain equilibrium conditions before recording the $dI/dV(V)$ spectra. Since broadening effects due to temperature and bias voltage modulation have a crucial influence on the linewidths of narrow peaks in scanning tunneling spectroscopy, it is essential to take these effects into account. Therefore the measured spectra were deconvoluted appropriately [13].

B. Theory

In addition to the experimental measurements, we have also studied the system theoretically, computing its geometrical and electronic structures. The geometrical structure was calculated with DFT, the electronic structure with DFT, MBPT, and NRG. While our DFT and MBPT methodologies are explained in this section, details regarding our NRG approach can be found in Sec. III D alongside its results.

1. Geometric structure

All DFT calculations concerning the structure are carried out in the framework of pseudopotentials using the SIESTA package [14–16]. The wave function is described by a double-zeta plus polarization basis (DZP) with s, p, and d orbitals included. We use five orbitals for H, 13 orbitals for C and O, and 15 orbitals for Au. The representation of quantities on meshes in reciprocal space is done with a cut-off energy of 250 Ry. For the $\vec{k}$ sampling of the freestanding layer, a 2×2 mesh in the two-dimensional Brillouin zone is used; if the surface is included, the sampling is increased to 4×6.

For determining the structure of a PTCDA monolayer on Au(111), the generalized gradient approximation (GGA) with the PBE functional [17] is used. Two issues have to be noted here: (1) since an incommensurate layer such as PTCDA/Au(111) cannot be treated with periodic boundary conditions, we have chosen for our calculations of PTCDA/Au(111) the commensurate unit cell in which PTCDA adsorbs on Ag(111) to obtain a system that can be treated within a supercell approach. On Ag(111), PTCDA forms a (6,1, −3,5) superstructure that is nearly rectangular with a size of 18.83 Å × 12.52 Å. As a result, the angle between the lattice vectors is changed by 1° and their lengths are changed by −2.5% and +0.6% in comparison to the freestanding PTCDA monolayer. The two PTCDA molecules within the superstructure unit cell absorb at inequivalent sites. While one molecule is nearly aligned to the lattice underneath, the second one is turned by an angle of 16° relative to a high symmetry direction of the lattice. (2) Since the van der Waals interaction is crucial for weakly bound systems like organic molecules on metal surfaces, we include it in the formulation of Ruiz *et al.* [18] ($\mathrm{vdW^{surf}}$) for all structure optimizations. As a result of our PBE + $\mathrm{vdW^{surf}}$ calculation for PTCDA/Au(111) in the structure of PTCDA/Ag(111) we obtain an average height of $z_0 = 3.18$ Å for PTCDA on Au(111), in good agreement with the experimental value 3.27 Å [19]. The substrate is approximated by three Au layers with ideal atom positions. We employ this geometry for all calculations unless noted otherwise.

In order to determine the adsorption site of a single Au atom on a PTCDA monolayer, we employ a DFT calculation for a PTCDA layer that includes the interaction between PTCDA and the substrate by a model potential to facilitate the focussing on the adsorption of the single Au atom. This model potential consists of a harmonic potential between the Au surface and the C and O atoms, with potential parameters chosen such that the previously obtained physisorption height ($z_0 = 3.18$ Å) and elasticity ($\partial^2 E(z)/\partial z^2 = 8.4\,\mathrm{eV/Å^2}$ for the entire PTCDA molecule) result. The potential is then used for the C and O atoms to describe the interaction between Au-PTCDA and Au(111). For this calculation, the unit cell is taken from the (102) plane of the β-PTCDA bulk crystal [20], which contains two planar PTCDA molecules in a rectangular unit cell of

19.30 Å × 12.45 Å. To find the optimal adsorption site of the gold atom, the potential energy surface is evaluated on a dense mesh of (x,y) points above the PTCDA layer. The height of the Au atom and the coordinates of the PTCDA monolayer are optimized for all (x,y) positions of the atom until all forces are less than $10^{-4}\ \frac{\mathrm{Ry}}{a_\mathrm{B}}$.

2. *Electronic structure*

The calculation of STM images is performed at the level of the local density approximation (LDA) and within the Tersoff-Hamann approach [21], employing a spatial extrapolation of the wave function into the vacuum with additional empty orbitals [22] above the PTCDA monolayer for the Au-PTCDA/Au(111) structure mentioned above.

For further electronic properties, we employ a hierarchy of (spin polarized) DFT calculations (LDA, local density approximation, and LSDA, local spin density approximation),[1] many-body perturbation theory (MBPT) and numerical renormalization group (NRG) calculations. We perform spin-polarized DFT calculations to determine the mean-field electronic structure, as this provides us with an additional estimate of the Coulomb interaction U within the relevant orbital that leads to the magnetic moment of 1 μ_B on the molecule. Strictly speaking, of course, the intraorbital Coulomb interaction *cannot* be modeled as an effective single-particle potential, see Sec. III C 3 below.

The electronic properties of organic molecules in LDA and GGA(+vdW$^\mathrm{surf}$) are often nearly identical. Both functionals suffer from a distinct underestimation of the gap between the highest occupied molecular orbital (HOMO) and the lowest unoccupied molecular orbital (LUMO). We therefore apply MBPT to L(S)DA, by which a notable improvement is achieved, resulting in much more realistic quasiparticle (QP) energies. The MBPT replaces the XC potential of DFT by the self-energy operator, for which we employ the GW approximation [23].

Including the metal substrate in a GW calculation is, however, a formidable task. Therefore we use a perturbative L(S)DA+GdW approach introduced in Ref. [24] as a further approximation, which yields reliable QP energies by employing a model for the dielectric screening due to the substrate. Here L(S)DA+GdW labels the perturbative method to calculate QP corrections on top of L(S)DA by considering the change of the self-energy operator $\Delta\Sigma = iG(W - W_\mathrm{metal}) = iGdW$. Previous investigations employing this method for PTCDA on Ag(111) have shown good agreement with experiment (for details, see Ref. [7]). These calculations are carried out with a code implemented by ourselves [24,25]. Here, the representation of the wave function is done by atom-centered Gaussian orbitals with s, p, d, and s^* symmetry with several shells per atom [22,26].

The L(S)DA+GdW [24] approach employs dielectric model functions. For the PTCDA monolayer, these functions are explicitly evaluated on the basis of RPA results, while the screening due to the Au substrate is considered by an additional parametrized dielectric function. The L(S)DA+GdW calculation starts from the L(S)DA result for the freestanding monolayer in the commensurate structure and at the adsorption height from GGA+vdW (see Sec. II B 1) and builds up the dielectric function using both sets of model functions mentioned above. Thus, in the calculation of the QP corrections, the substrate is only included in terms of its dielectric polarization.

To calculate projected densities of state (PDOS), we follow the method described in Ref. [8]. In particular, three calculations have to be performed: in the first calculation the complete system, e.g., (Au-)PTCDA/Au(111), is investigated and we evaluate all energies E_n and the corresponding wave functions $|\Psi_n\rangle$ in L(S)DA. In the second calculation, the Au (111) surface is excluded and the wave functions $|\varphi_i\rangle$ for a few relevant states of the molecular (Au-)PTCDA monolayer (in the commensurate structure) are computed in L(S)DA. Finally, the third calculation is a repetition of the second one, but within L(S)DA+GdW in which the QP corrections Δ_i are determined; here, the Au(111) surface is incorporated in the form of model functions [8], as mentioned above. The spectrum of state $|\varphi_i\rangle$ in the full system is then given by its projected density of states, i.e.,

$$\rho_i(E-\Delta_i) = \sum_n |\langle\Psi_n|\varphi_i\rangle|^2 \delta(E - E_n - \Delta_i), \qquad (1)$$

in which the QP correction Δ_i is employed for the full system. If Δ_i is set to zero, i.e., many-body effects are neglected, the above equation reverts to the standard projection operation within L(S)DA.

The QP shift Δ_i also determines the filling of the orbital, according to

$$n_i = \int_{-\infty}^{E_F} \rho_i(E-\Delta_i)dE \qquad (2)$$

with $\rho_i(E)$ being the PDOS of orbital i resulting from the L(S)DA (i.e., $\Delta_i = 0$). The QP shift Δ_i, in turn, depends on the occupation of the orbital, i.e.,

$$\Delta_i = (1-n_i)\Delta_i^{n=0} + n_i\Delta_i^{n=1} + 2(n_i - n_\mathrm{LDA})U_i \qquad (3)$$

The intraorbital Coulomb repulsion in orbital i is calculated as

$$U_i = \int |\varphi_i(\vec{r})|^2 W(\vec{r},\vec{r}\,')|\varphi_i(\vec{r}\,')|^2 d^3r d^3r', \qquad (4)$$

were W is the screened Coulomb interaction (which also enters the GW self-energy). In Eq. (3), $\Delta_i^{n=0}$ and $\Delta_i^{n=1}$ denote the (fictitious) QP shifts for a completely empty ($n_i = 0$) or occupied ($n_i = 1$) orbital i, which can be obtained from L(S)DA+GdW calculations of the monolayer (in which the substrate is only considered in terms of its polarizability). For further details see Ref. [8].

NRG calculations allow to incorporate dynamical correlation effects and describe the Kondo effect. Because the NRG requires a rotationally invariant mean-field density of states, we use the LDA-GdW as its starting point. Details can be found in Sec. III D.

[1] We have convinced ourselves that in LDA as well as in generalized gradient approximation (GGA) the electronic structure of the bare Au(111) surface is in good agreement with the result of Ref. [50]

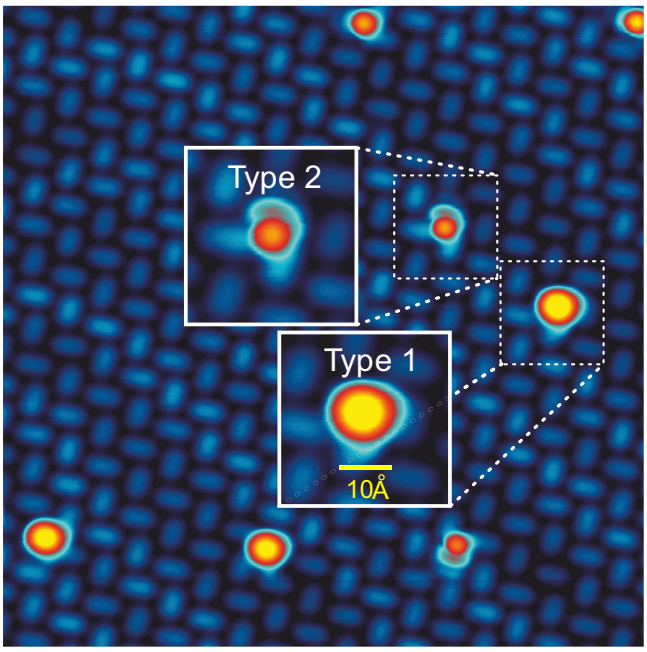

FIG. 1. (Color online) Constant current STM image (200 Å × 200 Å) after deposition of single Au atoms on a PTCDA monolayer on Au(111) (bias voltage $V = 50$ mV, tunneling current $I = 2.8 \times 10^{-11}$ A). In the insets the two observed types of Au-PTCDA complexes are shown.

III. RESULTS AND DISCUSSION

A. The Au-PTCDA complex and its structure

Figure 1 shows the PTCDA layer after deposition of Au atoms. The PTCDA molecules physisorb on the Au(111) surface and arrange into the so-called herringbone structure on Au(111). This structure is incommensurate and does not lift the herringbone reconstruction of the bare gold surface, as the brightness modulation of the PTCDA molecules in Fig. 1 clearly shows. On the PTCDA layer we observe two different types of features, both of which are related to single gold atoms. Type 1 complexes appear circular in the STM images and have a diameter of ∼10 Å. In contrast, type 2 complexes are smaller by a factor of ∼1.4 and in addition exhibit a halo next to the circular disk. Figure 2, in which differential conductance spectra of type 1 and type 2 complexes are displayed, clearly shows that the different sizes and shapes of both types go along with different spectral properties. While both types exhibit a sharp peak at zero bias, the remaining features indicate a very different electronic structure. Moreover, a closer look at the zero-bias peak reveals that the width and shape of this peak is well defined for type 1 complexes only [see also Fig. 7(b)], whereas both linewidths and lineshapes vary significantly among type 2 complexes (Fig. 3).

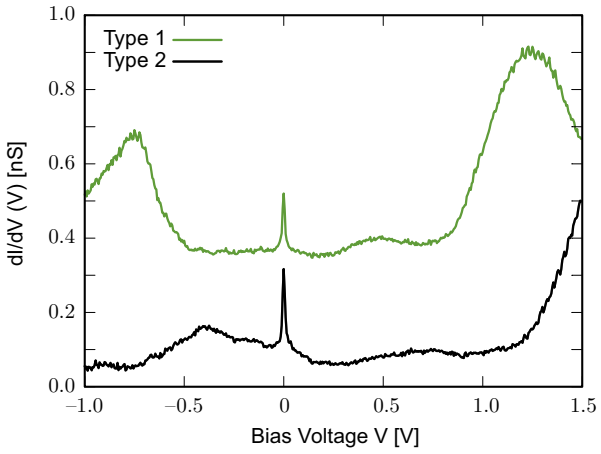

FIG. 2. (Color online) $dI/dV(V)$ spectra acquired over the center of type 1 (top) and type 2 (bottom) Au-PTCDA complexes. For clarity, the spectrum of type 1 is shifted by +0.5 nS (bias voltage and tunneling current at the stabilization point $V = 500$ mV and $I = 4.0 \times 10^{-11}$ A, lock-in modulation amplitude 5 mV at 713.3 Hz).

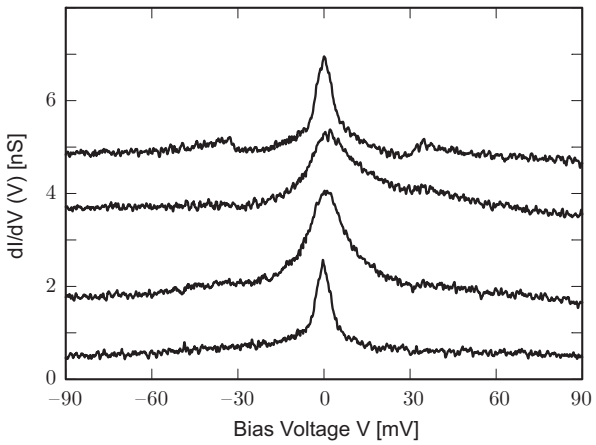

FIG. 3. $dI/dV(V)$ spectra acquired over the center of different type 2 complexes (bias voltage and tunneling current at the stabilization point $V = 360$ mV and $I = 2.5 \times 10^{-11}$ A, z-offset = +1.0 Å, lock-in modulation amplitude 1 mV at 5981 Hz). The spectra are vertically displaced for clarity.

To understand whether these differences in the electronic properties result from different Au adsorption positions in type 1 and type 2 complexes, we determine the precise positions of the Au atoms relative to the PTCDA layer. The analysis is carried out on the basis of large-scale high-resolution STM image (200 Å × 200 Å and 1024 pixel × 1024 pixel) by locating the centres of the respective circular disks in the PTCDA unit cell. Since the size and shape of the PTCDA unit cell is well known, we can correct the distortion of the measured high-resolution image by an affine homography. The resultant positions of the Au atoms are shown in Fig. 4(a). Because of the symmetry of the unit cell of the freestanding PTCDA layer, all data points can be displayed within one of its quadrants.[2] The figure reveals that the centres of both type 1 and 2 complexes are close to either of the two carbon atoms that are located midway along the long edges of the PTCDA molecule. Neglecting the environment, this allows for four equivalent adsorption positions on one PTCDA molecule.

[2]Although the surface breaks this symmetry, we neglect this effect because the monolayer is not adsorbed commensurately.

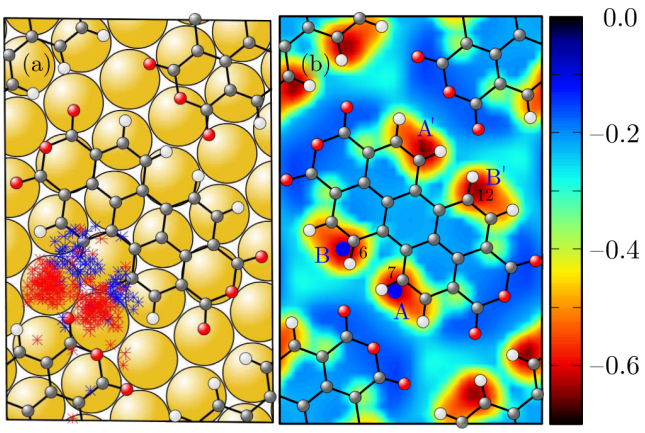

FIG. 4. (Color online) (a) Experimentally determined centres of type 1 (blue) and type 2 (red) Au atoms in the PTCDA unit cell on Au(111). The white, grey, and red circles indicate hydrogen, carbon, and oxygen atoms of PTCDA. The golden spheres denote the positions of the Au atoms in the topmost layer of the Au surface, assuming a commensurate arrangement of the molecules. (b) Potential energy surface (in eV) for an Au atom adsorbed on a PTCDA freestanding monolayer.

This experimentally observed adsorption site for Au atoms is also predicted by a DFT calculation for a PTCDA in which the interaction between PTCDA and the substrate is described by a model potential (see method Sec. II B 1 for details). The resulting potential energy surface for the Au atom on the PTCDA monolayer is shown in Fig. 4(b). Two nearly equivalent minima A and B with binding energies of 0.69 and 0.66 eV, respectively, are found. The potential energy above the center of a PTCDA molecule is approximately −0.25 eV. Remarkably, near the oxygen atoms the interaction with Au atoms nearly vanishes. Due to the symmetry of the monolayer there are four such minima per PTCDA molecule (A, A′, B, B′), i.e., eight minima per unit cell. At these minima, the Au atom is located above the C atoms labeled 1, 6, 7 or 12 of the perylene core, with a height of 2.1 Å above the monolayer and a distance of 2.2 Å to the nearest carbon atom. This bonding distance indicates the formation of a covalent bond between Au and PTCDA, in agreement with the finding in Ref. [12]. Hence, what at first sight appear to be Au atoms in Fig. 1 are in fact covalently bonded Au-PTCDA complexes. Obviously, their images are predominantly formed by the Au atom, which sticks out of the surface layer (cf. insets in Fig. 5).

To determine the influence of the metal substrate on the Au atom bonding, we have carried out a second set of calculations in which the topmost three layers of the Au(111) surface have explicitly been included. Although the PTCDA monolayer is therefore slightly deformed, the Au adsorption sites relative to the molecule stay the same as in the case of the freestanding layer. The binding energy in the minima, however, is larger (0.83 eV), due to the interaction with the surface. Essentially, the potential energy landscape for the freestanding layer is shifted rigidly by ∼0.15 eV to larger binding energies. The distance to the nearest carbon is again 2.2 Å, and the gold atom is located 5.4 Å above the topmost surface layer.

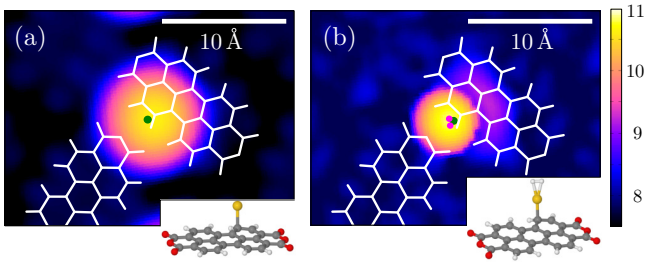

FIG. 5. (Color online) Theoretical constant current STM images of (a) Au on PTCDA/Au(111) and (b) Au on PTCDA/Au(111) with an additional hydrogen molecule adsorbed on the Au atom. The green circle denotes the position of the Au atom, the pink circles the positions of the hydrogen atoms. The tip height is given in angstrom. The insets below show the structure of the corresponding complexes.

We note that in Fig. 4(a) the STM image centers of type 2 complexes (red) are shifted by ∼1.5 Å from those of the type 1 complexes (blue) towards the gap between the molecules. At first glance, this might indicate a second adsorption site. However, such a site is not observed in our DFT calculations. The key to understanding the nature of type 2 complexes is their halo which appears in STM images (cf. Fig. 1). In Fig. 5(a), the simulated STM image of the covalently bonded Au-PTCDA complex is displayed. The image resembles experimentally observed type 1 complexes. If we add a hydrogen molecule in the calculation, both H atoms bind above the Au atom, in total with a binding energy of 0.35 eV. The distance between H and Au is 1.86 Å. If we now calculate the STM image of this complex adsorbed on the Au surface, a halo very similar to the one observed at type 2 complexes is found [Fig. 5(b)]. We therefore conclude that type 2 complexes in Fig. 1 most likely correspond to hydrogenated complexes.

This reasoning is corroborated by the observation that after a bake out of the low-temperature STM, which removes H_2 from the chamber, no type 2 atoms are observed any more (Fig. 6). The fact that in Fig. 4(a) the positions of type 2 complexes are slightly offset from type 1 complexes is an artefact of the site determination which does not take the different shapes of the two atoms types into account. Actually, comparing the simulated images in Fig. 5, it is evident that the center of the circular disk of type 1 complexes is located closer to the PTCDA molecule than the center of the (smaller) disk of type 2 complexes, in agreement with the experimental finding in Fig. 4(a).

Incidentally, the involvement of an additional H_2 molecule in type 2 complexes also explains the variability of their electronic structure (Fig. 3). In particular, the symmetric steps at $\simeq\pm30$ mV in some of the spectra are a strong indication of the presence of H_2. Those steps are known to derive from inelastic excitations. The observed frequency of $\simeq$30 meV fits well to translational [27,28] or rotational [29–33] modes of the hydrogen molecule.

B. Scanning tunneling spectra of the Au-PTCDA complex: Kondo effect

Having established the existence of covalently bonded Au-PTCDA complexes, we now study their electronic properties on the Au(111) surface. Thereby, we restrict our attention to

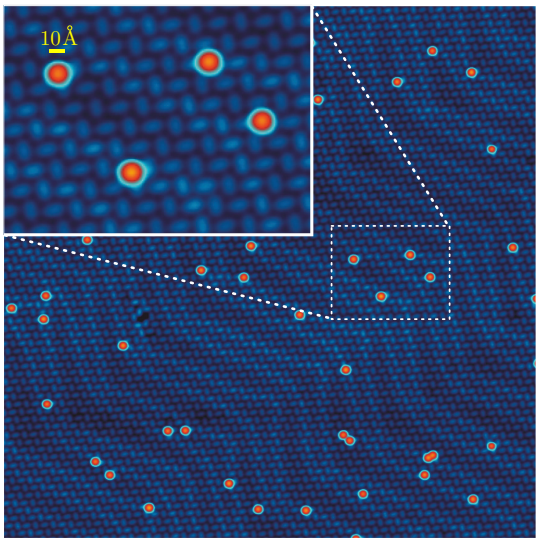

FIG. 6. (Color online) Constant current STM image (710 Å × 710 Å) taken after hydrogen decontamination of the low-temperature STM (bias voltage $V = 316$ mV, tunneling current $I = 2.5 \times 10^{-11}$ A). As highlighted in the inset, only type 1 Au-PTCDA complexes are observed.

type 1 (i.e., hydrogen-free) complexes. In the corresponding differential conductance spectrum in Fig. 2 we observe a peak at zero-bias voltage and three peaks at −0.8, +0.5, and 1.2 V. If we compare the peak at zero bias with the other peaks in the spectrum it is conspicuous that the former is much sharper and that it has a Lorentzian lineshape. This suggests that the zero-bias peak does not correspond to an electronic eigenstate of the Au-PTCDA complex. Since it is known from earlier work that charge transfer to the PTCDA molecule may bring forth the Kondo effect [5], and since the formation of the chemically bonded complex may well lead to such charge transfer and the formation of a radical, we conjecture that the zero-bias peak is in fact a Kondo resonance. This conjecture is corroborated by the analysis of its full width at half maximum (FWHM) and peak height [= zero-bias differential conductance $dI/dV(V = 0)$] as a function of temperature, as we will now show.

The extracted FWHM of the zero-bias peak are displayed in Fig. 7(a). The data show the expected temperature dependence for a Kondo resonance. We extract the Kondo temperature of the radical by fitting the expression [34]

$$\mathrm{FWHM} = \sqrt{(\alpha k_\mathrm{B} T)^2 + \left(2k_\mathrm{B} T_\mathrm{K}^{\mathrm{exp,FWHM}}\right)^2} \qquad (5)$$

to our data, with α and the Kondo temperature $T_\mathrm{K}^{\mathrm{exp,FWHM}}$ as fitting parameters. We find a Kondo temperature of $T_\mathrm{K}^{\mathrm{exp,FWHM}} = (30.7 \pm 1.0)$ K and $\alpha = (5.3 \pm 0.2)$, the latter of which is in good agreement with the theoretical value [35] of $\alpha = 5.4$.

In Fig. 7(c) the height of the zero-bias peak is plotted against the sample temperature. Here it is important to point out that the data points at all temperatures have been measured on the same Au atom and with the same tip. Moreover, for extracting heights of the zero-bias peaks that are directly comparable between the different temperatures, we always stabilize the tip above a PTCDA molecule at a fixed set point, before moving it above the Au-PTCDA complex at constant height and acquiring the differential conductance spectra there. Furthermore, we normalize all spectra to the same background differential conductance. Some spectra which were acquired with this method are shown in Fig. 7(d).

By using the empirical formula [36]

$$\frac{dI}{dV}(V = 0) = \frac{G_0}{\left[1 + \left(2^{1/s} - 1\right)\left(\frac{T}{T_\mathrm{K}^{\mathrm{zbc}}}\right)^2\right]^s} \qquad (6)$$

with $s = 0.22$ for a spin 1/2 system, we obtain from the data in Fig. 7(c) a Kondo temperature $T_\mathrm{K}^{\mathrm{exp,zbc}} = (38 \pm 8)$ K (zbc = zero-bias conductance) and $G_0 = (4.1 \pm 0.3)$ nS. Changing the distance between the tip and the Au-PTCDA complex does not affect the measured Kondo temperature. Within the error range, this value for $T_\mathrm{K}^{\mathrm{exp,zbc}}$ agrees well with the Kondo temperature which was extracted from the FWHM measurement series. However, we stress that there is no unique definition of the Kondo temperature and that different approaches to determine T_K may therefore lead to slightly different results. This will be discussed in more detail in Secs. III D 2 and III D 3 below. We can thus conclude that the Au-PTCDA complex is indeed a spin $\frac{1}{2}$ radical, and that this radical forms a Kondo ground state with the itinerant electrons of the metal substrate.

C. Electronic properties of the Au-PTCDA complex: density functional and many-body perturbation theory

Having proven that the Au-PTCDA complex undergoes the Kondo effect on the Au(111) surface, we now turn to a detailed analysis of the electronic properties of the molecule-metal complex. To this end, we carry out many-body perturbation calculations that are based on the spin-polarized local density approximation to density functional theory. Initially, we consider both PTCDA and the Au-PTCDA complex in the gas phase. We then turn to a PTCDA/Au(111) monolayer and finally to a monolayer in which one of the two PTCDA molecules carries an Au atom.

TABLE I. Energies (in eV) for the gas-phase PTCDA and Au-PTCDA in L(S)DA, GW, and L(S)DA+GdW measured with respect to E_Vac. In contrast to the results for PTCDA (top, calculated in LDA) those of the open-shell Au-PTCDA complex (bottom) are spin polarized. Due to the odd number of electrons, the LUMO+Au state is half-filled. For the nomenclature of the states of the Au-PTCDA complex see Table II and Fig. 8.

Level	L(S)DA	GW	L(S)DA+GdW
HOMO	−6.15	−7.35	−7.82
LUMO	−4.71	−2.75	−3.01
LUMO+1	−3.39	−1.15	−1.31
Gap	1.44	4.60	4.81
HOMO+Au	−7.25, −7.22	−8.44, −8.32	−8.92, −8.72
LUMO+Au	−6.37, −6.25	−7.36, −4.33	−7.77, −4.50
LUMO−Au	−5.46, −5.39	−3.60, −3.36	−3.87, −3.50
LUMO+1	−4.37, −4.34	−2.37, −2.28	−2.52, −2.44
Gap	0.12	3.03	3.27

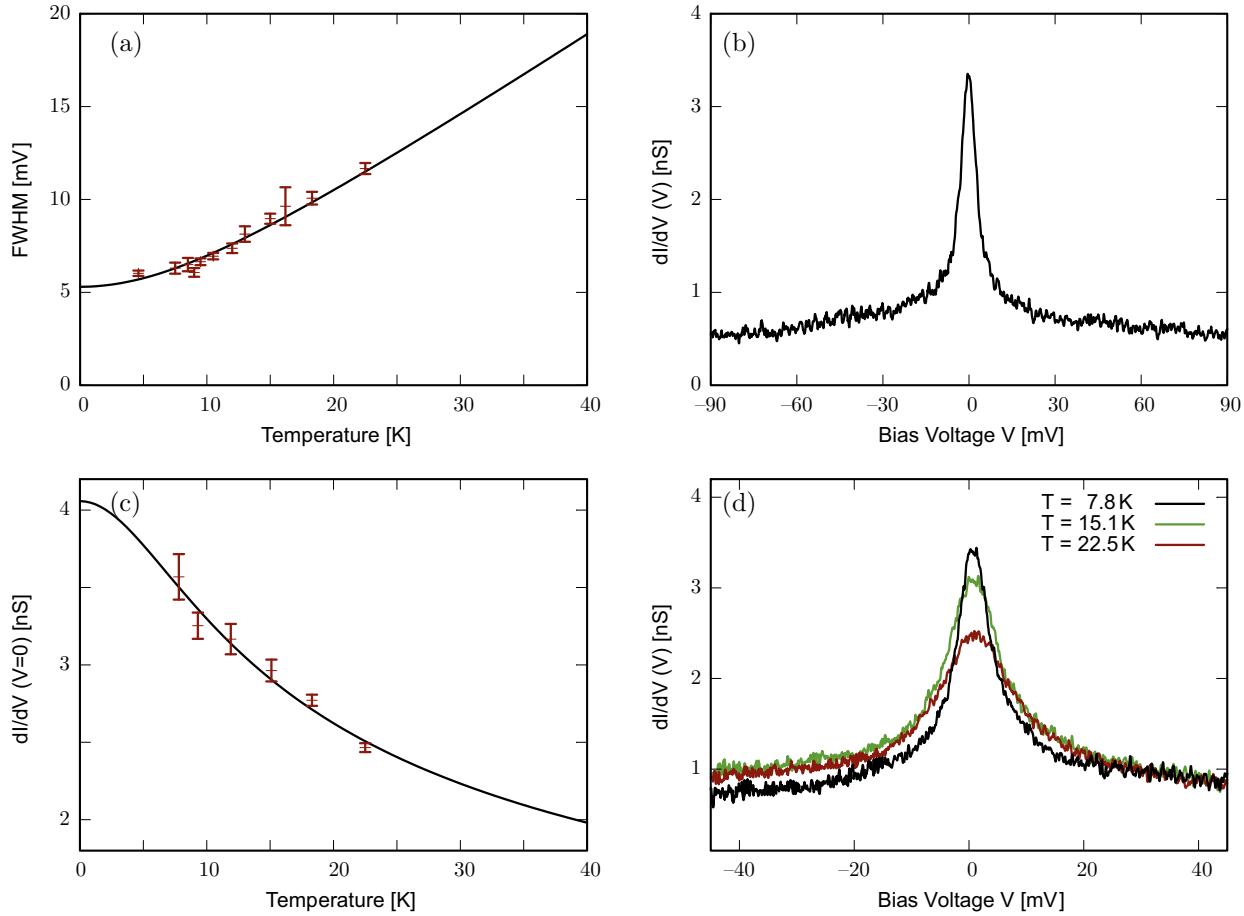

FIG. 7. (Color online) (a) FWHM of the differential conductance peak at zero bias, measured at different temperatures. Data points include measurements with different tips and on different Au-PTCDA complexes of type 1. Note that the FWHM after deconvolution to correct for broadening due to finite temperature and modulation amplitude are plotted. (b) $dI/dV(V)$ conductance (as measured, not deconvoluted) of one type 1 Au-PTCDA at $T \approx 5$ K. (c) Peak heights of the differential conductance peak at zero bias, measured at different temperatures. All data points were measured with the same tip on the same Au-PTCDA complex. (d) $dI/dV(V)$ conductance of the same radical as in (c) at specific temperatures. (b) and (d) Bias voltage and tunneling current at the stabilization point $V = 316$ mV and $I = 2.5 \times 10^{-11}$ A, z offset = $+1.0$ Å, lock-in modulation amplitude 1 mV at 6100 Hz.

1. Gas-phase molecules

We start with the isolated PTCDA molecule. This system has been investigated experimentally and theoretically in detail by Dori *et al.* [37]. We have performed calculations within LDA, the GW approximation and the simplified LDA+GdW method for this system. In the top part of Table I the energies for a single PTCDA molecule are listed. We note that replacing the LDA by the LSDA for isolated PTCDA yields the same result, due to its closed-shell singlet ground state. For PTCDA, a HOMO-LUMO gap of only 1.4 eV is observed in LDA. Using the GW approximation, the HOMO is shifted -1.2 eV downward, while the LUMO is moved almost $+2$ eV upward from the LDA value. This leads to a gap of 4.6 eV (compared to 4.9 eV in Ref. [37]). Compared to the GW approximation, in LDA+GdW the HOMO is moved downward slightly more, while the LUMO is moved upward less strongly; the gap, although moderately increased to 4.8 eV, is still in good agreement with the GW approximation. Similarly, the LUMO+1 state is shifted upward by $+2.2$ eV (GW) or $+2.1$ eV (LDA+GdW) with respect to LDA.

Next, we consider the gas-phase Au-PTCDA complex. The isosurfaces of its frontier wave functions are shown in Fig. 8 in comparison with those of the free PTCDA molecule. The LUMO of bare PTCDA hybridizes strongly with the Au 6s level, forming a bonding (LUMO+Au) and an antibonding (LUMO−Au) combination. Table II reveals that in addition

TABLE II. Orbital composition of the three most important states of the gas-phase Au-PTCDA complex in terms of projection amplitudes onto states of the Au atom (6s,6p) and the PTCDA molecule (HOMO, LUMO, LUMO+3). The states of the Au-PTCDA complex are labeled according to their dominant character as HOMO+Au, LUMO+Au, and LUMO−Au. Only the most significant contributions are listed.

	Au_{6s}	Au_{6p}	HOMO	LUMO	LUMO+3
HOMO+Au	0.14	0.00	0.74	0.01	0.00
LUMO+Au	0.29	0.07	0.16	0.31	0.03
LUMO−Au	0.12	0.07	0.01	0.64	0.07

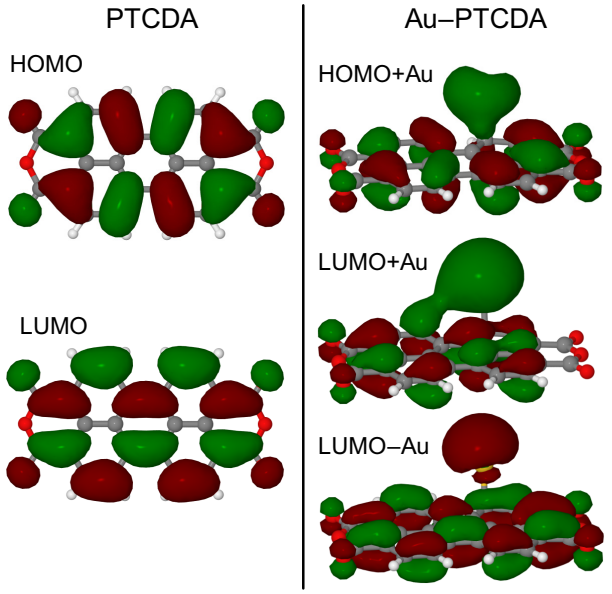

FIG. 8. (Color online) Wave functions of PTCDA (left) and Au-PTCDA (right) for orbitals around E_F calculated within LDA. Green indicates the positive isosurface, red the negative one.

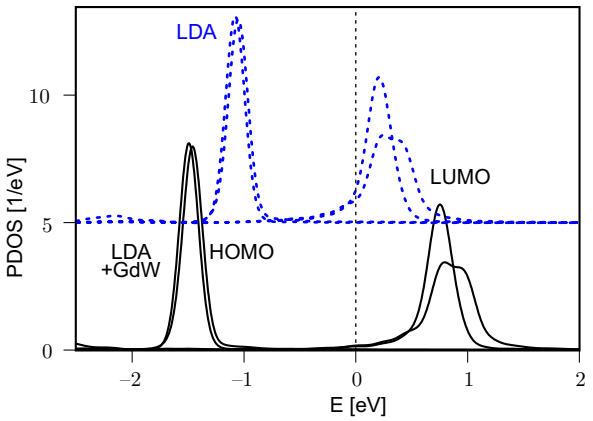

FIG. 9. (Color online) Projected density of states of a commensurate PTCDA monolayer adsorbed on Au(111) with two PTCDA molecules in the unit cell. The PDOS was obtained within the LDA (dashed blue, vertically shifted for clarity) and the LDA+GdW (black). The energies are given relative to the Fermi level of the Au(111) substrate.

to the Au 6s level, the PTCDA HOMO and PTCDA LUMO states, also the Au 6p and the PTCDA LUMO+3 contribute to the frontier orbitals of the Au-PTCDA complex (The numbers in each line of Table II do not sum up to one, because many other states contribute to a smaller extent). The most notable observation reported in Table II is that there is a sizable admixture of the PTCDA HOMO into the bonding combination of LUMO and Au 6s.

The Au-PTCDA complex has an odd number of electrons (Au $6s^1$). Hence its highest occupied level is half filled. This turns out to be the LUMO+Au state. Within LSDA, all Au-PTCDA levels are spin split by only ∼0.1 eV (see Table I). However, the GW approximation gives similar QP corrections for the Au-PTCDA complex as for the pure PTCDA. In particular, it opens a gap of 3.0 eV between the LUMO + Au ↑ and LUMO + Au ↓ states. This is a consequence of the fact that the orbital is half-filled and its two spin channels are separated by the Coulomb interaction U. The physical significance of the splitting will be further discussed below (Sec. III C 3) [38]. Note that for empty or doubly occupied orbitals such as HOMO+Au, LUMO−Au, or LUMO+1, QP corrections do not affect the spin-splitting significantly. For example, the fully occupied HOMO+Au state shifts down by more than −1 eV, while the unoccupied levels are moved up by +2 eV.

2. *PTCDA on the Au(111) surface*

In the following, we discuss the PTCDA monolayer on Au(111), which we model as a commensurate monolayer in order to be able to apply periodic boundary conditions (see Sec. II B 1 for more details). In DFT-LDA as well as DFT-GGA, we obtain nearly identical spectra for the monolayer, which, however, deviate strongly from the experimental finding that on Au(111) the PTCDA LUMO is not occupied [39].[3] Therefore we once again turn to the LDA+GdW approach, which has produced very realistic spectral results for the gas-phase PTCDA (see Table I) and for PTCDA/Ag(111) [7].

In Fig. 9, the corresponding PDOS as calculated in LDA and LDA+GdW is shown. Again, replacing LDA by LSDA in these calculations gives the same result, without spin-splitting. The two inequivalent adsorption sites in the commensurate unit cell (see Sec. II B 1) lead to different spectral line shapes of the PTCDA LUMO, with a stronger broadening for the PTCDA molecule that is aligned to the Au(111) lattice. The figure clearly illustrates the QP corrections as shifts of the corresponding peaks between the LDA and the LDA+GdW spectra (−0.4 eV for both HOMO peaks at −1.5 and −1.45 eV, and +0.5 eV for both LUMO peaks at 0.75 and 0.9 eV). Note that only the QP corrections lead to the prediction of the LUMO as being nearly empty (while in LDA the LUMO is occupied by 0.3 electrons), in agreement with the experimental finding.

As a consequence of the QP shifts, the HOMO-LUMO gap increases from 1.3 eV in LDA to 2.2 eV in LDA+GdW (Fig. 9). We note that for a PTCDA monolayer calculated in the same unit cell as considered here for PTCDA/Au(111) but *without* substrate, the QP shifts are distinctly larger (−1.0 for the HOMO and +1.1 eV for the LUMO). This can be explained by the absence of substrate screening. Yet, the HOMO-LUMO gap of this free-standing PTCDA monolayer (3.4 eV) is still smaller than the one of gas-phase PTCDA molecules (4.8 eV). Although the PTCDA molecules are only weakly bound through hydrogen bridges, they contribute environmental polarizability and this leads to a decreased gap. On the other hand, placing a *single* PTCDA molecule on the metal surface leads to a gap of 2.6 eV, showing that, as expected, the increase of the environmental polarizability by the metallic Au(111) substrate is much stronger than by adjacent molecules. Nevertheless, we

[3]We have performed calculations with six layers of Au instead of three. The charge transfer is the same as for three Au layers.

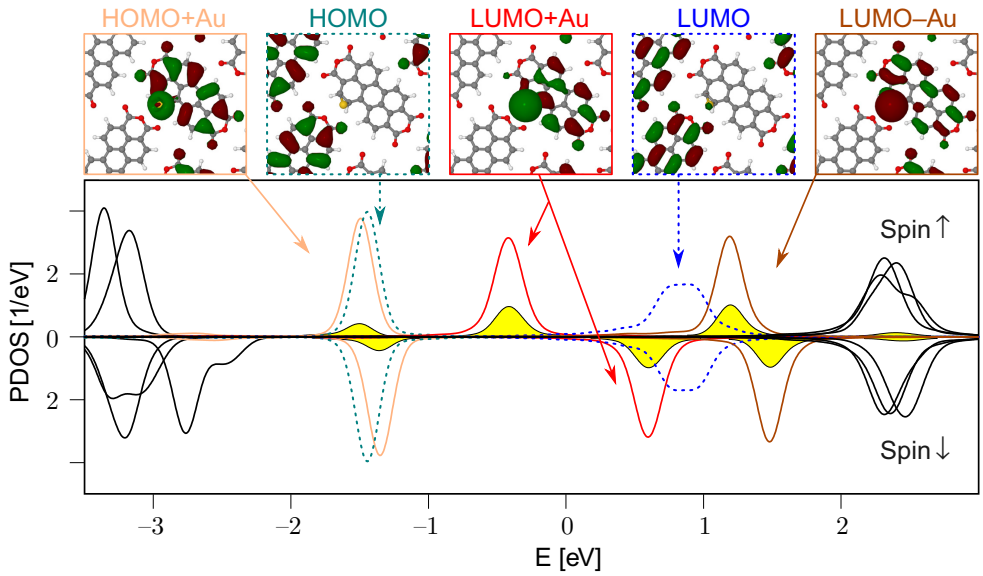

FIG. 10. (Color online) Projected density of states for the PTCDA molecule and the Au-PTCDA complex in the monolayer, adsorbed on Au(111). The PDOS was evaluated from LDA+GdW energies. The projection on the states of the Au-PTCDA complex is shown in shades of red (solid), while projections on the PTCDA molecule are shown in shades of blue (dashed). The yellow curve marks the projection on the states of the Au atom (6s and 6p) only. In addition the wave functions of some of the involved levels are plotted in corresponding colors. The energies are given relative to the Fermi level of the Au(111) substrate.

can conclude that both neighboring molecules and the Au(111) surface are instrumental for reducing the HOMO-LUMO gap below the value of the free molecule. Clearly, the effects of the metal substrate and the molecular environment on the gap are not additive.

3. *Au-PTCDA on the Au(111) surface*

Next, we perform spin-polarized electronic structure calculations (LSDA+GdW) for the Au-PTCDA complex adsorbed on the Au surface, in order to simulate the effect of the local Coulomb interaction in the LUMO+Au orbital at the mean-field level. While this treatment, which implies a rigid spin orientation, cannot describe the spin degree of freedom and thus fails to predict the correct low-energy spectrum [38], it can be used to gain insight into the high-energy spectrum that is dominated by the electronic degrees of freedom. Again a commensurate unit cell is employed, as discussed in the Sec. II B 1, with one PTCDA molecule and one Au-PTCDA complex per unit cell.

In Fig. 10, the LSDA+GdW projected density of states of this system is shown. The unit cell contains two PTCDA molecules, with an Au atom attached to one of them. Concomitantly, the system exhibits five molecular states in the energy range of Fig. 10, i.e., the HOMO and LUMO of the bare PTCDA, as well as HOMO+Au, LUMO+Au and LUMO−Au of Au-PTCDA. All states occur as spin-up and as spin-down. The projection onto the bare PTCDA molecule (blue) shows the HOMO at an energy of −1.6 eV (QP correction: −0.4 eV) and the LUMO at 0.8 eV (QP correction: +0.5 eV). Both levels are nearly spin-degenerate, confirming the expectation that the physics of PTCDA (cf. the discussion of the pure PTCDA/Au(111) monolayer in the previous Sec. III C 2) is not changed by a neighboring Au-PTCDA complex.

Regarding the projections onto the Au-PTCDA complex (red), we observe two types of behavior: on the one hand, the HOMO+Au of the Au-PTCDA complex is located at essentially the same energy as the HOMO of bare PTCDA, with a minor spin-splitting of 0.15 eV only, which is caused by slightly different QP corrections of −0.40 and −0.55 eV for spin-up and spin-down electrons, respectively. On the other hand, the LUMO-derived states of the Au-PTCDA complex show a strong spin splitting, amounting to 1.1 eV for the bonding LUMO+Au and 0.3 eV for the antibonding LUMO−Au orbital. As for the gas-phase complex, these splittings arise from quasiparticle corrections (−0.4 eV for the LUMO+Au ↑, +0.7 eV for the LUMO+Au ↓, +0.5 eV for the LUMO−Au ↑, and +0.8 eV for the LUMO−Au ↓). Because of the large splitting, only the spin-up state of the LUMO+Au orbital is found below the Fermi energy. The LUMO+Au is therefore a singly occupied molecular orbital (SOMO) with a nearly fully occupied majority spin state at −0.5 eV and a nearly empty minority spin state at 0.6 eV. Integrating the PDOS, we find that the LUMO+Au orbital is occupied with about one electron ($n = 0.5$).

Comparing the theoretical spectrum in Fig. 10 to the experimental spectrum in Fig. 2, it is tempting to assign the state measured at −0.8 eV to the LUMO+Au ↑ (theoretical value −0.5 eV) and the state measured at 0.5 eV to LUMO+Au ↓ (theoretical value 0.6 eV). The strong peak measured at 1.2 eV can be ascribed to a superposition of both spin channels of the antibonding LUMO−Au (theoretical values 1.2 and 1.5 eV). The latter assignment is consistent with the larger experimental FWHM of this peak (0.5 eV) as compared to the other electronic levels in the spectrum.

These assignments are further supported by the fact that all levels in the range −2.0 to +1.5 eV have in the calculation a substantial projection on the states of the Au atom (shown

in yellow in Fig. 10). This is a prerequisite for being able to see these states in STS spectra, because in experiment the spectrum is measured when the tip is above the Au atom and thus states localized there are approximately 2 Å closer to the tip than those localized on PTCDA. Because the wave function decreases roughly by one order of magnitude per angstrom [22], states without a contribution from Au are reduced in amplitude by two orders of magnitude and are expected to be invisible.

We note that the spin-splitting between LUMO + Au ↑ and LUMO + Au ↓ that is obtained in LSDA+GdW for Au-PTCDA on Au(111) is substantially smaller than the corresponding value of 3.27 eV in the gas-phase complex (Table I). As discussed in the previous Sec. III C 2 for the PTCDA molecule, the reduction of the gap is caused by the increased environmental polarizability, both due to the Au(111) surface and the surrounding PTCDA molecules and Au-PTCDA complexes.

The LSDA+GdW calculation can be used to evaluate the Coulomb repulsion U in the LUMO+Au orbital, using Eq. (4). This yields a value of 1.3 eV for the Au-PTCDA complex in a mixed PTCDA/Au-PTCDA monolayer on Au(111). In first order, this Coulomb repulsion can also be obtained as the energy difference between the fully occupied LUMO + Au ↑ and the completely empty LUMO + Au ↓ orbital. Note, however, that this difference (1.1 eV) is slightly smaller than the U obtained from Eq. (4). The origin of this discrepancy are QP renormalizations. The single-particle spectrum therefore shows an effective U. We will observe a similar behavior for the NRG calculation (see Sec. III D 1).

Next, we would like to include the low-energy region of the spectrum in Fig. 2 (i.e., the energy range around the Fermi level at $E = 0$) into our consideration. As mentioned above, this requires explicit accounting for the U-induced dynamical intraorbital correlations that create the spin degree of freedom. Moreover, the local spin scatters the conduction electrons, which in turn leads to a screening of the local moment that is characteristic of the Kondo ground state whose spectral signature can be found in the low-energy part of Fig. 2.

The dynamical correlations can be taken into account by performing an NRG calculation. In the present case, we use realistic input parameters for the level position of the LUMO+Au state (taken from the MBPT spectral function), its intraorbital Coulomb repulsion [taken, e.g., from Eq. (4)], and the coupling between the electrons in LUMO+Au state and the conduction electrons (taken from MPBT). However, the spin-polarized calculation is not feasible for this purpose. For a spin-rotationally invariant solution, we have to resort to a starting point given by an *unpolarized* LDA+GdW calculation.

The spectral function resulting from the LDA+GdW calculation is shown in the middle of Fig. 11, in comparison to the corresponding function from the LSDA+GdW at the top (replotted from Fig. 10). As expected from the partial occupancy of the LUMO+Au state in the spin-polarized calculation, the LUMO+Au level is found around the Fermi energy in the unpolarized calculation. Its occupancy can be calculated by Eqs. (2) and (3) from the quasiparticle shifts for fictitious zero/complete occupation ($\Delta^{n=0} = +0.64\,\text{eV}/\Delta^{n=1} = -0.37\,\text{eV}$), the filling within LDA ($n_{\text{LDA}} = 0.68$), and the Coulomb interaction U, which is

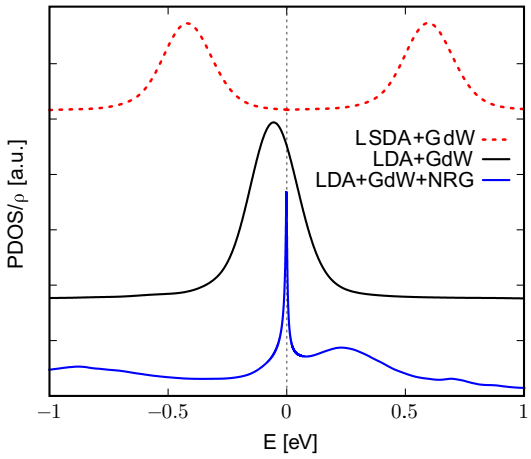

FIG. 11. (Color online) Projected density of states of the LUMO+Au orbital from an unpolarized LDA+GdW calculation (black) in comparison to the spin-polarized LSDA+GdW result (red dashed) of Fig. 10. In addition, the LDA+GdW+NRG result is included ($T = 0\,\text{K}$ and $U = 1.2\,\text{eV}$, see Sec. III D).

calculated according to Eq. (4) and amounts to $U = 1.3\,\text{eV}$ for this unpolarized calculation. We find a resulting occupation of $n = 0.71$ and an overall QP correction of $\Delta^{GdW} = -0.01\,\text{eV}$. We note that it is purely coincidental that we obtain a nearly negligible QP shift for the present situation.

Before turning to the NRG calculations and their detailed analysis in the next Sec. III D, we comment on the accuracy of the input parameters to the NRG, which are taken from LDA+GdW. First of all, there are structural uncertainties: a commensurate PTCDA monolayer is used in our DFT calculations, while point-on-line epitaxy is observed for PTCDA/Au(111) in experiment, and we find slightly different adsorption heights of PTCDA in our GGA + vdW$^{\text{surf}}$ calculation as compared to experiment (difference of the order 0.1 Å). Clearly, this may also influence the level positions with respect to the Fermi energy of the substrate, both for the bare PTCDA molecule and evidently also for the Au-PTCDA complex. We estimate this uncertainty to be of order 0.2 eV. Furthermore, the accuracy of GW and LDA+GdW calculations depends on the starting point (Hartree-Fock, LDA, ...). We use a scissor operator to anticipate the opening of the gap and therefore to reduce this dependency. The scissor operator is applied to the LDA spectrum before calculating G, W and thus Σ. This procedure approximately anticipates the finally resulting QP shifts and accelerates their self-consistent determination. Note that different QP shifts are obtained for all individual states. Nevertheless, errors of the QP corrections in GW cannot be reduced to less than 0.1 eV. The error of LDA+GdW is expected to be of the same size. As a consequence of these inaccuracies, and additionally because a finite $\vec{k}$ point mesh and a finite broadening for the calculation of the PDOS have been employed, we cannot exclude an uncertainty of $\Delta n = 0.05$ in the occupation of LUMO+Au state. This will affect the level position ϵ_0 and the hybridization in the same order. Finally, the Coulomb repulsion U slightly differs for different Au atom positions in the unit cell (positions A, A′, B, B′ in Fig. 4) in the range of 0.1 eV.

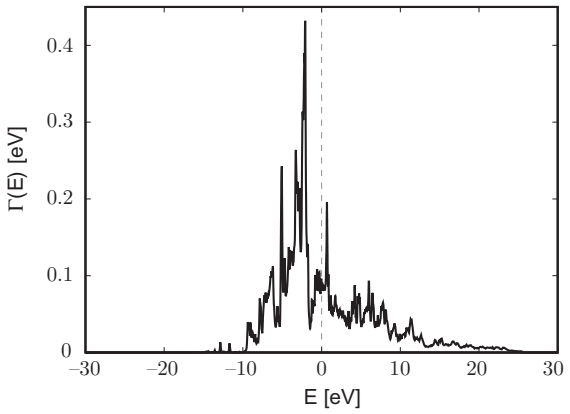

FIG. 12. The full energy-dependent hybridization function $\Gamma(E)$ obtained from the LDA+GdW PDOS. $\Gamma(E)$ is independent of the Coulomb interaction U and therefore always the same for every NRG calculation in which an energy-dependent hybridization function is used.

D. Electronic properties of the Au-PTCDA complex: Numerical renormalization group

1. Combining the LDA+GdW and the numerical renormalization group

We now discuss NRG calculations to incorporate dynamical correlation effects into the spectrum of the Au-PTCDA complex on the Au(111) surface. We employ the procedure outlined in Ref. [8]. In this approach, the LDA+GdW result is mapped onto a single-orbital Anderson model, which is then solved using the NRG approach, in order to incorporate the Kondo effect that is experimentally observed in the type 1 dI/dV spectrum of Fig. 2. Because only the LUMO+Au state shows a significant contribution to the spectral function around E_F, a single-orbital Anderson model is used to model the dynamical coupling of the LUMO+Au orbital to the substrate.

By treating the projected DOS obtained by the LDA+GdW as an effective mean-field spectrum $\rho_{GdW}(E)$, we are able to extract the bare level position ϵ_0 and the complex coupling functions $\Delta(E)$ between the Au-PTCDA complex and the substrate by equating

$$\rho_{GdW}(E) \equiv \lim_{\delta\to 0^+} \Im \frac{1}{\pi} \frac{1}{E - i\delta - \epsilon_0 - nU - \Delta(E - i\delta)}. \quad (7)$$

Here, U denotes the estimated intraorbital Coulomb interaction, and n the occupation number of the energy level consistent with $\rho_{GdW}(E)$. Since the LDA+GdW and LSDA+GdW predict slightly different values of U (see discussions above), we take U as a model parameter and vary the interaction within the predicted bounds: the LDA+GdW gives $U = 1.3$ eV and an occupancy $n = 0.71$, while the LSDA+GdW spectrum with an occupation of $n = 0.50$ yields $U = 1.1$ eV. The parameters U, ϵ_0 and the complex function $\Delta(z)$ enter an NRG [40,41] calculation, where $\Gamma(E) = \lim_{\delta\to 0^+} \Im\Delta(E - i\delta)$ defines the hybridization strength between the Au-PTCDA complex and the substrate. As we will see below, it is crucial to retain the *full energy dependence* of the hybridization function $\Gamma(E)$, which is plotted in Fig. 12, in our NRG calculation. Following Eq. (7), we find that ϵ_0 ranges from $\epsilon_0 = -0.88$ eV for $U = 1.1$ eV, $\epsilon_0 = -0.95$ eV for $U = 1.2$ eV to $\epsilon_0 = -1.02$ eV for $U = 1.3$ eV.

The resulting NRG spectrum for $U = 1.2$ eV (lower curve of Fig. 11) indeed shows the Kondo peak and two charge excitation peaks at -0.9 and 0.2 eV. The latter correspond to the two LUMO + Au $\uparrow$ and LUMO + Au $\downarrow$ levels of the spin-polarized LSDA+GdW mean-field spectrum at the top of Fig. 11 (located at -0.45 and 0.55 eV). Note that the charge excitation peaks of the NRG are shifted nearly rigidly with respect to the ones of the LSDA+GdW; in fact, they are found reasonably close to the *experimental* positions (-0.8 and 0.5 eV). The NRG calculation and experiment thus agree in showing a more particle-hole asymmetric situation than the LSDA+GdW calculation. Given the uncertainties of the input parameters into the NRG, a correspondence with experiment regarding the charge excitations to within 0.25 eV is an excellent result, showing that our modeling is describing the system at a quantitative level. Similar to the LSDA+GdW, we also observe in the NRG a slight reduction of the "effective U," defined as the difference between the two charge excitation peaks (1.1 eV for the spectrum in Fig. 11), below the input value going into the calculation (1.2 eV).

To illustrate the effect of the above mentioned uncertainty of the input parameter U, NRG spectra of the LUMO+Au state on Au(111) are shown in Fig. 13(a) for different interactions U and $T = 5$ K. With increasing interaction U one observes a narrowing of the Kondo peak and thus a decreasing of the Kondo temperature as expected from the analytical estimate of the Kondo temperature stated in Eq. (10) below.

We finally note in passing that for half-filling and absent orbital-substrate interaction the spin-polarized LSDA+GdW spectrum after averaging over the two spins and the high-energy part of NRG spectrum in Fig. 11 would be qualitatively very similar. Moreover, the local moment approach of Glossop and Logan [42] uses the spin-polarized mean-field solution as starting point: first, the mean-field spectrum is symmetrized to restore the rotational invariance in the spin space and then the missing Kondo resonance is calculated by including the low-energy two-particle corrections of a random phase approximation.

2. Results for the Kondo temperature

We now turn to a detailed analysis of the Kondo temperatures resulting from the NRG calculations. Since the Kondo temperature depends extremely sensitively on the physical parameters (molecule-metal coupling, energy level position, and Coulomb interaction), the comparison of the LDA+GdW+NRG-predicted to the experimental Kondo temperature is a very sensitive gauge of the accuracy of our first-principles DFT/MBPT analysis.

Since the Kondo energy scale is a crossover rather than a transition scale, there is, however, no unambiguous definition of the Kondo temperature. We therefore employ three different approaches to obtain the Kondo temperature, namely, (a) a fit to the T dependence of the zero-bias conductance, which should be a universal function of T/T_K. This leads to a Kondo temperature which we denote by T_K^{zbc} (zbc = zero-bias conductance). (b) The evaluation of the analytic formula

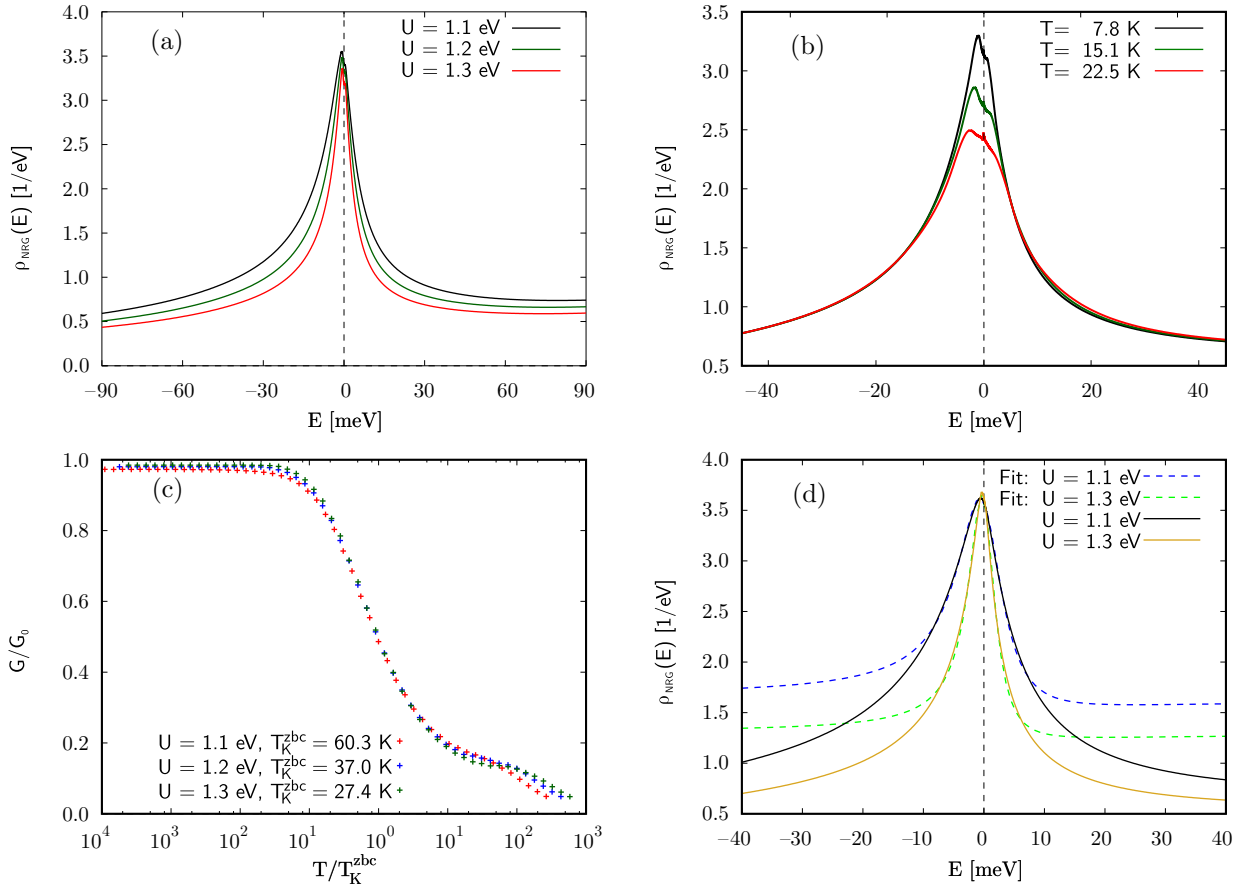

FIG. 13. (Color online) Results of the NRG calculations based on the LDA+GdW for the Au-PTCDA complex on Au(111). (a) Spectra for three different values $U = 1.1, 1.2, 1.3$ eV and $T = 5$ K. The Kondo temperature is increasing with decreasing U. (b) Spectra for different temperatures for $U = 1.2$ eV. (c) The temperature dependent differential conductance for different interactions U as a universal function of T/T_K^{zbc}. (d) Zero-temperature spectra for the interactions $U = 1.1$ and 1.3 eV and their Fano fits to extract the FWHM. For more details see main text.

for the Kondo temperature of the particle-hole asymmetric Anderson model, in which the same orbital parameters from our *ab initio* DFT/MBPT calculations that are used as input for the NRG enter, but where the full energy-dependent hybridization strength $\Gamma(E)$ is replaced by its value at the Fermi energy, i.e., $\Gamma = \Gamma(0)$. This leads to an analytic estimate of the Kondo temperature which we denote by $T_K(\Gamma, \epsilon_0, U)$. (c) The analysis of the FWHM of the zero-temperature spectral function around the chemical potential (i.e., of the Kondo resonance) provides T_K^{FWHM}.

a. Kondo temperature T_K^{zbc} from zero-bias conductance. Figure 13(b) displays the calculated LDA+GdW+NRG orbital spectral functions $\rho_{NRG}(E)$ for the LUMO+Au orbital at fixed $U = 1.2$ eV and at three different temperatures. The spectra are in a good agreement with the corresponding experimental results for the differential conductance $dI/dV(V)$ as depicted in Fig. 7(d), with the exception of the peak asymmetry, see below. The temperature dependent spectral function $\rho_{NRG}(E)$ enters the calculation of the differential conductance [43,44] in the tunneling regime,

$$\frac{dI}{dV}(V) = G_0 \int dE\, \pi\Gamma(E)\rho_{NRG}(E)(-f'_{tip}(E,V)), \quad (8)$$

where the reference conductance G_0 is given by [43]

$$G_0 = \frac{2e^2}{h}\frac{4\Gamma_{tip}(0)\Gamma(0)}{(\Gamma_{tip}(0)+\Gamma(0))^2}. \quad (9)$$

Note that G_0 depends only on $\Gamma(0)$ and $\Gamma_{tip}(0)$, the charge fluctuation scales at the chemical potential, induced by the coupling to the substrate and the tip, respectively. $f_{tip}(E,V)$ denotes the Fermi function of the STM tip and also includes the bias voltage V. For an STM tunneling contact, $\Gamma_{tip}(0) \to 0$, hence $G_0 \to (2e^2/h)(4\Gamma_{tip}(0)/\Gamma(0))$ and the tunnel current is strongly suppressed. For low temperatures, $-f'_{tip}(E,V) \to \delta(E - eV)$ and $dI/dV(V)$ becomes $\pi G_0 \Gamma(eV)\rho_{NRG}(eV)$.

Fitting the zero-bias conductance, Eq. (8), obtained from our LDA+GdW+NRG calculation with Eq. (6) yields Kondo temperatures ranging from $T_K^{zbc} = 27.4$ K for $U = 1.3$ eV to $T_K^{zbc} = 60.3$ K for $U = 1.1$ eV. These values are perfectly bracketing the experimentally estimated Kondo temperature of $T_K^{exp,zbc} = (38 \pm 8)$ K, and the best agreement with the experimental fit in Fig. 7(c) requires $U = 1.2$ eV, for which we obtain $T_K^{zbc} = 37.0$ K (Table III). In Fig. 13(c), the calculated differential conductance, normalized to G_0, is shown as a universal function of T/T_K^{zbc}, employing the fitted Kondo temperatures.

TABLE III. Experimental and calculated Kondo temperatures in K. For the calculated T_K^{zbc} and T_K^{FWHM} we have used the full energy-dependent $\Gamma(E)$, while for $T_K(\Gamma,\epsilon_0,U)$, Eq. (10) has been evaluated for $\Gamma = \Gamma(0) = 86$ meV. For further details, cf. main text.

		U		
	Exp.	1.1 eV	1.2 eV	1.3 eV
T_K^{zbc}	38 ± 8	60.3	37.0	27.4
$T_K(\Gamma,\epsilon_0,U)$	n/a	41.7	28.4	19.5
T_K^{FWHM}	30.7 ± 1	51.0	42.9	30.2

b. Analytic Kondo temperature $T_K(\Gamma,\epsilon_0,U)$ from the asymmetric Anderson model. In general, the Kondo temperature is defined as the universal energy scale governing the excitation and the thermodynamic response at low temperatures. Physical properties, however, also depend on the degree of particle-hole symmetry breaking. This degree enters (i) not only the analytic expression for T_K and (ii) governs the asymmetric shape of the spectral function [see Figs. 13(a), 13(b), and 13(d)] and, therefore, (iii) is also responsible for the asymmetric dI/dV at small bias voltages.

Krishna-murthy *et al.* [40] have shown that the Kondo temperature of the asymmetric Anderson model with a constant hybridization function $\Gamma(E) = \text{const.}$ is given by

$$T_K(\Gamma,\epsilon_0,U) = 0.182|E_0^*|\sqrt{\rho J_{\text{eff}}}\exp\left(-\frac{1}{\rho J_{\text{eff}}}\right) \quad (10)$$

for the regime where double occupation is energetically suppressed and the orbital remains close to integer valence. E_0^* is the self-consistent solution of $E_0^* = \epsilon_0 + (\Gamma/\pi)\ln(-U/E_0^*)$, describing the renormalization of the bare level due to high-energy charge fluctuations. $\rho J_{\text{eff}} = \rho J[1 + (\pi\rho K)^2]^{-1}$ contains not only the dimensionless Kondo coupling

$$\rho J = \frac{2\Gamma}{\pi}\left(\frac{1}{|E_0^*|} + \frac{1}{\epsilon_0 + U}\right), \quad (11)$$

but also a modification by the degree of particle-hole symmetry breaking

$$\rho K = \frac{\Gamma}{2\pi}\left(\frac{1}{|E_0^*|} - \frac{1}{\epsilon_0 + U}\right), \quad (12)$$

both obtained from the Schrieffer-Wolff transformation [45]. At particle-hole symmetry, ρK vanishes, and for weak coupling $E_0^* \approx \epsilon_0$.

Since the Kondo effect is dominated by the low-energy excitations, we use in Eq. (10) the value $\Gamma(E = 0) \approx 86$ meV extracted from the energy-dependent hybridization function as provided by the LDA+GdW approach and depicted in Fig. 12. For $U = 1.2$ eV, $\epsilon_0 = -0.95$ eV, and $\Gamma(E = 0) = 86$ meV, we obtain $T_K(\Gamma,\epsilon_0,U) = 28.4$ K, which agrees well with the numerical fit to the differential conductance presented in Fig. 13(c) ($T_K^{zbc} = 37.0$ K for $U = 1.2$ eV). The $T_K(\Gamma,\epsilon_0,U)$ for the other values of U can be found in Table III.

When obtaining T_K^{zbc} from the temperature dependence of the LDA+GdW+NRG zero-bias conductance, we found that a decreasing U yields an increasing Kondo temperature. This behavior can be analytically understood with the exponential dependence of T_K on ρJ, the latter given by Eq. (11). T_K has a minimum at particle-hole symmetry $\epsilon_0 = -U/2$ and two maxima, one at $\epsilon_0 = 0$ and the second at $\epsilon_0 = -U$. In the present case, with decreasing U, we move further away from the particle-hole symmetric point towards the mixed valence regime where $\epsilon_0 \approx -U$ and, therefore, the Kondo temperature is rising.

We have to bear in mind, however, that this analytical Kondo temperature neglects effects stemming from the energy dependency of $\Gamma(E)$. Therefore $T_K(\Gamma,\epsilon_0,U)$ can only serve as a preliminary estimate, needing modification by our full LDA+GdW+NRG approach for modeling of the experiment.

c. Kondo temperature T_K^{FWHM} from the width of the Kondo peak in the zero-temperature spectral function. Using Eq. (5), the Kondo temperature has been extracted from the experimental data [Fig. 7(a)]. We now apply the same procedure to the LDA+GdW+NRG data in Fig. 13(a). The result is shown in Fig. 13(d).

Since the NRG is able to reach arbitrarily small temperatures, a temperature dependent fit is not required, and Eq. (5) simplifies to

$$\text{FWHM}(T = 0) = 2k_B T_K^{FWHM}. \quad (13)$$

Furthermore, $dI/dV(V) \propto \rho(E = eV)$ in the tunneling regime for $T \to 0$, and T_K^{FWHM} can be estimated directly from the spectral function. However, away from particle-hole symmetry, the spectra and, therefore, the dI/dV curves are asymmetric. It is apparent in Fig. 13(a) that at energies $|E| > k_B T_K$ the spectra are modified by the charge scattering term ρK, as defined in Eq. (12). Given this asymmetry, three questions arise, namely (i) how to extract T_K^{FWHM}, (ii) do the different fit procedures yield comparable values, and (iii) how do the various T_K^{FWHM} compare with the other estimates of the Kondo temperature, namely T_K^{zbc} and $T_K(\Gamma,\epsilon_0,U)$?

The simplest approach would be to take the definition for the full width at half maximum (FWHM) literally. However, in addition to the Kondo peak, the spectra also contain broad charge-excitation peaks at higher energies that invalidate such a procedure. Due to this background, the estimates of T_K^{FWHM} are typically double the value of those obtained by the fit function (6).

To allow for an asymmetry [46,47] in the fitting process, we employ here a Fano-resonance line shape of the form $\rho(E) = \rho_0 + A\frac{(q+\epsilon)^2}{1+\epsilon^2}$ with $\epsilon = (E - E_0)/\Gamma$ for the Kondo peak to extract its FWHM. E_0 determines the location of the resonance, which is shifted slightly away from the chemical potential in accordance with the Friedel sum rule [48]. While q parametrizes the asymmetry of the spectrum, the width Γ defines the fit for T_K^{FWHM}. Figure 13(d) shows the zero-temperature spectra for two different interactions, $U = 1.1$ and 1.3 eV, and the corresponding Fano fits. Depending on the interaction U, we find Kondo temperatures extracted from our NRG spectra ranging from $T_K^{FWHM} = 30.2$ to 51.0 K (Table III), which again brackets the measured $T_K^{exp,FWHM} = (30.7 \pm 1.0)$ K.

We stress again that when using Eq. (5) in highly particle-hole asymmetric cases, one should bear in mind that the extracted T_K^{FWHM} depends on the fitted function, which requires significant modifications from a symmetric Lorentzian. Furthermore, as we show in the next paragraph,

TABLE IV. Experimental and calculated Kondo temperatures in K, here for a constant $\Gamma = 86$ meV. For details, cf. Sec. III D 3.

		U		
	Exp.	1.1 eV	1.2 eV	1.3 eV
T_K^{zbc}	38 ± 8	98.0	63.0	42.8
$T_K(\Gamma,\epsilon_0,U)$	n/a	41.7	28.4	19.5
T_K^{FWHM}	30.7 ± 1.0	74.8	57.0	42.9
T_K^{μ}	n/a	49.9	34.2	23.9
$T_K(\Gamma,\epsilon_0,U)/T_K^{\mu}$	–	0.836	0.830	0.810
$T_K(\Gamma,\epsilon_0,U)/T_K^{zbc}$	–	0.426	0.450	0.456
$T_K(\Gamma,\epsilon_0,U)/T_K^{FWHM}$	–	0.577	0.498	0.455

T_K^{FWHM} can only give the correct order of magnitude of the Kondo temperature, since its value is definition-dependent and does not need to coincide with the Kondo temperature defined in Eq. (10) that has been derived from the screening of the local spin moment. We have summarized the experimentally obtained and the calculated Kondo temperatures in Table III.

3. *Comparison of Kondo temperatures*

We now turn to a comparison of the various calculated Kondo temperatures among each other in order to provide a guideline for a reliable extraction of T_K from the experiment. In Sec. III B, we have extracted experimental Kondo temperatures from the FWHM of the spectral function, Eq. (5) and Fig. 7(a), and from the zero-bias conductance using the fit function Eq. (6) [see Fig. 7(c)]. Since the Kondo temperature is only a crossover scale, it is only defined up to an arbitrary constant of the order one. The question arises whether $T_K^{exp,zbc}$ and $T_K^{exp,FWHM}$ should indeed be expected to be identical *up to a universal scaling constant*.

The NRG provides optimal tools to systematically investigate the difference between the various definitions of the Kondo scale. In order to exclude an influence of the energy dependent hybridization function on this comparison, we have repeated the NRG calculations with a constant $\Gamma = 86$ meV and extracted new values of T_K^{zbc} and T_K^{FWHM} from these calculations. These new values, which can now be directly compared to the analytic estimate $T_K(\Gamma,\epsilon_0,U)$, are summarized in the upper part of Table IV. The table also contains values for T_K^{μ}, determined again for constant $\Gamma = 86$ meV. Wilson [40,41] has defined the Kondo temperature as the temperature T_K^{μ} at which the local moment is reduced to approximately 26% of the original value, by screening through the conduction electrons. (At $T = 0$, i.e., in the Kondo singlet ground state, the effective moment is zero.) Hence T_K^{μ} follows from the implicit equation

$$\mu_{eff}^2 = T_K^{\mu}\chi\left(T_K^{\mu}\right) = 0.07, \tag{14}$$

where μ_{eff}^2 is the effective local magnetic moment and $\chi(T)$ its isothermal magnetic susceptibility. Note that this screening has also entered the analytical estimate $T_K(\Gamma,\epsilon_0,U)$ in Eq. (10) in Sec. III D 2 b.

Calculating the ratios $T_K(\Gamma,\epsilon_0,U)/T_K^{\mu}$ and $T_K(\Gamma,\epsilon_0,U)/T_K^{zbc}$ for each of the three different values of $U = 1.1, 1.2, 1.3$ eV, corresponding to $E_0 = -0.88, -0.95, -1.02$ eV, we found nearly constant ratios $T_K(\Gamma,\epsilon_0,U)/T_K^{\mu} \approx 0.83$ and $T_K(\Gamma,\epsilon_0,U)/T_K^{zbc} \approx 0.45$. Consequently, all three definitions T_K^{μ}, $T_K(\Gamma,\epsilon_0,U)$ and T_K^{zbc} are fully equivalent and connected by universal scaling factors.

This should be contrasted with the situation regarding T_K^{FWHM}; Table IV shows that the ratios $T_K(\Gamma,\epsilon_0,U)/T_K^{FWHM}$ are *not* constant and U dependent, varying over a range from $\approx$0.58 to $\approx$0.46. This state of affairs does not change if the fitting procedure of the zero-bias conductance peak is changed. In particular, we tested three different procedures: (i) a Lorentz-fit to the symmetrized spectrum $\rho_{sym}(\omega) = 0.5(\rho(\omega) + \rho(-\omega))$, (ii) a Lorentz-fit to the low-energy part of the spectrum, and (iii) a fit using the Fano line shape as described above. All three fitting procedures yield roughly the same estimate for T_K^{FWHM}. We therefore conclude that the scale T_K^{FWHM} is nonuniversal and depends on the degree of particle-hole symmetry breaking. In particular, for small U, we find a T_K^{FWHM} that is smaller than the fit to the zero-bias conductance, while it approaches T_K^{zbc} for $U = 1.3$ eV where the spectrum is narrower and significantly more symmetric.

The above discussion shows that the difference between $T_K^{exp,zbc}$ and $T_K^{exp,FWHM}$ is due a nonuniversal scaling constant. Therefore, the most reliable way of extracting T_K from experiments remains the fit of the temperature-dependent zero-bias conductance (T_K^{zbc}), since at any temperature only excitations of the order of T enter, while T_K^{FWHM} measured at $T/T_K \ll 1$ always contains high-energy excitations in addition to errors stemming from nonequilibrium effects due to the finite current through the molecule. However, Table IV shows that T_K^{FWHM} can still serve as a reasonable estimate for T_K, providing the correct order of magnitude of the Kondo temperature.

It is interesting to note that the Kondo temperatures calculated with a constant Γ and listed in Table IV are significantly different from those obtained with the energy dependent $\Gamma(E)$, which turned out to match the experimental findings very well. The Kondo temperatures at constant Γ exceed the ones for nonconstant $\Gamma(E)$ by up to a factor of two. We can thus conclude that a combined full LDA+GdW+NRG approach is needed to explain the experimental data on a quantitative level. In particular, we achieve a perfect match between experiment ($T_K^{exp,zbc} \approx 38$ K) and theory ($T_K^{zbc} = 37$ K) for $U = 1.2$ eV, which is in the center of the range of U parameters calculated from DFT/MBPT using Eq. (4).

4. *LUMO+Au orbital occupancy n*

The NRG also provides information on the occupancy of the local LUMO+Au orbital. While the LDA+GdW predicts an occupancy of $n = 0.71$, the inclusion of correlation effects by the NRG reduces this value to $n = 0.55$. Such a reduction is expected, since the Coulomb repulsion strongly suppresses double occupancy of the orbital and thus constrains the filling much closer to half-integer values (note that in our definition a completely occupied orbital with two electrons of opposite spin has $n = 1$). However, the LDA+GdW and the LDA+GdW+NRG agree in predicting the binding of an extra fraction of an electron that is drawn from the substrate (LDA+GdW+NRG: 0.1 electrons, LDA+GdW: 0.4 electrons), in addition to the one electron from the Au

atom. We note in passing that 0.1 electrons is exactly the difference of occupation between Au-PTCDA and PTCDA on the Au(111) surface within LDA.

Furthermore, it is interesting to note in this context that in comparison to the LDA+GdW the LSDA+GdW occupation ($n_{\mathrm{LSDA+GdW}} = 0.50$) is closer to that of NRG ($n = 0.55$). As expected, this is coupled to a lower U derived from the LSDA+GdW ($U = 1.1$ eV) than from the LSDA+GdW ($U = 1.3$ eV). However, as argued above, the reduction of the occupancy in the LSDA+GdW is not occurring for the correct physical reason.

IV. SUMMARY AND CONCLUSION

In this work, we have shown that when doping a PTCDA/Au(111) monolayer with single Au atoms, Au-PTCDA complexes are formed by a spontaneous chemical reaction. A DFT calculation reveals that the Au-PTCDA complex is also stable in the gas phase. Due to an unpaired electron, drawn from the Au 6s orbital, this complex is a paramagnetic radical ($S = \frac{1}{2}$). Remarkably, the orbital in which the unpaired spin resides extends over the whole molecule and is related to the LUMO of free PTCDA. Specifically, it is the bonding combination of the Au 6s orbital and the LUMO of PTCDA. The split between bonding and antibonding orbitals in the gas phase complex amounts to approximately 1 eV if calculated at LDA level.

On the Au(111) surface, an additional small fraction of an electron (about 0.1 electrons) is drawn from the substrate into the bonding orbital of the Au-PTCDA complex. However, this additional charge transfer is effectively limited by a rather strong intraorbital Coulomb repulsion U. In fact, the bonding LUMO+Au orbital remains close to a singly occupied orbital. In this sense, the Au-PTCDA complex on Au(111) is intermediate between PTCDA on Au(111), where no charge transfer takes place [19], and PTCDA on Ag(111), where nearly two electrons are transferred from the metal surface to the molecule [49]. Apparently, the coupling between adsorbate and substrate is much weaker in the case of Au-PTCDA/Au(111) than in PTCDA/Ag(111), such that in spite of similar intraorbital repulsions double occupancy is only suppressed for Au-PTCDA/Au(111). On the other hand, comparing Au-PTCDA/Au(111) to PTCDA/Au(111), where the LUMO remains unfilled, we see that the charge transfer from the Au atom to the π system bypasses the charging barrier for PTCDA on Au(111) that is caused by the large work function of Au(111).

As a result of the restriction to single occupancy, the spin degree of freedom of the complex is retained when it is adsorbed on the Au(111) surface. The thus stabilized spin of the complex interacts with conduction electrons of the metal surface. As a consequence, the Kondo effect unfolds in this system. In our experimental STS spectra, it reveals itself by the sharp resonance in the single-particle spectral function at the chemical potential. Analyzing both the width (FWHM) and the height (zero-bias conductance) of this resonance as a function of temperature, we find a behavior that is consistent with the predicted temperature dependence of Kondo resonances, yielding Kondo temperatures of $\approx$38 K from the zero-bias conductance and $\approx$31 K from the FWHM, respectively. The observation of the Kondo effect in the present system is the unambiguous proof that the Au-PTCDA complex is indeed a paramagnetic radical with $S = \frac{1}{2}$.

On the theory side, we have a achieved a fully quantitative description of the Au-PTCDA complex, by applying a hierarchy of methods, employing density functional theory in the local density and generalized gradient approximations, including van der Waals corrections, as well many-body perturbation theory in the GW and LDA+GdW approximations, and the numerical renormalization group approach.

As far as geometric structure is concerned, the "adsorption site" found by theory, i.e., the site at which the reaction between the Au atom on the PTCDA molecule occurs, is in agreement with experiment. This means that the chemical structure of the complex is correctly predicted. Moreover, STM simulations allow the identification of some of the experimentally observed complexes as being contaminated by an adsorbed hydrogen molecule.

Electronic structure calculations for the gas-phase complex show the importance of quasiparticle corrections for predicting the correct excitation spectrum. These increase the gap to approximately 3 eV. This large gap is, however, reduced again to approximately 1 eV for the adsorbed complex (in an ordered monolayer structure), due to screening by the metal substrate and neighboring PTCDA molecules of the Au-PTCDA complexes, in good agreement with experiment. To predict the full excitation spectrum correctly, including the low-energy region that is shaped by the spin degree of freedom, we have applied the numerical renormalization group approach, mapping the MBPT result on the $S = \frac{1}{2}$ single-impurity Anderson Hamiltonian. Notably, in doing so, we take the full energy dependence of the coupling function into account, a fact that turns out to be crucial for the quantitatively correct description of the system.

The NRG yields the spectrum of the Au-PTCDA complex on the Au(111) surface. It consists of two charge excitation peaks, one below and the other above the chemical potential, both within 0.25 eV of the corresponding experimental values, and the Kondo resonance at the Fermi energy as the third feature. Due to the particle-hole asymmetry of the given system, the calculated Kondo resonance acquires an asymmetric line shape. In experiment, however, the asymmetry of the Kondo peak is less obvious, although the charge excitations peaks clearly show the particle-hole asymmetry also in the measured spectra.

In order to provide a guideline how the Kondo temperature can be extracted reliably from experiment for the present system and for particle-hole asymmetric systems in general, we have carried out a careful analysis of the scaling behavior of various definitions of the Kondo temperature T_{K}. Because the Kondo temperature defines a crossover scale, Kondo temperatures that are extracted from an experiment or an NRG calculation may vary up to a scaling factor. However, for valid extraction schemes, this scaling factor must be universal. If the scaling factor turns out to be nonuniversal in the sense that it depends on parameters of the model, the extraction scheme is inadequate.

In the present system, we find that Kondo temperatures extracted from the temperature dependence of both the zero-bias conductance and the local moment screening scale universally

with the analytic formula for the particle-hole asymmetric Anderson model, while the Kondo temperature derived from the FWHM of the zero-bias peak scales nonuniversally, no matter how the FWHM is determined. For the experiment, this means that we need to use the zero-bias conductance to obtain a Kondo temperature that is not prejudiced by nonuniversal aspects of the line shape. Applying this procedure to experiment and NRG, we obtain Kondo temperatures between 60 and 27 K for U in the range 1.1 to 1.3 eV. This allows us to narrow down possible U values from the range calculated in DFT/MBPT to around $U = 1.2\,\text{eV}$, since only for this value the NRG yields a Kondo temperature ($T_\text{K} = 37\,\text{K}$) close to experiment ($T_\text{K} \approx 38\,\text{K}$). The other case where experiment and theory agree, namely, 30.7 versus 30.2 K for the "Kondo temperature" derived from the width of the zero-bias conductance, can be discarded as coincidental, because this extracted parameter is nonuniversal and therefore not a good Kondo scale. Finally, we note that in spite of the fact that the Kondo effect is determined by low-energy excitation around the chemical potential, the replacement of the coupling function $\Gamma(E)$ by its value $\Gamma(0)$ at the Fermi energy is not sufficient. In the present case, this incurs an error of nearly a factor of 2 in the Kondo temperatures. Using the full energy dependence of the coupling function is therefore mandatory, if an accurate quantitative description of the system is sought.

Finally, we stress that the delocalized character of the spin-carrying π orbital makes the Au-PTCDA complex an interesting system in the investigation of spin phenomena and especially in the study of interactions between "magnetic molecules." Because the Kondo temperature depends very sensitively on molecule-metal coupling, energy-level position, and Coulomb interaction, the good agreement between experiment and theory, which we report here, proves that these parameters and, more generally, the structural and electronic properties of the Au-PTCDA complex are accurately described by DFT/MBPT. The possibility to predict the properties of a single complex accurately promises this system to be an ideal candidate for the quantitative study of interactions between extended molecular magnets.

ACKNOWLEDGMENTS

Two of us (BL and FBA) have received support by the Deutsche Forschungsgemeinschaft through AN 275/7-1 and support from the NIC Jülich for CPU time under project no. HHB00.

[1] M. N. Leuenberger and D. Loss, Quantum computing in molecular magnets, Nature (London) **410**, 789 (2001).

[2] G. D. Scott and D. Natelson, Kondo resonances in molecular devices, ACS Nano **4**, 3560 (2010).

[3] D. Gatteschi, R. Sessoli, and J. Villain, *Molecular Nanomagnets* (Oxford University Press, Oxford, 2006).

[4] I. Fernández-Torrente, D. Kreikemeyer-Lorenzo, A. Stróżecka, K. J. Franke, and J. I. Pascual, Gating the charge state of single molecules by local electric fields, Phys. Rev. Lett. **108**, 036801 (2012).

[5] R. Temirov, A. Lassise, F. B. Anders, and F. S. Tautz, Kondo effect by controlled cleavage of a single-molecule contact, Nanotechnol. **19**, 065401 (2008).

[6] C. Toher, R. Temirov, A. Greuling, F. Pump, M. Kaczmarski, M. Rohlfing, G. Cuniberti, and F. S. Tautz, Electrical transport through a mechanically gated molecular wire, Phys. Rev. B **83**, 155402 (2011).

[7] A. Greuling, R. Temirov, B. Lechtenberg, F. B. Anders, M. Rohlfing, and F. S. Tautz, Spectral properties of a molecular wire in the Kondo regime, Physica Status Solidi (b) **250**, 2386 (2013).

[8] A. Greuling, M. Rohlfing, R. Temirov, F. S. Tautz, and F. B. Anders, *Ab initio* study of a mechanically gated molecule: From weak to strong correlation, Phys. Rev. B **84**, 125413 (2011).

[9] L. Liu, K. Yang, Y. Jiang, B. Song, W. Xiao, L. Li, H. Zhou, Y. Wang, S. Du, M. Ouyang, W. A. Hofer, A. H. Castro Neto, and H.-J. Gao, Reversible single spin control of individual magnetic molecule by hydrogen atom adsorption, Sci. Rep. **3**, 1210 (2013).

[10] B. W. Heinrich, G. Ahmadi, V. L. Müller, L. Braun, J. I. Pascual, and K. J. Franke, Change of the magnetic coupling of a metal–organic complex with the substrate by a stepwise ligand reaction, Nano Lett. **13**, 4840 (2013).

[11] C. Krull, R. Robles, A. Mugarza, and P. Gambardella, Site- and orbital-dependent charge donation and spin manipulation in electron-doped metal phthalocyanines, Nat. Mater. **12**, 337 (2013).

[12] F. Mohn, J. Repp, L. Gross, G. Meyer, M. S. Dyer, and M. Persson, Reversible bond formation in a gold-atom organic-molecule complex as a molecular switch, Phys. Rev. Lett. **105**, 266102 (2010).

[13] J. Kröger, L. Limot, H. Jensen, R. Berndt, S. Crampin, and E. Pehlke, Surface state electron dynamics of clean and adsorbate-covered metal surfaces studied with the scanning tunnelling microscope, Prog. Surf. Sci. **80**, 26 (2005).

[14] We are using version 3.2 of the SIESTA, which is available at http://departments.icmab.es/leem/siesta.

[15] P. Ordejón, E. Artacho, and J. M. Soler, Self-consistent order-*N* density-functional calculations for very large systems, Phys. Rev. B **53**, R10441 (1996).

[16] J. M. Soler, E. Artacho, J. D. Gale, A. García, J. Junquera, P. Ordejón, and D. Sánchez-Portal, The SIESTA method for *ab initio* order-*N* materials simulation, J. Phys.: Condens. Matter **14**, 2745 (2002).

[17] J. P. Perdew, K. Burke, and M. Ernzerhof, Generalized gradient approximation made simple, Phys. Rev. Lett. **77**, 3865 (1996).

[18] V. G. Ruiz, W. Liu, E. Zojer, M. Scheffler, and A. Tkatchenko, Density-functional theory with screened van der waals interactions for the modeling of hybrid inorganic-organic systems, Phys. Rev. Lett. **108**, 146103 (2012).

[19] S. K. M. Henze, O. Bauer, T.-L. Lee, M. Sokolowski, and F. S. Tautz, Vertical bonding distances of PTCDA on Au(111) and Ag(111): Relation to the bonding type, Surf. Sci. **601**, 1566 (2007).

[20] T. Ogawa, K. Kuwamoto, S. Isoda, T. Kobayashi, and N. Karl, 3,4:9,10-Perylenetetracarboxylic dianhydride (PTCDA)

by electron crystallography, Acta Crystallograph. Sec. B **55**, 123 (1999).

[21] J. Tersoff and D. R. Hamann, Theory of the scanning tunneling microscope, Phys. Rev. B **31**, 805 (1985).

[22] T. Deilmann, P. Krüger, M. Rohlfing, and D. Wegner, Adsorption and STM imaging of tetracyanoethylene on Ag(001): An *ab initio* study, Phys. Rev. B **89**, 045405 (2014).

[23] L. Hedin, New method for calculating the one-particle Green's function with application to the electron-gas problem, Phys. Rev. **139**, A796 (1965).

[24] M. Rohlfing, Electronic excitations from a perturbative LDA+GdW approach, Phys. Rev. B **82**, 205127 (2010).

[25] M. Rohlfing, P. Krüger, and J. Pollmann, Quasiparticle band-structure calculations for C, Si, Ge, GaAs, and SiC using Gaussian-orbital basis sets, Phys. Rev. B **48**, 17791 (1993).

[26] J. Wieferink, P. Krüger, and J. Pollmann, Improved hybrid algorithm with Gaussian basis sets and plane waves: First-principles calculations of ethylene adsorption on ß-SiC(001)-(3×2), Phys. Rev. B **74**, 205311 (2006).

[27] W. H. A. Thijssen, D. Djukic, A. Otte, R. H. Bremmer, and J. M. van Ruitenbeek, Vibrationally induced two-level systems in single-molecule junctions, Phys. Rev. Lett. **97**, 226806 (2006).

[28] D. Djukic, K. S. Thygesen, C. Untiedt, R. H. M. Smit, K. W. Jacobsen, and J. M. van Ruitenbeek, Stretching dependence of the vibration modes of a single-molecule Pt–H_2–Pt bridge, Phys. Rev. B **71**, 161402 (2005).

[29] K. Svensson, L. Bengtsson, J. Bellman, M. Hassel, M. Persson, and S. Andersson, Two-Dimensional quantum rotation of adsorbed H_2, Phys. Rev. Lett. **83**, 124 (1999).

[30] L. Bengtsson, K. Svensson, M. Hassel, J. Bellman, M. Persson, and S. Andersson, H_2 adsorbed in a two-dimensional quantum rotor state on a stepped copper surface, Phys. Rev. B **61**, 16921 (2000).

[31] S. Li, A. Yu, F. Toledo, Z. Han, H. Wang, H. Y. He, R. Wu, and W. Ho, Rotational and vibrational excitations of a hydrogen molecule trapped within a nanocavity of tunable dimension, Phys. Rev. Lett. **111**, 146102 (2013).

[32] F. D. Natterer, F. Patthey, and H. Brune, Distinction of nuclear spin states with the scanning tunneling microscope, Phys. Rev. Lett. **111**, 175303 (2013).

[33] F. D. Natterer, F. Patthey, and H. Brune, Resonant-enhanced spectroscopy of molecular rotations with a scanning tunneling microscope, ACS Nano **8**, 7099 (2014).

[34] K. Nagaoka, T. Jamneala, M. Grobis, and M. F. Crommie, Temperature dependence of a single Kondo impurity, Phys. Rev. Lett. **88**, 077205 (2002).

[35] J. Lambe and R. C. Jaklevic, Molecular vibration spectra by inelastic electron tunneling, Phys. Rev. **165**, 821 (1968).

[36] D. Goldhaber-Gordon, J. Göres, M. A. Kastner, H. Shtrikman, D. Mahalu, and U. Meirav, From the Kondo regime to the mixed-valence regime in a single-electron transistor, Phys. Rev. Lett. **81**, 5225 (1998).

[37] N. Dori, M. Menon, L. Kilian, M. Sokolowski, L. Kronik, and E. Umbach, Valence electronic structure of gas-phase 3,4,9,10-perylene tetracarboxylic acid dianhydride: Experiment and theory, Phys. Rev. B **73**, 195208 (2006).

[38] According to the Mermin Wagner Theorem [51], it is unphysical to obtain a spin-polarized solution in a single orbital as the ground state of a system without an internal or external magnetic field in less than three dimensions. Quantum fluctuations will always lead to an unpolarised state with lower energy. Therefore, in the real system the spin-dependent single particle densities of state must be degenerate and the local magnetic moment is created by the (intraorbital) Coulomb repulsion that induces a dynamical correlation between the single particle densities of both spin channels and that therefore cannot be modelled as an effective single particle potential.

[39] S. Duhm, A. Gerlach, I. Salzmann, B. Bröker, R. Johnson, F. Schreiber, and N. Koch, PTCDA on Au(111), Ag(111) and Cu(111): Correlation of interface charge transfer to bonding distance, Org. Electron. **9**, 111 (2008).

[40] H. R. Krishna-murthy, J. W. Wilkins, and K. G. Wilson, Renormalization-group approach to the Anderson model of dilute magnetic alloys. II. Static properties for the asymmetric case, Phys. Rev. B **21**, 1003 (1980); **21**, 1044 (1980).

[41] R. Bulla, T. A. Costi, and T. Pruschke, Numerical renormalization group method for quantum impurity systems, Rev. Mod. Phys. **80**, 395 (2008).

[42] M. T. Glossop and D. E. Logan, Single-particle dynamics of the Anderson model: A local moment approach, J. Phys.: Condens. Matter **14**, 6737 (2002).

[43] Y. Meir and N. S. Wingreen, Landauer formula for the current through an interacting electron region, Phys. Rev. Lett. **68**, 2512 (1992).

[44] A. Schiller and S. Hershfield, Theory of scanning tunneling spectroscopy of a magnetic adatom on a metallic surface, Phys. Rev. B **61**, 9036 (2000).

[45] J. R. Schrieffer and P. A. Wolff, Relation between the Anderson and Kondo Hamiltonians, Phys. Rev. **149**, 491 (1966).

[46] L. Merker, S. Kirchner, E. Muñoz, and T. A. Costi, Conductance scaling in Kondo-correlated quantum dots: Role of level asymmetry and charging energy, Phys. Rev. B **87**, 165132 (2013).

[47] E. Muñoz, C. J. Bolech, and S. Kirchner, Universal out-of-equilibrium transport in Kondo-correlated quantum dots: Renormalized Dual fermions on the keldysh contour, Phys. Rev. Lett. **110**, 016601 (2013).

[48] D. C. Langreth, Friedel sum rule for Anderson's model of localized impurity states, Phys. Rev. **150**, 516 (1966); F. B. Anders, N. Grewe, and A. Lorek, On the validity of sum rules and Fermi-liquid properties in calculations for strongly correlated electrons, Z. Phys. B Condens. Matter **83**, 75 (1991).

[49] M. Rohlfing, R. Temirov, and F. S. Tautz, Adsorption structure and scanning tunneling data of a prototype organic-inorganic interface: PTCDA on Ag(111), Phys. Rev. B **76**, 115421 (2007).

[50] N. Takeuchi, C. T. Chan, and K. M. Ho, Au(111): A theoretical study of the surface reconstruction and the surface electronic structure, Phys. Rev. B **43**, 13899 (1991).

[51] N. Mermin and H. Wagner, Absence of ferromagnetism or antiferromagnetism in one- or two-dimensional isotropic Heisenberg models, Phys. Rev. Lett. **17**, 1133 (1966).

CHAPTER 4

A chemically driven quantum phase transition in a two-molecule Kondo system

It doesn't matter how beautiful your theory is, it doesn't matter how smart you are. If it doesn't agree with experiment, it's wrong. – *Richard P. Feynman*

4.1 Introduction

On the way to spin-based devices and quantum computation it is crucial to understand the physics of two interacting QIs as mentioned in the introduction of this thesis. Hence, full control of the properties of a QI is indispensable. In chapter 3 we have described quantitatively the formation of a QI – a Kondo spin-$1/2$ system – which is embedded in a self-assembled molecular layer. As described in chapter 3 the geometry of a single Au-PTCDA complex, called monomer in the following, is fixed with respect to its neighbors and the substrate. Furthermore its physical properties are well defined – hence fulfilling all requirements for investigating the interaction between two QIs.

Since the spin of a monomer resides in a π orbital and thus is delocalized over the entire complex it has a main advantage compared to common molecular magnets: it is easier to tailor the interaction between delocalized spins since they are not shielded by organic ligands as it is the case for common molecular magnets where the spin usually is located in a d or f orbital of a metal ion that is surrounded by organic ligands. Furthermore the extended nature of the spin-carrying π orbital allows to investigate systematically the effect of direct non-magnetic chemical interaction between two monomers on the magnetic properties of those. If we take into account that a Au atom can bind to the PTCDA molecule in one of four positions (see chapter 3) and that within the unit cell of the PTCDA layer there are two inequivalent molecules we can distinguish between 32 structurally distinct dimers, i.e. directly neighboring monomers.

In the following article in section 4.2 we demonstrate that in the present case, i.e. if the spin-carrying orbital is extended in space, the magnetic properties of the QIs are not determined by direct or indirect exchange interaction, but rather by the non-magnetic chemical interaction. This means the magnetic properties of the system are directly coupled to the wave function overlap between the two monomers and thus to the formation of bonding and anti-bonding orbitals. Interestingly, in this scenario a competition between kinetic energy gain due to the Kondo effect and binding energy gain because of the chemical interaction is the driving force of a quantum phase transition (QPT) in the dimer. Only tiny changes in the wave function overlap, i.e. slightly different dimer configurations, are enough to drive the system through a quantum critical point (QCP) from an underscreened triplet to a molecular singlet ground state. Astonishingly, here the Kondo effect stabilizes the triplet against the singlet state that is promoted by chemical hybridization.

The interaction and therefore also the ground state of the dimers we detect by means of scanning tunneling spectroscopy (STS). Using density functional theory (DFT) we show that the spin-carrying π orbitals of the monomers hybridize and thus split into bonding and antibonding states

and furthermore that there is a strong correlation between the realized ground state of the dimer and the orbital splitting between the bonding and antibonding states. This finding we quantitatively explain by using a TIAM which we solve by the numerical renormalization group (NRG) approach. All parameters for our model we obtain from ab-initio calculations (DFT+many-body perturbation theory (MBPT)). The evaluation of the needed parameters and a detailed description of the TIAM can be found in the supplementary information to the article in section 4.3. Furthermore, the supplement in section 4.3 contains useful information about the ground states of the dimer in the gas-phase and additional information about the spectral functions and the corresponding processes.

4.2 A chemically driven quantum phase transition in a two-molecule Kondo system

The following article has been published in the journal **Nature Physics**:

- **T. Esat**, B. Lechtenberg, T. Deilmann, C. Wagner, P. Krüger, R. Temirov, M. Rohlfing, F. B. Anders, and F. S. Tautz, "A chemically driven quantum phase transition in a two-molecule Kondo system," *Nature Physics*, vol. 12, no. 9, p. 867, 2016.

Author contributions:
R.T., C.W., **T.E.** and F.S.T. conceived the experiments. **T.E.** and R.T. conducted the experiments. **T.E.** analysed the experimental data. T.D., P.K. and M.R. performed density functional and many-body perturbation calculations and analysed the resultant data. B.L., F.S.T. and F.B.A. developed the theoretical model. B.L. and F.B.A. carried out the numerical renormalization group calculations and analysed the resultant data. **T.E.** has prepared the figures. **T.E.**, R.T., F.B.A. and F.S.T. wrote the paper, with significant contributions from all authors.

Note that a short article about our paper *A chemically driven quantum phase transition in a two-molecule Kondo system* has been published by Dr. Markus Ternes in the **Physik Journal**:

- M. Ternes, "Auf die Bindung kommt es an," *Physik Journal*, vol. 15, no. 7, p. 24, 2016.

A chemically driven quantum phase transition in a two-molecule Kondo system

Taner Esat,[1,2] Benedikt Lechtenberg,[3] Thorsten Deilmann,[4] Christian Wagner,[1,2] Peter Krüger,[4] Ruslan Temirov,[1,2] Michael Rohlfing,[4] Frithjof B. Anders,[3] and F. Stefan Tautz[1,2]

[1] *Peter Grünberg Institute (PGI-3), Forschungszentrum Jülich, 52425 Jülich, Germany*
[2] *Jülich Aachen Research Alliance (JARA), Fundamentals of Future Information Technology, 52425 Jülich, Germany*
[3] *Lehrstuhl für Theoretische Physik II, Technische Universität Dortmund, Otto-Hahn-Str. 4, 44221 Dortmund, Germany*
[4] *Institut für Festkörpertheorie, Westfälische Wilhelms-Universität Münster, 48149 Münster, Germany.*

The magnetic properties of nanostructures that consist of a small number of atoms or molecules are typically determined by magnetic exchange interactions. Here, we show that non-magnetic, chemical interactions can have a similarly decisive effect if spin-moment-carrying orbitals extend in space and therefore allow the direct coupling of magnetic properties to wavefunction overlap and the formation of bonding and anti-bonding orbitals. We demonstrate this for a dimer of metalmolecule complexes on the Au(111) surface. A changing wavefunction overlap between the two monomers drives the surface-adsorbed dimer through a quantum phase transition from an underscreened triplet to a singlet ground state, with one configuration being located extremely close to a quantum critical point.

When two local moments on a metal surface interact, this is usually discussed in terms of a competition between the Kondo effect and the Ruderman-Kittel-Kasuya-Yosida (RKKY) interaction [1–5]. The RKKY is an indirect exchange interaction which is mediated by the conduction electrons [6–8]. Depending on distance, it favours ferromagnetic or antiferromagnetic alignments of local moments, whereas the Kondo effect tends to quench the moments locally with the help of the conduction electrons [9–12]. Here, we describe a different scenario, in which the competition between the kinetic energy gain due to conduction electron scattering and the binding energy gain due to the chemical interaction between the moment-carrying orbitals is the driving force of a quantum phase transition in a system of two local moments on a metal surface. Interestingly, in this scenario the coupling to the metal surface, which at low temperature leads to the Kondo effect, already at high temperature favours the alignment, whereas the chemical interaction promotes the local quenching of the moments. We expect this mechanism to be generic and widespread, because it relies only on very general features of chemical interactions and Kondo physics. Moreover, because it is straightforward to engineer the chemistry, the mechanism will allow for an easy tuning of the magnetic interaction between local moments.

Dimers of a metal-molecule complex

The magnetic properties of nanostructures are at present the focus of an intense research effort in physics, chemistry and materials science. The reason is the drive to design miniaturized spin-based devices, for example, for spintronics or quantum computation. In this context, dimers of two atoms or molecules constitute important model systems, because they are simple and yet embody the crucial physics: the competition of interactions within the nanostructure with those between the nanostructure and its environment.

To demonstrate the novel scenario, we use dimers formed by two metal-molecule complexes that each consist of a 3,4,9,10-perylenetetracarboxylic-dianhydride (PTCDA) molecule, adsorbed on the inert Au(111) surface, and a single Au atom. In each monomer, the 6s electron of the Au atom is transferred onto the molecule into an empty π-orbital that is only weakly coupled to the substrate, and consequently forms a well-defined spin moment delocalized over the entire PTCDA molecule [13]. We investigate the interactions between the spins on both monomers by scanning tunnelling spectroscopy (STS) to detect the ground state of the dimer. Specifically, we show that the dimers are indeed located very close to a quantum critical point (QCP) [14, 15], so that depending on the precise chemistry, distinct ground states (local singlet or local triplet) are realized.

Fig. 1a is a large scale image of a PTCDA layer on which Au atoms have been deposited. Each bright spot corresponds to an Au-PTCDA complex [13]. On the Au(111) surface, single Au-PTCDA complexes undergo a $S = 1/2$ Kondo effect, as revealed by a zero-bias peak in their STS spectra [13]. Fig. 1a also shows dimers which have formed spontaneously upon Au deposition. Some (but not all) of these dimers show broader or even gapped zero-bias peaks (Fig. 1b). This suggests that the local moments on the two monomers interact with each other.

Because of the low symmetry of the monomer – the Au atom binds to the PTCDA in one of four positions (Fig. 1c) – and the herringbone structure of the PTCDA layer – with two inequivalent molecules in the unit cell – there are in fact 32 structurally distinct dimers. An analysis of a large automatically collected ensemble of spectra (see Supplementary Information for details) reveals that broadened or gapped zero-bias peaks occur

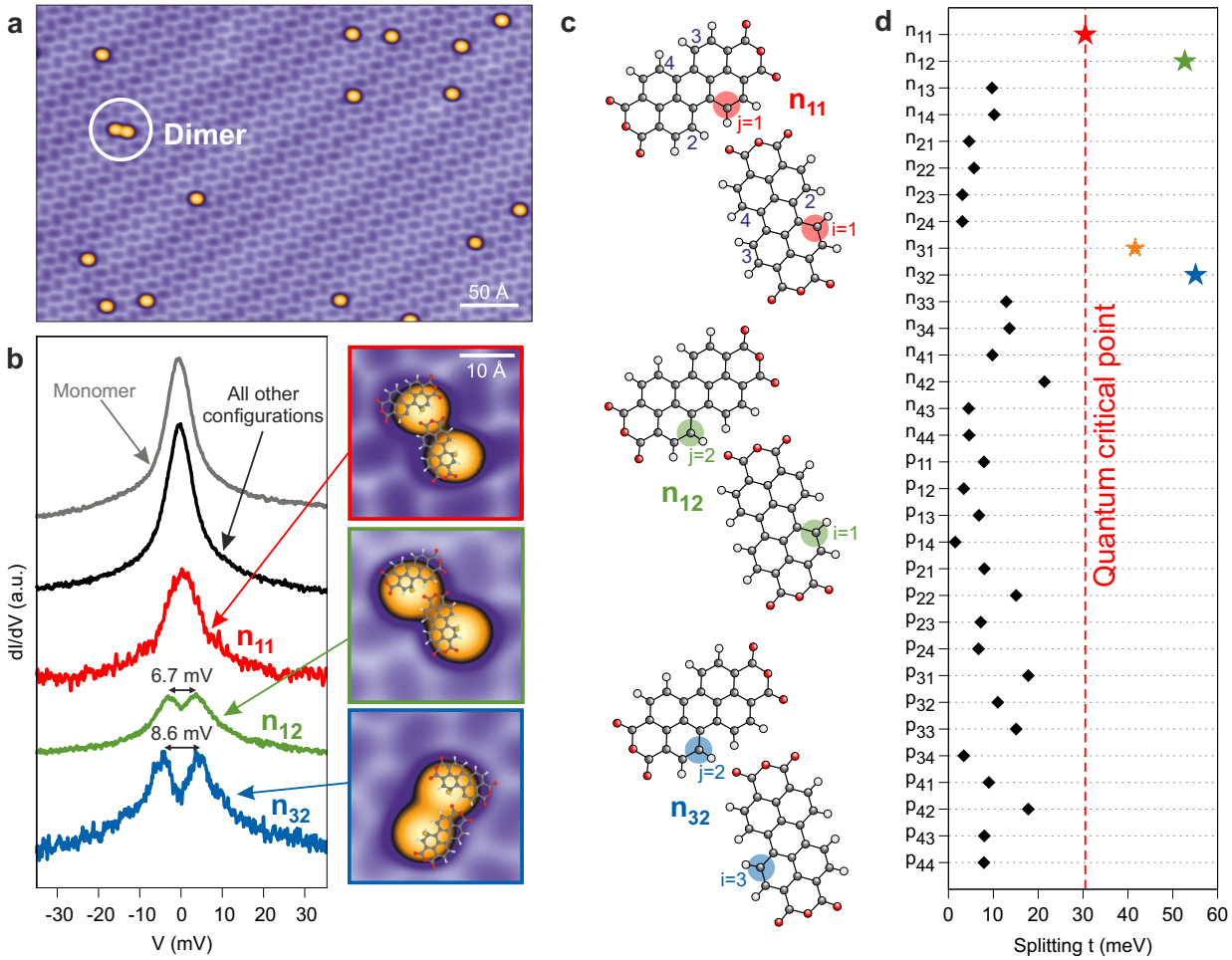

FIG. 1. **Structure and spectral properties of dimers consisting of Au-PTCDA complexes on the Au(111) surface.** **a**, Constant-current STM image after deposition of Au atoms on a PTCDA monolayer on Au(111) (bias voltage $V = 316\,\mathrm{mV}$, tunnelling current $I = 25\,\mathrm{pA}$). **b**, dI/dV conductance spectra of Au-PTCDA monomers and several dimers, the latter recorded on one of the two Au atoms. Insets: STM images of the corresponding dimers with Au-PTCDA molecules overlayed. n_{ij} configurations are explained in **c**. **c**, Herringbone structure of PTCDA on Au(111) [16]. The white, grey and red circles indicate hydrogen, carbon and oxygen atoms of PTCDA. Numbers indicate possible Au binding sites. Dimer configurations are classified as n_{ij} (p_{ij}) when the molecules are normal (parallel, see Supplementary Information) to each other, with the index i (j) specifying the binding sites of the Au atoms on top of two molecules forming the dimer. **d**, Hybridization-induced splitting t of the respective monomer orbitals (see text) for the various dimer configurations, calculated in DFT in the local density approximation (LDA). Symbols refer to dimer's spectral properties, black diamonds: unbroadened Kondo peaks, stars: broadened or gapped zero-bias peaks (colour code matches **b**). The red dashed line indicates the QCP as predicted for the parity-broken model, $t_\mathrm{c} \simeq 30.5\,\mathrm{meV}$.

exclusively in the n_{11}, n_{12} and n_{32} configurations. The label n_{ij} (p_{ij}) stands for a dimer consisting of two complexes whose PTCDA backbones are normal (parallel) to each other, with the Au atom in the first (second) complex in position $i(j)$ (see Fig. 1c and Supplementary Information).

Gaps in the zero bias peak

For atoms on surfaces, gapped zero-bias peaks have been associated with a competition between the Kondo effect and the RKKY [1–4] or exchange interactions [17]. In this scenario, a clear correlation of the spectra to the distance between the local moments is expected. In the present case, however, such a correlation does not exist (see Supplementary Information). This suggests that the gap formation in the present case is based on a different mechanism. It has been shown that direct tunnelling between two impurities – that is, the formation of a chemical bond – can also yield a spectral function with a gap at zero bias [18]. A first hint regarding the origin of the gap in the present case comes from the fact that the dimer configuration has a profound influence on the spectra, as depicted in Fig. 1b. Whereas n_{11} dimers show a single broadened zero-bias peak, the n_{12}

and n_{32} dimers exhibit gaps of $\simeq 7$ meV and $\simeq 9$ meV, respectively.

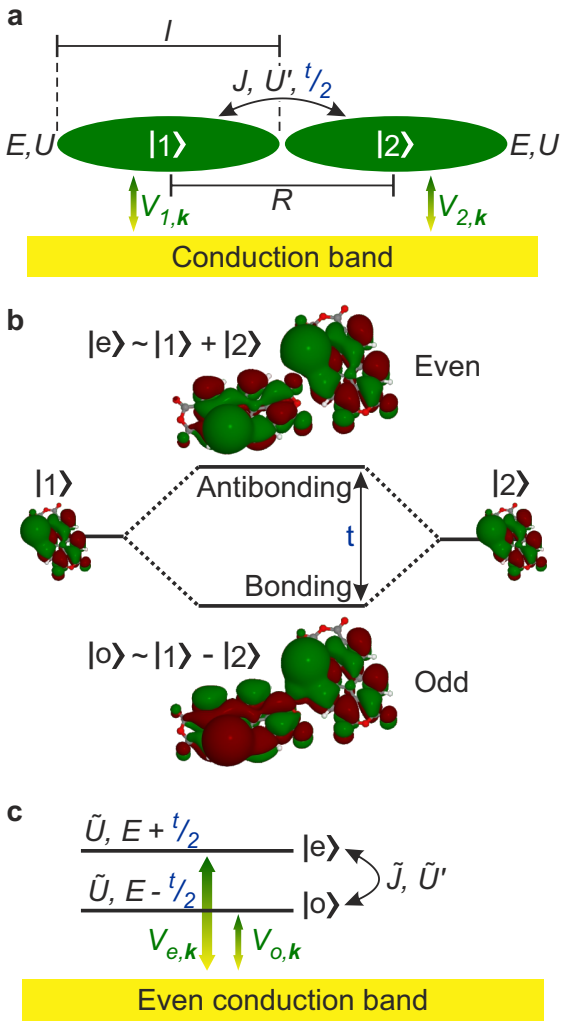

FIG. 2. **TIAM and chemical interaction of Au-PTCDA dimers. a**, Schematic sketch of the TIAM, with the level energies E, intra- and interorbital Coulomb repulsions U and U', direct exchange J, hybridization matrix elements $V_{1,\mathbf{k}}$, $V_{2,\mathbf{k}}$, and a tunnelling term $t/2$ between the two monomers. R is the distance between the monomers, l the linear extension of each monomer orbital. **b**, Bonding and antibonding orbitals of the n_{12} dimer (see Fig. 1c) as obtained from DFT. The bonding orbital is of odd character whereas the antibonding orbital is even (see text). **c**, TIAM after transformation to the basis involving even and odd linear combinations of monomer orbitals. Note that $\tilde{U}$, $\tilde{U}'$, $\tilde{J}$, $V_{\mathrm{e},\mathbf{k}}$ and $V_{\mathrm{o},\mathbf{k}}$ denote the parameters after transformation (see Supplementary Information).

To explain this finding, we analyze the influence of the dimer configuration on the interaction between the monomers with density functional theory (DFT). Indeed, we find that the moment-carrying monomer valence orbitals hybridize, splitting into a pair of bonding and antibonding states. The splitting ranges from $t = 1$ meV to 55 meV, suggesting a weak chemical interaction. As Fig. 1d reveals, there exists a strong correlation of a dimer's spectral properties to the orbital splitting t (but not to the Au-Au distance). Only the two largest splittings ($\gtrsim 50$ meV) in n_{32} and n_{12} give rise to a gap (note that the configuration n_{31}, for which the predicted splitting amounts to 41.6 meV, was not observed in our experimental ensemble (along with the n_{41} and n_{42} configurations)), whereas an intermediate splitting of $\simeq$ 30 meV leads to a single broadened zero-bias peak in n_{11}. For all other configurations, the orbital splitting is below $\simeq$ 20 meV, and these show zero-bias peaks with essentially the same width as observed for monomers (Fig. 1b). Encouraged by the predictive power of the DFT simulation, we now turn to a fully quantitative description comprising a combination of DFT, many-body perturbation theory (MBPT) and the numerical renormalization group (NRG) approach [19–21].

Two impurity Anderson model (TIAM)

To describe a dimer in the presence of the surface we use the two-impurity Anderson model (TIAM) [10, 22–24]. In the TIAM, sketched schematically in Fig. 2a, the dimer of Au-PTCDA complexes is modelled by a pair of extended monomeric π-orbitals, separated by a distance R. In Hilbert space, the corresponding degenerate states, denoted $|1\rangle$ (monomer 1) and $|2\rangle$ (monomer 2), define a parity symmetry, even if the actual dimer does not possess inversion symmetry in real space. To account for the hybridization between the monomeric π-orbitals, we introduce a tunnelling term $t/2$, whose value is determined by the wavefunction overlap. The TIAM furthermore comprises intra- and interorbital Coulomb repulsion energies U and U', hybridization matrix elements $V_{1,\mathbf{k}}$ and $V_{2,\mathbf{k}}$ which quantify the coupling of $|1\rangle$ and $|2\rangle$ to the conduction band, and the Heisenberg exchange interaction J between $|1\rangle$ and $|2\rangle$. The resulting Hamiltonian of the TIAM can be found in Methods.

In the TIAM, the hybridization between the initially degenerate states $|1\rangle$ and $|2\rangle$ splits them into a pair of bonding and antibonding states. One of them has even, the other odd character under the parity symmetry as defined above. Therefore, we denote these hybridized states as $|\mathrm{e}\rangle$ and $|\mathrm{o}\rangle$. In terms of monomeric states they are given by $|\mathrm{e/o}\rangle = \frac{1}{\sqrt{2}}(|1\rangle \pm |2\rangle)$. As we have seen already, an analogous splitting into bonding and antibonding states is observed for the real dimer in DFT calculations. Although the actual Au-PTCDA dimer does not exhibit real-space inversion symmetry, the bonding and antibonding wavefunctions of the real dimer can nevertheless be classified as even or odd, as Fig. 2b shows: in particular we find in DFT that for all possible n_{ij} and p_{ij} configurations the bonding state, which has no node between the monomers, is odd, in the sense that the phase of its wave function is opposite on the two monomers, which can most easily be seen on the respective Au atoms

in Fig. 2b. By the same token, the antibonding state is even. According to our model, this implies $t > 0$.

Because of the mentioned strong correlation between the dimer's spectral properties and its orbital splitting t (Fig. 1d), it is natural to discuss the physics of the dimer in terms of $|\mathrm{e}\rangle$ and $|\mathrm{o}\rangle$ states. As a starting point of the discussion, the energy level scheme of the gas-phase dimer is displayed and discussed in the Supplementary Information. Briefly, the ground state of the gas-phase dimer is the local singlet sketched in Fig. 3f, followed by the local triplet manifold of Fig. 3e at slightly higher energy. The former is lowered below the latter by antiferromagnetic exchange $J_{\mathrm{ex}} = t^2/(U - U')$. We note in passing that J_{ex}, generated within the TIAM by finite tunnelling $t/2$ between the monomer orbitals, has the same order of magnitude as the *ab initio* prediction of J (see Supplementary Information). Therefore, we neglected the additional Heisenberg exchange and set $J = 0$.

Finally, we stress that the Au-PTCDA dimer can be described well by taking the limit $R \to 0$, because the linear dimensions l of the π-orbitals belonging to states $|1\rangle$ and $|2\rangle$ are similar to R, as shown schematically in Fig. 2a. This is the underlying reason why the RKKY interaction between the monomers in the dimer will be weak (see Supplementary Information), and it also distinguishes the present limit from the one used in ref. [18], where the gap formation has been investigated for $R \to \infty$.

Before solving the TIAM, we transform it into the bases of even and odd dimer and conduction electron states (Fig. 2c), in which the parity of the dimer state has a crucial influence on its coupling to the substrate: specifically, in the limit $R \to 0$ the odd conduction band decouples completely from the dimer (Supplementary Information and refs. [9, 25–27]), whereas the even conduction band always couples to $|\mathrm{e}\rangle$ with strength $V_{e,\mathbf{k}} = \frac{1}{\sqrt{2}}(V_{1,\mathbf{k}} + V_{2,\mathbf{k}})$. The coupling of $|\mathrm{o}\rangle$ to the even conduction band is controlled by symmetry: if $V_{1,\mathbf{k}} = V_{2,\mathbf{k}}$, that is, in the parity-symmetric case, $|\mathrm{o}\rangle$ is decoupled from the even conduction band, whereas in the more realistic case $V_{1,\mathbf{k}} \neq V_{2,\mathbf{k}}$, when parity symmetry is broken, $|\mathrm{o}\rangle$ couples weakly to the even conduction band, with $V_{\mathrm{o},\mathbf{k}} = \frac{1}{\sqrt{2}}(V_{1,\mathbf{k}} - V_{2,\mathbf{k}})$. Differences in the coupling of $|1\rangle$ and $|2\rangle$ to the conduction band turn out to be the key feature for understanding the STS spectra.

Solution of the TIAM and a quantum critical point

We now turn to a discussion of the physics of the dimer as it is unveiled in the solution of the parity-symmetric ($V_{1,\mathbf{k}} = V_{2,\mathbf{k}}$) TIAM. To solve the TIAM, we employ physical quantities E, U, U' and the energy-dependent hybridization function $\Gamma_{\mathrm{e}}(\omega)$ as evaluated from *ab initio* calculations (DFT+MBPT) (see Methods, Supplementary Information and refs. [28–30]) and apply the NRG approach [19–21] to obtain the spectral functions $\rho_{\mathrm{e/o},\sigma}(\omega)$ that are proportional to the imaginary parts of the single-particle Green's functions $\Im\{\langle d_{\mathrm{e/o},\sigma}|d^{\dagger}_{\mathrm{e/o},\sigma}\rangle(\omega - io^{+})\}$ and which can be compared to the experimental dI/dV spectra (see Methods and Supplementary Information).

We see in Fig. 3a that $\rho_{\mathrm{e},\sigma}(\omega)$ exhibits a Kondo peak (red curve), readily recognizable as a typical $S = 1$ underscreened Kondo resonance by its sharp peak profile, in analogy to the results reported in the context of the underscreened Kondo effect in a molecular transistor [31], and indicating that for $t < 31\,\mathrm{meV}$ the dimer is in a local triplet ground state, partially screened by the even conduction band of the substrate, which results in a doubly degenerate ground state for the combined dimer/substrate system. This state is schematically shown in Fig. 3e.

To discuss the nature of the spectral functions $\rho_{\mathrm{e/o},\sigma}(\omega)$ it is instructive to consider them as a spectrum of excitations of the dimer that occur on injection ($\omega > 0$) or extraction ($\omega < 0$) of an electron with energy $|\omega|$ into the $|\mathrm{e}\rangle$ or $|\mathrm{o}\rangle$ orbital. An example of such a process is shown in Fig. 3b, where the tip injects an electron into the even orbital and, because of the large intraorbital Coulomb repulsion $\tilde{U}'$, the dimer responds by ejecting an electron into the even conduction band. Because the odd orbital is decoupled from the even conduction band, (see above), this ejection can only happen from $|\mathrm{e}\rangle$, and thus an electron with opposite spin is ejected. Comparing Figs. 3b and e, it is clear that this injection provokes a transition between two degenerate triplet states, namely from $S_z = 1$ to $S_z = 0$. As a consequence of this spin-flip excitation, the previously mentioned Kondo resonance at $\omega = 0$ appears in $\rho_{\mathrm{e},\sigma}(\omega)$ (Fig. 3a).

Figure 3a also shows that for $t > 32\,\mathrm{meV}$ the Kondo effect collapses, pointing to a change of the many-body ground state at a critical splitting parameter $t_{\mathrm{c}} \simeq 31.5\,\mathrm{meV}$. Further insight into this QPT can be obtained by looking at the odd spectral functions $\rho_{\mathrm{o},\sigma}(\omega)$ for the underscreened Kondo phase in Fig. 3c (red curves). As Fig. 3d shows, on injection into the odd orbital the system responds by a change from a Kondo-screened local triplet into a local singlet state (compare Fig. 3d with Fig. 3f). Again, the ejection of the electron can only occur from $|\mathrm{e}\rangle$. Unlike the triplet-triplet transition in Fig. 3b, this is not a zero-energy transition, but involves a finite transition energy. As a consequence, the spectral signature of this process occurs at finite ω (thresholds in the red curves in Fig. 3c). The threshold energy ω_{th} is related to the energy difference between two competing ground states (local triplet versus local singlet) of the dimer. By increasing t, the energy of the local singlet can be lowered with respect to the Kondo-screened local triplet, up to the point where the two become degenerate. This happens at $t_{\mathrm{c}} \simeq 31.5\,\mathrm{meV}$, where the red threshold peak in Fig. 3c indeed reaches $\omega = 0$. Evidently, as the local singlet becomes the new ground state of the dimer, the Kondo resonance in Fig. 3a must collapse.

For $|\omega| > |\omega_{\mathrm{th}}|$ the spectra in Fig. 3c exhibit a decay that is typical for absorption edges in other physical contexts, most notably X-ray absorption edges [32].

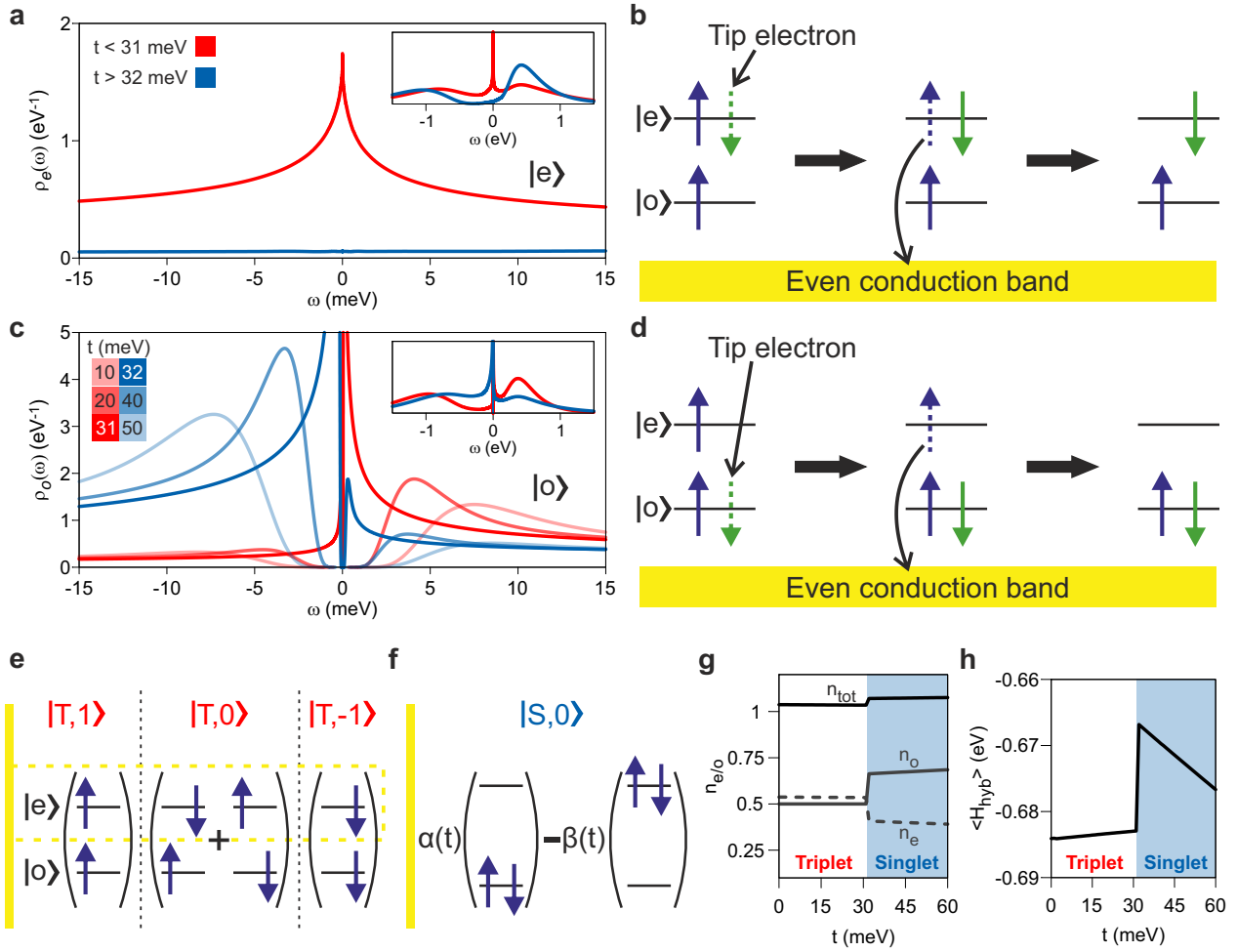

FIG. 3. **Spectral functions and ground states of surface-adsorbed Au-PTCDA dimers in the parity-symmetric case ($V_o = 0$).** **a**, Even spectral functions $\rho_{e,\sigma}(\omega)$, calculated using the NRG method with parameters $E = -1.09\,\text{eV}$, $U = 1.4\,\text{eV}$, $U' = 0.12\,\text{eV}$ and the energy-dependent $\Gamma_e(\omega)$ with $\Gamma_e(0) = 173\,\text{meV}$ for varying t as given in the legend. Red curve: dimer in local triplet. Blue curve: dimer in local singlet. **b**, Process that underlies the spectral function $\rho_{e,\sigma}(\omega)$ for $\omega > 0$ (electron injection from tip) and $t < t_c$ (dimer initially in the local triplet state). The dimer remains in the triplet manifold, undergoing a transition from $S_z = 1$ to $S_z = 0$ (see **e**). Through this spin-flip scattering, the conduction electrons partially screen the local $S = 1$ spin of the dimer. **c**, As panel **a**, but odd spectral functions $\rho_{o,\sigma}(\omega)$. **d**, As panel **b**, but for $\rho_{o,\sigma}(\omega)$. The dimer changes from the triplet manifold ($S_z = 1$) to the local singlet (component α, see **f**). **e**, Ground state of the dimer for $t < t_c$. The three states $S_z = 1, 0, -1$ of the local triplet are shown. The yellow dashed line illustrates both the entanglement of the local moment with the conduction band of the substrate at high temperature as well as its partial screening at low temperature (underscreened Kondo effect), the latter leading to a $S = 1/2$ doublet ground state of the surface-adsorbed dimer. **f**, Ground state of the dimer for $t > t_c$. The singlet is a superposition of two states. Coefficients α and β depend on t and the substrate. For $t = 0$ and a particle-hole symmetric substrate density of states $\alpha = \beta = 1/\sqrt{2}$. For $t > 0$, $|\alpha| > |\beta|$. The relative sizes of $|\alpha|$ and $|\beta|$ control the relative heights of the thresholds in the spectral function in panel **c**. The two ground states of the combined dimer/substrate system are topologically distinct by their degeneracies: the partially Kondo-screened local triplet in **e** is doubly degenerate, the singlet in **f** is non-degenerate. **g**, Occupation numbers n_e, n_o and $n_{tot} = n_e + n_o$ as a function of t. At the QCP ($t = t_c$) steps in the occupation occur. **h**, Expectation value of the hybridization energy $\langle H_{hyb}\rangle$ as a function of t. At the QCP $t = t_c$ the hybridization $|\langle H_{hyb}\rangle|$ decreases sharply. For $t < t_c$ the triplet ground state is stabilized by $\langle H_{hyb}\rangle$.

Here, the conduction electrons scatter from the charged dimer, the charge being created by injection or extraction of an electron by the STM tip. Hence, the spectral shape of the odd orbital is determined by charge screening, whereas the one of the even orbital is determined by spin screening (Kondo effect). Ultimately, the different spectral shapes of $\rho_{e,\sigma}(\omega)$ and $\rho_{o,\sigma}(\omega)$ are a consequence of the fact that, in the parity-symmetric case, the odd orbital is decoupled from the conduction band: this means that it acts as a structureless scatterer, whereas

the even orbital constitutes a scattering potential that is established adiabatically, because its internal degree of freedom (spin) correlates successive conduction electron scattering events [32].

Signatures of the QPT at $t_c \simeq 31.5\,\mathrm{meV}$ can also be traced in the high-energy part of the $\rho_{e/o,\sigma}(\omega)$ spectra. Comparing red and blue spectra in the insets of Fig. 3a and c, we observe that on passing through the QPT from below, – that is, from $t < t_c$ to $t > t_c$ – spectral weight of the even orbital is redistributed abruptly from negative to positive ω, whereas the opposite happens for the odd orbital. A closer look at the orbital occupation in Fig. 3g reveals that for $t < t_c$ the even and odd occupancy is almost the same, and of integer valence, consistent with the local triplet state depicted in Fig. 3e. In contrast, above the QPT the odd orbital is dominantly occupied, indicating a singlet as in Fig. 3f with asymmetric and t-dependent quantum weights $\alpha(t)$ and $\beta(t)$ – that is, $|\alpha|^2 > |\beta|^2$. The marginal jump in n_{tot} at the QPT is due to fact that the odd orbital, which is now more strongly occupied, is not coupled to the conduction electrons, which increases the overall occupancy of the local states of the dimer by $\simeq 3$ percent. Nevertheless, the dimer still remains close to integer valence.

Finally, we address the mechanism which at finite $t < t_c$ stabilizes the local triplet state with one electron each in the $|e\rangle$ and $|o\rangle$ orbitals (Fig. 3e) against the local singlet in Fig. 3f, and thus leads to the QPT at finite t_c. Usually the separation of a local triplet from a local singlet is governed by the exchange interaction [22], as is also found in the present case for the gas-phase dimer (see Supplementary Information). However, DFT predicts a negligibly small exchange $|J_{ex}| \approx |t^2/(U - U')| \ll t_c$, and its energy scale is absent in any of the relevant quantities in the present system. Moreover, this exchange interaction is antiferromagnetic and thus favours the singlet. The stabilization of the local triplet state at finite t is therefore realized solely by the gain of additional hybridization energy due to the strong entanglement between the local moment and the conduction band of the substrate (Fig. 3h). This entanglement, which involves only $|e\rangle$, and is therefore stronger in the triplet than in the singlet, is shown schematically by the dashed yellow line in Fig. 3e. Although at low temperature the subsequent underscreened Kondo effect reduces the triplet moment to an effective $S = 1/2$ and yields a further energy gain, the major contribution to stabilizing the triplet even above the Kondo temperature stems from charge fluctuations due to the coupling to the substrate, as demonstrated by the change of the hybridization energy at the QCP. At the QCP ($t = t_c$), the energy gain due to the entanglement is precisely offset by the single-particle energy gain that occurs by filling more electrons into the bonding orbital $|o\rangle$ (Fig. 3f for $|\alpha| > |\beta|$). For $t > t_c$ local singlet formation is favoured over the energy gain through the entanglement: the QPT occurs, and at low temperature the Kondo effect breaks down.

Origin of the gap in the STS spectra

Before the final comparison between simulations and experiment can be made, one last issue needs to be resolved. In spite of yielding the essentially correct physics, the parity-symmetric model of Fig. 3a,c has one critical shortcoming: a gap is found only in the odd spectral function, which is not observable in STM, because $|o\rangle$ is completely decoupled from the even conduction electron band. However, the experimental dI/dV spectra of Fig. 1b exhibit a gap. As it turns out, parity breaking can explain the appearance of a gap in the STS spectra and, considering the lack of symmetry in the dimer, the breaking of parity symmetry is in fact expected (for example, the couplings of monomers 1 and 2 to the substrate are slightly different, see Supplementary Information).

Parity breaking has two consequences: first, the odd orbital now couples directly to the even conduction band. Therefore, spectral features of the odd orbital are mixed weakly into the even spectral function $\rho_{e,\sigma}(\omega)$ (see Supplementary Information). Second, the spectral function as seen in STM is now given by $\rho_\sigma(\omega) \propto \Im\{\langle d_{e,\sigma} + q d_{o,\sigma} | d^\dagger_{e,\sigma} + q d^\dagger_{o,\sigma}\rangle(\omega - i0^+)\}$, with non-zero $q = V_{o,\mathbf{k}}/V_{e,\mathbf{k}} \approx 0.1$ (see Methods and Supplementary Information). If $\rho_\sigma(\omega)$ is factored out, it becomes clear that, in addition to the even spectral function $\rho_{e,\sigma}(\omega)$, also the odd spectral function $\rho_{o,\sigma}(\omega)$ and two mixed terms even/odd and odd/even contribute to the STS spectrum of the dimer. Note that parity breaking also shifts the QCP from $t_c = 31.5\,\mathrm{meV}$ to $30.5\,\mathrm{meV}$.

Figure 4a,b shows the spectral function $\rho_\sigma(\omega)$ of the parity-broken model, based on input parameters from DFT+MBPT, at two different temperatures. Note that, in this case, $\rho_\sigma(\omega)$ spectra were generated precisely for the set of t values predicted by DFT+MBPT for the dimers found in the experiment (see Fig. 1b-d). The agreement of the experimental spectra with the NRG result at $T = 9.5\,\mathrm{K}$ is excellent, notably without any fitting parameters. The agreement covers the monomer spectra and the configuration dependence of the dimer spectra – that is, the observation of a single broadened zero bias peak for n_{11} and gapped peaks for n_{12} and n_{32} dimers (Fig. 1b-d).

In particular, the comparison of Fig. 4b (parity-broken) with Fig. 3a (parity-symmetric) shows that below the QPT, when the Kondo resonance dominates the spectrum, the contribution of the odd state to the spectral function, and hence the STS spectra, is negligible. However, in the local singlet state, once the Kondo resonance has collapsed, the odd contribution becomes dominant in Fig. 4a,b and appears as a gap in the spectrum. The physics of the gapped 'Kondo peak' is hence not the Kondo effect itself, but a remnant of excitation thresholds in the odd orbital. This implies that the width of the gap indicates how close the dimer is to the QCP: the smaller the gap, the closer the system is to the QCP. In particular, the configuration n_{11} with $t = 30.5\,\mathrm{meV}$ (red curve in Fig. 4a) is so close to the QCP that, at the tem-

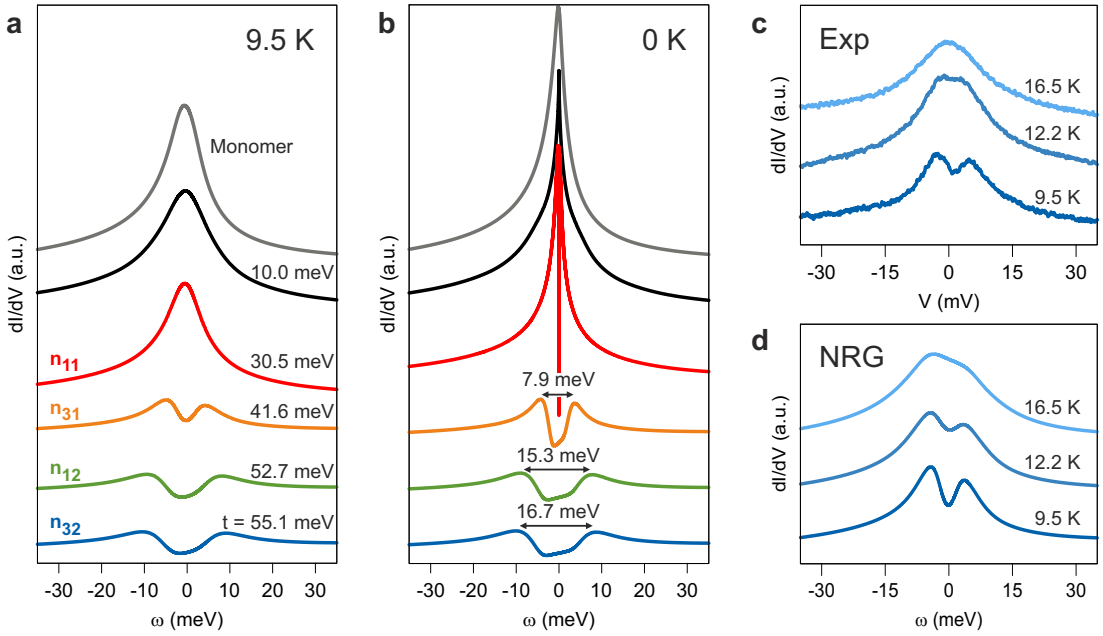

FIG. 4. **Spectral functions of Au-PTCDA dimers in the parity-broken case, analysed with the NRG method. a**, dI/dV spectra from NRG method for different values of t and $q = V_o/V_e = 0.1$, $T = 9.5\,\mathrm{K}$. Parameters $E_1 = E_2 = -1.09\,\mathrm{eV}$, $U_1 = U_2 = 1.4\,\mathrm{eV}$, $U' = 0.12\,\mathrm{eV}$, $\Gamma_e(0) = 172\,\mathrm{meV}$, $\Gamma_o(0) = 1.7\,\mathrm{meV}$, and $J = 0$ are extracted from *ab initio* calculations (see Supplementary Information). Note, however, that the fully energy-dependent $\Gamma_e(\omega)$ and $\Gamma_o(\omega) = q^2\Gamma_e(\omega)$ are used in the NRG method. Colours as in Fig. 1b,d. **b**, dI/dV spectra from the NRG method for $T = 0.42\,\mathrm{mK}$, all other parameters as in **a**. **c**, Experimental dI/dV conductance spectra of an n_{32} dimer recorded at different temperatures. **d**, dI/dV spectra from the NRG method for the same temperatures as in **c**, using parameters from **a** and $t = 40\,\mathrm{meV}$ (as best fit of the gap) and $q = 0.1$.

perature of the experiment, the absorption edges above and below the Fermi level merge to a single peak. This is nicely revealed by the calculated spectrum at $T \simeq 0$ in Fig. 4b, which exhibits an extremely narrow gap.

Close to the QCP, the size of the spectral gap depends very sensitively on t and U' – and, through the Kondo temperature, also exponentially on the Coulomb interaction U. Therefore, a reduction of t by less than 15 meV matches the width of the calculated gap to the experiment. This can be seen in Fig. 4c,d where for $t = 40$ meV our simulations fully reproduce the experimentally measured temperature evolution of the dI/dV spectrum of the n_{32} dimer.

Outlook

To put the results of the present study in perspective, we compare to conventional two-impurity Kondo physics with a finite separation R between the two impurities [3, 9–11]. There, one usually encounters an RKKY-mediated spin interaction. Although this interaction can also favour local singlet formation against which a sufficiently large Kondo coupling leads to an energy gain for the triplet through the Kondo effect, the Kondo-screening of the local triplet is then complete and occurs through a two-stage Kondo effect, involving even as well as odd conduction electron states. As a consequence, no QPT and only a crossover is found in the conventional two-impurity case, because the two potential scattering terms (stemming from particle-hole asymmetry) of the even and odd conduction electron channels form a marginal relevant operator, pushing the system away from the QCP [9]. In contrast, one potential scattering term, as present in our case, is not relevant, the two competing ground states remain topologically distinct and the QPT survives. We note that the delocalized nature of the spin moment also distinguishes the present case from systems studied previously [18], where a gap formation in the single-particle spectrum at zero bias was also observed due to chemically binding orbitals, but where this occurs in the regime of far-separated point-like impurities with essentially independent spins that couple to two conduction bands, leading to two distinct Kondo effects for the bonding and antibonding orbitals.

The profound difference between the conventional scenario [3] and our situation is related to the spatially extended nature of the individual monomer π-orbitals, which are large compared to the lattice spacing of the underlying substrate as well as the shortest distance between the two monomers. As a consequence, there is a competition between direct chemical wavefunction overlap between the two monomers on the one hand, favouring a local singlet state with orbital ordering, and the entanglement of the local moment with the substrate on the other hand, promoting almost equally populated lo-

cal orbitals. The magnetic properties of the dimer emerge as a result of this competition, whereas the RKKY interaction turns out to be irrelevant. Because this competition relies only on general principles of chemical interaction and Kondo physics, we expect this mechanism to be of general validity, opening up a new avenue to engineering magnetic interactions. We stress that, in the present case, mere changes of the relative orientations of the monomers, and thus tiny changes in the wave function overlap, are enough to drive the system through the QCP. Thus, we have here an extremely sensitive chemical handle on the magnetic properties of a supermolecular architecture.

I. METHODS

Sample preparation. An atomically clean Au(111) surface was prepared in ultra-high vacuum (UHV) by repeated cycles of Ar^+ sputtering and annealing at 430 °C, followed by a final annealing step at 180 °C for 30 min. A submonolayer film of PTCDA was deposited from a Knudsen cell onto the clean Au(111) surface at room temperature. Experiments were carried out at $T = 9.5$ K in a CREATEC STM. Heating a thin gold wire we evaporated gold atoms onto the PTCDA submonolayer *in-situ* at $T = 12$ K, thus preventing clustering.

Tip preparation. The electrochemically etched tungsten tip was treated in UHV by field emission and afterwards *in-situ* by applying controlled voltage pulses and indentations into the clean gold surface until the spectroscopic signature of the Au(111) surface appeared.

TIAM. The Hamiltonian of the TIAM reads $H = H_\mathrm{d} + H_0 + H_\mathrm{hyb}$, where H_0 describes a single conduction band, H_d the dimer that is represented by π-states $|1\rangle$ and $|2\rangle$ (corresponding to the LUMO+Au orbitals, see Supplementary Information) on monomers 1 and 2, and H_hyb the hybridization between the conduction band and the dimer. In detail,

$$H_0 = \sum_{\mathbf{k},\sigma} \epsilon_{\mathbf{k},\sigma} c^\dagger_{\mathbf{k},\sigma} c_{\mathbf{k},\sigma} \,, \tag{1}$$

where $c^\dagger_{\mathbf{k},\sigma}$ ($c_{\mathbf{k},\sigma}$) creates (annihilates) an electron with spin σ in state $\mathbf{k}$ and the conduction band dispersion is given by $\epsilon_{\mathbf{k},\sigma}$,

$$\begin{aligned} H_\mathrm{d} = &\sum_{j,\sigma} E_j d^\dagger_{j,\sigma} d_{j,\sigma} + U \sum_j n_{j,\uparrow} n_{j,\downarrow} + \frac{2U' - J}{2} \sum_{\sigma,\sigma'} n_{1,\sigma} n_{2,\sigma'} \\ &- 2J \mathbf{S}_1 \mathbf{S}_2 + J \left(d^\dagger_{1,\uparrow} d^\dagger_{1,\downarrow} d_{2,\downarrow} d_{2,\uparrow} + \mathrm{h.c.} \right) \\ &+ \frac{t}{2} \sum_\sigma \left(d^\dagger_{1,\sigma} d_{2,\sigma} + d^\dagger_{2,\sigma} d_{1,\sigma} \right), \end{aligned} \tag{2}$$

where $d^\dagger_{j,\sigma}$ ($d_{j,\sigma}$) creates (annihilates) an electron with spin σ in the π-orbital of monomer j with the energy E_j, $\mathbf{S}_j$ denotes the spin in orbital j and J is a Heisenberg spin interaction, and

$$H_\mathrm{hyb} = \sum_{j\in\{1,2\},k,\sigma} V_{j,k} c^\dagger_{\mathbf{k},\sigma} e^{i\mathbf{k}\mathbf{R}_j} d_{j,\sigma} + \mathrm{h.c.} \,, \tag{3}$$

where $V_{j,\mathbf{k}}$ denotes the hybridization strength, $\mathbf{R}_j$ being the location of the π-orbital belonging to state $|\mathrm{j}\rangle$. For simplicity, we assume $V_{1,\mathbf{k}} \approx V_{2,\mathbf{k}}$. U and U' denote the intra- and interorbital Coulomb repulsions, respectively, whereas $t/2$ is a tunnelling due to direct chemical hybridization between the monomers. To ensure rotational invariance of the spin, a Hund's rule exchange and a pair-hopping term [33], both proportional to J, have been included.

Parameters of the TIAM. The parameters for the TIAM are obtained from the LDA+GdW calculation [28–30] for the n_{32} configuration. By treating the projected DOS obtained by LDA+GdW as an effective mean-field spectrum $\rho_j(\omega)$, we extract the bare level position E_j and energy-dependent hybridization function $\Gamma_j(\omega) = \pi \sum_\mathbf{k} |V_{j,\mathbf{k}}|^2 \delta(\omega - \epsilon_\mathbf{k})$ between a monomer and the substrate by equating

$$\rho_j(\omega) \equiv \lim_{\delta\to 0^+} \Im \frac{1}{\pi} \frac{1}{\omega - i\delta - E_j - nU - \Delta_j(\omega - i\delta)} . \tag{4}$$

Here, U is calculated by LDA+GdW, n is the occupation number of the energy level consistent with $\rho_j(\omega)$, whereas $\Delta_j(z)$ is given by $\pi\Delta_j(z) = \int d\omega \Gamma_j(\omega)/(z-\omega)$. Employing the full energy-dependent coupling functions $\Gamma_j(\omega)$ has turned out to be crucial for an accurate description even of the monomer [13]. U in the n_{32} configuration is calculated as 1.40 or 1.48 eV for monomers 1 and 2, respectively. Note that, owing to the metallic nature of the Au(111) substrate and the dielectric response of the neighbouring monomers, these values of U are smaller by a factor of about 2 compared to the values of $U = 2.87$ eV for the gas-phase Au-PTCDA complex. In the NRG calculations we treat both monomers ($j = 1, 2$) as identical, using a uniform $U = 1.4$ eV for both monomers (for the other configurations, this quantity ranges from 1.39 to 1.53 eV, with a difference of 0.03 to 0.13 eV between the two monomers (see Supplementary Information)). For the level energy we thus obtain $E_j = -1.09$ eV.

U' for the n_{32} configuration is obtained as 0.12 eV, reduced by a factor of nearly 7 from the gas-phase value (for the other configurations, this quantity ranges from 0.06 to 0.14 eV (see Supplementary Information)). To calculate the exchange interaction J we apply the approximation of Heitler-London [34], generalizing it to a combination of arbitrary orbitals. We find J smaller than 0.1 meV for all configurations. This is consistent with $J_\mathrm{ex} \propto t^2/(U - U')$. Therefore, we set the Heisenberg J to zero in the TIAM, for simplicity. Finally, we set the hopping term t to the energy difference $E_\mathrm{e} - E_\mathrm{o}$ between the bonding and antibonding states. More details about the *ab initio* calculations can be found in the Supplementary Information.

Solution of the TIAM. Because the impurities are very close to each other, we consider the limiting case $R \to 0$. To solve the TIAM, we transform to a new basis which consists of even and odd combinations of states $|1\rangle$ and $|2\rangle$. These couple to the even conduction band with matrix elements $V_{\mathrm{e},\mathbf{k}}$ and $V_{\mathrm{o},\mathbf{k}}$, respectively, see Fig. 2c. If parity is a symmetry operation of the dimer, which requires $E_1 = E_2$ and $V_{1,\mathbf{k}} = V_{2,\mathbf{k}}$, the odd orbital decouples from the even conduction band ($V_{\mathrm{o},\mathbf{k}} = 0$). We consider parity breaking by introducing a scaling factor r which reflects a small overall difference in the hybridization strengths of the two monomers, such that $\Gamma_1(\omega) = r^2\Gamma_2(\omega)$. The parameter $q = V_{\mathrm{o},\mathbf{k}}/V_{\mathrm{e},\mathbf{k}} = (r-1)/(r+1)$, which we set to 0.1, is related to the asymmetry in the hybridization strengths ($V_{1,\mathbf{k}} \neq V_{2,\mathbf{k}}$) of both dimer orbitals in the old basis. More details about the transformation to the even/odd basis can be found in the Supplementary Information.

NRG. For the NRG calculation, a self-written code was used [13, 20, 26]. The energy discretization parameter was chosen as $\Lambda = 1.8$. Our calculation of spectral functions is based on the method of refs. [20, 21, 35]. Because we focus on the low-energy physics in the absence of a magnetic field, we omitted z-averaging and have kept instead a large number of $N_s = 3000$ states after each iteration. More details on the NRG method can be found in the Supplementary Information.

Conductance spectra. Experimental differential conductance spectra $dI/dV(V)$ were recorded with a conventional lock-in technique with the feedback loop switched off. The following parameters were employed: modulation frequency 6073 Hz (Fig. 1b) or 889 Hz (Fig. 4c), modulation amplitude 1 mV.

To obtain theoretical spectra that can be directly compared to experimental dI/dV spectra, we first calculate the spectral function $\rho_\sigma(\omega) = \Im G_\sigma(\omega - i0^+)/\pi$, where $G_\sigma = \langle A_\sigma | A_\sigma^\dagger \rangle$ is the Green's function of electrons in the substrate-coupled dimer ($A_\sigma^\dagger = 1/\sqrt{1+q^2}(d_{e,\sigma}^\dagger + q d_{o,\sigma}^\dagger)$). This spectral function can be interpreted by diagrams such as those shown in Fig. 3b and d, representing the appropriate electron injection and extraction processes to and from the dimer (see Supplementary Information). Thus, if the electrons are injected from the STM tip into the dimer or extracted from the dimer into the tip, the spectral properties of the substrate-coupled dimer can be interrogated by elastic tunnelling spectroscopy (dI/dV spectra). Convolving $\rho_\sigma(\omega)$ with the derivative of the Fermi functions yields the differential conductance $dI/dV(V)$ up to a prefactor. If parity symmetry is fulfilled ($q = 0$), only the even state contributes to the STS spectrum. We assume that the tip-dimer coupling is much smaller than the substrate-dimer coupling, and hence the tip does not affect the physical properties of the substrate-dimer system. We have not taken into account any position-dependent STM matrix elements. Because we solve the TIAM in the limit $R \to 0$, and thus neglect any spatial dependence, this approximation is justified.

II. ACKNOWLEDGEMENTS

B.L. and F.B.A. received support by the Deutsche Forschungsgemeinschaft through AN275/7-1. B.L., F.B.A. and M.R. acknowledge support from the NIC Jülich for CPU time under projects no. HHB00 and HMS17.

III. AUTHOR CONTRIBUTIONS

R.T., C.W., T.E. and F.S.T. conceived the experiments. T.E. and R.T. conducted the experiments. T.E. analysed the experimental data. T.D., P.K. and M.R. performed density functional and many-body perturbation calculations and analysed the resultant data. B.L., F.S.T. and F.B.A. developed the theoretical model. B.L. and F.B.A. carried out the numerical renormalization group calculations and analysed the resultant data. T.E. has prepared the figures. T.E., R.T., F.B.A. and F.S.T. wrote the paper, with significant contributions from all authors.

IV. ADDITIONAL INFORMATION

Supplementary information is available in the online version of the paper. Correspondence and requests for materials should be addressed to F.S.T.

V. COMPETING FINANCIAL INTERESTS

The authors declare no competing financial interests.

[1] Y.-S. Fu, Q.-K. Xue, and R. Wiesendanger, Spin-Resolved Splitting of Kondo Resonances in the Presence of RKKY-Type Coupling. *Phys. Rev. Lett.* **108**, 087203 (2012).

[2] N. Tsukahara, S. Shiraki, S. Itou, N. Ohta, N. Takagi, and M. Kawai, Evolution of Kondo Resonance from a Single Impurity Molecule to the Two-Dimensional Lattice. *Phys. Rev. Lett.* **106**, 187201 (2011).

[3] H. Prüser, P. E. Dargel, M. Bouhassoune, R. G. Ulbrich, T. Pruschke, S. Lounis, and M. Wenderoth, Interplay between the Kondo effect and the Ruderman Kittel Kasuya Yosida interaction. *Nature Communications* **5**, 5417 (2014).

[4] P. Wahl, P. Simon, L. Diekhöner, V. S. Stepanyuk, P. Bruno, M. A. Schneider, and K. Kern. Exchange Interaction between Single Magnetic Adatoms. *Phys. Rev. Lett.* **98**, 056601 (2007).

[5] E. Minamitani, H. Nakanishi, W. A. Dio, and H. Kasai. Effect of RKKY Interaction on the Scanning Tunneling Spectra of a Classic Kondo System Two Magnetic Atoms Adsorbed on a Metal Surface. *Journal of the Physical Society of Japan* **78**, 084705 (2009).

[6] M. A. Ruderman and C. Kittel. Indirect Exchange Coupling of Nuclear Magnetic Moments by Conduction Electrons. *Phys. Rev.* **96**, 99–102 (1954).

[7] T. Kasuya. Theory of Metallic Ferro- and Antiferromagnetism on Zener's Model. *Progress of Theoretical Physics* **16**, 45–57 (1956).

[8] K. Yosida. Magnetic Properties of Cu-Mn Alloys. *Phys. Rev.* **106**, 893–898 (1957).

[9] I. Affleck, A. W. W. Ludwig, and B. A. Jones. Conformal-field-theory approach to the two-impurity Kondo problem: Comparison with numerical renormalization-group results. *Phys. Rev. B* **52**, 9528–9546 (1995).

[10] B. A. Jones, C. M. Varma, and J. W. Wilkins. Low-Temperature Properties of the Two-Impurity Kondo Hamiltonian. *Phys. Rev. Lett.* **61**, 125–128 (1988).

[11] B. A. Jones and C. M. Varma. Critical point in the solution of the two magnetic impurity problem. *Phys. Rev. B* **40**, 324–329 (1989).

[12] R. M. Fye, J. E. Hirsch, and D. J. Scalapino. Kondo effect versus indirect exchange in the two-impurity Anderson model: A Monte Carlo study. *Phys. Rev. B* **35**, 4901–4908 (1987).

[13] T. Esat, T. Deilmann, B. Lechtenberg, C. Wagner, P. Krüger, R. Temirov, F. B. Anders, M. Rohlfing, and F. S. Tautz. Transfering spin into an extended π orbital of a large molecule. *Phys. Rev. B* **91**, 144415 (2015).

[14] S. Sachdev. Quantum Criticality: Competing Ground States in Low Dimensions. *Science* **288**, 475–480 (2000).

[15] K. J. Franke, G. Schulze, and J. I. Pascual. Competition of Superconducting Phenomena and Kondo Screening at the Nanoscale. *Science* **332**, 940–944 (2011).

[16] T. Ogawa, K. Kuwamoto, S. Isoda, T. Kobayashi, and N. Karl. 3,4:9,10-Perylenetetracarboxylic dianhydride (PTCDA) by electron crystallography. *Acta Crystallographica Section B* **55**, 123–130 (1999).

[17] J. Bork, Y.-H. Zhang, L. Diekhoner, L. Borda, P. Simon, J. Kroha, P. Wahl, and K. Kern. A tunable two-impurity Kondo system in an atomic point contact. *Nat Phys* **7**, 901–906 (2011).

[18] T. Jabben, N. Grewe, S. Schmitt. Spectral properties of the two-impurity Anderson model with varying distance and various interactions. *Phys. Rev. B* **85**, 045133 (2012).

[19] R. Bulla, T. A. Costi, and T. Pruschke. Numerical renormalization group method for quantum impurity systems. *Rev. Mod. Phys.* **80**, 395–450 (2008).

[20] R. Peters, T. Pruschke, and F. B. Anders. Numerical renormalization group approach to Green's functions for quantum impurity models. *Phys. Rev. B* **74**, 245114 (2006).

[21] A. Weichselbaum and J. von Delft. Sum-Rule Conserving Spectral Functions from the Numerical Renormalization Group. *Phys. Rev. Lett.* **99**, 076402 (2007).

[22] W. Hofstetter and H. Schoeller. Quantum Phase Transition in a Multilevel Dot. *Phys. Rev. Lett.* **88**, 016803 (2001).

[23] S. Nishimoto, T. Pruschke, and R. M. Noack. Spectral density of the two-impurity Anderson model. *Journal of Physics: Condensed Matter* **18**, 981–995 (2006).

[24] C. Jayaprakash, H. R. Krishna-murthy, and J. W. Wilkins. Two-Impurity Kondo Problem. *Phys. Rev. Lett.* **47**, 737–740 (1981).

[25] B. A. Jones and C. M. Varma. Study of two magnetic impurities in a Fermi gas. *Phys. Rev. Lett.* **58**, p. 843–846 (1987).

[26] B. Lechtenberg and F. B. Anders. Spatial and temporal propagation of Kondo correlations. *Phys. Rev. B* **90**, 045117 (2014).

[27] L. Borda. Kondo screening cloud in a one-dimensional wire: Numerical renormalization group study. *Phys. Rev. B* **75**, 041307 (2007).

[28] M. Rohlfing. Electronic excitations from a perturbative LDA + GdW approach. *Phys. Rev. B* **82**, 205127 (2010).

[29] A. Greuling, M. Rohlfing, R. Temirov, F. S. Tautz, and F. B. Anders. Ab initio study of a mechanically gated molecule: From weak to strong correlation. *Phys. Rev. B* **84**, 125413 (2011).

[30] A. Greuling, R. Temirov, B. Lechtenberg, F. B. Anders, M. Rohlfing, and F. S. Tautz. Spectral properties of a molecular wire in the Kondo regime. *physica status solidi (b)* **250**, 2386–2393 (2013).

[31] N. Roch, S. Florens, T. A. Costi, W. Wernsdorfer, and F. Balestro. Observation of the Underscreened Kondo Effect in a Molecular Transistor. *Phys. Rev. Lett.* **103**, 197202 (2009).

[32] P. Nozières and C. T. De Dominicis. Singularities in the X-Ray Absorption and Emission of Metals. III. One-Body Theory Exact Solution. *Phys. Rev.* **178**, 1097–1107 (1969).

[33] A. M. Oleś. Antiferromagnetism and correlation of electrons in transition metals. *Phys. Rev. B* **28**, 327–339 (1983).

[34] W. Heitler and F. London. Wechselwirkung neutraler Atome und homöopolare Bindung nach der Quantenmechanik. *Zeitschrift für Physik* **44**, 455–472 (1927).

[35] R. Bulla, A. C. Hewson, and T. Pruschke. Numerical renormalization group calculations for the self-energy of the impurity Anderson model. *J. Phys.: Condens. Matter* **10**, 8365–8380, 1998.

4.3 Supplementary Information to A chemically driven quantum phase transition in a two-molecule Kondo system

The Supplementary Information to the paper *A chemically driven quantum phase transition in a two-molecule Kondo system* have been also published online in the journal **Nature Physics**:

- **T. Esat**, B. Lechtenberg, T. Deilmann, C. Wagner, P. Krüger, R. Temirov, M. Rohlfing, F. B. Anders, and F. S. Tautz, "A chemically driven quantum phase transition in a two-molecule Kondo system," *Nature Physics*, vol. 12, no. 9, p. 867, 2016.

Supplementary Information to A chemically driven quantum phase transition in a two-molecule Kondo system

Taner Esat,[1,2] Benedikt Lechtenberg,[3] Thorsten Deilmann,[4] Christian Wagner,[1,2] Peter Krüger,[4] Ruslan Temirov,[1,2] Michael Rohlfing,[4] Frithjof B. Anders,[3] and F. Stefan Tautz[1,2]

[1]*Peter Grünberg Institute (PGI-3), Forschungszentrum Jülich, 52425 Jülich, Germany*
[2]*Jülich Aachen Research Alliance (JARA), Fundamentals of Future Information Technology, 52425 Jülich, Germany*
[3]*Lehrstuhl für Theoretische Physik II, Technische Universität Dortmund, Otto-Hahn-Str. 4, 44221 Dortmund, Germany*
[4]*Institut für Festkörpertheorie, Westfälische Wilhelms-Universität Münster, 48149 Münster, Germany.*

I. AUTOMATED COLLECTION OF STS SPECTRA

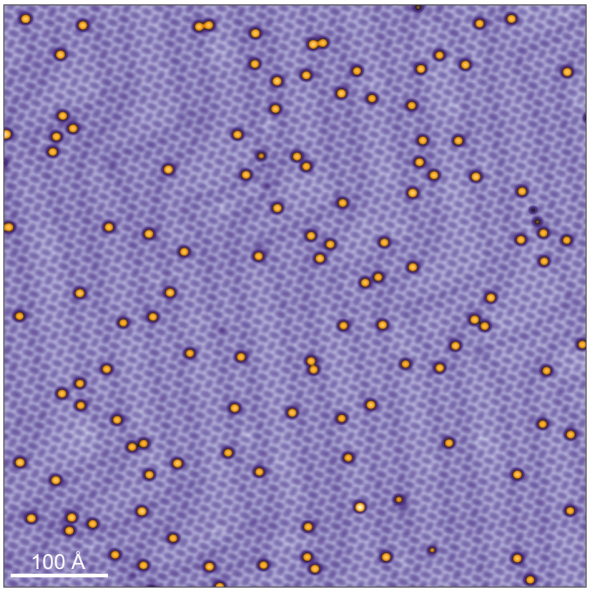

FIG. S1. **Au-PTCDA complexes on the Au(111) surface.** Constant current STM image after deposition of Au atoms on a PTCDA monolayer on Au(111) (bias voltage $V = 500\,\mathrm{mV}$, tunnelling current $I = 50\,\mathrm{pA}$).

For collecting a large ensemble of dI/dV conductance spectra of Au-PTCDA monomers and dimers we automated the procedure of scanning tunnelling spectroscopy (STS) by the following sequence of steps after measuring a large-scale topographic STM image, for example as displayed in Fig. S1:

(i) detecting the position of Au-PTCDA complexes, based on the circular features that correspond to the Au atoms, by using an algorithm for circle detection based on Hough transforms;

(ii) scanning several small topographic STM images (50 Å by 50 Å) of the detected Au-PTCDA complex until there is no drift detectable (the position of the Au atom serves as the centre of the STM image);

(iii) determining the centre of the Au atom as in step (i) and measuring at least two dI/dV conductance spectra in the centre of the Au atom.

For all Au-PTCDA complexes that were detected in step (i), steps (ii) and (iii) are automatically repeated. To prevent clustering of Au atoms we performed all experiments at low Au coverages. The lowest coverage is shown in Fig. 1a in the paper. Most of the data has been acquired at this coverage. Fig. S1 shows the highest coverage at which experiments have been conducted.

II. DISTANCE DEPENDENCY OF THE DIMER'S SPECTRAL PROPERTIES

As mentioned in the paper, for atoms on surfaces, gapped zero bias peaks have been associated with a competition between the Kondo effect and the RKKY or direct exchange interaction. In this scenario, a clear correlation of the spectra to the distance between local moments is expected. If the Au-Au distances for various dimer configurations are evaluated (Fig. S2), no such correlation is found. In addition to the findings of ref. [1], the data in Fig. S2 therefore provide further support to the central premise employed in our modelling, namely that in Au-PTCDA the local moment is delocalised over the entire complex. Accordingly, the Au-Au distance is not a relevant parameter, and the $R \to 0$ limit of the TIAM is appropriate.

Moreover, in the present context the RKKY interaction can be a ruled out on more general grounds by considering the relevant length scales: since the RKKY interaction oscillates between ferromagnetic and antiferromagnetic coupling on the length scale of the Fermi wavelength of the metal substrate, which in our case is comparable with the size of a Au-PTCDA complex, it is likely that the RKKY interaction between Au-PTCDA complexes, in which the moments are delocalised over the entire complex, cancels out.

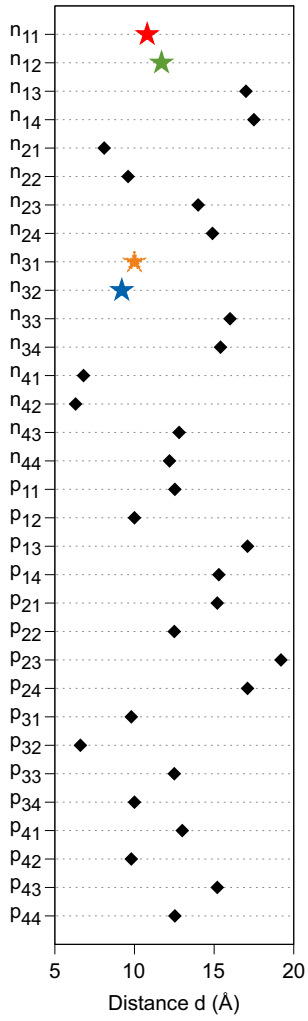

FIG. S2. **Distance dependency of the dimers' spectral properties.** Au-Au distances for the various dimer configurations. Symbols refer to dimer's spectral properties, black diamonds: unbroadened Kondo peaks, stars: broadened or gapped zero bias peaks (colour-code matches Fig. 1c and d in the paper).

III. PARAMETERS OF THE TIAM FROM *AB-INITO* CALCULATIONS

A. Introduction: Au-PTCDA Monomer

Recently we have investigated the structural (and electronic) properties of one Au atom bound to a PTCDA monolayer on the Au(111) surface. Detailed results can be found in reference [1]. Before moving to the dimer, we briefly recapitulate the most important results regarding the monomer.

In the gas phase the Au atom chemically binds to a PTCDA molecule and forms a complex with a binding energy E_b of 0.58 eV. In the electronic spectrum we observe three levels around E_F, namely HOMO+Au, LUMO+Au and LUMO−Au, all of which consist of linear combinations of PTCDA HOMO and LUMO and the Au 6s orbital. Since Au has a single occupied 6s orbital, HOMO+Au is occupied with two electrons, LUMO+Au with one electron and LUMO−Au is empty. This situation also holds for the PTCDA monolayer at Au(111), albeit with increased binding energies E_b because of the stronger interaction to the surrounding.

In the present study of the electronic properties of the dimer we only refer to the LUMO+Au level which is responsible for the Kondo physics.

B. Structure of the Dimer

In contrast to the study of the monomer [1], the calculations for the dimer were performed in the unit cell resulting from the [102] plane of the β-phase of bulk PTCDA [2]. The dimer structures are optimized in a 2×2 cell of the PTCDA monolayer that contains eight PTCDA molecules. Here we analyse the situation in which two Au atoms (bound to the PTCDA monolayer) are in immediate vicinity. Since in our experiment we never observe the binding of two Au atoms to the same PTCDA molecule, we concentrate on the case where two Au atoms bind to neighbouring PTCDA molecules. Within our DFT calculations of the isolated PTCDA layer, the total energies of all possible 32 configurations n_{ij} (see Fig. 1c in main text) and p_{ij} (see Fig. S3 for nomenclature) vary by less than 10 meV. This agrees with experiment, where most configurations are indeed observed. To include the Au(111) surface in the DFT calculation, the Au surface was distorted to fit into the PTCDA unit cell, albeit ensuring that the volume of the gold atoms is not changed. The surface atoms are placed at the experimental molecule-surface distance of 3.3 Å[3]. As in ref. [1], we observe that the Au-PTCDA binding energies E_b rigidly increase nearly independently of the configuration when the substrate is included (no additional optimisation step has been performed).

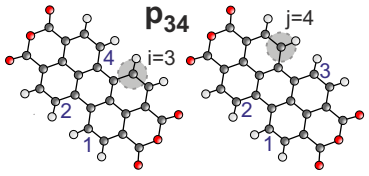

FIG. S3. **Structure of dimers consisting of Au-PTCDA complexes on the Au(111) surface.** Herringbone structure of PTCDA on Au(111) [2]. The white, grey and red circles indicate hydrogen, carbon and oxygen atoms of PTCDA. Numbers indicate possible Au binding sites. Dimer configurations are classified as n_{ij} (p_{ij}) when the molecules are normal (parallel) to each other, with the index i (j) specifying the binding sites of the Au atoms on top of two molecules forming the dimer. For the n_{ij} dimer configurations see Fig. 1c in the main text.

C. Intraorbital Coulomb interaction U

The intraorbital Coulomb interaction on monomer i is given by

$$U_i = \int |\Psi^i_{\mathrm{LUMO+Au}}(\mathbf{r})|^2 W(\mathbf{r},\mathbf{r}\,')|\Psi^i_{\mathrm{LUMO+Au}}(\mathbf{r}\,')|^2 d\mathbf{r}d\mathbf{r}\,', \tag{S1}$$

where $W(\mathbf{r},\mathbf{r}\,')$ denotes the screened Coulomb interaction (see ref. [1]) and $\Psi^i_{\mathrm{LUMO+Au}}$ the wave function of the LUMO+Au orbital on monomer i ($|i\rangle$ in the Dirac notation in the paper). For monomer j an analogous formula holds. Note that both, U_i and U_j, depend on the dimer configuration.

The Coulomb interaction U within the LUMO+Au orbital has been evaluated in ref. [1] for a *single* Au atom bound to the PTCDA monolayer. In that case, we found values ranging from 1.2 to 1.3 eV, depending on the binding site. In the present case of dimers we calculate values between 1.40 and 1.53 eV (Tab. I). Also, different values U_i and U_j are obtained for the two LUMO+Au orbitals within one dimer (Tab. I). The generally larger U values calculated in this work are caused by the different computational set up, namely slightly different unit cells and the usage of the experimental molecule surface distance. For a monomer within the same supercell as used here for the dimer, U is slightly larger (up to 0.2 eV) than the value we obtained in ref. [1].

TABLE I. U for different dimer configurations n_{ij} (in eV), noted as (U_i/U_j).

n_{ij}	$j=1$	$j=2$	$j=3$	$j=4$
$i=1$	1.51/1.53	1.41/1.46	1.43/1.48	1.43/1.52
$i=2$	1.40/1.53	1.40/1.47	1.41/1.48	1.41/1.52
$i=3$	1.39/1.52	1.40/1.48	1.41/1.48	1.41/1.52
$i=4$	1.42/1.51	1.42/1.47	1.43/1.46	1.43/1.52

D. Interorbital Coulomb interaction U'

In analogy to Eq. S1 the interorbital Coulomb interaction U' is given by

$$U'_{ij} = \int |\Psi^i_{\mathrm{LUMO+Au}}(\mathbf{r})|^2 W(\mathbf{r},\mathbf{r}\,')|\Psi^j_{\mathrm{LUMO+Au}}(\mathbf{r}\,')|^2 d\mathbf{r}d\mathbf{r}\,'. \tag{S2}$$

The calculated values are displayed in Tab. II. The effect of the substrate on U' is much stronger than on U (Tab. III). While U is reduced by a factor of 2 if the surrounding PTCDA molecules and the surface are included in the calculation, U' is reduced roughly by a factor of 7. Given the distance of approximately 11 Å between the centers of both monomers, this stronger reduction due to metal screening is expected.

TABLE II. U'_{ij} for different dimer configurations n_{ij} (in eV).

n_{ij}	$j=1$	$j=2$	$j=3$	$j=4$
$i=1$	0.12	0.12	0.07	0.07
$i=2$	0.10	0.10	0.06	0.06
$i=3$	0.12	0.14	0.07	0.08
$i=4$	0.12	0.13	0.07	0.07

TABLE III. Calculated U and U' for the n_{32} dimer (in eV).

	(U_i/U_j)	U'_{ij}
gas-phase dimer	2.87/2.87	0.97
dimer in a PTCDA monolayer	2.17/2.26	0.62
isolated dimer on Au surface	1.50/1.55	0.16
dimer in a PTCDA monolayer on Au surface	1.40/1.48	0.14

E. Exchange interaction J

To calculate the Heisenberg exchange interaction J, we follow the Heitler-London (HL) approximation [4] for the hydrogen molecule and generalize the calculation to an arbitrary combination of orbitals, i.e. in the present calculation the wave function of the hydrogen 1s orbital is replaced by the LUMO+Au wave function.

Following HL, the ground state energy for two interacting subsystems A and B (in the present case A and B are the two monomers) is given by

$$E = E_{\mathrm{A}} + E_{\mathrm{B}} + \frac{e^2}{4\pi\epsilon_0}\frac{1}{R^2} + \frac{C \pm J}{1 \pm S^2}. \tag{S3}$$

Here E_{A} and E_{B} are the total energies for both subsystems, C is the Coulomb interaction between them, J is the exchange interaction and S is the orbital overlap. The plus sign refers to the singlet, the minus sign to the triplet state.

Evaluating these for the different dimer configurations n_{ij} and p_{ij}, $|J|$ is in the range of $J_{\mathrm{ex}} \approx t^2/(U-U')$ and the additional direct exchange J in the TIAM (see Methods) is set to zero.

F. Calculation of the tunnelling $t/2$

To calculate the tunnelling $t/2$, which corresponds to the level splitting between even and odd combinations of monomer LUMO+Au orbitals, we perform LDA calculations of two Au-PTCDA complexes in the gas phase, enforcing double occupancy in the lower level E_{bonding} of the dimer and zero occupancy in its upper level $E_{\mathrm{antibonding}}$. Note that both levels of the dimer are linear combinations of the LUMO+Au orbitals on both monomers. t is then defined as

$$t = (E_{\mathrm{antibonding}} - E_{\mathrm{bonding}}). \tag{S4}$$

TABLE IV. Calculated t (in meV).

n_{ij}	$j=1$	$j=2$	$j=3$	$j=4$
$i=1$	30.5	52.7	9.7	10.2
$i=2$	4.6	5.7	3.1	3.1
$i=3$	41.6	55.1	12.9	13.6
$i=4$	9.8	21.4	4.5	4.6
p_{ij}	$j=1$	$j=2$	$j=3$	$j=4$
$i=1$	7.9	3.4	6.8	1.5
$i=2$	8.0	15.1	7.2	6.7
$i=3$	17.8	11.0	15.1	3.4
$i=4$	9.0	17.8	8.0	7.9

In Tab. IV values of t are listed for all possible dimer configurations. Because of the nodal structure of the monomer wave functions, displayed in Fig. 2b of the paper, the bonding (antibonding) state corresponds to $|o\rangle$ ($|e\rangle$).

G. Parity breaking

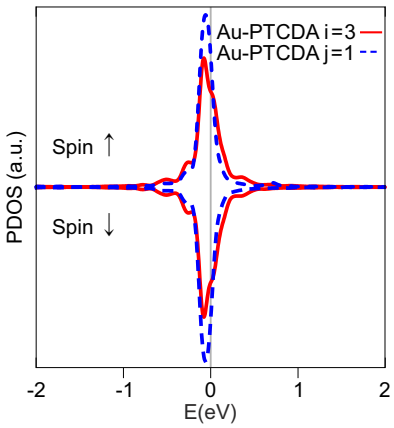

FIG. S4. **Parity breaking in dimers.** LDA PDOS of LUMO+Au for the monomer Au-PTCDA $i=3$ and $j=1$ of n_{31} (broadening of 0.04 eV).

Fig. S4 shows the projected densities of states (PDOS) for the LUMO+Au state of the $i=3$ and $j=1$ monomers in the dimer n_{31}, calculated by DFT in the LDA approximation. The PDOS of $i=3$ and $j=1$ monomers exhibits different peak widths, because of their different alignments on the Au(111) surface. This indicates different hybridisation strengths $\bar{V}_i \neq \bar{V}_j$, defined in Eq. (S6) below, for the two monomers. The hybridisation is slightly larger for the $i=3$ monomer, because it is aligned to the Au(111) lattice underneath, while the $j=1$ monomer is misaligned by 17 degrees relative to the high-symmetry lines of the Au(111) lattice. Although the results of this calculation cannot be directly compared to experiment, since in reality the PTCDA layer is incommensurate, this calculation nevertheless suggests that the parity-symmetric model is not justified for n_{ij} configurations, i.e. parity is broken. In contrast, for parallel configurations p_{ij}, the PDOS is nearly identical for i and j monomers.

IV. SOLUTION OF THE TIAM

A. Definition of the model in the even and odd basis

The local dynamics of a quantum impurity problem only depends on the energy dependence of the coupling function [5–8]. Throughout the paper, we have used the simplification $V_{1,\mathbf{k}} = rV_{2,\mathbf{k}}$, based on the assumption that the energy dependence of the monomer coupling functions

$$\begin{aligned}\Gamma_1(\omega) &= \pi \sum_{\mathbf{k}} |V_{1,\mathbf{k}}|^2 \delta(\omega - \epsilon_{\mathbf{k}}) \\ &= r^2 \pi \sum_{\mathbf{k}} |V_{2,\mathbf{k}}|^2 \delta(\omega - \epsilon_{\mathbf{k}}) = r^2 \Gamma_2(\omega) \end{aligned} \quad \text{(S5)}$$

only differs by an overall scaling factor r. Hence the k-dependence of $V_{j,\mathbf{k}}$ only enters $\Gamma_j(\omega) = \pi \bar{V}_j^2 \rho_c(\omega)$ via the energy-dependent effective density of states $\rho_c(\omega)$ of the conduction band, and we measure the relative coupling strengths by $\bar{V}_1 = r\bar{V}_2$. These relative couling strengths are defined via

$$\pi \bar{V}_j^2 = \int_{-\infty}^{\infty} d\omega \Gamma_j(\omega) \quad \text{(S6)}$$

and define absolute coupling strengths $\bar{V}_e = (\bar{V}_1 + \bar{V}_2)/\sqrt{2}$ and $\bar{V}_o = (\bar{V}_1 - \bar{V}_2)/\sqrt{2}$ that enter the NRG as the coupling between the dimer and the Wilson chain. For fully identical monomers r becomes $r = 1$.

The origin of the coordinate system is placed in the middle between the two orbital positions, so that the orbitals are located at the positions $\mathbf{R}_1 = \mathbf{R}/2$ and $\mathbf{R}_2 = -\mathbf{R}/2$ respectively. For the NRG, it is useful [9–14] to include spatial dependency into the two non-orthogonal energy-dependent field operators

$$c_{\sigma,\pm}(\omega) = \frac{1}{\sqrt{N\rho_c(\omega)}} \sum_{\mathbf{k}} \delta(\omega - \varepsilon_{\mathbf{k}}) c_{\mathbf{k}\sigma} e^{\pm i\mathbf{k}\mathbf{R}/2} \quad \text{(S7)}$$

which are combined to even (e) and odd (o) parity eigenstates [9–12]

$$c_{\sigma,e}(\omega) = \frac{1}{N_e(\omega, \mathbf{R})} \left(c_{\sigma,+}(\omega) + c_{\sigma,-}(\omega) \right) \quad \text{(S8a)}$$

$$c_{\sigma,o}(\omega) = \frac{1}{N_o(\omega, \mathbf{R})} \left(c_{\sigma,+}(\omega) - c_{\sigma,-}(\omega) \right) \quad \text{(S8b)}$$

where $\varepsilon_{\mathbf{k}}$ is the single-particle energy of the conduction electrons. The dimensionless normalization functions

$$N_e^2(\omega, \mathbf{R}) = \frac{4}{N\rho_c(\omega)} \sum_{\mathbf{k}} \delta(\omega - \varepsilon_{\mathbf{k}}) \cos^2\left(\frac{\mathbf{k}\mathbf{R}}{2}\right) \quad \text{(S9a)}$$

$$N_o^2(\omega, \mathbf{R}) = \frac{4}{N\rho_c(\omega)} \sum_{\mathbf{k}} \delta(\omega - \varepsilon_{\mathbf{k}}) \sin^2\left(\frac{\mathbf{k}\mathbf{R}}{2}\right) \quad \text{(S9b)}$$

are computed from the anti-commutation relation $\{c_{\sigma,\alpha}(\omega), c^\dagger_{\sigma',\alpha'}(\omega')\} = \delta(\omega-\omega')\delta_{\alpha\alpha'}\delta_{\sigma\sigma'}$.

Then $H_{\rm hyb}$ is given in energy representation [9–14] by

$$\begin{aligned} H_{\rm hyb} = &\frac{1}{2}\sum_\sigma \int d\omega \sqrt{\rho_c(\omega)} \\ &\times \Big\{ N_e(\omega,\mathbf{R}) c^\dagger_{e,\sigma}(\omega)(\bar{V}_1 d_{1,\sigma} + \bar{V}_2 d_{2,\sigma}) \\ &+ N_o(\omega,\mathbf{R}) c^\dagger_{o,\sigma}(\omega)(\bar{V}_1 d_{1,\sigma} - \bar{V}_2 d_{2,\sigma}) \Big\} + \text{h.c.} \end{aligned} \tag{S10}$$

in this even/odd conduction electron operator basis. Consequently, the two impurities couple to two effective conduction bands, one with even parity and the other with odd parity. Since the impurities are very close to each other, we neglect the detailed spatial dependence and let $\mathbf{R} \to 0$ (see paper). Then $N_o(\omega, \mathbf{R}\to 0) \to 0$, and the odd-parity band decouples from the impurity, yielding

$$H_{\rm hyb} = \sum_\sigma \int d\omega \sqrt{\rho_c(\omega)} [c^\dagger_{e,\sigma}(\omega)(\bar{V}_1 d_{1,\sigma} + \bar{V}_2 d_{2,\sigma}) + \text{h.c.}]. \tag{S11}$$

Assuming identical orbital energies $E = E_1 = E_2$ in both monomers, the single-particle eigenbasis in the presence of the tunnelling term $t/2$ in the dimer is given by the even- and odd-parity orbitals

$$d_{e/o,\sigma} = \frac{1}{\sqrt{2}}(d_{1,\sigma} \pm d_{2,\sigma}). \tag{S12}$$

With these new impurity operators and the limit $\mathbf{R} \to 0$, $H_{\rm hyb}$ can be simplified to

$$H_{\rm hyb} = \sum_{\mathbf{k},\sigma} [c^\dagger_{\mathbf{k},\sigma}(V_{e,\mathbf{k}} d_{e,\sigma} + V_{o,\mathbf{k}} d_{o,\sigma}) + \text{h.c.}] \tag{S13}$$

without referring to an energy representation and using the new hybridisations

$$V_{e/o,\mathbf{k}} = \frac{1}{\sqrt{2}}(V_{1,\mathbf{k}} \pm V_{2,\mathbf{k}}). \tag{S14}$$

Note that in the limit $\mathbf{R} \to 0$ the even conduction electron band is identical to the original band, and the odd band vanishes.

The local dimer Hamiltonian H_d takes the form

$$\begin{aligned} H_{\rm d} = &\sum_\sigma \left[E_e d^\dagger_{e,\sigma} d_{e,\sigma} + E_o d^\dagger_{o,\sigma} d_{o,\sigma} \right] \\ &+ \frac{1}{2} \sum_{abcd\in\{e,o\},\sigma\sigma'} \tilde{U}_{abcd} d^\dagger_{a,\sigma} d^\dagger_{b,\sigma'} d_{c,\sigma'} d_{d,\sigma}, \end{aligned} \tag{S15}$$

$t = E_e - E_o$, $E = (E_e + E_o)/2$, where the non-vanishing matrix elements of $\tilde{U}_{abcd}$ are given by

$$\tilde{U} = \tilde{U}_{aaaa} = \frac{U+U'}{2} + J \tag{S16}$$

$$\tilde{U}' = \tilde{U}_{abba} = \frac{U+U'}{2} - J \tag{S17}$$

$$\tilde{J} = \tilde{U}_{abab} = \tilde{U}_{aabb} = \frac{U-U'}{2}, \tag{S18}$$

ensuring rotational invariance in spin space [15]. The general form (S15) is equivalent to

$$\begin{aligned} H_{\rm d} = &\sum_{\alpha=\{e,o\},\sigma} E_\alpha d^\dagger_{\alpha,\sigma} d_{\alpha,\sigma} + \tilde{U} \sum_\alpha n_{\alpha,\uparrow} n_{\alpha,\downarrow} \\ &+ \frac{2\tilde{U}' - \tilde{J}}{2} \sum_{\sigma,\sigma'} n_{e,\sigma} n_{o,\sigma'} - 2\tilde{J} \mathbf{S}_e \mathbf{S}_o \\ &+ \tilde{J} \left(d^\dagger_{e,\uparrow} d^\dagger_{e,\downarrow} d_{o,\downarrow} d_{o,\uparrow} + \text{h.c.} \right), \end{aligned} \tag{S19}$$

using the three parameters $\tilde{U}, \tilde{U}'$ and $\tilde{J}$.

A word is in order regarding parity. Since the effective conduction band does not have inversion symmetry relative to the origin, which is defined as the midpoint between both monomer orbitals $|1\rangle$ and $|2\rangle$, and since the local environments around the monomer orbitals are in general slightly different, the single particle energies are therefore slightly different, too, i.e. $E_1 \neq E_2$. Nevertheless, we are still able to diagonalize the single-particle basis of the two monomer orbitals into a new basis of a bonding and an antibonding orbital, albeit with a modified unitary transformation

$$d_{e,\sigma} = a_1 d_{1,\sigma} + a_2 d_{2,\sigma} \tag{S20}$$

$$d_{o,\sigma} = a_2 d_{1,\sigma} - a_1 d_{2,\sigma}. \tag{S21}$$

These $d_{e,\sigma}$ and $d_{o,\sigma}$ lack even and odd symmetry for generic linear combinations $a_1^2 + a_2^2 = 1$.

Using the same unitary transformation of the hybridisation matrix, Eq. (S14) will be modified in analogy to Eq. (S20). Consequently, even for $V_{1,\mathbf{k}} = V_{2,\mathbf{k}}$ a finite matrix element $V_{o,\mathbf{k}}$ is generated which is enhanced by the slight symmetry breaking of $V_{1,\mathbf{k}} \neq V_{2,\mathbf{k}}$. Hence the Hamiltonian in the even/odd basis is the generic description where t parameterizes the total splitting stemming from $E_1 - E_2$ as well as the tunnelling term, and $q = V_{o,\mathbf{k}}/V_{e,\mathbf{k}}$ denotes the generic degree of asymmetry. It turns out that the precise value of $q \ll 1$ (we set $q = 0.1$) does not influence the gap formation, the gap width as well as the location of quantum phase transition significantly.

B. Conduction electron transmission function

Since only the linear combination

$$\begin{aligned} A^\dagger_\sigma &= \frac{1}{\sqrt{\bar{V}_1^2 + \bar{V}_2^2}} \left(\bar{V}_1 d^\dagger_{1,\sigma} + \bar{V}_2 d^\dagger_{2,\sigma} \right) \\ &= \frac{1}{\sqrt{1+q^2}} (d^\dagger_{e,\sigma} + q d^\dagger_{o,\sigma}) \end{aligned} \tag{S22}$$

of orbitals couple to the substrate according to Eq. (S11), the spectrum of conduction electron transmission function accessible to the STM is given by $\rho_\sigma(\omega) = \Im G_\sigma(\omega - i0^+)/\pi$ where

$$G_\sigma(z) = \langle A_\sigma | A_\sigma^\dagger \rangle(z)\,. \tag{S23}$$

The orbital diagonal contributions are defined as

$$\rho_{e,\sigma}(\omega) = \frac{1}{\pi}\Im\langle d_{e,\sigma}|d_{e,\sigma}^\dagger\rangle(\omega - i0^+) \tag{S24}$$

$$\rho_{o,\sigma}(\omega) = \frac{1}{\pi}\Im\langle d_{o,\sigma}|d_{o,\sigma}^\dagger\rangle(\omega - i0^+), \tag{S25}$$

while the mixed contributions can be calculated by the difference between $\rho_\sigma(\omega)$, $\rho_{e,\sigma}(\omega)$ and $\rho_{o,\sigma}(\omega)$ with the appropriate weight factors and do not contain new information. Besides, the mixed contributions vanish for the parity symmetric case ($q = 0$) and, therefore, their contributions to the measured spectra for a small parity asymmetry $q \ll 1$ is expected to be weak.

C. Numerical renormalization group (NRG)

The numerical renormalization group (NRG) is a well established approach [5–7] – see also the review of Bulla et al. [8] – for solving thermodynamical and dynamical properties of quantum impurity systems, including their non-equilibrium dynamics [16–19]. In the NRG, the hybridization function $\Gamma(\omega)$ is discretized logarithmically [5] with the discretization parameter $\Lambda > 1$ dividing the energy into the intervals $[\Lambda^{-(n+1)}D, \Lambda^{-n}D]$ and $[-\Lambda^{-n}D, -\Lambda^{-(n+1)}D]$ regarding the bandwidth D covering positive and negative energies. Here we have used $\Lambda = 1.8$. The discretized bath Hamiltonian can be mapped via a Householder transformation [5, 8] onto a semi-infinite Wilson chain with the impurity coupled to the first chain site. The Nth link along the chain represents an exponentially decreasing energy scale $D_N \sim \Lambda^{-N/2}$. Using this hierarchy of scales, the sequence of finite-size Hamiltonians $\mathcal{H}_N$ for the N-site chain [5–7] is solved iteratively, discarding the high-energy states at the conclusion of each step to maintain a manageable number of states. The reduced basis set of $\mathcal{H}_N$ so obtained is expected to faithfully describe the spectrum of the full Hamiltonian on a scale of D_N, corresponding to the temperature $T_N \sim D_N$. Details of the approach can be found in the review by Bulla et al. [8].

It has been recognised that the set of all discarded states in the NRG not only spans the complete Fock-space, but also serves as an approximate eigenbasis for the Hamiltonian [16, 17]. Consequently, a sum-rule conserving method for spectral properties was derived [20, 21] which we used here for the calculation of the spectral functions [20–22]. In principle, discretization artefacts in the NRG can be reduced by z-averaging [16, 17, 23] which improves the shape of high-energy features in the spectrum. Since we focus on the low energy physics in the absence of an external magnetic field, we omit z-averaging and have kept instead a large amount of $N_s = 3000$ states after each iteration.

D. Ground state of the gas-phase dimer

As a reference point for the ground states of the surface-adsorbed dimer we discuss the ground states of the gas-phase dimer, for which there are no hybridisations $V_{1,\mathbf{k}}$ and $V_{2,\mathbf{k}}$.

Since the isolated Au-PTCDA monomers carry a $S = 1/2$ moment in their LUMO+Au orbital, the two Au-PTCDA monomers, brought together in close vicinity, maintain a four-fold spin-degenerate ground state consisting of the local triplet manifold $|\uparrow_1,\uparrow_2\rangle$, $|\downarrow_1,\downarrow_2\rangle$, $\frac{1}{\sqrt{2}}(|\uparrow_1,\downarrow_2\rangle + |\downarrow_1,\uparrow_2\rangle)$ and one local singlet state $\frac{1}{\sqrt{2}}(|\uparrow_1,\downarrow_2\rangle - |\downarrow_1,\uparrow_2\rangle)$, if all additional interactions besides U, U' are neglected ($t = 0$, $J = 0$). The two local singlet states with double occupancy of one of the two monomer orbitals, i.e. $|\uparrow\downarrow_1, 0_2\rangle$ and $|0_1,\uparrow\downarrow_2\rangle$, are shifted to $U - U'$ above the four-fold degenerate ground state.

Evidently, the same degeneracy is also found in the even/odd basis. The corresponding level scheme is schematically sketched in Fig. S5a. The ground state comprises the local triplet manifold $|\uparrow_e,\uparrow_o\rangle$, $|\downarrow_e,\downarrow_o\rangle$, $\frac{1}{\sqrt{2}}(|\uparrow_e,\downarrow_o\rangle + |\downarrow_e,\uparrow_o\rangle)$ which is shown in the paper in Fig. 3e. However, the local singlet state $\frac{1}{\sqrt{2}}(|\uparrow_e,\downarrow_o\rangle - |\downarrow_e,\uparrow_o\rangle)$ is separated from the local triplet and shifted to higher energies by $2\tilde{J} = U - U'$. This shift is effected by the fourth term in Eq. (S19). At the same time, the large pair hopping term (last term of Eq. (S19)) leads to an entanglement of the two doubly occupied states. While the local singlet state $\frac{1}{\sqrt{2}}(|\uparrow\downarrow_e, 0_o\rangle + |0_e,\downarrow\uparrow_o\rangle)$ is shifted to an energy $U - U'$ above the ground state, the energy of the combination $\frac{1}{\sqrt{2}}(|\uparrow\downarrow_e, 0_o\rangle - |0_e,\downarrow\uparrow_o\rangle)$ is lowered, leading again to a four-fold spin-degenerate ground state which once more consists of the local triplet manifold and one local singlet state.

The level scheme in Fig. S5a is slightly modified if the tunnelling $t/2$ between the monomer valence orbitals of the gas-phase dimer is taken into account. This tunnelling generates an antiferromagnetic exchange $J_{\mathrm{ex}} \approx t^2/(U - U')$ which promotes, independently of the sign of t, the local singlet $\alpha(t)|0_e,\uparrow\downarrow_o\rangle - \beta(t)|\uparrow\downarrow_e, 0_o\rangle$, depicted in Fig. 3f in the paper, to become the ground state of the gas-phase dimer. J_{ex}, however, is too small to explain the width and the temperature dependence of the gap in the experimentally observed spectra. Hence, the exchange interaction cannot be the decisive interaction between the monomers. The complete level scheme of the gas-phase dimer with non-zero tunnelling $t/2$ is displayed in Fig. S5b. Here, $\alpha(t)$ and $\beta(t)$ are coefficients that depend on the splitting t and define the admixtures of the even and odd states to the local singlet states.

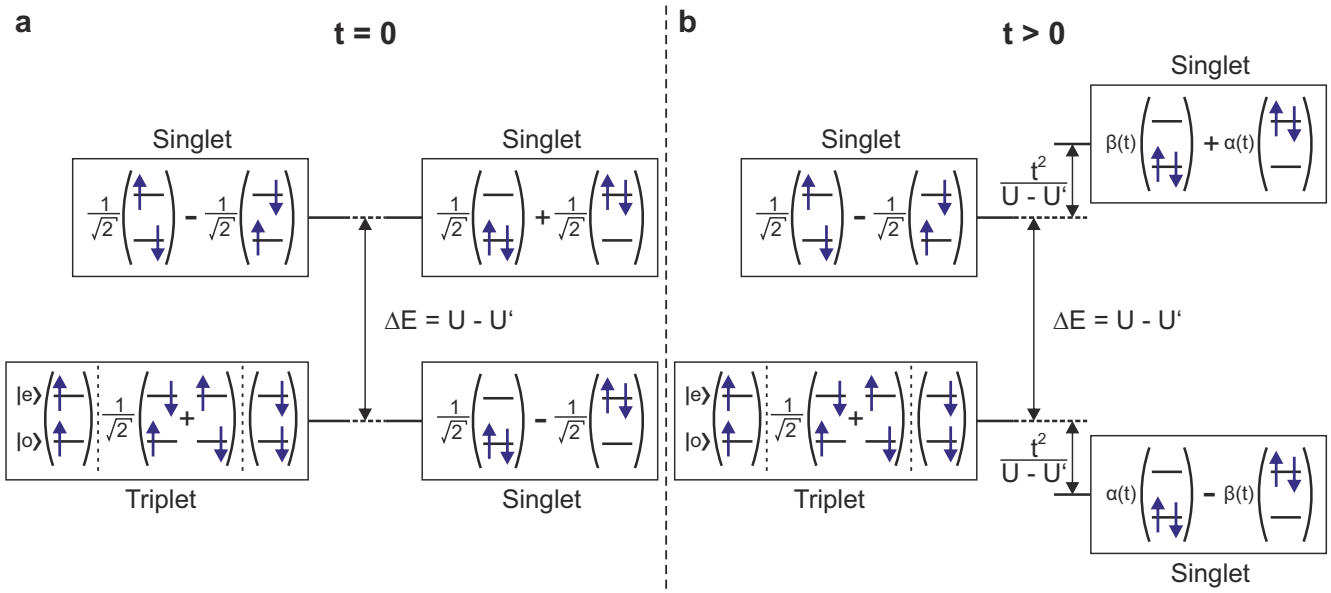

FIG. S5. **Ground states of the gas-phase dimer in the even/odd basis.** The vertical axis is the energy axis (no true scale). Since no coupling to the substrate exists, singlet und triplet states in the Figure are all local. Heisenberg J is set to zero. **a** Level scheme of the dimer for $t = 0$. Note that in this case the single-particle energies of $|e\rangle$ and $|o\rangle$ are degenerate. **b** As panel a, but for $t > 0$. The single-particle energies of $|e\rangle$ and $|o\rangle$ are not any more degenerate, $|o\rangle$ lies below $|e\rangle$. A finite tunnelling $t/2$ generates an antiferromagnetic exchange $J_{\rm ex} \approx t^2/(U - U')$ which lifts the degeneracy of the ground state. Note that for $t < 0$ precisely the same level scheme results, except that the energetic order of $|o\rangle$ and $|e\rangle$ is interchanged.

Once the dimer is adsorbed on the Au surface, the coupling to the conduction band modifies the level scheme further. This is discussed in detail in the paper. Briefly, at low temperatures the triplet manifold depicted in Fig. S5b couples antiferromagnetically to the local even conduction electron spins via an effective Kondo coupling $J_{\rm K}$. Consequently, the entanglement of the local moment with the conduction band of the substrate yields an energy gain of the local triplet over the local singlet ground state in Fig. S5b, yielding (for not too large splitting t) a doubly degenerate partially screened local triplet as the ground state of the surface-adsorbed dimer. With increasing splitting t, however, the energy of the local singlet $\alpha(t)|0_e, \uparrow\downarrow_o\rangle - \beta(t)|\uparrow\downarrow_e, 0_o\rangle$ is lowered, and once $|t|$ exceeds critical values $|t_c^{\pm}|$, defining two quantum critical points (QCPs), quantum phase transitions (QPT) to $\alpha(t)|0_e, \uparrow\downarrow_o\rangle - \beta(t)|\uparrow\downarrow_e, 0_o\rangle$ as the new ground state occur. This new ground state is topologically distinct from the previous one by its different degeneracy. The QPT at $t_c^+ > 0$ is discussed in detail in the paper.

E. Spectral functions and corresponding processes

The diagrams in Fig. 3b and d in the paper are visualisations of the Lehmann representation of the spectral functions $\rho_{e/o,\sigma}(\omega)$ $(T = 0)$:

$$\rho_{e/o,\sigma}(\omega) \propto \sum_{\rm n} \langle {\rm g}|d^\dagger_{e/o,\sigma}|{\rm n}\rangle\langle {\rm n}|d_{e/o,\sigma}|{\rm g}\rangle\delta(\omega + E_{\rm n} - E_{\rm g}) + \langle {\rm g}|d_{e/o,\sigma}|{\rm n}\rangle\langle {\rm n}|d^\dagger_{e/o,\sigma}|{\rm g}\rangle\delta(\omega - E_{\rm n} + E_{\rm g}). \quad \text{(S26)}$$

Here $|{\rm g}\rangle$ refers to the ground and $|{\rm n}\rangle$ to arbitrary excited states of the coupled dimer/substrate system. Eq. (S26) is valid only at $T = 0$. For $T > 0$, as evaluated in our NRG simulations, Boltzman factors need to be included and the sum over n must be replaced by a double sum. If $|{\rm g}\rangle$ is degenerate, Eq. (S26) must be summed over the ground states as well. Furthermore, note that $|{\rm g}\rangle$ is a complicated many-body ground state of the Kondo problem with moments screened by the conduction electrons, while Fig. 3b and d in the paper show elementary processes drawn from the perspective of weakly coupled subsystems dimer/substrate, hence are valid in a strictly a higher temperature limit $T \gg T_{\rm K}$ but $T \ll U$ only. Nevertheless, low order scattering diagrams of this type can be used to illustrate the physical processes at the heart of the corresponding spectral functions.

The first term in Eq. (S26) describes a process with $\omega < 0$, i.e. first an electron is extracted from the ground state of the dimer into the probing STM tip before being re-injected, while the second term applies for $\omega > 0$, i.e. first an electron is injected from the probing STM tip into the dimer before being re-extracted. By calculating matrix elements of $d_{e/o,\sigma}$ $(d^\dagger_{e/o,\sigma})$ between the ground

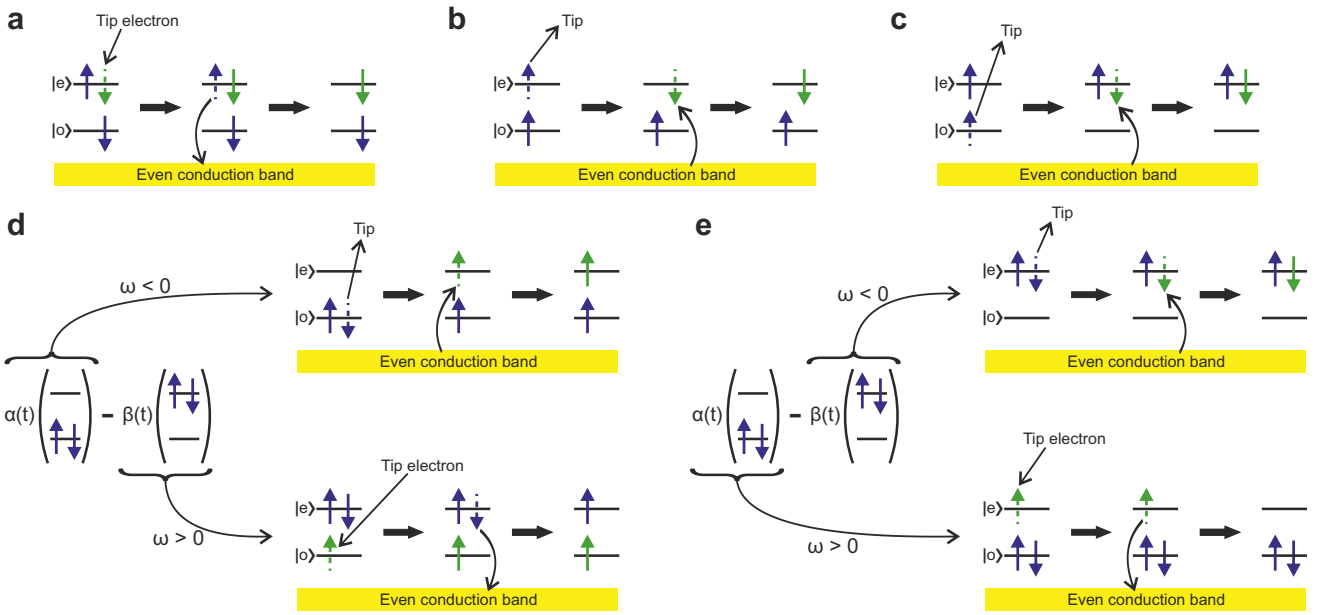

FIG. S6. **Diagrams of different processes due to electron injection (extraction) to (from) the even/odd state.** Symbols as in Fig. 3b and d in the paper. Note that the $|o\rangle$ orbital decouples from the even conduction band (parity-symmetry), and accordingly no transitions between the two can occur. For a detailed discussion, refer to the text of the supplement.

and excited states and summing over all excited states, the response of the surface-adsorbed dimer to electron extraction (injection) is being probed. Note that in the diagrams in Fig. 3b and d in the paper and in Fig. S6 only contributions to $\langle \mathrm{n}|d_{e/o,\sigma}|\mathrm{g}\rangle$ for $\omega < 0$ and contributions to $\langle \mathrm{n}|d^\dagger_{e/o,\sigma}|\mathrm{g}\rangle$ for $\omega > 0$ are shown, while the Hermitian conjugate matrix elements in Eq. (S26), which describe the reverse processes, are not displayed.

In Fig. S6 a few additional processes of relevance to the spectral functions displayed in Figs. 3a and c in the paper are shown. Fig. S6a shows the injection of an electron into $|e\rangle$. However, while in Fig. 3b in the paper the dimer initially is in the $S_z = 1$ state of the local triplet manifold, here the injection occurs into one component of the $S_z = 0$ state. The system responds by a zero-energy spin-flip transition into the $S_z = -1$ state of the triplet manifold. This process thus also contributes to the Kondo resonance in Fig. 3a in the paper, like the process in Fig. 3b in the paper.

The processes in Figs. S6b and c are analogous to the ones in Figs. 3b and d in the paper, respectively, but for $\omega < 0$, i.e. initial electron extraction. Thereby, Fig. S6b, in which the electron is extracted from $|e\rangle$, again represents a zero-energy transition within the triplet manifold, while in Fig. S6c the electron is extracted from $|o\rangle$ and the system makes a finite-energy transition to a component of the local singlet state shown in Fig. 3f in the paper. Comparing the final state in Fig. S6c to the final state of the process in Fig. 3d in the paper, it is clear why in the spectral function in Fig. 3c in the paper the thresholds at $\omega < 0$ have less weight than the ones at $\omega > 0$, as long the system is below the QPT ($t < t_c$, red curves in Fig. 3c): The quantum weight of the final state of Fig. S6c in the singlet of Fig. 3f is smaller than that of the final state of Fig. 3d, because for $t > 0$ we have $|\alpha(t)|^2 > |\beta(t)|^2$.

All diagrams discussed so far in the paper and the supplement refer to the surface-adsorbed dimer being in the partially Kondo-screened local triplet state ($t < t_c$, red curves in Figs. 3a and c in the paper). In contrast, the processes in Figs. S6d and e start from the local singlet ground state ($t < t_c$), injecting into or extracting from $|o\rangle$ (Fig. S6d) and $|e\rangle$ (Fig. S6e), respectively. These processes hence correspond to the blue curves in Figs. 3a and c in the paper. The processes in Fig. S6d lead to a finite-energy transition from a component of the local singlet (Fig. 3f in the paper) to a state of the local triplet manifold (Fig. 3e in the paper). Comparing the upper and lower processes in Fig. S6d, it is clear why the thresholds in the blue curves in Fig. 3c in the paper have more weight for $\omega < 0$ than for $\omega > 0$: this is again controlled by the quantum weights $|\alpha(t)|^2 > |\beta(t)|^2$. The processes in Fig. S6e do not lead to a response of the surface-adsorbed dimer (i.e. its state does not change), yielding a flat spectral function (blue curve in Fig. 3a).

F. Analysis of the spectral functions ρ_e and ρ_o for broken parity $q = 0.1$

As argued in the paper, for the dimer adsorbed on the Au(111) surface parity symmetry is broken. For completeness and comparison with the parity-

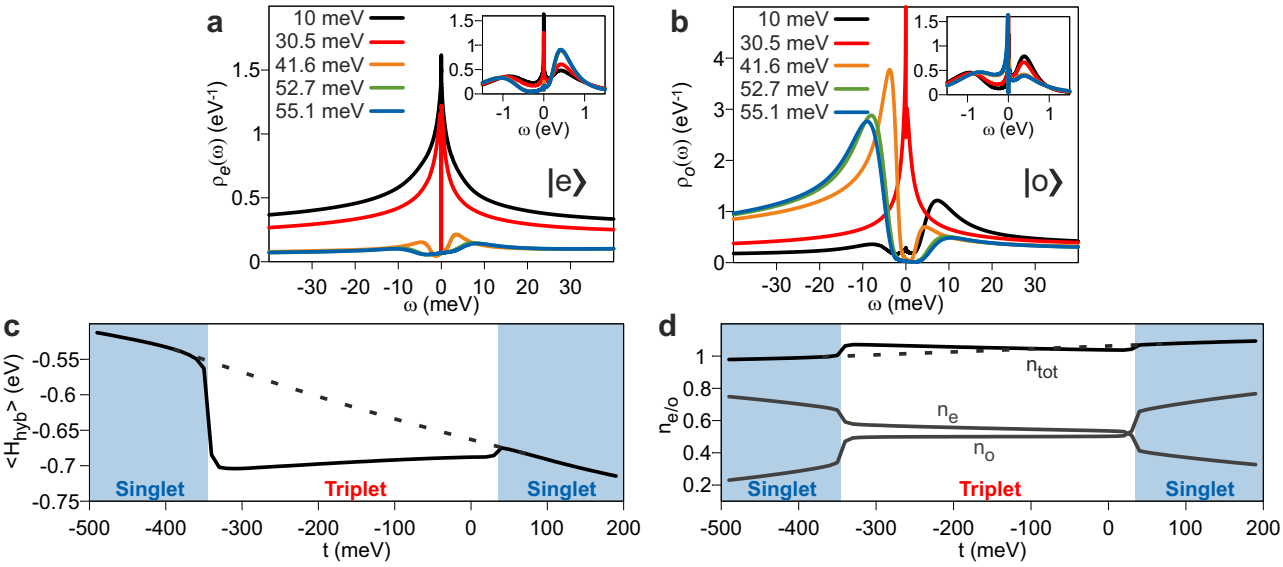

FIG. S7. **Spectral functions of Au-PTCDA dimers in the parity-broken case $q = V_o/V_e = 0.1$, analysed with NRG. a** Even spectal functions for varying t as given in the legend. **b** Odd spectral functions for varying t. Colours as in Fig.1b in the main text. **c** Expectation value of the hybridisation energy $\langle H_{\rm hyb}\rangle$ as a function of t. At the QCPs $t_c^{\pm}$ the hybridisation $|\langle H_{\rm hyb}\rangle|$ changes sharply. For $t_c^- < t < t_c^+$ the triplet ground state is stabilized by $\langle H_{\rm hyb}\rangle$. The dashed line indicates the overall increase of the energy gain due to hybridisation in the singlet state. **d** Occupation numbers n_e, n_o and $n_{\rm tot} = n_e + n_o$ as a function of t. At the QCPs $t_c^{\pm}$ steps in the occupation occur. The dotted line indicates the overall increase of $n_{\rm tot}$ in the singlet state.

symmetric case (spectral functions in Fig. 3a and c in the paper), the corresponding diagonal spectral functions of the even and odd states Eq. (S25) are shown in Fig. S7a and b, respectively. These spectral functions contribute to the total spectral function $\rho_\sigma(\omega) \propto \Im\{\langle d_{e,\sigma} + q d_{o,\sigma} | d^\dagger_{e,\sigma} + q d^\dagger_{o,\sigma}\rangle(\omega - i0^+)\}$ of the surface-adsorbed dimer as shown in Fig. 4a and b in the paper. To be consistent with Fig. 4a and b in the paper, the discrete t values obtained by DFT for the dimers are used in Fig. S7a and b, too (note the corresponding colour coding).

As the main difference to Figs. 3a and c in the paper we observe that features of the odd orbital (specifically, the absorption edges) are mixed weakly into the even spectral function, which can be traced back to the fact that in the parity-broken case both states $|e\rangle$ and $|o\rangle$ couple to the substrate. Also note that parity breaking shifts the QCP from $t_{\rm c} = 31.5\,$meV to $30.5\,$meV.

In Fig. S7c and d the hybridisation energy and the occupation numbers of the even/odd states are shown for the parity-broken case. Different from Figs. 3g and h in the paper, where corresponding information is given for the parity-symmetric case, we have plotted $\langle H_{\rm hyb}\rangle$, n_e, n_o and $n_{\rm tot}$ for both positive and negative t. This reveals two QCP, one at $t_{\rm c}^+$, the other at $t_{\rm c}^-$. The $t_{\rm c}$ quoted in the paper must be identified with $t_{\rm c}^+$.

Fig. S7c shows that in the local singlet regime ($t < t_{\rm c}^-$ and $t_{\rm c}^+ < t$), $\langle H_{\rm hyb}\rangle$ decreases nearly linearly as function of t, as indicated by the dashed line interpolating the energy in the local triplet regime: the more the even orbital is depleted, the more its electron becomes itinerant, resulting in larger $|\langle H_{\rm hyb}\rangle|$. However, in the local triplet regime additional hybridisation energy is gained due to the strong entanglement of the local moment with the conduction band of the substrate. This is observed in the interval $t_{\rm c}^- < t < t_{\rm c}^+$, where $\langle H_{\rm hyb}\rangle$ lies below the interpolated singlet hybridisation energy. In contrast to the parity-symmetric case in Fig. 3h in the paper, $\langle H_{\rm hyb}\rangle$ changes continuously across the QCP, and only its derivative diverges at the QCP.

The asymmetry between t_c^+ and t_c^- (Figs. S7c and d) is generated by the pronounced energy-dependence of the coupling to the substrate, which shifts the energy of the more strongly hybridising even state above the one of the odd state already for $t = 0$. Then, only a relatively small additional tunnelling $t/2$ is needed to drive the system across the QCP.

We finally note that the presented microscopic mechanism based on a chemically driven QPT is generic. Including an additional finite direct J only influences the values of the critical splitting $t_{\rm c}^{\pm}$, but not the quantum critical scenario. Only for a very large direct antiferromagnetic coupling J the QPT is destroyed and no Kondo effect can be detected.

[1] T. Esat, T. Deilmann, B. Lechtenberg, C. Wagner, P. Krüger, R. Temirov, F. B. Anders, M. Rohlfing, and F. S. Tautz. Transfering spin into an extended π orbital of a large molecule. *Phys. Rev. B* **91**, 144415 (2015).

[2] T. Ogawa, K. Kuwamoto, S. Isoda, T. Kobayashi, and N. Karl. 3,4:9,10-Perylenetetracarboxylic dianhydride (PTCDA) by electron crystallography. *Acta Crystallographica Section B* **55**, 123–130 (1999).

[3] S. Henze, O. Bauer, T.-L. Lee, M. Sokolowski, and F. S. Tautz, Vertical bonding distances of PTCDA on Au(111) and Ag(111): Relation to the bonding type. *Surface Science* **601**, 1566–1573 (2007).

[4] W. Heitler and F. London. Wechselwirkung neutraler Atome und homöopolare Bindung nach der Quantenmechanik. *Zeitschrift für Physik* **44**, 455–472 (1927).

[5] K. G. Wilson. The renormalization group: Critical phenomena and the Kondo problem. *Rev. Mod. Phys.* **47**, 773–840 (1975).

[6] H. R. Krishna-murthy, J. W. Wilkins, and K. G. Wilson. Renormalization-group approach to the Anderson model of dilute magnetic alloys. I. Static properties for the symmetric case. *Phys. Rev. B* **21**, 1003–1043 (1980).

[7] H. R. Krishna-murthy, J. W. Wilkins, and K. G. Wilson. Renormalization-group approach to the Anderson model of dilute magnetic alloys. II. Static properties for the asymmetric case. *Phys. Rev. B* **21**, 1044–1083 (1980).

[8] R. Bulla, T. A. Costi, and T. Pruschke. Numerical renormalization group method for quantum impurity systems. *Rev. Mod. Phys.* **80**, 395–450 (2008).

[9] C. Jayaprakash, H. R. Krishna-murthy, and J. W. Wilkins. Two-Impurity Kondo Problem. *Phys. Rev. Lett.* **47**, 737–740 (1981).

[10] B. A. Jones and C. M. Varma. Study of two magnetic impurities in a Fermi gas. *Phys. Rev. Lett.* **58**, 843 (1987).

[11] B. A. Jones, C. M. Varma, and J. W. Wilkins. Low-Temperature Properties of the Two-Impurity Kondo Hamiltonian. *Phys. Rev. Lett.* **61**, 125–128 (1988).

[12] I. Affleck, A. W. W. Ludwig, and B. A. Jones. Conformal-field-theory approach to the two-impurity Kondo problem: Comparison with numerical renormalization-group results. *Phys. Rev. B* **52**, 9528–9546 (1995).

[13] L. Borda. Kondo screening cloud in a one-dimensional wire: Numerical renormalization group study. *Phys. Rev. B* **75**, 041307 (2007).

[14] B. Lechtenberg and F. B. Anders. Spatial and temporal propagation of Kondo correlations. *Phys. Rev. B* **90**, 045117 (2014).

[15] A. M. Oleś. Antiferromagnetism and correlation of electrons in transition metals. *Phys. Rev. B* **28**, 327–339 (1983).

[16] F. B. Anders and A. Schiller. Real-Time Dynamics in Quantum-Impurity Systems: A Time-Dependent Numerical Renormalization-Group Approach. *Phys. Rev. Lett.* **95**, 196801 (2005).

[17] F. B. Anders and A. Schiller. Spin precession and real-time dynamics in the Kondo model: Time-dependent numerical renormalization-group study. *Phys. Rev. B* **74**, 245113 (2006).

[18] E. Eidelstein, A. Schiller, F. Güttge, and F. B. Anders. Coherent control of correlated nanodevices: A hybrid time-dependent numerical renormalization-group approach to periodic switching. *Phys. Rev. B* **85**, 075118 (2012).

[19] F. Guettge, F. B. Anders, U. Schollwoeck, E. Eidelstein, and A. Schiller. Hybrid NRG-DMRG approach to real-time dynamics of quantum impurity systems. *Phys. Rev. B* **87**, 115115 (2013).

[20] R. Peters, T. Pruschke, and F. B. Anders. Numerical renormalization group approach to Green's functions for quantum impurity models. *Phys. Rev. B* **74**, 245114 (2006).

[21] A. Weichselbaum and J. von Delft. Sum-Rule Conserving Spectral Functions from the Numerical Renormalization Group. *Phys. Rev. Lett.* **99**, 076402 (2007).

[22] R. Bulla, A. C. Hewson, and T. Pruschke. Numerical renormalization group calculations for the self-energy of the impurity Anderson model. *J. Phys.: Condens. Matter* **10**, 8365, 1998.

[23] M. Yoshida, M. A. Whitaker, and L. N. Oliveira. Renormalization-group calculation of excitation properties for impurity models. *Phys. Rev. B* **41**, 9403–9414 (1990).

CHAPTER 5

In search of collective spin phenomena

If quantum mechanics hasn't profoundly shocked you, you haven't understood it yet. – Niels Bohr

5.1 Introduction

In the previous chapters we have tailored single spin-1/2 metal-molecule complexes (see Chapter 3) and investigated the interaction between two of them and demonstrated that in the presence of delocalized spins the magnetic properties of dimers are defined by a competition between the Kondo effect and the chemical interaction (see Chapter 4).

However, besides the interaction of two individual QIs, also the collective interaction of many QIs is of particular interest, since these could lead to Kondo lattices [111], Kondo insulators [112], heavy electron superconductors [113] and many more interesting phenomena which are related to heavy fermion systems [112].

This chapter is dedicated to the study of QIs which form well-ordered structures and therefore may lead collective spin phenomena. For our studies we have chosen the exemplary system 1,4,5,8-naphthalene-tetracarboxylic dianhydride (NTCDA) on Ag(111), since it is known that NTCDA molecules form well-ordered structures on the Ag(111) surface [114] and because photoemission experiments indicate that the system possibly shows the Kondo effect [115, 116]. However, a clear proof for the Kondo effect and detailed studies of the individual NTCDA molecules within the ordered structures on the atomic length scale are missing so far.

In the following we will demonstrate by means of scanning tunneling microscopy and spectroscopy that the NTCDA molecules indeed undergo the Kondo effect. In particular, we will show that the Kondo effect is extremely sensitive to the adsorption sites of the NTCDA molecules on the Ag(111) surface and that the Kondo effect originates from the interaction of the delocalized spin in the former LUMO of NTCDA, which is partially filled by charge transfer from the surface, with the itinerant electrons in the metal. In addition to the effect of the adsorption site we will reveal that also intermolecular interactions play an important role in the formation of the Kondo resonance and thus emphasize the possibility of collective behavior in the system. Furthermore, we will show that the delocalized nature of the spin carrying orbital and quantum interference effects result in a spatial variation of the line shape of the Kondo resonance above the NTCDA molecules. Moreover, we will demonstrate that the inelastic cross sections for molecular vibrations are enhanced in the presence of the Kondo effect and that this effect originates from the larger density of states (DOS) at the Fermi energy in the presence of the Kondo resonance. Finally, we will reveal anomalies close the Fermi level which cannot be simply described by the properties of a single QI and thus might be indications for collective behavior.

5.2 Experimental methods

5.2.1 Sample preparation

The experiments have been performed on a Createc STM with a base temperature of $T = 9.5\,\mathrm{K}$ and on a Specs JT-STM with a base temperature of $T = 4.3\,\mathrm{K}$. The JT-STM offered also the capability of applying an external magnetic field up to 3 T in out-of-plane direction. In both experimental setups an *in situ* sample preparation in ultra-high vacuum (UHV) conditions was possible.

The Ag(111) crystal was prepared by repeated cycles of Ar^+ sputtering and annealing to 800 K for 15 minutes. Submonolayers of NTCDA have been deposited onto the clean Ag(111) surface held at $T \approx 80\,\mathrm{K}$ from a home-built Knudsen cell. After the deposition of the molecules the sample has been annealed to 350 K for ≈ 5 minutes and afterwards cooled down to $T \approx 80\,\mathrm{K}$ within $\approx 2-3$ minutes. In order to minimize contaminations the sample has been transferred immediately after the preparation into the STM.

The electrochemically etched tungsten tip was cleaned by field emission in UHV and afterwards *in situ* by applying voltage pulses and indentations into the clean Ag(111) surface.

5.2.2 Spectroscopy

Differential conductance dI/dV spectra have been acquired using the conventional lock-in technique with the current feedback loop switched off. Typical parameters were: modulation amplitude 0.6 mV and frequency 833 Hz. To ensure a featureless DOS of the tip we measured reference spectra on the clean Ag(111) surface before starting measurements on the NTCDA molecules. dI/dV spectra at different locations above the same molecule have been measured as follows: the tip was located above the CH site of the NTCDA molecule (tunneling current $I = 200\,\mathrm{pA}$, bias voltage $V = 50\,\mathrm{mV}$), then the feedback loop was switched off and the tip was moved at constant height to different locations above the molecule, followed by the measurement of dI/dV spectra. To aid comparison, all dI/dV spectra of the NTCDA molecules from inside of a molecular layer have been normalized to the background conductance of the bright molecule at $V = -75\,\mathrm{mV}$ (for the definition of the bright molecule see section 5.3).

The spectroscopic images of the first (second) derivative dI/dV (d^2I/d^2V) have been measured at constant height using the conventional lock-in technique with the same parameters as mentioned above. For this purpose the tip was positioned above the CH site of the NTCDA molecule with the stabilization parameters $I = 200\,\mathrm{pA}$ and $V = 50\,\mathrm{mV}$ and subsequently the current feedback loop was switched off.

The $dI/dV(V,z)$ maps have been acquired with the tip and molecule being in contact. For this purpose the tip was positioned above one of the carboxylic oxygens of the NTCDA molecule with the stabilization parameters $I = 200\,\mathrm{pA}$ and $V = 50\,\mathrm{mV}$. Then the current feedback loop was switched off and the bias voltage was set to $V = 0\,\mathrm{mV}$. Next the tip was approached towards the carboxylic oxygen while observing the current through the junction. Once the current increased abruptly by one order of magnitude the approach was immediately stopped, since this change indicates the formation of a covalent bond between tip and molecule. For more details regarding the bond formation see Ref. [52]. Note that the bond can be cleaved by small voltage pulses ($V_{\mathrm{pulse}} \approx 100 - 500\,\mathrm{mV}$ for $\approx 10\,\mathrm{ms}$) without destroying neither the tip nor the molecule. The height where the bond formation occurred was defined as $z = 0\,\text{Å}$. Finally, $dI/dV(V)$ spectra have been measured at different z, i.e. for distances where the molecule was lifted from the surface ($z > 0$) or was pushed towards the surface ($z < 0$). From the $dI/dV(V)$ spectra at different z we then constructed differential conductance maps as a function of V and z.

5.3 Structure and electronic properties

In Fig. 5.1a an STM image of the so-called relaxed phase of NTCDA on Ag(111) is shown. The NTCDA molecules form a brick-wall structure with a rectangular unit cell of the size $11.57\,\text{Å} \times 15.04\,\text{Å}$ that consists of two inequivalent molecules due to different adsorption sites – on top or bridge position – on the Ag(111) lattice [117, 114, 118]. The superstructure matrix of the relaxed NTCDA phase is given by $\begin{pmatrix} 4 & 0 \\ 3 & 6 \end{pmatrix}$ [114]. At small bias voltages the two molecules can be clearly distinguished by their appearance in the STM image (see Fig. 5.1a) and will be referred to as bright and dark molecules, respectively. However, it is not known which of the molecules, i.e. bright or dark, is located on which adsorption site, i.e. on top or bridge position.

The difference in the appearance of the two molecules in the STM image stems from their different electronic structure close to the Fermi level. This can be seen in Fig. 5.1b. The dI/dV conductance spectra acquired above the CH site of the bright and dark molecule look very similar, with one crucial exception: the dI/dV conductance spectrum of the bright molecule shows a well-pronounced sharp peak at zero bias. The peak at zero bias is also present in the case of the dark molecule as the dI/dV conductance spectra, which have been acquired on a smaller bias voltage window, in Fig. 5.1c show, but much less pronounced. In the case of the bright molecule the full width at half maximum (FWHM) of zero bias peak is $\approx 29\,\mathrm{mV}$, whereas for the dark molecule it is $\approx 47\,\mathrm{mV}$. These values have been obtained by

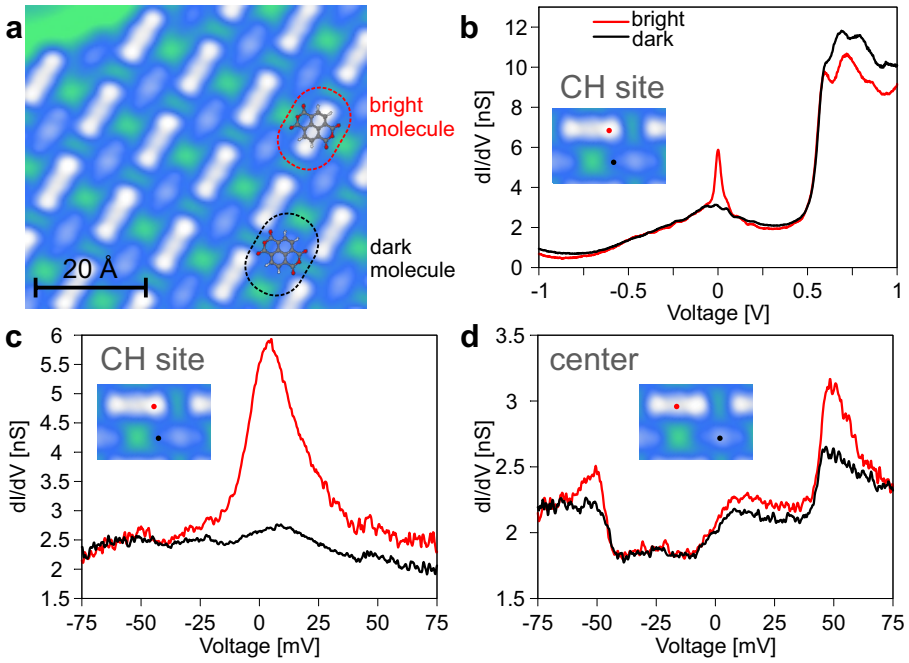

Figure 5.1: **a** Constant current STM image of the relaxed phase of NTCDA on Ag(111) ($I = 200\,\mathrm{pA}$, $V = 50\,\mathrm{mV}$). A graphical representation of the gas-phase NTCDA molecule has been overlaid over the bright and dark molecules for reasons of illustration. The white, grey and red circles indicate hydrogen, carbon and oxygen atoms of NTCDA. **b** Overview dI/dV conductance spectra of the bright and dark molecule at $T = 4.3\,\mathrm{K}$. The spectra have been measured above at the CH site of the particular NTCDA molecule as indicated in the inset. **c** As panel b, but for a smaller voltage range. **d** dI/dV conductance spectra of the bright and dark molecule at $T = 4.3\,\mathrm{K}$, recorded at the center of the particular molecule as indicated in the inset.

fitting the zero bias peaks with a Fano line shape (see also section 5.5). Furthermore, the dI/dV conductance spectra in Fig. 5.1c reveal two small side peaks at approximately $\pm 48\,\mathrm{mV}$ that will be discussed in more detail below. The broad peak beneath the zero bias peak is attributed to the former lowest unoccupied molecular orbital (LUMO) of the NTCDA molecule which has been partially filled by charge transfer from the Ag 4s states [115, 116] and, maybe, from the Shockley states [116] and is located at $\approx -40 \pm 30\,\mathrm{mV}$ and has a FWHM of approximately $270 \pm 50\,\mathrm{mV}$ (values obtained from a fit with a Gaussian function). For simplicity this new hybridized state will be still called LUMO in the following. The cutting of the LUMO by the Fermi level indicates a metallic nature of the NTCDA layer. The feature at $\approx +500\,\mathrm{mV}$ is a signature of the interface state [119, 120].

Besides the distinct electronic properties of the bright and dark molecules at the Fermi level also spatial variations of the electronic fingerprints are observed within individual molecules as seen in Fig. 5.1d, which shows dI/dV conductance spectra that have been measured at center of the NTCDA molecules. The spectra for the bright and dark molecule are almost identical and only differ in the intensity of the side peaks at $\approx \pm 48\,\mathrm{mV}$. Furthermore, the peak at zero bias is replaced by a step-like feature and also the side peaks look like sharp steps. Nevertheless, the peak-like shape of the features at $\approx \pm 48\,\mathrm{mV}$ is still visible, in particular this can be seen in the spectrum of the bright molecule (see Fig. 5.1d).

Before discussing the origin of these features it is also important to note that depending on the coverage and/or the exact sample preparation recipe NTCDA molecules adsorbed on the Ag(111) surface have the tendency to self-assemble in different phases [114, 118] than the relaxed phase in Fig. 5.1a. One of these phases which will be used below in order to describe the origin of the observed features is shown in Fig. 5.2a. Note that both phases are found on the same sample that has been prepared according the recipe in section 5.2.1. The NTCDA molecules show the same alignment as in the relaxed phase, i.e. a brick-wall structure, but the unit cell of this structure is approximately $10.9 \pm 0.2\,\text{Å} \times 13.8 \pm 0.2\,\text{Å}$ (estimated from the STM images) and hence compressed in comparison to the unit cell of the relaxed phase. This small change in the size of the unit cell results in an additional superimposed image modulation as seen in Fig. 5.2a: the appearance of the NTCDA molecules changes gradually from bright to dark. The periodicity of this modulation is 11 unit cells. Note that this structure does not match any of the superstructures that have been observed earlier. In the following this structure will be referred to as rippled phase because of its appearance in the STM images. As seen in Fig. 5.2b and c the gradual change from bright to dark molecule is again a consequence of the electronic properties close to the Fermi level: the zero bias peak and the side peaks gradually lose intensity from the bright to the dark molecule. The only quantitative difference between the spectra of the bright and dark molecules of the rippled phase and of the relaxed phase is related to the FWHM of the zero bias peak: the FWHM of the bright and dark molecule in the rippled phase are given by $\approx 23\,\mathrm{mV}$ and $\approx 43\,\mathrm{mV}$, respectively, and thus marginally narrower than in the relaxed phase.

In the following sections we will systematically analyze the origin of the different electronic features in the dI/dV conductance spectra, namely of the peak at zero bias, the side peaks and the differences between CH site and center, and furthermore we will look out for indications of collective spin phenomena.

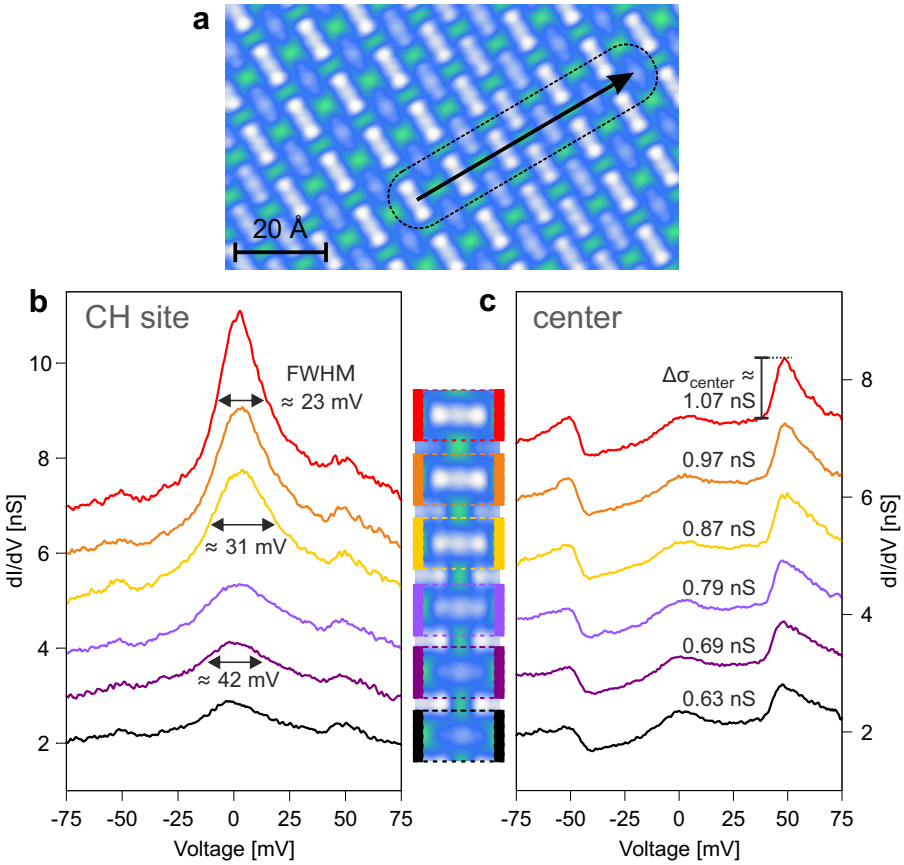

Figure 5.2: **a** Constant current STM image of the rippled phase of NTCDA on Ag(111) ($I = 200\,\mathrm{pA}$, $V = 50\,\mathrm{mV}$). The arrow indicates the gradual transition from the bright to the dark molecule. **b** dI/dV conductance spectra of the different NTCDA molecules in the rippled phase at $T = 4.3\,\mathrm{K}$. The spectra have been recorded at the CH site of the particular molecule. The different colors correspond to the different molecules as indicated by the colored frames around the molecules. Spectra are shifted for clarity. **c** dI/dV conductance spectra of the different NTCDA molecules in the rippled phase at $T = 4.3\,\mathrm{K}$, measured at the center of the particular molecule. Colors as in panel b. Spectra are shifted for clarity.

5.4 Kondo effect

The peak at zero bias has been also observed previously by Ziroff et al. in high-resolution photoemission spectroscopy experiments of NTCDA/Ag(111) [115]. Ziroff et al. estimated the linewidth (FWHM) of this feature to be about $\approx 30\,\mathrm{meV}$ at a temperature of $T \approx 20\,\mathrm{K}$, which is in good agreement with the FWHM of the zero bias peak of the bright molecule ($\approx 29\,\mathrm{mV}$ in the relaxed phase and $\approx 23\,\mathrm{mV}$ in the rippled phase at $T = 4.3\,\mathrm{K}$). Furthermore, they found that the emergence of this feature depends on the exact position of the LUMO with respect to the Fermi level and that its width and intensity strongly depend on the experimental temperature. From this behavior they concluded that the peak at zero bias must be related to the Kondo effect.

In the following we will demonstrate that the zero bias peaks of the bright and dark molecules are indeed Kondo resonances and that they only differ by their Kondo temperatures T_K. For this purpose we make use of the fact that the coupling between molecule and substrate, and hence the Kondo effect, can be tuned gradually by controlled lifting of the molecule as demonstrated in previous works where PTCDA molecules have been lifted from the Ag(111) surface [52, 121, 122, 123].

Fig. 5.3a and b show $dI/dV(V,z)$ maps of the bright and dark molecules. The maps have been acquired by lifting the respective molecule from the edge of a molecular island. A detailed description of the experimental procedure can be found in section 5.2.2. The $dI/dV(V,z)$ maps show qualitatively the same characteristics. As soon as the carboxylic oxygen is contacted by the STM tip both molecules show a well pronounced and sharp peak at the Fermi energy. Pushing the molecules closer to the surface leads to a broadening of the zero bias peak and at the same time to an increase in its intensity. After a certain pushing distance the zero bias peak disappears and a new broad peak at negative bias voltages becomes clearly visible. Further pushing shifts the new peak to more negative energies. On the other hand, lifting the molecules from the contact point results in narrowing of the zero bias peak and in a decrease of its intensity. The main difference between the $dI/dV(V,z)$ maps of the bright and dark molecules is that they are shifted by approximately $0.9\,\text{Å}$ along the z-axis with respect to each other.

All the features observed in the $dI/dV(V,z)$ maps reflect the characteristics of the Kondo effect and are in good agreement with the previous results obtained for the lifting of PTCDA. The underlying physics can be understood in simple terms by considering the asymmetric single impurity Anderson model (see section 2.2.1). Note that a more detailed description of the effects during the pushing and lifting experiments in the presence of the Kondo effect can be found in previous works [52, 121, 122, 123]. For the asymmetric single impurity Anderson model Krishna-murthy et al. have

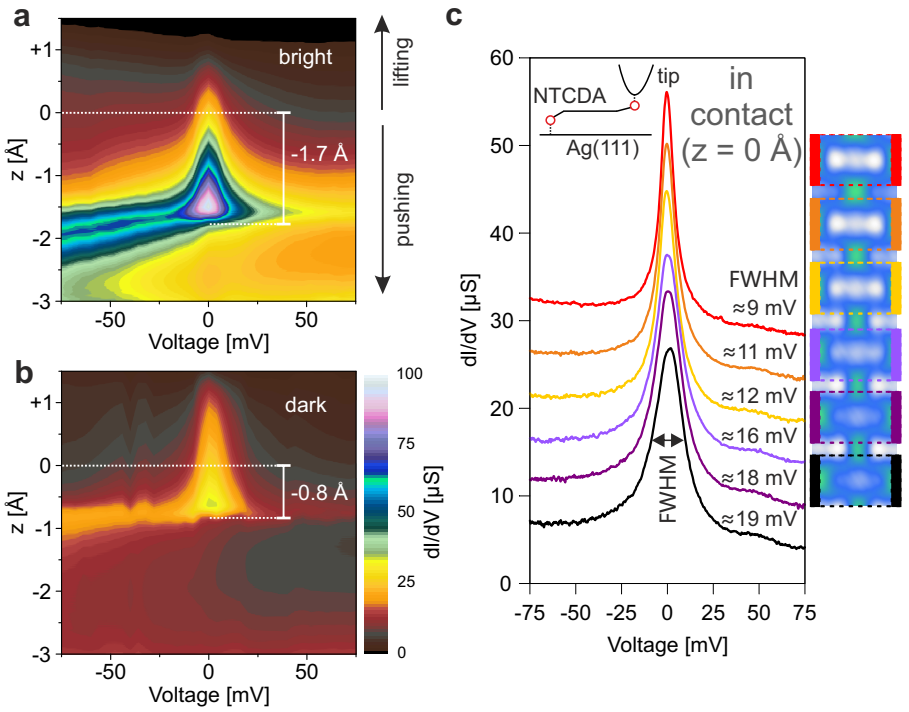

Figure 5.3: **a** $dI/dV(V,z)$ map for a bright molecule from an edge of a NTCDA island measured at $T = 9.5\,\mathrm{K}$. $z = 0\,\text{Å}$ corresponds to the height where the molecule-tip bond formation occurred. For more details see section 5.2.2. The arrows indicate the lifting and pushing directions, respectively. The color scale quantifies the differential conductance as shown in panel b. **b** As panel a, but for a dark molecule from an edge of an island. **c** dI/dV conductance spectra of the different NTCDA molecules in the rippled phase, recorded directly after the formation of the molecule-tip bond as indicated in the inset. The data was acquired at $T = 4.3\,\mathrm{K}$. Colors as in Fig. 5.2b and c. Spectra are shifted for clarity.

shown that the Kondo temperature can be described by [76]

$$T_{\mathrm{K}}(\Gamma, \epsilon_0, U) = 0.182|E_0^*|\sqrt{|\rho J_{\mathrm{eff}}|}\exp\left(-\frac{1}{|\rho J_{\mathrm{eff}}|}\right) \tag{5.1}$$

when the orbital occupancy remains close to integer values and double occupation is energetically supressed. ϵ_0 describes the position of the bare level and E_0^* the renormalization of the bare level due to high energy charge fluctuations, given by the self-consistent solution of $E_0^* = \epsilon_0 + (\Gamma/\pi)\ln(-U/E_0^*)$ with the constant hybridization function $\Gamma(E) = \Gamma$ and the Coulomb interaction U. $\rho J_{\mathrm{eff}} = \rho J[1 + (\pi\rho K)^2]^{-1}$ contains the dimensionless Kondo coupling

$$\rho J = -\frac{2\Gamma}{\pi}\left(\frac{1}{|E_0^*|} + \frac{1}{\epsilon_0 + U}\right) \tag{5.2}$$

and also a modification due to the degree of particle-hole symmetry breaking

$$\rho K = \frac{\Gamma}{2\pi}\left(\frac{1}{|E_0^*|} - \frac{1}{\epsilon_0 + U}\right), \tag{5.3}$$

both obtained from the Schrieffer-Wolff transformation [77]. At $T = 0\,\mathrm{K}$ the FWHM of the Kondo resonance is given by $2k_{\mathrm{B}}T_{\mathrm{K}}$.

Now, pushing the NTCDA molecule towards the surface leads to a stronger hybridization Γ and consequently to additional charge transfer into the molecule and thus to a shift of ϵ_0 to more negative energies. Furthermore, the decreasing molecule-surface distance results in a larger metallic screening and thus in a smaller Coulomb interaction U. According to the formula for T_{K}, all these changes of the parameters Γ, ϵ_0 and U result in a larger Kondo temperature T_{K}, explaining the broadening of the Kondo resonance with increasing pushing distance. The disappearance of the Kondo resonance at a certain molecule-surface distance is related to the filling of the LUMO: as soon as the LUMO is doubly occupied, the Kondo effect breaks down. Hence, the new broad peak which appears after the breakdown of the Kondo peak can be attributed to the filled LUMO.

The effect during the lifting is just opposite. The hybridization Γ between the molecule and the surface decreases and consequently results in a shift of ϵ_0 towards the Fermi level. Furthermore, the Coulomb interaction U increases, since the metallic screening decreases with further lifting distance. Thus, according to eq. (5.1) the Kondo temperature T_{K} decreases and leads to a narrowing Kondo resonance.

In addition to the fact that we are dealing in both scenarios with the Kondo effect, we can conclude from the $dI/dV(V, z)$ maps that the Kondo effect must be originating from the interaction of an unpaired electron in the LUMO of NTCDA, which has been filled by charge transfer from the substrate, and the itinerant electrons from the metal. Moreover, the filling

of the LUMO must be close to single occupancy, since the Kondo effect occurs, and this unpaired spin must be delocalized over the entire molecule, because of the extended nature of the LUMO. Due to the delocalized nature of the spin-carrying orbital a magnetic exchange or non-magnetic chemical interaction between neighboring molecules seems likely and will be discussed below.

But before that we first focus on the different FWHMs of the Kondo resonances of the bright and dark molecules. From the $dI/dV(V,z)$ maps we can actually deduce that the Kondo temperatures of both molecules must be different. This can be seen by looking at the shift between the $dI/dV(V,z)$ maps of the bright and dark molecule: to obtain the same FWHM of the Kondo resonance, the dark molecule has to be lifted by a larger amount than the bright molecule. Since lifting causes a decrease of T_K, the Kondo temperature $T_\mathrm{K}^\mathrm{dark}$ of the dark molecule must be initially higher than the Kondo temperature $T_\mathrm{K}^\mathrm{bright}$ of the bright molecule. That both molecules have different FWHM and thus also different Kondo temperatures can be also seen in Fig. 5.2b: as we move from the bright to the dark molecule in the rippled phase the Kondo resonance broadens, i.e. the Kondo temperature increases from bright to dark. This trend stays also the same when we contact the molecules. Fig. 5.3c shows the dI/dV conductance spectra of the molecules in the rippled phase directly after the formation of the molecule-tip bond. Again the Kondo resonance broadens from the bright to the dark molecule and decreases in intensity. The reason for the overall narrower Kondo resonances of contacted molecules in comparison to non-contacted ones is related to the procedure of the bond formation between tip and molecule. During the bond formation the molecule already jumps slightly to the tip, which correlates with the lifting of the molecule [121]. Hence, the Kondo temperature is already decreased by forming the contact and thus results in a narrower FWHM. However, the fact that the trend is the same for contacted and non-contacted molecules proves that the bond formation does not change the physics of the system qualitatively.

An analysis of the behavior of the Kondo resonance in magnetic field reveals that not only the Kondo temperature is decreased by lifting, but that the Kondo effect is also driven from the strong coupling ($T < T_\mathrm{K}$) [75, 76] to the weak coupling regime ($T > T_\mathrm{K}$) [75, 76] in the process. In Fig. 5.4 the dI/dV conductance spectra for a bright molecule from the edge of an island are shown for different lifting distances and for magnetic fields of $B = 1.0\,\mathrm{T}$ and $B = 2.5\,\mathrm{T}$. For $B = 1.0\,\mathrm{T}$ the behavior is similar to the one in Fig. 5.3a, where no external magnetic field is applied: the FWHM of the Kondo resonance simply decreases gradually from 10.6 mV at $z = 0\,\text{Å}$ to 7.5 mV at $z = 0.9\,\text{Å}$. But for $B = 2.5\,\mathrm{T}$ the situation is different. The shape of the Kondo resonance starts to change at $z = 0.8\,\text{Å}$ and for $z = 0.9\,\text{Å}$ a splitting of the Kondo resonance is clearly visible. For a spin $1/2$ Kondo effect

a splitting of the Kondo resonance should occur above the critical magnetic field [124]

$$B_C \approx 0.5 k_B T_K/(g\mu_B). \tag{5.4}$$

Here g is Landé factor and μ_B the Bohr magneton. Since we are close to $k_BT \approx 0.37\,\mathrm{mV}$ and hence much smaller than the FWHM of the Kondo resonance, we can estimate the estimate the Kondo temperature T_K to be given by approximately

$$T_\mathrm{K} \approx \mathrm{FWHM}/(2k_\mathrm{B}), \tag{5.5}$$

provided we are in the strong-coupling regime.

For the Kondo peak in Fig. 5.4 at $z = 0.9\,\text{Å}$ this yields a Kondo temperature of $T_\mathrm{K} \approx 43.5\,\mathrm{K}$. According to eq. (5.4) this results in critical magnetic field of $B_C \approx 16.2\,\mathrm{T}$ for $g = 2$. Hence, no splitting should be observable at $B = 2.5\,\mathrm{T}$. But since a splitting is clearly visible at $B = 2.5\,\mathrm{T}$, the Kondo temperature must be roughly $T_\mathrm{K} \approx 6.7\,\mathrm{K}$ at $z = 0.9\,\text{Å}$ according to eq. (5.4). This means that the Kondo temperature T_K is actually of the same order as the experimental temperature T or even less, since $T_\mathrm{K} \approx 6.7\,\mathrm{K}$ represents a upper limit. Thus, we are in the weak coupling regime, and eq. (5.5) is not valid.

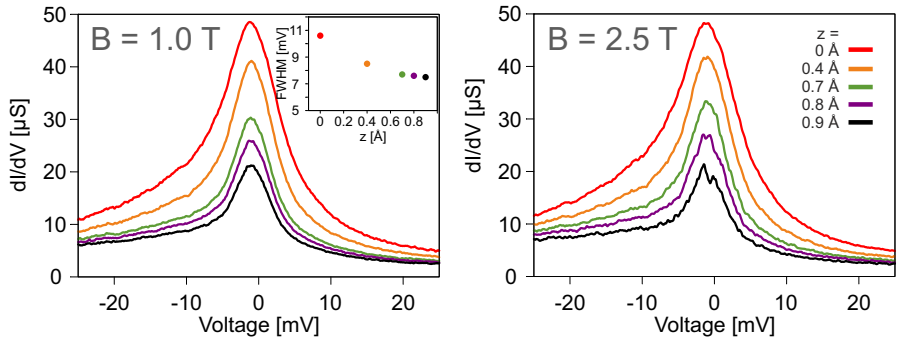

Figure 5.4: dI/dV conductance spectra of a bright molecule from an edge of a NTCDA island at different lifting distances $z > 0$ and magnetic fields of $B = 1.0\,\mathrm{T}$ (left panel) and $B = 2.5\,\mathrm{T}$ (right panel) measured at $T = 4.3\,\mathrm{K}$. The inset in the left panel shows the FWHM of the Kondo resonance as a function of the lifting distance $z > 0$. $z = 0\,\text{Å}$ corresponds to the height where the molecule-tip bond formation occurred.

Generally speaking, the discrepancy between the Kondo temperatures estimated from the FWHM and the critical magnetic field is related to the fact the FWHM of the Kondo resonance is a non-universal parameter and therefore inappropriate for estimating the Kondo scale $k_\mathrm{B}T_\mathrm{K}$ [125]. As soon as T_K approaches and drops below the experimental temperature T during the lifting procedure, the FWHM of the Kondo resonance starts to increase

although T_K is decreasing, because the Kondo system undergoes a crossover from the strong coupling to the weak coupling regime at this point. Hence, the FWHM will always lead to an incorrect value for T_K in this regime. This is comparable to the situation where T_K is kept fixed and T is increased above T_K – which also results in a broadening of the Kondo resonance and finally in a disappearance of the Kondo effect (see section 2.2.1). A more detailed description of the crossover from the strong to the weak coupling regime during the lifting experiments can be found elsewhere [126].

For $B < 2.5\,\mathrm{T}$ the splitting is suppressed by the thermal fluctuations $k_B T$. The splitting occurs once the Zeeman energy $g_0 \mu_B B$ exceeds the thermal energy or is nearly the same, which in our case happens roughly at $B = 2.5\,\mathrm{T}$. Since the Zeeman energy $g_0 \mu_B B \approx 0.29\,\mathrm{mV}$ is slightly smaller for $B = 2.5\,\mathrm{T}$ than the thermal fluctuations $k_B T \approx 0.37\,\mathrm{mV}$ at $T = 4.3\,\mathrm{K}$, the gap is not well developed, but nevertheless clearly visible.

In conclusion all observed features during the lifting experiments with and without an external magnetic field reflect the characteristics of a Kondo effect and thus prove unambiguously that the zero bias peak in both molecules is indeed the Kondo resonance, but with different Kondo temperatures $T_K^{\mathrm{bright}} < T_K^{\mathrm{dark}}$.

The different Kondo temperatures of the bright and dark molecules are most probably related to the different adsorption sites on the Ag(111) lattice. Since T_K depends exponentially on Γ, ϵ_0 and U, already small changes in the environment can lead to drastic changes in the Kondo temperature. The relation to the adsorption site is corroborated by the behavior which we observe within the rippled phase. Since the unit cell in the rippled phase is compressed in comparison to the unit cell of the relaxed phase, it is assumed that the molecules in the rippled phase undergo a continuous transition between the adsorption sites of the relaxed phase. Thus the parameters Γ, ϵ_0 and U change slightly from bright to dark molecule in the rippled phase and result in the different FWHMs of the Kondo resonances.

However, the Kondo temperatures of the NTCDA molecules are not solely determined by the different adsorption sites, also intermolecular effects play a crucial role. In Fig. 5.5a the dI/dV conductance spectra of an isolated single molecule are shown. As clearly seen, neither at the CH site nor in the center of the single molecule a Kondo resonance is observable. Only the steps at finite energies are visible in both spectra, but with a different magnitude in comparison to the features observed in the center of the NTCDA molecules which are embedded into an island (see Fig. 5.1d and Fig. 5.2c). The origin of these features will be discussed in section 5.6. Also clusters of NTCDA molecules which consists of less than 4 molecules, but are ordered in a brick-wall structure, do not show any Kondo resonance. As an example for the form of such clusters see Fig. 5.5, where two clusters made of two NTCDA molecules each are shown. The electronic fingerprints of molecules in such clusters are equal to those of an isolated single molecule. The Kondo effect

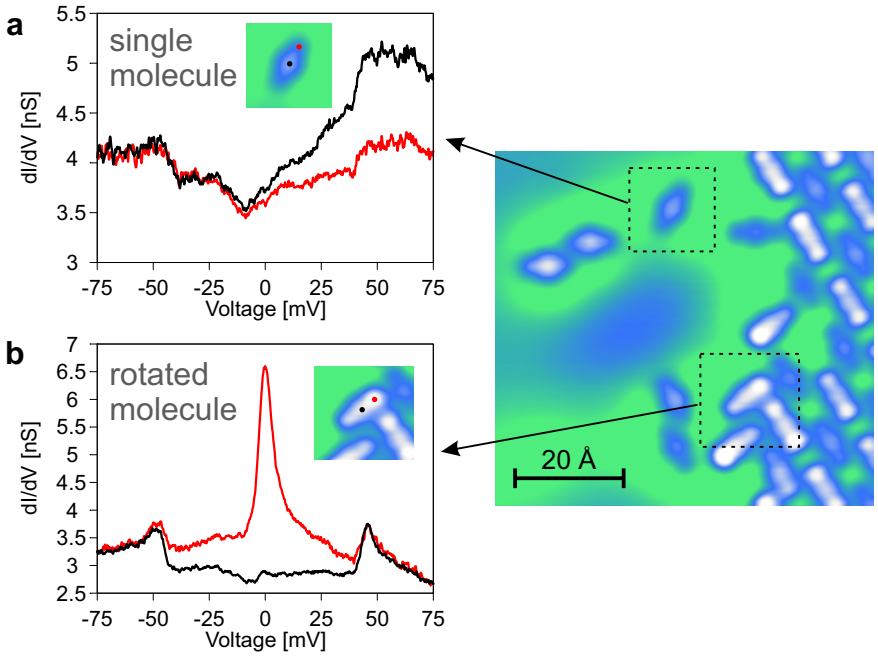

Figure 5.5: **a** dI/dV conductance spectra of an isolated single NTCDA molecule measured at different locations above the molecule as indicated in the inset. Measurements were performed at $T = 4.3\,\mathrm{K}$. **b** As panel a, but for a rotated molecule at the edge of a NTCDA island (rippled phase). The right panel shows an overview constant current STM image of the area where the single and rotated molecule are located ($I = 200\,\mathrm{pA}$, $V = 50\,\mathrm{mV}$).

is only observable in NTCDA islands that consist of more than 4 molecules.

Furthermore, the orientation of the molecules with respect to each other has a strong influence on the Kondo resonance. In Fig. 5.5b the dI/dV conductance spectra of a NTCDA molecule at an edge of an island that is rotated by $\approx 90°$ with respect to the normal molecules in the brick-wall structure is shown. For simplicity this molecule will be called rotated molecule in the following. As it can be seen in the spectra the rotated molecule shows the same features as the molecules from inside the island (see Fig. 5.5c and d), but the Kondo resonance is much narrower and also the side peaks are clearly visible at the CH site of the molecule. In this particular case the FWHM of the Kondo resonance is approximately 7.1 mV and thus by factor ≈ 3.4 (≈ 6.1) narrower in comparison to the bright (dark) molecule in the rippled phase.

All these observations indicate that the intermolecular interactions between the molecules are also crucial for the formation of the Kondo effect. However, currently the exact physical mechanism is not known. Possible mechanisms could be the following:

1. Intermolecular interactions in the well-ordered structures influence the hybridization of the NTCDA molecules with the Ag(111) surface, e.g. by lifting the molecules to larger adsorption heights, and thus drive the system into the Kondo regime (half-filling and $\Gamma \ll U$) by modifying the parameters Γ, ϵ_0 and U. Hence, one possible explanation for the absence of the Kondo effect in single molecules could be that they are more strongly hybridized with the surface and thus receive more charge transfer, so that the filling of the LUMO is closer to double occupancy.

2. A magnetic exchange interaction J between neighboring molecules in the well-ordered structures leads to a coupling of the spins. Depending on the sign and magnitude of J the Kondo temperature of the coupled spins can be increased or decreased in comparison to the Kondo temperature of the uncoupled spins [127, 128].

3. A non-magnetic chemical interaction between neighboring molecules can have the same decisive effect as the magnetic exchange interaction, i.e. it can also lead to a broadening or narrowing of the Kondo resonance (see also chapter 4).

At the moment none of these mechanism can be ruled out. Also an interplay of several effects is imaginable. However, in order to find out how the intermolecular interactions effect the Kondo temperature more studies on different artificial structures consisting of NTCDA molecules supported by *ab initio* calculations are necessary.

Nevertheless, the indications for interactions between molecules emphasize the possibility that any of the observed features in the dI/dV conductance spectra could be related to collective spin phenomena.

5.5 Role of quantum interference

The spatial variations of the dI/dV conductance spectra within a particular molecule are related to different physical phenomena and will be discussed step-by-step in the following. First of all we will focus on transformation of the Kondo resonance from a peak at the CH site to a step-like feature at the center of the molecules and will demonstrate that this step-like feature is also a manifestation of the observed Kondo effect at the CH sites. In scanning tunneling spectroscopy the line shape of the Kondo resonance is determined by quantum interference effects between different tunneling channels of the electrons and is described by the so-called Fano line shape [82, 83] (see also section 2.2.1.3):

$$\rho(E) \propto \rho_0 + \frac{(q+\epsilon)^2}{1+\epsilon^2}, \tag{5.6}$$

with the normalized energy

$$\epsilon = \frac{E - E_{\mathrm{K}}}{(\Delta/2)} \tag{5.7}$$

and the form factor

$$q = \frac{t_2}{\pi \rho_0 V t_1}. \tag{5.8}$$

Here E_{K} describes the position of the Kondo resonance, V the hybridization between the molecule and substrate, Δ the FWHM of the Kondo resonance, t_1 the tunneling probability directly into the substrate and t_2 the tunneling probability into the Kondo resonance. The form factor q is responsible for the line shape of the Kondo resonance.

Fig. 5.6a shows the fits of the Fano line shape to the spectra of the bright molecule (from Fig.5.1c) and of the rotated molecule (from Fig.5.5b). In both cases the fitted Fano line shape is in good agreement with the measured data. The q-factors and FWHMs, which have been extracted from the fits, are summarized in table 5.1. As seen, the features at the CH site and center of the molecules show approximately the same FWHM. This correlation suggests that the step-like features in the center of the molecules also represent the Kondo effect, but with a different line shape.

type of molecule	location	Δ	q
bright	CH site	$\approx 23.7\,\mathrm{mV}$	≈ 8.68
	center	$\approx 22.1\,\mathrm{mV}$	≈ 1.15
rotated	CH site	$\approx 7.1\,\mathrm{mV}$	≈ 7.67
	center	$\approx 6.8\,\mathrm{mV}$	≈ 1.05

Table 5.1: FWHMs Δ and q factors extracted from the fits of the Fano line shape to the dI/dV conductance spectra of the bright molecule in the rippled phase and the rotated molecule. See also Fig. 5.6a.

The change in the line shape can be attributed to the form factor as seen in table 5.1: at the CH site the Kondo resonance has a form factor of $q \gtrsim 7$ for both molecules, whereas at the center of the molecules the q factor drops to almost ≈ 1. Under the assumption that ρ_0 and V are the same at the CH site and at the center, then the change in q must be related to the tunneling probabilities t_1 and t_2. This means that at the CH site the tunneling mainly occurs through the Kondo resonance ($t_1 \ll t_2$), whereas at the center of the molecule also direct tunneling into the substrate becomes significant ($t_1 \gg t_2$).

The reason for the different tunneling weights at the CH site and the center of the NTCDA molecule can be related to the nature of the wave function $\Psi(r)$ of the LUMO. Near the center of the molecule the LUMO has a nodal plane and thus leads to $|\Psi(r)|^2 \approx 0$. This is illustrated in

Fig. 5.6b, which shows the local density of states (LDOS) of the LUMO 4 Å above the gas-phase NTCDA molecule. Since the LDOS of the LUMO almost vanishes at the center of the molecule, direct tunneling into the metal substrate is enhanced in this region, whereas above the CH site the electrons mainly tunnel in the LUMO, i.e. into the Kondo resonance. Thus, the ratio between the tunneling probabilities t_1 and t_2 is different at the CH site and at the center of the molecule and therefore also the q factor which defines in scanning tunneling spectroscopy the shape of the Kondo resonance. Nevertheless, both features, i.e. the peak at zero bias at the CH site and the step-like feature at the center, are manifestations of the same Kondo effect.

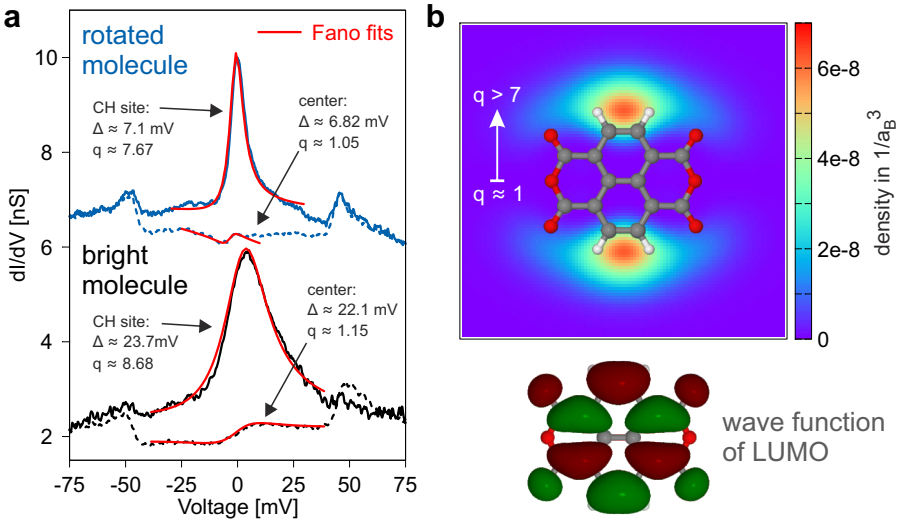

Figure 5.6: **a** Illustration of the fits of the Fano line shape to the dI/dV conductance spectra of the bright and rotated molecule that have been measured at the CH site and at the center of the particular molecule. **b** Local density of states (LDOS) of the LUMO of NTCDA calculated 4 Å above the gas-phase molecule (top panel). A graphical representation of the gas-phase NTCDA molecule has been overlaid for clarity. The bottom panel shows the top view of the LUMO of the gas-phase NTCDA molecule. The different colors indicate the positive ($\Psi(r) > 0$) and negative ($\Psi(r) < 0$) contributions of the wave function.

5.6 Origin of the side peaks

Having demonstrated that the step-like feature is also associated with the Kondo effect, we turn our focus to the second striking feature in the dI/dV spectra, namely the side peaks at $\approx \pm 48\,\mathrm{mV}$. First, we will describe the origin of side peaks based on the dI/dV spectra that have been acquired at the center of the molecules and thereafter we will explain the differing intensities of the side peaks at the CH site and at the center.

Sharp steps in the dI/dV conductance spectrum, which are symmetrically distributed around the Fermi level as seen in Fig. 5.1d or Fig. 5.2c, are usually associated with inelastic tunneling processes that can occur, for example, as a result of an excitation of a molecular vibration [129, 130] or spin-flip excitation [28].

The facts that the side peaks can also be seen in the dI/dV spectra of an isolated single NTCDA molecule (see Fig. 5.5a), and that they were not effected by the external magnetic field, indicate that the side peaks are not related to spin-flip excitations, but rather to molecular vibrations. This is also emphasized by the fact that spin-flip excitations are usually in the order of a few mV [28], whereas energies of molecular vibrations can also be in the order of several 100 mV [129, 130]. Note that the side peaks in the isolated single NTDCA molecule are located at $\approx \pm 42\,\mathrm{mV}$ and hence are slightly shifted in energy with respect to the side peaks which we observed for molecules that are embedded into a molecular island. This small shift in energy is most likely related to intermolecular interactions in the layer.

no.	symmetry	energy
1	B_{3g}	41.6 mV (335.35 cm^{-1})
2	B_{1u}	46.2 mV (372.41 cm^{-1})
3	B_{3g}	50.4 mV (406.62 cm^{-1})
4	A_g	50.7 mV (408.96 cm^{-1})
5	B_{1g}	52.8 mV (425.53 cm^{-1})

Table 5.2: Vibrational modes of a gas-phase NTCDA molecule in the range from 40 mV to 50 mV. Data taken from the supplementary information of Ref. [131].

Indeed, *ab initio* calculations reveal several vibrational modes in the energy range from 40 mV to 50 mV [131]. In table 5.2 the energies and symmetries of these modes are listed. Note that the gas-phase NTCDA molecule has a D_{2h} symmetry. In analogy to Ref. [130] we can exclude several of these modes by symmetry considerations. According to the theory for inelastic tunneling in scanning tunneling spectroscopy the molecular vibration must be symmetric with respect to a mirror plane if the initial, i.e. before the scattering process, and final state, i.e. after the scattering process, of the

tunneling electrons both are symmetric with respect to the same mirror plane [132]. If the initial and final states have different symmetries with respect to the same mirror plane, then the molecular vibration must be antisymmetric [132]. In our case the initial state is given by the molecular orbital into which the electron can tunnel resonantly, i.e. the LUMO of NTCDA. The symmetry of the final state, i.e. the state into which the electron is scattered by the inelastic interaction with the molecular vibration, can be determined from spectroscopic images that have been recorded at the energy of the vibrations. Usually the second derivative d^2I/dV^2 is used, since this one is more sensitive to inelastic contributions in the current.

Since the STM is limited to only two dimensions we have to restrict our considerations regarding the symmetry to the same two dimensions. In Fig. 5.7a the two perpendicular mirror planes m_x and m_y for the LUMO of the gas-phase NTCDA molecule are shown in the same perspective as the molecule appears in the STM images. From this image we can deduce that the initial state has odd (even) symmetry with respect to m_x (m_y). The symmetry for the final state can be evaluated from the spectroscopic image of the second derivative d^2I/dV^2 as mentioned above. Such a spectroscopic image of the rippled phase is shown in Fig. 5.7b. As seen, the final state is symmetric with respect to m_x and m_y. This can be concluded from the absence of a nodal plane along m_x and m_y. Hence, the vibrational mode must be odd (even) with respect to m_x (m_y). These conditions are only fulfilled by the two modes with B_{3g} symmetry in the table 5.2.

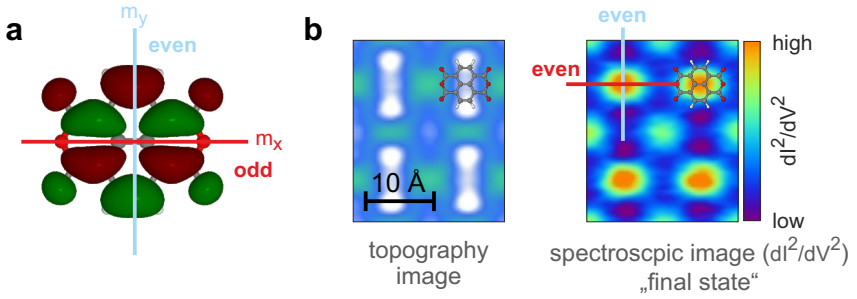

Figure 5.7: **a** Illustration of the two perpendicular mirror planes m_x and m_y for the LUMO of the gas-phase NTCDA molecule. The symmetry of the LUMO is odd (even) with respect to m_x (m_y). **b** Left panel shows a topography image measured at constant height above the molecules of the rippled phase at the energy of the vibrational mode at $\approx \pm 48\,\mathrm{mV}$. Right panel shows the corresponding d^2I/dV^2 image of the vibrational feature at $\approx \pm 48\,\mathrm{mV}$. The mirror planes m_x and m_y are also indicated. The final state is symmetric with respect to m_x and m_y.

However, the side peaks cannot be described solely by the excitation of one of these two vibrational modes. The relative change in the conductance

at an inelastic step due to an excitation of a molecular vibration is typically in the order of $\sim 0.1 - 10$ per cent [132]. But as seen from table 5.3 the inelastic cross section η, which is determined by the ratio of the step height $\Delta\sigma$ and the background conductance σ just before the inelastic step, differ strongly from the values that have been observed up to now – only the cross section of the single molecules is in the expected range. Furthermore, the appearance of the inelastic step is more peak-like, as mentioned already in section 5.3. All these deviations from the usual observations for inelastic tunneling indicate that there must be a further process involved in the formation of the side peaks. Note that for point defect PTCDA molecules in ordered PTCDA/Ag(111) structures also an increase of the inelastic cross section was observed [133]. In contrast to the normal PTCDA molecules in the ordered structures, the point defect molecules showed a Kondo effect [133].

type of molecule	cross section (center)	cross section (CH site)
single	$\approx 12.1\,\%$	$\approx 11.4\,\%$
rotated	$\approx 26.7\,\%$	$\approx 21.3\,\%$
bright	$\approx 42.2\,\%$	$\approx 11.2\,\%$
dark	$\approx 27.4\,\%$	$\approx 7.8\,\%$

Table 5.3: Inelastic cross sections of the side peaks at $\approx \pm 48\,\mathrm{mV}$ for different types of molecules. The inelastic cross sections have been evaluated at the CH site and center of the molecules.

In fact the side peaks at $\approx \pm 48\,\mathrm{mV}$ can be interpreted as replicas of the Kondo resonance at the Fermi level as we will demonstrate in the following. The strong correlation between the Kondo resonance and the side peaks can be seen by considering the dI/dV conductance spectra for the different molecules in rippled phase (see Fig. 5.2b and c): the intensity (FWHM) of the Kondo resonance at the CH site and of the side peaks at the center decreases (increases) from bright to dark molecule. In Fig. 5.8 the step height $\Delta\sigma_{\mathrm{center}}$ at the center is plotted against the height $\sigma_{\mathrm{CH}}(0)$ of the Kondo resonance at the CH site. As seen, the correlation can be described by a linear fit of the form $\Delta\sigma_{\mathrm{center}} = c * \sigma_{\mathrm{CH}}(0) + b$ with $c = 0.13$ and $b = 0.30\,\mathrm{nS}$. From this linear fit we can conclude that in the absence of the Kondo resonance the step height $\Delta\sigma_{\mathrm{center}}$ must be given by $0.30\,\mathrm{nS}$. This value matches the step height of a single molecule ($\approx 0.34\,\mathrm{nS}$, see Fig. 5.5a). Furthermore, the parameter $c = 0.13$ corresponds to the inelastic cross section of $\approx 12.1\,\%$ for a single molecule (see table 5.3). From these observations, and in particular because of the linear dependence between the step height and the intensity of the Kondo resonance, we conclude that the increase of the inelastic cross section must be directly related to the higher density of states (DOS) at zero bias in the presence of the Kondo effect.

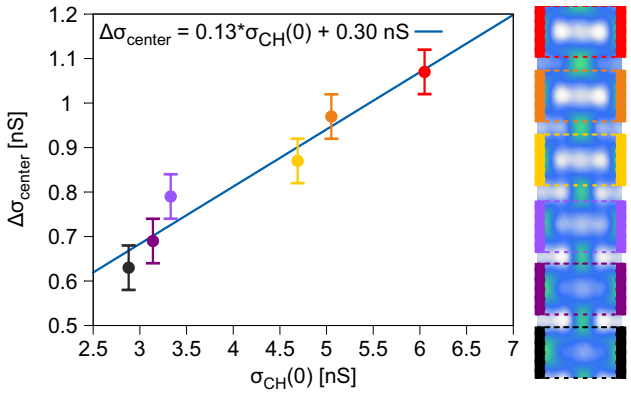

Figure 5.8: Plot of the step height $\Delta\sigma_{\text{center}}$ at the center as a function of the height $\sigma_{\text{CH}}(0)$ of the Kondo resonance at the CH site. The values are obtained from the different molecules in the rippled phase of NTCDA (see Fig. 5.2b and c). Color coding as in Fig. 5.2. Data points have been fitted by a linear function of the form $\Delta\sigma_{\text{center}} = c * \sigma_{\text{CH}}(0) + b$.

Hence, the side peaks can be considered as a reappearance of the Kondo resonance as satellite peaks at finite bias and explained in the simple framework of the Tersoff-Hamann theory by extending it to inelastic electron tunneling (IET). The peak-like shape and the large cross sections are then directly related to inelastic tunneling process: the opening of the inelastic tunneling channel results also in a new *probing channel* for the Kondo resonance as illustrated in Fig. 5.9a for positive bias voltages. A tunneling electron with sufficient energy can excite a molecular vibration with the energy $\hbar\Omega$ and lose this energy. After the energy loss, the electron tunnels into the DOS of the many-body Kondo state. Hence, the Kondo resonance is probed again at the threshold energy of $\hbar\Omega$. But, since the electron can only tunnel into the empty states in the DOS, only half of the Kondo peak is probed at the threshold energy. The same considerations also apply for negative bias voltages and lead to the final dI/dV conductance spectrum which is depicted in Fig. 5.9b: at the threshold energies $\pm\hbar\Omega$ the inelastic tunneling electrons probe half of the Kondo peak, respectively, and lead the occurrence of sharp satellite peaks of the Kondo resonance at the threshold energies. Hence, the increase of the cross section for inelastic tunneling results simply from the fact that in the presence of the Kondo resonance the DOS is much higher at the Fermi level than in the case without the Kondo effect.

Varying values of the inelastic cross section at different locations on a molecule are usually ascribed to the spatial modulation of the wave function due to the vibration, since the inelastic cross section is proportional to the change of the wave function caused by the molecular vibration [132]. But

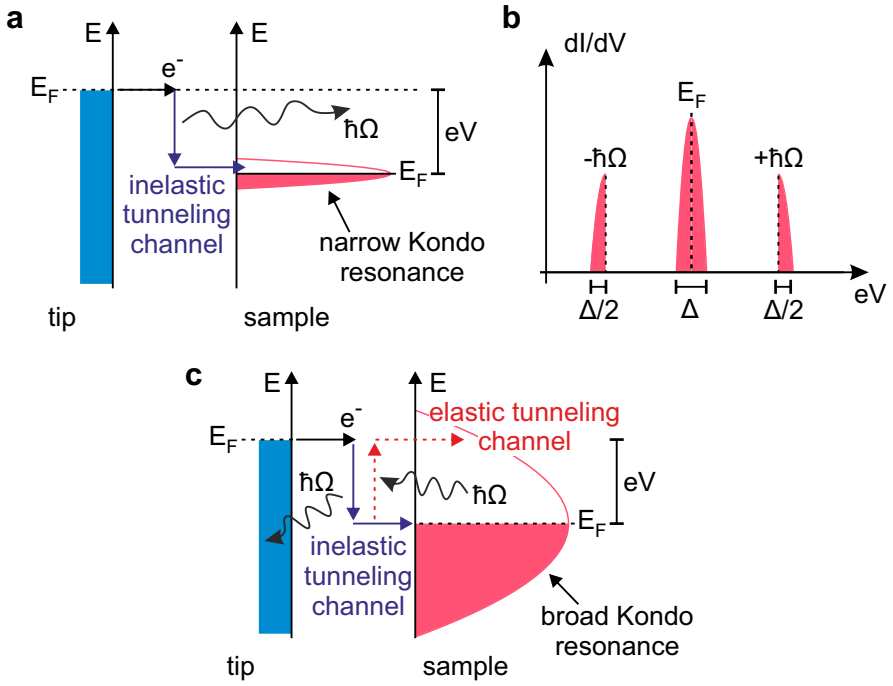

Figure 5.9: **a** Energy diagram for an inelastic tunneling process of an electron in the presence of a narrow Kondo resonance. During the inelastic tunneling process the electron loses its energy and excites a molecular vibration with the energy $\hbar\Omega$. After the energy loss, the electron probes the DOS at the Fermi energy, i.e. in this case the Kondo resonance. **b** Illustration of the final dI/dV conductance spectrum as a result of the processes indicated in panel a. **c** As panel a, but for a broad Kondo resonance. In addition to the inelastic tunneling channel their is an elastic tunneling path for the electrons, where a virtual vibration is excited and readsorbed again. The elastic contribution always counteracts the inelastic contribution.

in our case the different intensities of the side peaks at the CH site and at the center of the NTCDA molecules cannot be explained by a different modulation of the wave function due to the vibration, because for an isolated single NTDCA molecule the inelastic cross section is the same at the CH site and at the center of the molecule (see side peak at $\approx -48\,\mathrm{mV}$ in Fig. 5.5a). Hence, under the assumption that the form of the molecular vibration does not change for the NTCDA molecules in a layer, there should also be no variation in the intensity of the side peaks at different locations on the NTCDA molecules in the well-ordered structures. But, as seen in Fig. 5.1c/d and Fig. 5.2b/c, their is a strong deviation in the intensities of the side peaks at the CH site and at the center of the molecules in the well-ordered structures.

In our case the difference in the intensities of the side peaks at the CH site and at the center of the NTCDA molecules seem to be related to the FWHM of the Kondo resonance. This relation can be seen by comparing the spectra of the bright and rotated molecules (see Fig. 5.6a). In the case of the bright molecule the side peaks are only barely visible at the CH site, whereas for the rotated molecule the intensity of the side peaks is almost equal to the intensities observed in the center of the molecule. One possible explanation for the observed difference between the spectra at the CH site of both molecules could be as follows. In the case of a large FWHM of the Kondo resonance one could imagine that some DOS of the Kondo resonance, i.e. the flanks, extend into the energy range of the molecular vibrations at $\pm\hbar\Omega$. Thus, the electrons can tunnel via elastic tunneling into the DOS of the Kondo resonance at $\pm\hbar\Omega$ or via inelastic tunneling into the DOS at zero bias (see Fig. 5.9c). Note that in this context the term elastic tunneling means that a virtual vibration is excited and then readsorbed again. For a narrow Kondo resonance the situation is entirely different: it has basically no DOS at $\pm\hbar\Omega$, hence the electrons can only tunnel into the Kondo resonance via inelastic tunneling (see Fig. 5.9a). By inference this means that for the broad Kondo resonance the electrons which probe the flanks of the Kondo resonance at $\pm\hbar\Omega$ lead to an additional elastic tunneling channel, whereas for a narrow Kondo resonance the elastic tunneling channel is reduced or even absent. From IET theory it is known that elastic tunneling processes, where a virtual vibration is excited and readsorbed, always counteract inelastic tunneling and thus reduce the total cross section [132] – the sum of the elastic and inelastic contribution. Hence, the apparent reduction of the side peaks can be attributed to the presence of an elastic tunneling channel in the presence of a broad Kondo resonance.

The same considerations also apply for the different locations, i.e. the CH site and the center, of the bright and dark molecule. As described above, at the CH site the electrons have an elastic and inelastic tunneling channel, because of the broad Kondo resonance, and thus the total cross section is reduced. At the center, the Kondo resonance appears as a step-like feature that does not extend into the energy range of the molecular vibrations at $\pm\hbar\Omega$ (see section 5.5). Thus, there is no elastic tunneling channel for the electrons at the center of the molecule and therefore the intensities of the side peaks are not reduced. The strong correlation between the intensities of the side peaks at the center of the molecule and the intensity of the Kondo resonance at the CH site (see Fig.5.8) stems from the fact that the electrons which tunnel via inelastic tunneling probe the DOS of the LUMO, i.e. of the Kondo resonance which is also observable at the CH site.

5.7 Collective behavior?

All the features in the dI/dV conductance spectra, i.e. the spatial variation of the Kondo resonance and the origin of the side peaks, could be explained based on the properties of a single molecule, including quantum interference effects and inelastic tunneling processes. Hence, no clear sign could be observed so far for the presence of collective spin phenomena up to know.

However, besides the already discussed features, we also observed anomalies close the Fermi level, namely a splitting of the Kondo resonance. Note that although we use the word anomaly here all these features could be reproduced by different tips, but not every time. Currently, it is not known on which conditions the appearance of these anomalies depend. However, in Fig. 5.10a such dI/dV spectra of the NTCDA molecules in the rippled phase are shown. As clearly seen, the Kondo resonance appears to be split at the CH site and the center of the molecules. Furthermore, the amount of splitting ΔV is different at the CH site and at the center of the molecules. Interestingly, the splitting ΔV increases at the CH site from bright to dark molecule, whereas at the center the splitting ΔV changes only marginally – one might think that the splitting is slightly decreasing from bright to dark molecule (Fig. 5.10b, values for the splitting ΔV have been obtained by fitting the split Kondo resonance with two Lorentzian functions). The different splitting ΔV at the different locations above the molecule excludes any connection to excitations of molecular vibrations, since the excitation energy of a vibration should not change within a molecule. The same also applies for spin-flip excitations of single molecules.

Nevertheless, there are signs that the splitting ΔV must be related to some kind of spin phenomenon. In Fig. 5.11a dI/dV spectra, which also show anomalies, of the bright and dark molecule in the relaxed phase are shown. First of all it is conspicuous that the splitting ΔV in this case is different from the splittings which we observed for the bright and dark molecules in the rippled phase. They differ partially by more than 10 mV (compare Fig. 5.10b and Fig. 5.11b). Such a behavior was not observed for the side peaks at ± 48 mV – the excitation energy of the molecular vibration changed neither within the molecule nor for the different structures. In Fig. 5.11b the splitting ΔV at different locations on the bright and dark molecule is plotted as function of the external magnetic field B. Note that the splitting at the CH site of the bright molecule is not presented, since it was not possible to extract a splitting for this location (see also Fig. 5.11a). As seen, there is a weak dependence of the splitting ΔV on the magnetic field B: the splittings at the CH site and the center of the dark molecule seem to increase with the magnetic field. For the splitting at the center of the bright molecule it is difficult to make a clear statement: for magnetic fields up $B = 1.5$ T the splitting clearly increases with the magnetic field, but much stronger than in the case of the dark molecule, whereas at $B = 2.0$ T it seems again to

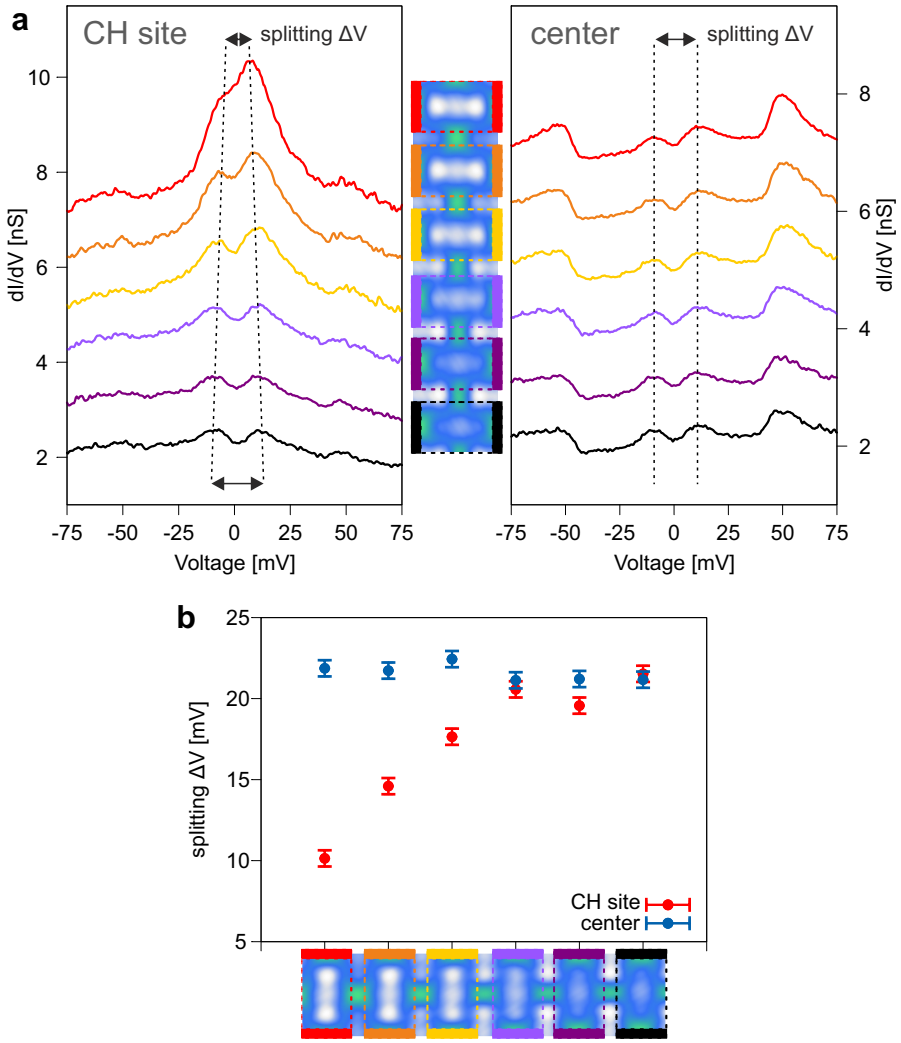

Figure 5.10: **a** dI/dV conductance spectra of the different NTCDA molecules in the rippled phase at $T = 4.3\,\mathrm{K}$. Anomalies at the Fermi level, i.e. a splitting ΔV of the Kondo resonance, is clearly visible. The spectra have been recorded at the CH site (left panel) and at the center (right panel) of the particular molecule. The different colors correspond to the different molecules as indicated by the colored frames around the molecules. Spectra are shifted for clarity. **b** Illustration of the splitting ΔV for the different molecules in the rippled phase.

decrease.

Although, currently it is not possible to explain the exact origin of this splitting, it seems likely that it is related to (complex) spin phenomena and thus might indicate a collective spin behavior in this system. The fact that also the Kondo effect shows some dependence on the intermolecular interactions (see section 5.4) emphasizes the possibility of collective phenomena. However, to reveal the true origin of this splitting more studies of the system are necessary – in particular of the anomalies at different magnetic fields in order to confirm the observations made up to now.

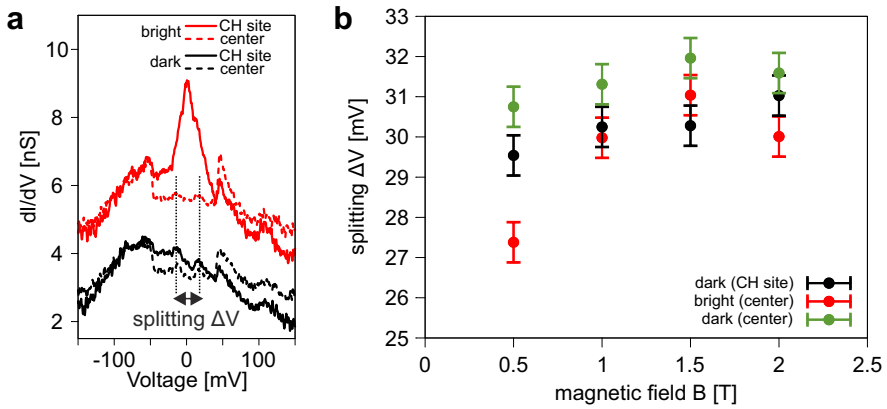

Figure 5.11: **a** dI/dV conductance spectra of the bright and dark molecule in the relaxed phase at $T = 1.2\,\mathrm{K}$. Like in Fig. 5.10 anomalies close the Fermi level are visible. **b** Plot of the splitting ΔV as a function of the external magnetic field B. Data points correspond to the spectra from panel a at different magnetic fields.

5.8 Conclusion

In this chapter we have studied the system NTCDA on Ag(111) and searched for indications of collective spin phenomena on the atomic length scale. By means of scanning tunneling microscopy and spectroscopy we have analyzed the origin of the different features that we observed in the dI/dV conductance spectra.

In particular we have shown that both distinct molecules in the relaxed phase of NTCDA undergo the Kondo effect, but with different Kondo temperatures, by gradually tuning the Kondo effect by lifting experiments with and without an external magnetic field. Furthermore we concluded from the analysis of the electronic properties of the NTCDA in the rippled phase that the different Kondo temperatures originate from the different adsorption sites on the Ag(111) lattice. But, in addition to the effect of the adsorption

site we also demonstrated that intermolecular interactions play also an important role in the formation of the Kondo effect. Spatial variations of the line shape of the Kondo resonance on the NTCDA molecules we linked to quantum interference effects of the wave function of the LUMO. A detailed analysis revealed that the q factor of the Fano line shape decreases from the CH site to the center of the molecule.

Furthermore, we demonstrated that the side peaks primarily originate from molecular vibrations, but that their shape and intensity is also influenced by the Kondo effect. From the linear dependence between the inelastic cross section of the side peaks and the intensity of the Kondo resonance we concluded that the inelastic tunneling channel opens a new probing channel for the Kondo resonance, and that the enhancement of the inelastic cross section is linked to the higher density of states at the Fermi level in the presence of the Kondo effect.

Concluding, we can say that we have shown that most of the observed features in the dI/dV spectra of the NTCDA molecules can be explained by the properties of an individual NTCDA molecule, and that the spatial variations of the intensity and shape of these features result from quantum interference effects – a consequence of the fact that the spin carrying orbital extends over the entire molecule and is spatially modulated. Hence, the spatial properties of the delocalized spins are directly coupled to the spin carrying orbital and cannot be considered separately. Furthermore, indications of intermolecular interactions emphasize the fact that delocalized spins interact more easily with their environment and thus offer the possibility to tune the spin properties by the environment or to couple many spins. In particular this could lead to collective spin phenomena. Interestingly, we also observed anomalies close to the Fermi level which cannot be simply explained by the properties of a single entity, namely that the Kondo resonance appears to be split in some cases. The fact that the splitting reacts on an external magnetic field and that the amount of splitting varies spatially indicate that the anomalies could be related to collective spin phenomena. However, to make an unambiguous statement about the origin of the anomalies further studies are necessary. In particular the behavior of the anomalies in an external magnetic field have to be studied more extensively.

CHAPTER 6

Formation of a spin hybrid

Magnetism, as you recall from physics class, is a powerful force that causes certain items to be attracted to refrigerators. – *Dave Barry*

The results presented in this chapter have been published after the submission of this thesis in the journal **Physical Review B**:

- **T. Esat**, R. Friedrich, F. Matthes, V. Caciuc, N. Atodiresei, S. Blügel, D. E. Bürgler, F. S. Tautz, and C. M. Schneider, "Quantum interference effects in molecular spin hybrids," *Physical Review B*, vol. 95, no. 9, p. 094409, 2017.

6.1 Introduction

In order to design miniaturized spin-based devices, e.g. for data storage, spintronics or quantum computation, the interest in magnetic properties of nanostructures is currently in the focus of research. However, the precise design of magnetic nanostructures is a quite challenging task, since small changes, e.g. in the size, shape and purity, can lead to drastic changes of the magnetic properties, e.g. switching fields.

These problems due to inhomogeneities could be avoided by using single-molecule magnets with large magnetic moments and high magnetic anisotropy, since molecules can be synthesized in large numbers with identical properties. However, at the moment such single-molecule magnets are limited to the operation at cryogenic temperatures, because thermal fluctuations can easily change the magnetization at higher temperatures. Stabilizing the magnetization of a molecule by magnetic exchange coupling to a ferromagnetic building block is one solution for this problem [134, 135]. An alternative solution is to tailor a hybrid molecular magnet from a non-magnetic molecule by spin dependent hybridization. Besides the fact that the electronic and magnetic properties of the molecule are tuned, e.g. by inducing a magnetic moment or other spin-dependent features [136, 137], also the magnetic properties of the underlying ferromagnetic substrate are affected. Such effects can lead to magnetic hardening or softening of the newly formed unit consisting of the chemisorbed molecule and its proximate metal neighbors [136, 138, 139]. Since such new hybrid systems promise unique magnetic functionalities, they are currently studied intensively [140, 141, 136, 142].

The idea of this work is based on the latter approach, namely on the spin-dependent hybridization of a non-magnetic, aromatic molecule on a ferromagnetic surface. Here the key is that the spin-dependent hybridization between the d-states of the ferromagnetic metal and the π-orbitals of the molecule lead to a spin-imbalanced electronic structure of the chemisorbed molecule [143, 144]. Besides the question if it is possible to form such a hybrid molecular magnet, the main focus of this work is placed on the question if it is possible to have different spin-dependent effects, i.e. enhancement and inversion of the spin polarization in comparison to the polarization of the

surrounding ferromagnetic surface, on the same molecule at the same time, e.g. on different aromatic rings. To address this question and to find out if it is possible to tailor a hybrid molecular magnet that exhibits varying spin features for different units, i.e. different aromatic rings, we have decided to use the molecule 2,4,6-triphenyl-1,3,5-triazine or shortly TPT (Fig. 6.1). TPT consists of a central triazine ring and three phenyl groups. Furthermore, it has a three-fold symmetry and is non-magnetic in the gas-phase. For the ferromagnetic building block we haven chosen Co islands on Cu(111), since this system has already been studied in detail and because it is known that its spin polarization is spatially modulated [145]. This makes the Co islands an ideal system to investigate the spin-dependent hybridization and in particular to study the possibility to make a hybrid molecular magnet that exhibits varying spin features for different units. The study was carried out by means of (SP-)STM/STS and was supported by *ab initio* calculations performed by Rico Friedrich, Vasile Caciuc, Nicolae Atodiresei and Stefan Blügel from the Forschungszentrum Jülich (Peter Grünberg Institute and Institute for Advanced Simulation).

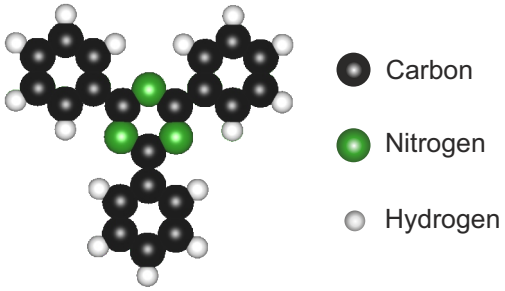

Figure 6.1: Graphical representation of the 2,4,6-triphenyl-1,3,5-triazine (TPT) molecule in the gas-phase.

6.2 Spin-dependent hybridization of molecules

Before we dedicate ourselves to the experimental study of TPT molecules adsorbed on Co islands, we briefly introduce the main idea of hybrid molecular magnets, namely the spin-dependent hybridization of molecules on ferromagnetic surfaces. However, a detailed discussion of adsorption phenomena of molecules on conducting surfaces is beyond the scope of this thesis. Thus, the spin-dependent hybridization of molecules on ferromagnetic surfaces will be discussed based on a simple model according to the presentation of Galbiati et al. [137].

Bringing a molecule, which has discrete levels in the gas-phase, in proximity of a metal surface leads to a coupling of the initially discrete molecular levels to the quasi-continuous band of states of the metal surface. This hybridization of the molecular levels has in general two main consequences [146]:

1. The lifetime τ of a molecular level is no longer infinite, since there is some probability of escaping to the metal surface. Thus, the molecular energy level gets broadened. The width of the broadened molecular level can be described by $\Gamma \approx \hbar/\tau$.

2. The interaction with the metal surface furthermore leads to an energy shift of the molecular level from the gas-phase value ϵ_0 to ϵ_{eff} (effective molecular level).

In the case of a ferromagnetic metal the DOS of the two spin directions, i.e. the spin-up ($\uparrow$) and spin-down ($\downarrow$), are different, as already mentioned in section 2.1.1. The model by Barraud et al. [147] predicts that this spin imbalance is also reflected in the molecule after adsorption on the ferromagnetic surface. Thus, the broadening and energy shifting of the molecular levels becomes spin-dependent. That implies that an initially spin-degenerate molecular level becomes spin split, i.e. it exhibits two different energies $\epsilon_{\text{eff}}^{\uparrow} \neq \epsilon_{\text{eff}}^{\downarrow}$ and widths $\Gamma^{\uparrow} \neq \Gamma_{\downarrow}$ for the two spin channels after the hybridization with the ferromagnetic surface. This induced spin polarization strongly depends on the coupling strength between the ferromagnetic surface and the molecule. In a simple framework the spin-dependent broadening of the molecular level can be expressed by

$$\Gamma^{\uparrow(\downarrow)}(E) = 2\pi \sum_i |V_i^{\uparrow(\downarrow)}|^2 \delta(E_i - E), \tag{6.1}$$

where $V_i^{\uparrow(\downarrow)}$ denotes the spin-dependent hybridization between the state i of the ferromagnetic metal and the discrete molecular level. The hybridized system consisting of the ferromagnetic surface and the molecule is referred to as hybrid molecular magnet.

In order to demonstrate the possibilities of tailoring the spin properties of the hybrid molecular magnet we will focus on two extreme cases that represent the limits of strong and weak hybridization between the ferromagnetic surface and the molecule [147]. For simplicity, we consider a constant hybridization $V_i^{\uparrow(\downarrow)} = V$ between the ferromagnetic surface and the molecule. Note that in a more realistic picture the hybridization strongly depends on the wave-function overlap between surface and molecular states. However, in this simplified case of constant hybridization the spin-dependent broadening of the molecular level is directly proportional to the DOS $D_{\mathrm{FM}}^{\uparrow(\downarrow)}$ of the ferromagnetic metal: $\Gamma^{\uparrow(\downarrow)}(E) \propto D_{\mathrm{FM}}^{\uparrow(\downarrow)}(E)$. The effects of the hybridization on the molecule, namely the spin-dependent broadening and shifting of the molecular level, can be characterized by a Lorentzian distribution in the simplest scenario. Then, the DOS $D_{\mathrm{Hybrid}}^{\uparrow(\downarrow)}(E)$ of the hybrid molecular magnet can be expressed by [147]

$$D_{\mathrm{Hybrid}}^{\uparrow(\downarrow)}(E) = \frac{\Gamma^{\uparrow(\downarrow)}/2\pi}{(E - \epsilon_{\mathrm{eff}}^{\uparrow(\downarrow)})^2 + (\Gamma^{\uparrow(\downarrow)}/2)^2}. \tag{6.2}$$

Note that the influence of the ferromagnetic surface is encoded in the parameters $\epsilon_{\mathrm{eff}}^{\uparrow(\downarrow)}$ and $\Gamma^{\uparrow(\downarrow)}$. According to section 2.1.1 the spin polarization of the hybrid molecular magnet at a certain energy E is defined by

$$P_{\mathrm{Hybrid}}(E) = \frac{D_{\mathrm{Hybrid}}^{\uparrow}(E) - D_{\mathrm{Hybrid}}^{\downarrow}(E)}{D_{\mathrm{Hybrid}}^{\uparrow}(E) + D_{\mathrm{Hybrid}}^{\downarrow}(E)} \tag{6.3}$$

and thus can be strongly modulated by the parameters $\epsilon_{\mathrm{eff}}^{\uparrow(\downarrow)}$ and $\Gamma^{\uparrow(\downarrow)}$. For example, the spin polarization $P_{\mathrm{Hybrid}}(E)$ of the hybrid molecular magnet can be inverted ($P_{\mathrm{Hybrid}}(E) = -P_{\mathrm{FM}}(E)$) or enhanced ($P_{\mathrm{Hybrid}}(E) > P_{\mathrm{FM}}(E)$) in some energy intervals in comparison to the spin polarization $P_{\mathrm{FM}}(E)$ of the bare ferromagnetic surface.

In Fig. 6.2a an example for the inversion of the spin polarization of the hybrid molecular magnet at the Fermi energy E_{F} is shown. This scenario corresponds to a strong metal-molecule interaction. For the strong coupling scenario the effect of the hybridization yields a large broadening of the molecular level. Thus, we encounter the situation $\Gamma^{\uparrow(\downarrow)} \gg \Delta E^{\uparrow(\downarrow)}$ with $\Delta E^{\uparrow(\downarrow)} = E_{\mathrm{F}} - \epsilon_{\mathrm{eff}}^{\uparrow(\downarrow)}$ in this limit. Hence, eq. (6.2) can be approximated by $D_{\mathrm{Hybrid}}^{\uparrow(\downarrow)}(E_{\mathrm{F}}) \approx 2/(\pi\Gamma^{\uparrow(\downarrow)}(E_{\mathrm{F}})) \propto 1/D_{\mathrm{FM}}^{\uparrow(\downarrow)}(E_{\mathrm{F}})$. According to eq. (6.3) the spin polarization of the hybrid molecular magnet is then approximated by

$$P_{\mathrm{Hybrid}}(E_{\mathrm{F}}) \approx -\frac{\Gamma^{\uparrow}(E_{\mathrm{F}}) - \Gamma^{\downarrow}(E_{\mathrm{F}})}{\Gamma^{\uparrow}(E_{\mathrm{F}}) + \Gamma^{\downarrow}(E_{\mathrm{F}})} \propto -\underbrace{\frac{D_{\mathrm{FM}}^{\uparrow}(E_{\mathrm{F}}) - D_{\mathrm{FM}}^{\downarrow}(E_{\mathrm{F}})}{D_{\mathrm{FM}}^{\uparrow}(E_{\mathrm{F}}) + D_{\mathrm{FM}}^{\downarrow}(E_{\mathrm{F}})}}_{P_{\mathrm{FM}}(E_{\mathrm{F}})}. \tag{6.4}$$

Hence, the spin polarization $P_{\mathrm{Hybrid}}(E_{\mathrm{F}})$ of the hybrid molecular magnet is opposite to the polarization $P_{\mathrm{FM}}(E_{\mathrm{F}})$ of the original ferromagnetic surface at the Fermi level.

An example for the possible enhancement of the spin polarization of the hybrid molecular magnet at the Fermi energy E_{F} is shown in Fig. 6.2b. This case corresponds to a weak metal-molecule interaction, i.e. the broadening and the shift of the molecular level is small. Thus, we have the situation $\Gamma^{\uparrow(\downarrow)} \ll \Delta E^{\uparrow(\downarrow)}$ here. The DOS of the hybrid molecular magnet then can be approximated by $D^{\uparrow(\downarrow)}_{\mathrm{Hybrid}}(E_{\mathrm{F}}) \approx \Gamma^{\uparrow(\downarrow)}(E_{\mathrm{F}})/(\Delta E^{\uparrow(\downarrow)})^2 \propto D^{\uparrow(\downarrow)}_{\mathrm{FM}}(E_{\mathrm{F}})/(\Delta E^{\uparrow(\downarrow)})^2$. Hence, we can obtain an enhancement of the spin polarization when the more (less) broadened spin channel of the molecule is closer (further away) from the Fermi level, as illustrated in Fig. 6.2b. However, if an enhancement or just the same polarization as the ferromagnetic surface is obtained, depends strongly on the parameters $\epsilon^{\uparrow(\downarrow)}_{\mathrm{eff}}$ and $\Gamma^{\uparrow(\downarrow)}$.

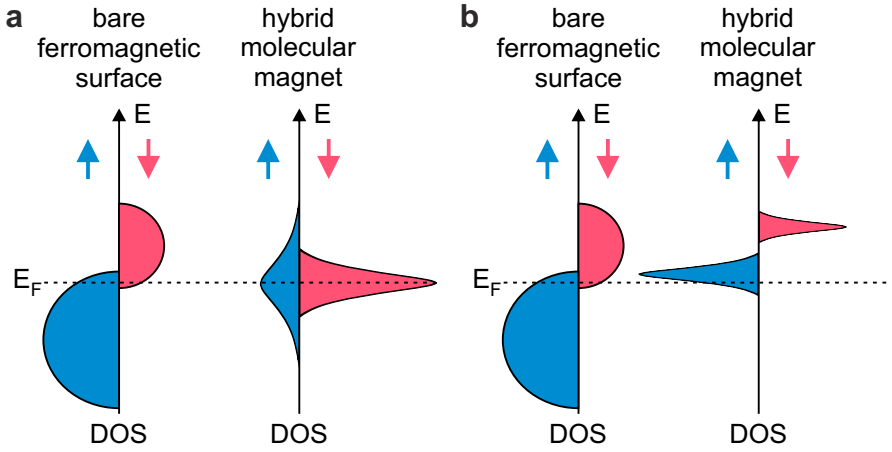

Figure 6.2: **a** For a strong hybridization the spin polarization of the hybrid molecular magnet is inverted in comparison to the spin polarization of the bare ferromagnetic surface, because of $D^{\uparrow(\downarrow)}_{\mathrm{Hybrid}}(E_{\mathrm{F}}) \propto 1/D^{\uparrow(\downarrow)}_{\mathrm{FM}}(E_{\mathrm{F}})$. **b** In the case of weak coupling the spin polarization of the hybrid molecular magnet is proportional to the spin polarization of the bare ferromagnetic surface. Depending on the exact broadening and shift of the molecular levels the spin polarization of the hybrid molecular magnet can be enhanced in comparison to the bare ferromagnetic surface. Illustrations adapted from Ref. [137].

6.3 Sample and magnetic tip preparation

All measurements in this chapter have been carried out in the commercially available Specs JT-STM at a base temperature of $T = 4.3\,\mathrm{K}$ and magnetic fields up to $3\,\mathrm{T}$ (out-of-plane) in ultra-high vacuum (UHV) conditions.

The Cu(111) crystal was prepared by repeated cycles of Ar^+ sputtering and subsequent annealing to 700 K for 10 minutes. In the next step a submonolayer amount of Co ($\lesssim 0.4$ monolayers (ML)) was deposited at a rate of ≈ 0.2 ML/min from a rod by electron bombardment heating onto the clean Cu(111) surface held at room temperature. This preparation procedure leads to the formation of triangular and double layer Co islands of varying sizes [148, 149]. In order to minimize contaminations and also intermixing of the Co islands with the Cu atoms from the Cu(111) surface the sample was directly transferred into the STM [150]. The electronic and magnetic properties of the Co islands were checked by SP-STM before the deposition of the TPT molecules. The TPT molecules were sublimated from a home-built Knudsen cell (deposition temperature approximately 415 K) onto the precooled sample ($\lesssim 70$ K) to reduce the mobility of the adsorbed molecules. The coverage with TPT molecules was chosen such that less than four TPT molecules adsorbed per Co island. The pressure during the deposition of Co and the TPT molecules did not exceed 2×10^{-10} mbar.

In order to investigate also the magnetic properties of the sample a spin-sensitive tip is needed. Besides the obvious choice of ferromagnetic materials for the fabrication of the tips [151, 152, 153], also antiferromagnetic materials can be used [154, 155, 156]. Although antiferromagnetic materials do not show a net magnetization, tips fabricated from of these materials can be used for spin sensitive measurements, since the tunneling process in STM occurs mainly through a single atom at the tip apex – which has a certain spin polarization in an antiferromagnetic tip. But also uncompensated spins at the apex of an antiferromagnetic tip can lead to spin sensitivity. Antiferromagnetic materials have also the advantage that they only exhibit weak stray fields and an influence of the tip on the investigated magnetic structures can therefore be excluded, making them more suitable for small and sensitive structures. For this reason we have used bulk Cr tips for our spin sensitive measurements. Note that besides the use of bulk materials it is also possible to coat non-magnetic STM tips with (anti)ferromagnetic materials [157, 158, 159, 27].

The Cr tips have been fabricated by electrochemical etching of polycrystalline Cr rods in 5 M NaOH. The Cr rods have been obtained from a 99.95 % Cr foil. Before making use of the electrochemically etched bulk Cr tips they have been cleaned *ex situ* in distilled water and isopropanol and furthermore in UHV by electron bombardment heating (1 kV, 2.6 mA, 30 s) to remove the remaining oxides. Although it is known that the apex of the tip is likely spin-polarized, the direction of the magnetization, its strength and also the response to an external magnetic field are usually unknown. Indeed, not all fabricated Cr tips showed the desired properties (high out-of-plane sensitivity) in the first instance. Therefore, the Cr tips have also been treated *in-situ* by applying short voltage pulses ($4 - 10$ V, 10 ms) between the STM tip and sample in order to obtain appropriate magnetic tips.

The magnetic sensitivity of the Cr tips has been checked by spectroscopic imaging of clean Co islands at different magnetic fields.

Differential conductance dI/dV spectra have been acquired using conventional lock-in technique with the feedback loop switched off. Parameters at the stabilization point before switching off the feedback loop were bias voltage $V = -200\,\mathrm{mV}$ and tunneling current $I = 200\,\mathrm{pA}$. Spectroscopic images of the first derivative dI/dV have been measured simultaneously with constant current images also using the conventional lock-in technique. The typical parameters were a modulation amplitude of 10 mV with a modulation frequency of 801 Hz. To ensure a featureless DOS of the tip, we measured reference spectra on the clean Cu(111) surface before starting measurements on the Co islands and TPT molecules. All differential conductance spectra which are shown in this chapter have been averaged over two measurements, one being a forward, the other a backward sweep of the bias voltage.

6.4 Co islands on Cu(111)

In this section the main properties of the Co island are only briefly introduced, since the growth, electronic and magnetic properties of this system have already been intensively investigated before [160, 161, 162, 163, 159, 145, 164, 165, 166, 167].

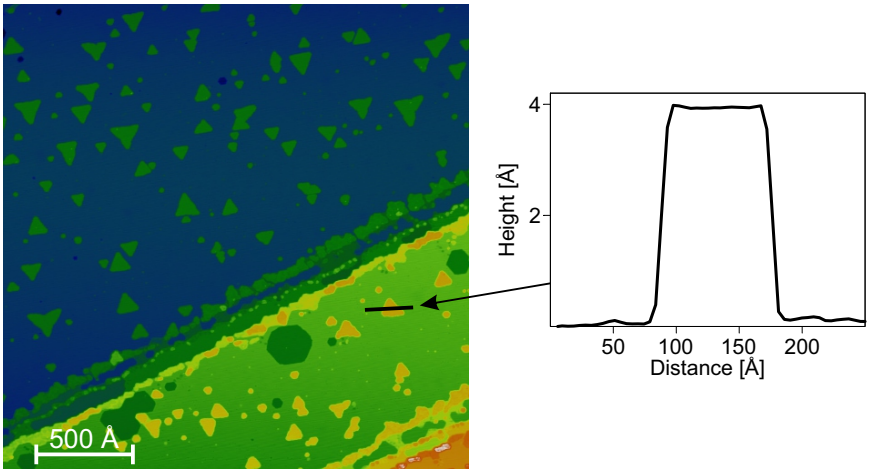

Figure 6.3: Constant current STM image of Co islands grown on Cu(111) ($V = 500\,\mathrm{mV}$, $I = 200\,\mathrm{pA}$). The Co islands show the typical triangular shape. One can clearly distinguish between two differently oriented Co islands (rotated by 60° with respect to each other). The black line in the STM image indicates the position of the line scan which reveals the typical bilayer height of the Co islands.

In Fig. 6.3 an STM overview image of Co islands on the Cu(111) surface is shown. The sample has been prepared according to the procedure described in section 6.3. As clearly seen from Fig. 6.3 most of the Co islands show the typical triangular shape, although there are some deviations from the perfect triangular shape, like the blunt corners and irregularities at the edges of the islands. The height of the Co islands is approximately 3.9 Å, corresponding to the typical bilayer height. Furthermore, it is readily identifiable that the Co islands have two different orientations on the Cu(111) surface which are rotated by 60° with respect to each other. The reason for the two different orientations stems from different layer stackings of the bilayer Co islands. The first Co layer can adsorb either on fcc or on hcp sites of the Cu(111) surface, while in both cases the edges of the Co islands form {100} microfacets with the Cu(111) surface [149]. The second Co layer has no preferred crystallographic orientation [149]. Consequently, the bilayer Co islands can have four different layer stackings and two orientations, which are rotated by 60° with respect to each other, on the Cu(111) surface as illustrated in Fig. 6.4. Since the Cu(111) substrate follows an fcc stacking with a ABCABCABC sequence, the Co islands can be classified as fcc (unfaulted) or hcp (faulted) regarding the stacking of the first Co layer with respect to the stacking of the substrate (see Fig. 6.4). Negulyaev et al. have also shown that the formation of fcc (unfaulted) Co islands is more likely compared to the formation of hcp (faulted) islands [149]. The relative probability is given by approximately 3:2 (fcc to hcp). Based on this knowledge we have also identified the studied Co islands as fcc (unfaulted) or hcp (faulted) from statistical analysis of many Co islands.

A typical dI/dV conductance spectrum which has been acquired in the center of a Co island is shown in Fig. 6.5a. The spectrum shows a sharp peak at approximately $-330\,\mathrm{mV}$, which corresponds to the spin-polarized d-like surface state of Co [163]. The broad peak at $\approx +310\,\mathrm{mV}$ corresponds also to a spin-polarized d-like surface state [163, 169]. Furthermore, a free electron-like sp surface state which is not directly visible in the differential conductance spectra, because it is not a localized peak but smeared out over a broad energy range, can be visualized by measuring spectroscopic images. This is illustrated in Fig. 6.5b, where a quantum inference pattern is clearly visible due to the scattering of the sp electron waves at the boundaries of the Co island. This quantum confinement gives rise to the observed standing waves. The d-like surface state is not influenced by the electron confinement because of its energetically and spatially localized nature [170]. Note that the difference of electrons with opposite spin in the DOS at a certain energy (see inset in Fig. 6.5a), and the spatially modulated DOS of the sp surface state leads to a spatially modulated spin polarization of the Co islands [145]. This spatial modulation of the spin polarization is the key for understanding the magnetic properties of the TPT molecules in section 6.7 and will be discussed there in more detail.

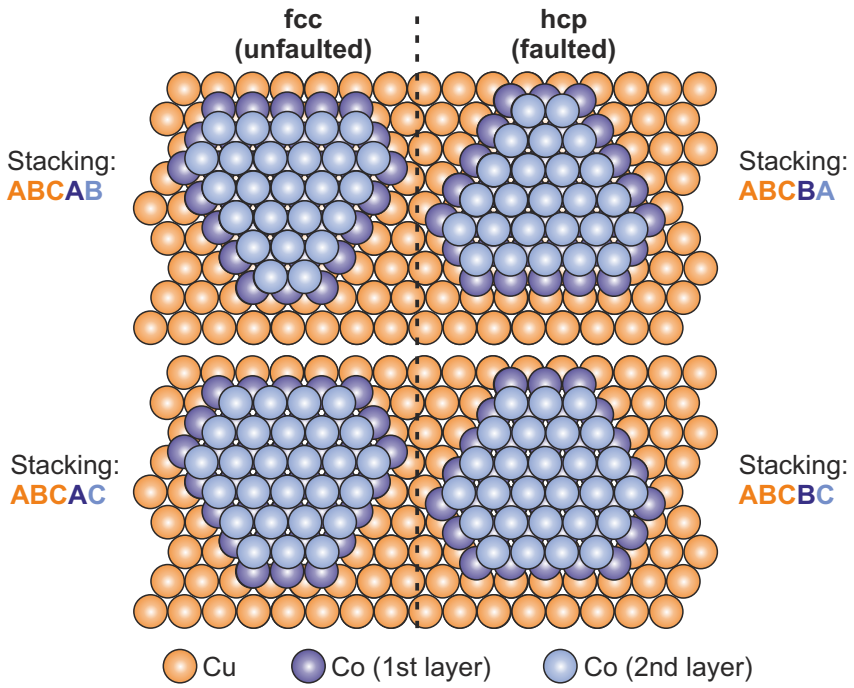

Figure 6.4: Illustration of the different stackings of the Co islands on Cu(111) using the hard sphere model. The adsorption of Co atoms on fcc or hcp sites of the Cu(111) surface leads to the formation of fcc (unfaulted) or hcp (faulted) Co islands, respectively. Model has been adapted from [149, 168].

The electronic properties show no significant difference for faulted and unfaulted Co islands. Only the d-like surface state shifts slightly in energy ($< 50\,\mathrm{mV}$) for differently oriented Co island as well for different island sizes [164]. These small variations on the Co island necessitate that the spin-polarized measurements, namely for parallel and anti-parallel configuration, must always be carried out on the same molecule, because otherwise the data is not comparable. Furthermore, it is important to note that the Co islands show inhomogeneities at the edges regarding their electronic properties [161]. They have to be taken into account if TPT molecules close to the edges are investigated.

Before we start looking at TPT molecules adsorbed on the Co islands we have to check the magnetic properties of the Co islands. The Co islands exhibit an out-of-plane magnetization (parallel to the surface normal) and can be switched by an external magnetic field. Hence, the easiest way to check the magnetization of the Co islands is to measure the dI/dV signal, e.g. by spectroscopic imaging, for a fixed bias voltage at different magnetic fields applied in the out-of-plane direction. Since the spin-polarized current and therefore also the differential conductance depends strongly on the relative

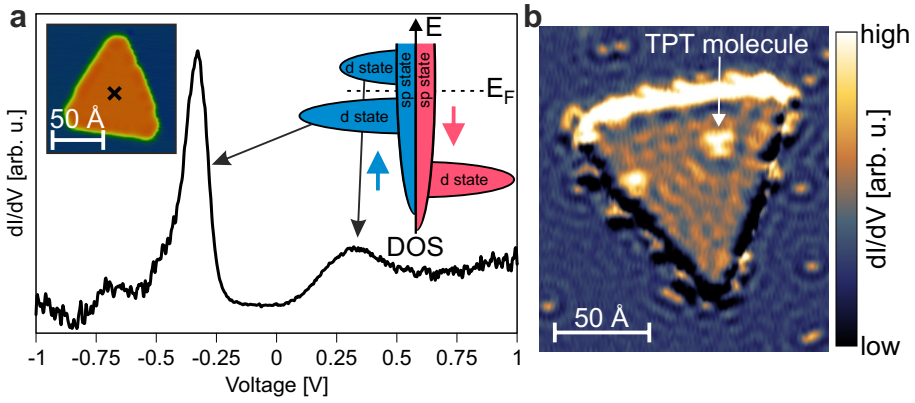

Figure 6.5: **a** Differential conductance dI/dV spectra acquired in the center of a Co island. For the measurement a non-magnetic tungsten tip has been used. Left inset shows the STM image of the corresponding Co island with the marked spectroscopy location ($V = 500\,\mathrm{mV}$, $I = 200\,\mathrm{pA}$). Right inset illustrates the spin-polarized density of states (DOS) of Co islands according to Ref. [163, 169]. **b** Spectroscopic image of a Co island at $V = +690\,\mathrm{mV}$. The spatially modulated pattern is a result of the sp electron confinement in the Co island. A detailed analysis of the adsorption of the TPT molecules is presented in section 6.5.

orientation of the magnetization directions of the Co islands and the tip, a change in the magnetization should be immediately visible in the dI/dV signal, e.g. by a change in the contrast in the spectroscopic images. Thus, we have taken spectroscopic images of Co islands with a bulk Cr tip at different magnetic fields. The results are shown in Fig. 6.6. At a magnetic field of $B = -1.5\,\mathrm{T}$ all Co islands have the same color. By changing the magnetic field to $B = +0.5\,\mathrm{T}$ the contrast of the Co islands (except one) is inverted from bright to dark. With further increase of the magnetic field first one Co island changes its contrast from dark to bright ($B = +1.5\,\mathrm{T}$) and finally at $B = +2.0\,\mathrm{T}$ all Co islands appear bright again. The same behavior is observed when the magnetic field is reversed. From these observation we can conclude that the magnetization of the tip and the Co islands must be changing due to the external magnetic field, because otherwise only one change in the contrast would be excepted for the identical Co island. From previous studies it is known that the Co islands switch in magnetic fields between $B = \pm 0.5\,\mathrm{T}$ and $B = \pm 2.5\,\mathrm{T}$ depending on their size [160, 162, 166]. We can therefore conclude that the first contrast change at $B = +0.5\,\mathrm{T}$ is due the magnetization reversal of the tip. Such a behavior of bulk Cr tips has been also observed in previous studies and explained by uncompensated spins which are sensitive to the external magnetic field [162]. All bulk Cr tips that have been used in this work showed similar behavior.

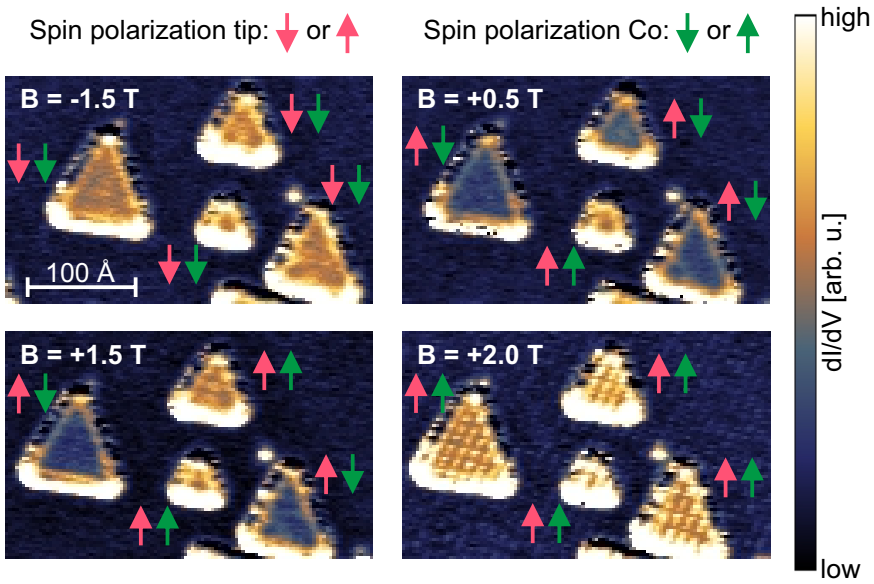

Figure 6.6: Spectroscopic images of Co islands on Cu(111) at different external magnetic fields B measured with a spin-polarized bulk Cr tip ($V = -500\,\mathrm{mV}$, $I = 1\,\mathrm{nA}$). Changes in the contrast correspond to the magnetization reversal of the tip ($B = +0.5\,\mathrm{T}$) or the Co islands ($B \geq +0.5\,\mathrm{T}$). The arrows next to the Co islands indicate the spin polarization of the tip and the particular Co island, respectively. The pattern in the spectroscopic image for $B = +2.0\,\mathrm{T}$ is due to noise and not related to the standing waves within the Co island.

6.5 Adsorption of TPT on Co islands

Having investigated the properties of bare Co islands, TPT molecules have been deposited on the same sample at low temperatures (see also section 6.3). Note that for the studies in this section a non-magnetic tungsten tip has been used. Fig. 6.7 shows an STM image of a Co island after the adsorption of the molecules. The TPT molecules can be clearly identified by their shape which resembles the structure of the gas-phase molecule. This is emphasized by the overlaid graphical representation of the TPT molecule in the inset of Fig. 6.7. Fragments of the molecules are barely found, which indicates that most of the molecules stay intact after adsorption on the Co islands. Only at the edges of the Co islands impurities are observed, which are assumed to be fragments of the TPT molecule, since their shapes and sizes coincide with the phenyl rings of the intact molecules.

An analysis of many adsorbed TPT molecules reveals two preferred adsorption orientations on the Co islands (also recognizable in Fig. 6.7), which is reasonable if we consider the symmetries of the Co island and the TPT

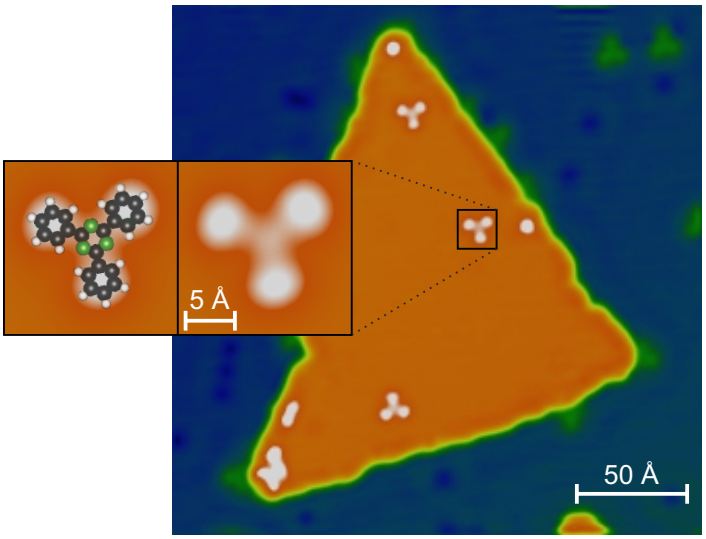

Figure 6.7: Constant current STM image of a Co islands grown on Cu(111) after the deposition of the molecule TPT ($V = -200\,\mathrm{mV}$, $I = 200\,\mathrm{pA}$). The magnified STM image of a TPT molecule has been overlaid with a graphical representation of the gas-phase TPT molecule for reasons of illustration (inset).

molecule. Due to the six-fold rotational symmetry of the Co islands we should expect 6 different adsorption geometries at first glance, but since the TPT molecule has a three-fold symmetry, the 6 adsorptions geometries are three-fold degenerate, thus leading to 2 different adsorption orientations.

To determine the exact adsorption position of the TPT molecules on the Co islands we have recorded STM images with atomic resolution. Since it is difficult to resolve the atomic structure of the Co islands with a bare metal tip in the presence of adsorbed TPT molecules without causing too much interaction, we have made use of a functionalized tip. From other works it is known that functionalized tips can show unmatched spatial resolution [172, 173, 174, 174, 175, 176, 177, 178]. Thus, we have picked up CO molecules from the Cu(111) surface and imaged a TPT molecule and the underlying Co island with atomic resolution by coming closer to the surface (Fig. 6.8a and b). Interestingly, we found that by coming closer to the surface the TPT molecule appears much smaller than in reality [1]. This can be clearly seen in Fig. 6.8a, which shows the same area for two different tip-

[1]Note that this effect only occurred for the functionalized tip and is most probably related to the peculiarities of this imaging mode. Since the CO molecule is not stiff on the tip, but has some degrees of freedom to move without breaking the CO-tip bond, the most probable explanation is that the CO molecule bends at closer tip-surface distances due to the stronger interaction with the TPT molecule. This bending then results in a distortion of the measured TPT molecule.

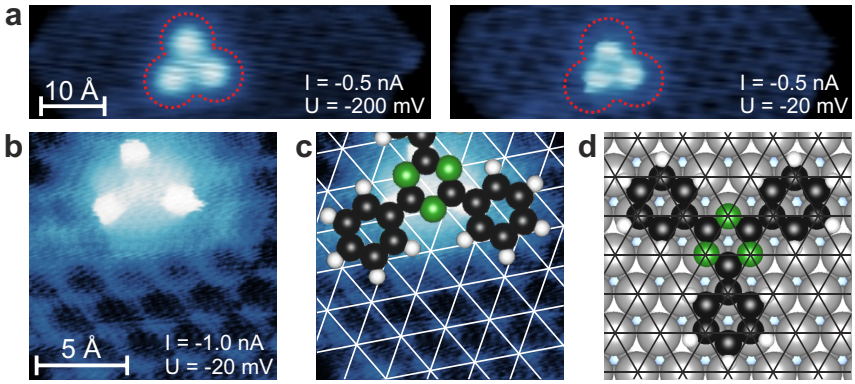

Figure 6.8: **a** Constant current STM images of a TPT molecule adsorbed on a fcc (unfaulted) Co island grown on Cu(111) for different tip-sample distanctes obtained with a CO functionalized tip. Already for small currents the atomic structure of the Co island is somewhat visible (left panel). For a smaller bias voltage (right panel), i.e. for a smaller tip-sample distance, the TPT molecule appears smaller compared to the left panel as indicated by the dotted red contour. **b** As panel a, but for even smaller tip-sample distance. The real size of the TPT molecule is actually given by the blurred blue cloud. Atomic lattice of Co(111) is clearly visible. **c** STM image of panel b overlaid with the atomic structure of the Co island and the structure of the gas-phase TPT molecule. **d** Calculated adsorption geometry of TPT on 2Co/5Cu. Taken from Friedrich et al. [171].

sample distances. With decreasing tip-sample distance this effect becomes even more pronounced and the real size of the molecule is actually given by the blurred cloud which surrounds the bright center of the molecule. In Fig. 6.8b the atomic structure of the Co(111) surface is clearly seen. Note that the TPT molecule seems to be even smaller than in Fig. 6.8a. The real size is again given by the blurred cloud. By overlaying the atomic lattice of the Co island and the structure of the gas-phase TPT molecule we can precisely identify the adsorption position of TPT (Fig. 6.8c): the nitrogen atoms of the triazine ring adsorb on top of the Co atoms, leading to a symmetric adsorption geometry for all phenyl rings and thus to two distinguishable orientations on the Co islands. Note that the adsorption geometry was only experimentally determined for a TPT molecule adsorbed on a fcc (unfaulted) type Co island. Nevertheless, we can assume that this adsorption site remains also valid for hcp (faulted) type Co islands, since all types of islands, i.e. with different stackings, exhibit the same symmetry (see Fig. 6.4) and electronic properties at the surface.

Our finding is also confirmed by the DFT+vdW calculations performed by Friedrich et al., as they find the highest binding energy (3.55 eV) for the experimentally observed adsorption geometry [171]. As seen from Fig. 6.8d

the calculated adsorption geometry is in excellent agreement with the experimental one. For reasons of simplicity the DFT+vdW calculations have been only carried out for a fcc type stacking of the Co.

This good agreement of the adsorption geometry forms the basis for the comparison of the electronic and also magnetic properties between experiment and theory in the next sections.

6.6 Electronic properties of TPT on Co islands

An important prerequisite for the formation of a hybrid molecular magnet (see also section 6.2) is the hybridization with the ferromagnetic building block, i.e. in this case with the Co island. Thus, we have to investigate the electronic properties of the adsorbed TPT molecules in order to check if this precondition is fulfilled. For this purpose we have measured differential conductance spectra at different locations on the molecule, namely on the triazine and phenyl rings. Note that for the studies in this section a non-magnetic tungsten tip has been used. Fig. 6.9a shows typical dI/dV spectra which reveal the main electronic features that we have observed during our measurements on different TPT molecules and also for different tips. Besides minor differences, all spectra show the same features, namely three peaks located at approximately $-340\,\mathrm{mV}$, $+170\,\mathrm{mV}$ and $+600\,\mathrm{mV}$. Note that the peak at $-340\,\mathrm{mV}$ is just located in the same energy region as the d-like surface state of the Co (compare with Fig. 6.5a). This, and also the fact that only broad features are observed, leads to the conclusion that the molecule is strongly hybridized with the Co island, thus fulfilling the basic requirement for a hybrid molecular magnet.

The slightly different electronic properties of the phenyl rings at higher energies, mainly above $V = +700\,\mathrm{mV}$, seems surprising at first glance, since the adsorption site is identical for all phenyl rings, as our analysis of the adsorption geometry in section 6.5 reveals. But if we take into account the presence of the standing waves due to the electron confinement of the sp electrons, then the most probable explanation for the small deviations is that they are related to the spatial modulation of the sp surface state. This seems reasonable, since the periodicity of standing waves at this energy is of the order of 10 Å (see Fig. 6.5b) and thus comparable with the size of the molecule. These small deviations on the different rings emphasize why it is important to carry out the spin-polarized measurements for different spin configurations between tip and sample on the same molecule.

Based on the estimated adsorption geometry (section 6.5) Friedrich et al. also calculated the projected density of states (PDOS) for an adsorbed TPT molecule. The surface was modeled by seven atomic layers (2 Co and 5 Cu) with fcc stacking and periodic boundary conditions, which means that effects related to the quantum confinement of the electrons are neglected in

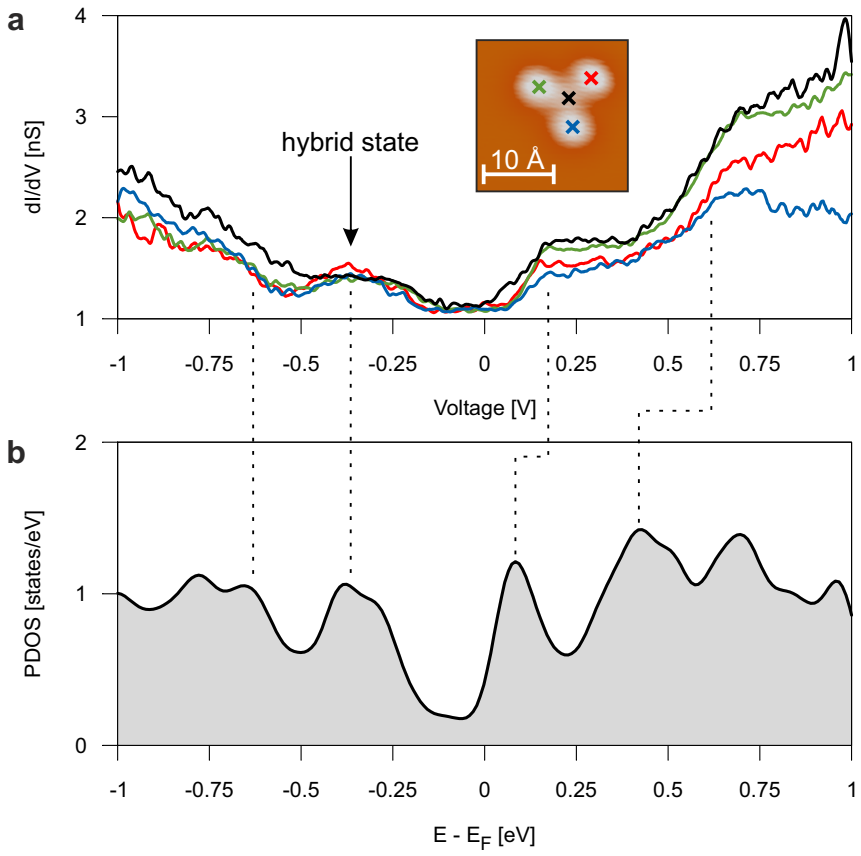

Figure 6.9: **a** Differential conductance dI/dV spectra acquired on the different aromatic rings of the TPT molecule. For the measurement a non-magnetic tungsten tip has been used. Inset shows the STM image of the corresponding TPT molecule with the marked spectroscopy locations ($V = -200\,\mathrm{mV}$, $I = 200\,\mathrm{pA}$). **b** Projected density of states (PDOS) of the TPT molecule adsorbed on 2Co/5Cu. Taken from Friedrich et al. [171].

the calculations. The preliminary results [2] are shown in Fig. 6.9b and are in good agreement with the experimental spectra (compare with Fig. 6.9a). A peak at $-340\,\mathrm{mV}$ can be clearly identified. This demonstrates that the peak at $-340\,\mathrm{mV}$ in the experimental spectra (see Fig. 6.9a) is not just the d-like surface state, measured through the TPT molecule, but a manifestation of a new molecular state due to the hybridization with the Co island. Also, a peak close to the Fermi level is recognizable and can be associated to the peak at $+170\,\mathrm{mV}$ in the experimental data. Furthermore, the gap-like structure close the the Fermi level is reproduced. The states at energies

[2] The theoretical results still need to be checked for the influence of an on-site Coulomb U in the DFT+U approach, as several previous studies revealed its importance for Co based systems [141, 179, 180, 171].

$> +500\,\text{meV}$ and $< -500\,\text{meV}$ are not clearly resolved in the experimental data, which might be due to shorter decay lengths of the states into the vacuum, since these effects are not considered in the PDOS. Although these are preliminary results and have to be treated with caution, the agreement with the experiment is good.

The strongest spin-dependent effect is expected to appear for the peak at $-340\,\text{mV}$, since this state is most probably hybridized with the spin-polarized d-like surface state of the Co island which exhibits the strongest spin polarization [160, 181]. For simplicity, this peak will be called hybrid state in the following. Note that we do not observe major differences between TPT molecules which are adsorbed on fcc (unfaulted) or hcp (faulted) Co islands, respectively. The only difference is that the position of the hybrid state shifted slightly ($< 50\,\text{mV}$), which correlates with the shift of the d-like surface state of Co [164].

6.7 Magnetic properties of the hybrid system

Having investigated the electronic properties of the TPT molecules on the Co islands, we finally turn to their magnetic properties. For this purpose we use a bulk Cr tip prepared according to the description in section 6.3. The tip showed the same behavior as the one in section 6.4. This means that the magnetization direction of the Cr tip is changed by an applied external magnetic field of $B = \pm 0.5\,\text{T}$ [3]. We have used this feature to measure spin-resolved spectroscopic images and differential conductance spectra of the TPT molecules for parallel (P) and anti-parallel (AP) alignments of the tip and sample magnetization directions.

But before we turn to the spin-resolved spectroscopic images and dI/dV spectra of TPT it is important to define the parallel and anti-parallel configurations. To this end we applied an external magnetic field of $B = +1.75\,\text{T}$ in order to align the magnetization of the Co islands with the external field. The switching of the Co islands was confirmed by taking a spectroscopic image at $-500\,\text{mV}$ (analog to the procedure in section 6.4). Then we switched the magnetization of the tip by sweeping the external magnetic field to $B = -0.5\,\text{T}$ and measured again a spectroscopic image at $-500\,\text{mV}$. We define the state in which we observed a high differential conductance signal as parallel and accordingly the state with low conductance as anti-parallel. The spectroscopic images of the Co islands (with the adsorbed TPT molecules) are shown in Fig. 6.10 and correspond to the parallel and anti-parallel states, respectively. Before measuring spin-resolved spectroscopic images and dI/dV spectra of TPT we always confirmed the actual

[3] Since the Cr tip has no net magnetization here the term magnetization direction refers to uncompensated spins at the Cr tip apex whose direction could be changed by an external magnetic field.

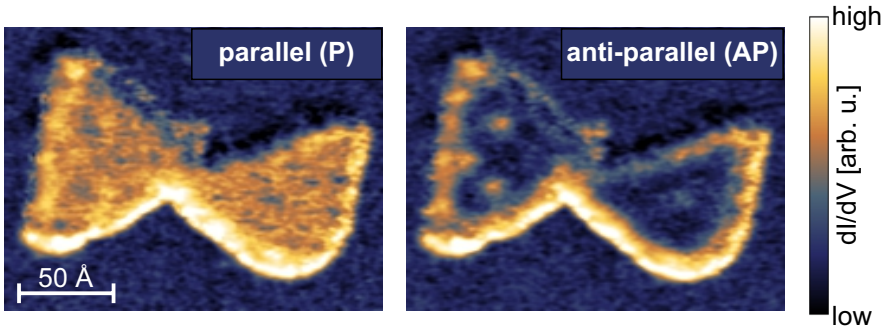

Figure 6.10: Spectroscopic images of Co islands on Cu(111) with adsorbed TPT molecules for parallel and anti-parallel magnetization orientations between tip and Co island measured with a magnetic bulk Cr tip ($V = -500\,\mathrm{mV}$, $I = 1.5\,\mathrm{nA}$). The switching between the two states is caused by the magnetization reversal of the magnetic tip in the external magnetic field B.

state (P or AP) by spectroscopic images of the particular Co islands.

To investigate the spatial distribution of the spin polarization of the TPT molecules, we recorded spectroscopic images in the P and AP magnetization configurations between tip and Co island. Then we calculated the spatially resolved map of the spin asymmetry

$$A = \frac{dI/dV_{\mathrm{AP}} - dI/dV_{\mathrm{P}}}{dI/dV_{\mathrm{AP}} + dI/dV_{\mathrm{P}}}, \tag{6.5}$$

where dI/dV_{AP} and dI/dV_{P} are the differential conductance signals in AP and P configuration, respectively. The spin asymmetry A is related to the spin polarization P_{S} of the sample at the position of the tip, and to the spin polarization P_{T} of the tip via

$$A = -P_{\mathrm{S}} P_{\mathrm{T}}. \tag{6.6}$$

Since the spin polarization of the tip, P_{T}, does not vary spatially above the sample for a fixed bias voltage, we can assume that variations in the spatially resolved spin asymmetry maps are linked to the spin polarization of the sample, that is, $A \propto P_{\mathrm{S}}$.

Fig. 6.11a shows a constant current STM image of TPT molecules adsorbed on a Co island, and Fig. 6.11b and c the spectroscopic images in AP and P configurations, respectively. The spectroscopic images have been measured at the energy of the hybrid state of TPT, that is, $V = -310\,\mathrm{mV}$ in this particular case, because the strongest spin-dependent effect is expected for this state. The resultant spatially resolved map of the spin asymmetry according to eq. (6.5) is shown in Fig. 6.11d. To make the analysis easier, the map of the spin asymmetry has been smoothed by removing the high

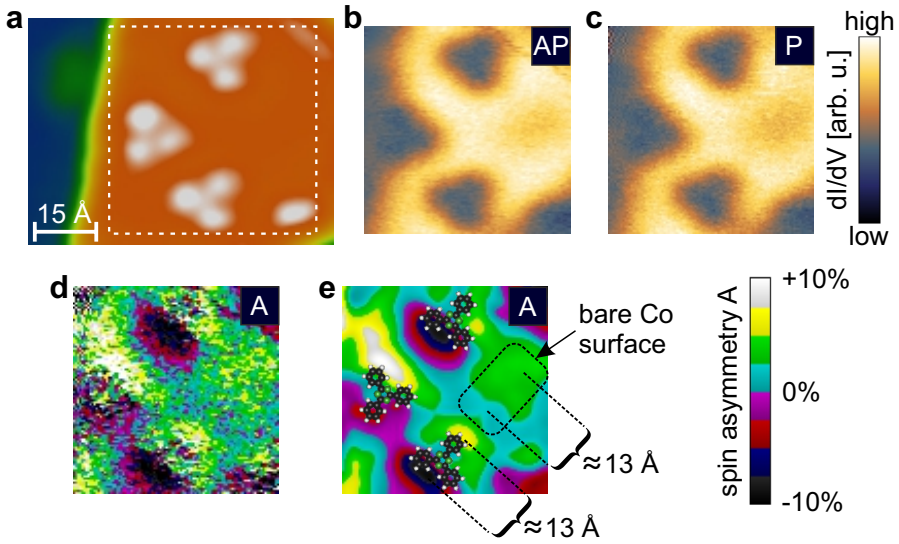

Figure 6.11: **a** Constant current STM image of a Co islands with adsorbed TPT molecules ($V = -200\,\mathrm{mV}$, $I = 200\,\mathrm{pA}$). **b** Spectroscopic image of the Co island with adsorbed TPT molecules at the energy of the hybrid state for anti-parallel magnetization directions between tip and sample measured with a magnetic bulk Cr tip ($V = -310\,\mathrm{mV}$, $I = 1.5\,\mathrm{nA}$). Image section corresponds to the indicated area in panel a. **c** As panel b, but for the parallel state. **d** Spin asymmetry map calculated from the spectroscopic images in panel b and c according to $A = (AP - P)/(AP + P)$. **e** The spin asymmetry map from panel d after applying a 2D-FFT filter to remove the high frequency noise. For the purpose of illustration the graphical representation of the TPT molecule has been overlaid. The positions of the TPT molecules have been extracted from the constant current image which has been recorded simultaneously.

frequency noise using a 2D-FFT filter, and in addition graphical representations of the TPT molecule have been overlaid. The final spin asymmetry map is shown in Fig. 6.11e by using a discrete color scale.

As seen in Fig. 6.11e, the spin asymmetry A, and consequently the spin polarization P_S of the sample, shows a strong spatial modulation within the Co island. The strongest effects occur around the TPT molecules, namely that spin asymmetry A exhibits positive and negative values. This change occurs on a length scale of approximately 13 Å as indicated in Fig. 6.11e. Such a change in the sign of the spin asymmetry is not observed in the area where no molecules are adsorbed – there the spin polarization only shows positive values, but also changes on a length scale of ≈ 13 Å from minimum to maximum (see Fig. 6.11e). Hence, we conclude that the inversion of the spin polarization must be related to the presence of the TPT molecules and

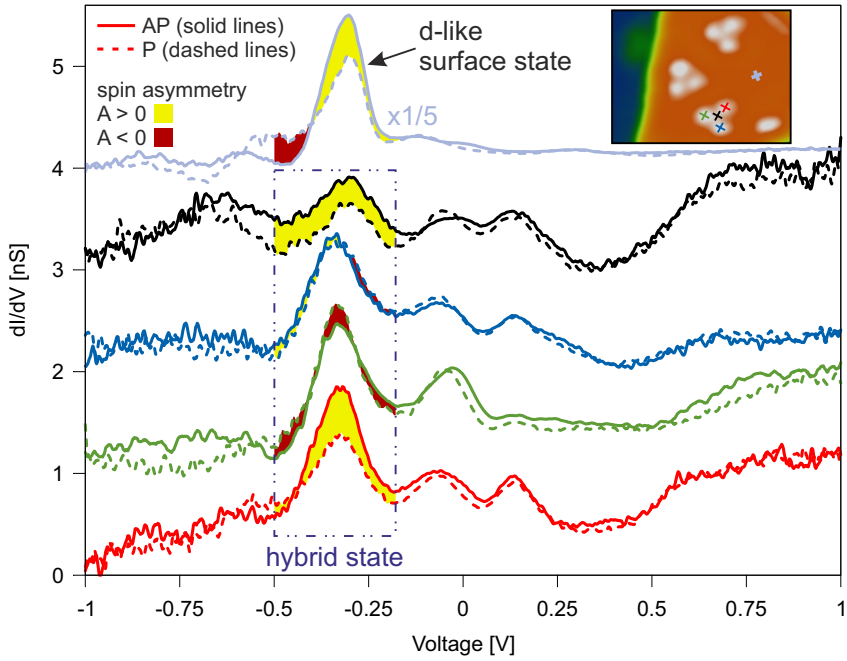

Figure 6.12: Spin-resolved differential conductance dI/dV spectra acquired on the different aromatic rings of the TPT molecule for parallel (P) and anti-parallel (AP) configuration between tip and Co island. The filled areas between the dI/dV spectra for AP and P configuration indicate the sign of the spin asymmetry A. For the measurement a magnetic bulk Cr tip has been used. The different spectroscopy locations on the TPT molecule are marked in the STM image in the inset ($V = -200\,\mathrm{mV}$, $I = 200\,\mathrm{pA}$). The Co island is the same as in Fig. 6.11. Spectra are shifted for clarity.

cannot be explained solely by the properties of the Co island.

Interestingly, the aromatic rings of the TPT molecules are located in areas with varying spin polarizations. Consequently, they exhibit different spin polarizations, as also exemplarily revealed by the spin-resolved dI/dV spectra of one of the TPT molecules in Fig. 6.12. The spin polarization of the hybrid state is inverted (green curve) or has the same sign (red curve) in comparison to the spin polarization of the d-like surface state (gray curve), or shows no spin polarization (blue curve) – all in good agreement with the findings in the spin asymmetry map (compare Fig. 6.11e and Fig. 6.12). Furthermore, the spin-resolved dI/dV spectra in Fig. 6.12 reveal that the strongest spin-dependent effect indeed occurs for the hybrid state. All other states show hardly any spin polarization. Currently, it is not known if the STM tip was not spin sensitive in these energy ranges, or if the TPT molecules are not spin-polarized in these energy ranges. Note that the peak at $\approx -80\,\mathrm{mV}$ was not detected in the spin-averaged measurements before

and thus is most probably a tip state. This is emphasized by the fact that also in the differential conductance spectra on the bare Co islands (gray curve) a peak at this energy ($\approx -80\,\mathrm{mV}$) is recognizable. Having a tip state in the gap-like structure of the TPT/Co spectrum (see also section 6.6) is unfortunate but reveals how difficult it is to prepare a STM tip with good electronic properties (i.e. flat DOS), spatial resolution (e.g. no double tips) and with magnetic contrast. Before discussing the possible origin of the varying spin polarizations on the TPT molecules we note that the spin-resolved spectra of the Co island (gray curves) show the typical behavior known from literature [160, 162].

The varying spin polarizations on the aromatic rings of the TPT molecules cannot be explained by a different hybridization of the aromatic rings, because TPT adsorbs highly symmetric on the Co islands (see section 6.5). Hence, the three phenyl rings have the same adsorption sites and should be hybridized equally with the Co island. Thus, the spin-dependent properties should be also equal (see also section 6.2), but, as seen in Fig. 6.11e and Fig. 6.12, they exhibit different spin polarizations. Since the spin polarization is not only different on the aromatic rings of the TPT molecules, but also on the surrounding of the molecules, i.e. on the nearby Co surface, it seems likely that these strong variations are related to the spatially modulated spin polarization of the Co islands. As mentioned in section 6.4 it has been shown in previous works that Co islands exhibit varying spin polarizations due the difference between the spatially modulated DOS of the sp surface state and the non-modulated d-like surface state [145]. Depending on the energy the periodicity of the spatial modulation of the spin polarization is in the order of $\gtrsim 15\,\text{Å}$ [145]. The changes in the spin polarization in Fig. 6.11e also occur on a length scale of $\approx 13\,\text{Å}$, as mentioned above, and thus are most likely linked to the spin-dependent interference pattern of the Co island.

Hence, one possible explanation for the strongly varying spin polarizations around the TPT molecules is that the molecules act as additional scattering centers for the electrons of the sp surface state, and thus modulate the intensity of the spin-dependent quantum interference pattern of the Co island. Since the wave function of the sp surface state cannot vanish abruptly at the edges of the TPT molecule, but rather extends into the molecules, a superposition of the spin polarization of TPT and of the modulated sp surface state is detected above the TPT molecules in the spin-resolved measurements. In Fig. 6.13a the different states, i.e. the non-modulated d-like surface state, the hybrid state and the spatially modulated sp surface state, which contribute to the spin-resolved signal, are schematically illustrated as a function of the position on the Co island. Note that the spin polarization of the hybrid state must be inverted in comparison to the d-like surface state of the Co island in order to explain the magnitudes of the observed spin asymmetries (Fig. 6.13b).

An inversion of the spin polarization of the hybrid state in comparison to the d-like surface state is reasonable, since we deduced in section 6.6 that the TPT molecules must be strongly hybridized with the Co islands, and a strong hybridization results in a inversion of the spin polarization according to the simple model in section 6.2.

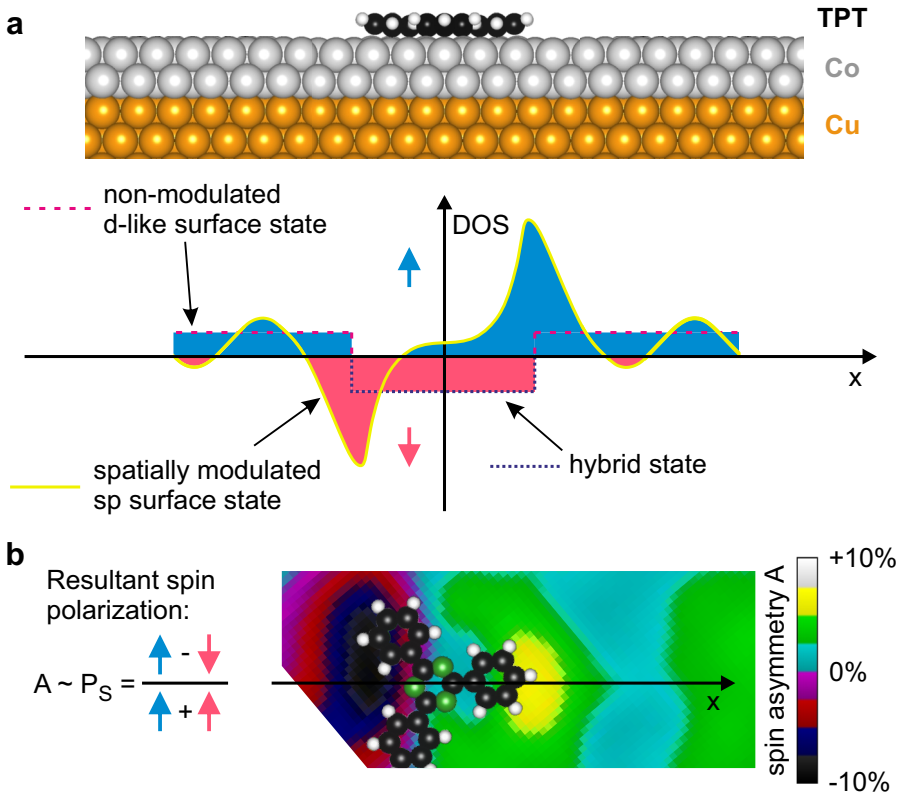

Figure 6.13: **a** Illustration of the spin-resolved DOS of the non-modulated d-like surface state, the hybrid state and the spatially modulated sp surface state depending on the position on the Co island. Upper panel, i.e. the side view of the system TPT/Co/Cu(111), taken from Friedrich et al. [171]. **b** The DOS illustrated in panel a results in a spin polarization pattern as observed in the experiment. The shown spin asymmetry map is an image section of Fig. 6.11e.

A further interesting feature is revealed by the calculated spin-resolved PDOS by Friedrich et al. as seen in Fig. 6.14. For the spin-up channel the theory predicts a gap close to the Fermi level where the density of states vanishes, indicating a half-metallic nature. Although this are preliminary results and have to be treated with caution, the agreement between theory and experiment was quite good up to this point and therefore the prediction should be credible. In the spin-averaged spectra also a gap-like feature was

observed in this energy range, which emphasizes that the predicted gap could be also existent in the experiment. But unfortunately we have been not able to measure the gap by spin-resolved measurements in an appropriate manner because of the present tip state. However, revealing the gap with a spin-polarized tip is quite challenging task, since the spin polarization of magnetic tips are usually less than 50% and to verify the gap actually a polarization of 100% would be needed. Nevertheless, it might be possible to observe this gap by using a superconducting tip to probe the absolute spin polarization [182] since it is located close to the Fermi energy.

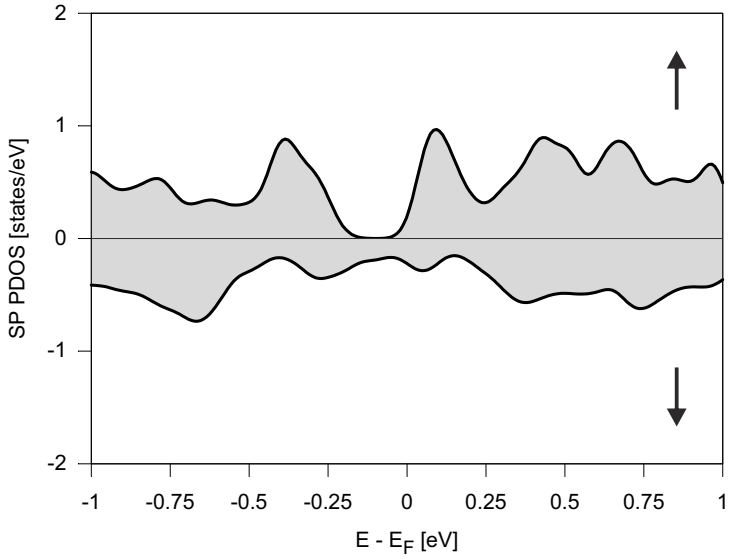

Figure 6.14: Spin-polarized projected density of states (SP PDOS) of the TPT molecule adsorbed on 2Co/5Cu. Taken from Friedrich et al. [171].

6.8 Conclusion

In this chapter we have analyzed systematically the formation of a hybrid molecular magnet on a ferromagnetic substrate by means of (SP-)STM/STS. For this purpose we have introduced the ferromagnetic building block, Co islands on Cu(111), in the first part of the chapter. Based on our data we have shown that Co grows as bilayer-high triangular islands on Cu(111) when deposited at room temperature and that two different types of Co islands can be distinguished with respect to their stacking, namely fcc-type (unfaulted) and hcp-type (faulted) Co islands. Furthermore, we have demonstrated the out-of-plane magnetization and the switching behavior of the Co island by an external magnetic field using a spin-polarized tip made from bulk Cr.

Having discussed the main properties of the ferromagnetic substrate, we analyzed the adsorption of the non-magnetic TPT molecule on the Co

islands. In order to obtain atomic resolution on the Co islands with the adsorbed TPT molecules we made use of a functionalized tip. From the atomically resolved STM images we have extracted the precise adsorption geometry and found that the TPT molecules adsorb highly symmetric on the Co island: the nitrogen atoms of the triazine ring adsorb above the Co atoms, which leads to equal adsorption sites for all phenyl rings. Our findings have been also confirmed by the ab initio calculations performed by Friedrich et al., as they found the highest binding energy for the experimentally estimated adsorption site. Furthermore, we have deduced from the differential conductance spectra acquired on TPT that the molecule must be strongly hybridized with Co, since a substantially broadened peak at the same energy as the d-like surface state of Co was observed. Thus, this state was labeled hybrid state.

In the end, having confirmed all requirements for the formation of a hybrid molecular magnet, we investigated the adsorbed TPT molecule by means of SP-STM/STS using a bulk Cr tip. Therefore we measured a spatially resolved map of the spin asymmetry and spin-resolved differential conductance spectra on different locations on the TPT molecule. We found that the spin polarization shows variations on the different aromatic rings and that it can be enhanced or inverted in comparison to the spin polarization of the d-like surface state of the surrounding Co island. Furthermore, we concluded that this variability in the spin polarization must be linked to the spin-dependent quantum interference pattern on the Co island by analyzing the spatially resolved spin asymmetry map.

Concluding, we can say that we have demonstrated successfully the formation of a hybrid molecular magnet, i.e. a molecule that is spin-dependent hybridized with a ferromagnetic surface, and that it is also possible to have aromatic rings with different spin polarizations on the same molecule. Interestingly, the different spin polarizations on the TPT molecules do not stem from a different hybridization of the aromatic rings with the Co island, but are a consequence of the superposition of the spin polarization of TPT and the spatially modulated spin-polarized sp surface state. This demonstrates that it is also important to consider effects due to quantum confinement when tailoring magnetic nanostructures.

In further studies it would be interesting to find out to what extent the spin properties of hybrid molecular magnets can be modified by spin-dependent quantum interference patterns. Also, the prediction of a half-metallic nature highly encourages further studies of the system in close collaboration with theory to obtain an exhaustive understanding of the system. Furthermore, it would be interesting to analyze the effect of the magnetic field on the hybrid molecular magnet in more detail and to find out if the aromatic rings react differently on the magnetic field, e.g. if they switch at different magnetic fields.

CHAPTER 7

Summary and Outlook

In summary we have investigated in this thesis the magnetic properties of QIs with delocalized spins and showed that such systems offer a wealth of new possibilities for tailoring spin-based systems by interaction with each other or their environment. Hereafter we will briefly summarize the results of the several investigated systems and furthermore we will discuss further interesting studies based on the results that we obtained in this thesis.

In order to systematically investigate the spin-dependent interaction between two QIs, first we have tailored in chapter 3 a single QI – a metal-molecule complex – with a net spin. In order to achieve full control of the geometric structure of the QIs with respect to the substrate and also to other neighboring QIs the metal-molecule complex has been embedded in a self-assembled molecular layer. The metal-molecule complex has been formed by adsorption of single Au atoms on a PTCDA layer physisorbed on the Au(111) surface and resulted in well-defined single QIs regarding their geometric, electronic and magnetic properties. By means of scanning tunneling microscopy and spectroscopy and temperature dependent measurements we have demonstrated that the Au-PTCDA complex undergoes a Kondo spin-$1/2$ effect with the itinerant electrons of the metal substrate and determined the Kondo temperature of the system to be $T_{\mathrm{K}} = (38 \pm 8)\,\mathrm{K}$. Furthermore, using density functional theory and many-body perturbation theory we showed that this unpaired spin resides in a π orbital of the metal-molecule complex which is formed due to the strong hybridization between the $6s$ orbital of the Au atom and the LUMO of the PTCDA molecule. Since this newly formed π orbital extends over the entire Au-PTCDA complex also the spin is delocalized over the entire complex. We quantitatively described the properties of the spin degree of freedom of the QI by using a single impurity Anderson model, with all parameters obtained from *ab initio* calculations. The renormalization group approach, based on the SIAM, yielded an excellent agreement with the experimental observations by predicting a Kondo resonance with a Kondo temperature of $T_{\mathrm{K}} = 37\,\mathrm{K}$.

After having established a quantitative description of a single Au-PTCDA complex, i.e. of a monomer, we dedicated ourselves in chapter 4 to the systematic investigation of the interaction between two complexes. Astonish-

ingly, it turned out that the magnetic properties of two directly neighboring monomers, i.e. of a dimer, which interact are not determined by direct or indirect exchange interaction. Interestingly, in this scenario the non-magnetic chemical interaction dictates the magnetic properties of a dimer. The reason for this stems from the fact the spin-carrying orbital is extended in space and thus the magnetic properties of the system are directly coupled to the wave function overlap between the two monomers. By using a hierarchy of methods, ranging from scanning tunneling microscopy and spectroscopy to density functional theory and many-body perturbation theory and to the numerical renormalization group method based on a two impurity Anderson model, we described the magnetic properties of a dimer quantitatively – again with excellent agreement between theory and experiment. We have shown that only tiny changes in the wave function overlap between two monomers are sufficient to drive a quantum phase transition between a partially Kondo screened triplet and a molecular singlet ground state. Amazingly, the driving force of the quantum phase transition is a competition between kinetic energy gain due to the Kondo effect and binding energy gain due to the chemical interaction between the spin-carrying orbitals. Furthermore, it is remarkable that in the present case the entanglement of the local moment with the substrate, i.e. the Kondo effect, stabilizes the local triplet against the local singlet that is promoted by chemical hybridization. These several unusual features compared to conventional two-impurity Kondo physics highlight the importance of this work on the way to spin-based devices.

In addition to the interaction of individual QIs, we also investigated the properties of QIs in well-ordered structures and searched for indications of collective spin phenomena on the atomic length scale in chapter 5, namely in the system NTCDA on Ag(111). For this purpose we made use of versatility of the scanning tunneling microscope. By lifting single NTCDA molecules from the edge of an island and performing dI/dV spectroscopy simultaneously with and without external magnetic fields we revealed that both distinct molecules in the molecular islands undergo the Kondo effect, but with different Kondo temperatures, and that the spin resides in the LUMO and hence is delocalized over the entire molecule. Furthermore, we showed that the difference in the Kondo temperatures stems from the different adsorption sites on the Ag(111) surface. Further studies of single NTCDA molecules and of rotated molecules at the edge of an island disclosed that the Kondo effect is not solely determined by the adsorption sites, but that also intermolecular interactions play an important role. Spatial variations of the line shape of the Kondo resonance within the molecules we linked to quantum interference effects of the wave functions of the LUMO. In particular we have shown that the q factor of the Fano line shape decreases from the CH site to the center of the molecule. Furthermore, we demonstrated that the side peaks at finite bias voltage primarily originate from molecu-

lar vibrations, but that their shape is influenced by the Kondo effect and that the unusually high values of the inelastic cross section are linked to the higher density of states at the Fermi level in the presence of the Kondo resonance. Interestingly, we also observed anomalies close to the Fermi level, namely that in some cases the Kondo resonance appears to be split. The fact that the amount of splitting varies spatially on the molecules and that the anomalies react on an external magnetic field indicate that they could be related to collective spin phenomena. However, to make an unambiguous statement about their origin further studies are necessary. Altogether we demonstrated that in well-ordered structures the magnetic properties of QIs with delocalized spins depend strongly on the interaction with the surface and also on intermolecular interactions. This work demonstrates the various possibilities for tuning the magnetic properties of QIs.

Moreover, we have also studied the spin dependent hybridization of a non-magnetic and aromatic molecule on a ferromagnetic surface – Co islands grown on Cu(111) – in chapter 6. First we have demonstrated the out-of-plane magnetization and the switching behavior of the Co islands in an external magnetic field by means of spin-polarized scanning tunneling microscopy – achieving good agreement with the results from literature. In the next step we have analyzed the adsorption of single TPT molecules on the Co islands and demonstrated that the TPT molecules adsorb highly symmetrically on the islands by making use of the unmatched spatial resolution of functionalized STM tips. Furthermore, we have shown, based on differential conductance spectra, that the TPT molecules strongly hybridize with the d-like surface state of the Co. Finally, we focused on the magnetic properties of the TPT molecules. Astonishingly, our spin-resolved differential conductance spectra for parallel and anti-parallel magnetization orientations of the tip and Co islands revealed that the spin polarization shows variations on the different aromatic rings of the TPT molecule in spite of the fact that the molecule is adsorbed highly symmetric. This surprising finding we linked to the spin dependent quantum interference pattern on the Co islands by measuring a spatially resolved spin asymmetry map of a Co island with adsorbed TPT molecules. Interestingly, the presence of TPT molecules on the Co islands leads to a modification of the spin dependent quantum interference pattern in such a way that the spin polarization can be enhanced or even inverted on the island itself. These effects extend into the TPT molecule and result in different spin-polarizations of the aromatic rings. These surprising findings may pave the way for a new approach in tailoring the magnetic properties of nanostructures.

Besides the outstanding findings which have been presented in this thesis and which already led to new and surprising insights into the complex interaction of magnetic nanostructures with each other and with their environment our research also paves the way to further interesting experiments based on the systems studied here. In the following some ideas for such

experiments will be proposed.

First of all the studies of two interacting QIs in chapter 4 where we observed a quantum phase transition with one dimer being extremely close to the quantum critical point allow us further studies on the competition between two many-body ground states. One could for example think of studying the effect of an external magnetic field on the properties of the system. An external magnetic field might allow us to switch between the two many-body ground states in a controlled manner. It would be also interesting to see what effect the relative distance of the dimers to the quantum critical point has on the behavior of the system in an external magnetic field. Furthermore, this system offers the unique possibility to study the lifetime of excited many-body ground states close to a quantum critical point in the most simple system which can show quantum critical behavior. These measurements could be carried out by using pump-probe scanning tunneling microscopy and could provide new insights into quantum phase transitions and the nature of many-body states. Further interesting studies could be based on experiments where the building blocks of the monomers are changed. By using similar but larger molecules than PTCDA, e.g. TTCDA and QTCDA, it might be possible to couple more than two monomers with each other by chemical interaction. This could lead to complex quantum systems like Kondo lattices or heavy fermion systems. Another possibility is to replace the Au atom of the monomer by a magnetic atom, e.g. with Fe or Co. Thereby it might be possible to induce a magnetic anisotropy in the system and thus to tailor ordered and magnetic structures on the atomic level.

Also the research presented in chapter 6 leaves enough scope for further interesting studies. First of all the fact that theory predicts a half-metallic nature in one spin channel of the tailored hybrid molecular magnet, which consists of a TPT molecule and a Co island which have hybridized, has to be checked by appropriate experiments. As already mentioned in chapter 6 it is a quite challenging task to verify the half-metallic nature of the system since spin-polarized tips with a polarization of 100% would be needed. However, by using a superconducting tip it might be possible to measure the absolute spin polarization of both spin channels close to the Fermi level and thus to proof the half-metallic nature. Furthermore, the behavior of the hybrid molecular magnet in an external magnetic field has to be investigated in more detail. Here one should specially focus on the switching behavior of the hybrid molecular magnet, i.e. if it is possible to switch the different aromatic rings independently from each other. If possible, this could lead to non-volatile and spin-based logic within single hybrid molecular magnets.

CHAPTER 8

List of publications

- **T. Esat**, R. Friedrich, F. Matthes, V. Caciuc, N. Atodiresei, S. Blügel, D. E. Bürgler, F. S. Tautz, and C. M. Schneider, "Quantum interference effects in molecular spin hybrids," *Physical Review B*, vol. 95, no. 9, p. 094409, 2017.

- P. Leinen, M. F. B. Green, **T. Esat**, C. Wagner, F. S. Tautz, and R. Temirov, "Hand Controlled Manipulation of Single Molecules via a Scanning Probe Microscope with a 3D Virtual Reality Interface," *JoVE (Journal of Visualized Experiments)*, no. 116, p. e54506, 2016.

- **T. Esat**, B. Lechtenberg, T. Deilmann, C. Wagner, P. Krüger, R. Temirov, M. Rohlfing, F. B. Anders, and F. S. Tautz, "A chemically driven quantum phase transition in a two-molecule Kondo system," *Nature Physics*, vol. 12, no. 9, p. 867, 2016.

- D. E. Bürgler, V. Heß, **T. Esat**, S. Fahrendorf, F. Matthes, C. Schneider, C. Besson, K. Y. Monakhov, P. Kögerler, A. Ghisolfi, et al., "Spin-Hybrids: A Single-Molecule Approach to Spintronics," *e-Journal of Surface Science and Nanotechnology*, vol. 14, no. 0, pp. 17-22, 2016.

- C. R. Braatz, **T. Esat**, C. Wagner, R. Temirov, F. S. Tautz, and P. Jakob, "Switching orientation of adsorbed molecules: Reverse domino on a metal surface," *Surface Science*, vol. 643, pp. 98-107, 2016.

- P. Leinen, M. F. B. Green, **T. Esat**, C. Wagner, F. S. Tautz, and R. Temirov, "Virtual reality visual feedback for hand-controlled scanning probe microscopy manipulation of single molecules," *Beilstein Journal of Nanotechnology*, vol. 6, no. 1, pp. 2148-2153, 2015.

- **T. Esat**, T. Deilmann, B. Lechtenberg, C. Wagner, P. Krüger, R. Temirov, F. B. Anders, M. Rohlfing, and F. S. Tautz, "Transfering spin into an extended π orbital of a large molecule," *Physical Review B*, vol. 91, no. 14, p. 144415, 2015.

- M. F. B. Green, **T. Esat**, C. Wagner, P. Leinen, A. Grötsch, F. S. Tautz, and R. Temirov, "Patterning a hydrogen-bonded molecular monolayer with a hand-controlled scanning probe microscope," *Beilstein Journal of Nanotechnology*, vol. 5, no. 1, pp. 1926-1932, 2014.

Bibliography

[1] Y. Igarashi, T. Altman, M. Funada, and B. Kamiyama, *Computing: A historical and technical perspective*. CRC Press, 2014.

[2] R. Rojas, *The first computers: History and architectures*. MIT press, 2002.

[3] S. H. Lavington, *Early British computers: the story of vintage computers and the people who built them*. Manchester University Press, 1980.

[4] L. Bogani and W. Wernsdorfer, "Molecular spintronics using single-molecule magnets," *Nature Materials*, vol. 7, no. 3, pp. 179–186, 2008.

[5] T. Dietl, D. D. Awschalom, M. Kaminska, and H. Ohno, *Spintronics*, vol. 82. Academic Press, 2009.

[6] S. A. Wolf, D. D. Awschalom, R. A. Buhrman, J. M. Daughton, S. Von Molnar, M. L. Roukes, A. Y. Chtchelkanova, and D. M. Treger, "Spintronics: a spin-based electronics vision for the future," *Science*, vol. 294, no. 5546, pp. 1488–1495, 2001.

[7] M. N. Baibich, J. M. Broto, A. Fert, F. N. Van Dau, F. Petroff, P. Etienne, G. Creuzet, A. Friederich, and J. Chazelas, "Giant magnetoresistance of (001)Fe/(001)Cr magnetic superlattices," *Physical Review Letters*, vol. 61, no. 21, p. 2472, 1988.

[8] G. Binasch, P. Grünberg, F. Saurenbach, and W. Zinn, "Enhanced magnetoresistance in layered magnetic structures with antiferromagnetic interlayer exchange," *Physical Review B*, vol. 39, no. 7, p. 4828, 1989.

[9] M. Julliere, "Tunneling between ferromagnetic films," *Physics Letters A*, vol. 54, no. 3, pp. 225–226, 1975.

[10] L. Kouwenhoven and L. Glazman, "Revival of the Kondo effect," *Physics World*, vol. 14, no. 1, p. 33, 2001.

[11] M. Ternes, A. J. Heinrich, and W.-D. Schneider, "Spectroscopic manifestations of the Kondo effect on single adatoms," *Journal of Physics: Condensed Matter*, vol. 21, no. 5, p. 053001, 2008.

[12] M. N. Leuenberger and D. Loss, "Quantum computing in molecular magnets," *Nature*, vol. 410, no. 6830, pp. 789–793, 2001.

[13] T. D. Ladd, F. Jelezko, R. Laflamme, Y. Nakamura, C. Monroe, and J. L. O'Brien, "Quantum computers," *Nature*, vol. 464, no. 7285, pp. 45–53, 2010.

[14] D. Loss and D. P. DiVincenzo, "Quantum computation with quantum dots," *Physical Review A*, vol. 57, no. 1, p. 120, 1998.

[15] C. H. Bennett and D. P. DiVincenzo, "Quantum information and computation," *Nature*, vol. 404, no. 6775, pp. 247–255, 2000.

[16] D. P. DiVincenzo, "Quantum computation," *Science*, vol. 270, no. 5234, p. 255, 1995.

[17] P. W. Shor, "Algorithms for quantum computation: Discrete logarithms and factoring," in *Foundations of Computer Science, 1994 Proceedings., 35th Annual Symposium on*, pp. 124–134, IEEE, 1994.

[18] L. K. Grover, "Quantum computers can search arbitrarily large databases by a single query," *Physical Review Letters*, vol. 79, no. 23, p. 4709, 1997.

[19] R. Wiesendanger, *Scanning probe microscopy and spectroscopy: methods and applications*. Cambridge University Press, 1994.

[20] C. J. Chen, *Introduction to scanning tunneling microscopy*, vol. 2. Oxford University Press New York, 1993.

[21] V. Madhavan, W. Chen, T. Jamneala, M. F. Crommie, and N. S. Wingreen, "Tunneling into a single magnetic atom: spectroscopic evidence of the Kondo resonance," *Science*, vol. 280, no. 5363, pp. 567–569, 1998.

[22] J. Li, W.-D. Schneider, R. Berndt, and B. Delley, "Kondo scattering observed at a single magnetic impurity," *Physical Review Letters*, vol. 80, no. 13, p. 2893, 1998.

[23] A. Zhao, Q. Li, L. Chen, H. Xiang, W. Wang, S. Pan, B. Wang, X. Xiao, J. Yang, J. G. Hou, *et al.*, "Controlling the Kondo effect of an adsorbed magnetic ion through its chemical bonding," *Science*, vol. 309, no. 5740, pp. 1542–1544, 2005.

[24] V. Iancu, A. Deshpande, and S.-W. Hla, "Manipulating Kondo temperature via single molecule switching," *Nano Letters*, vol. 6, no. 4, pp. 820–823, 2006.

[25] A. Zhao, Z. Hu, B. Wang, X. Xiao, J. Yang, and J. G. Hou, "Kondo effect in single cobalt phthalocyanine molecules adsorbed on Au (111) monoatomic steps," *The Journal of chemical physics*, vol. 128, no. 23, p. 234705, 2008.

[26] J. Kondo, "Resistance minimum in dilute magnetic alloys," *Progress of Theoretical physics*, vol. 32, no. 1, pp. 37–49, 1964.

[27] R. Wiesendanger, "Spin mapping at the nanoscale and atomic scale," *Reviews of Modern Physics*, vol. 81, no. 4, p. 1495, 2009.

[28] A. J. Heinrich, J. A. Gupta, C. P. Lutz, and D. M. Eigler, "Single-atom spin-flip spectroscopy," *Science*, vol. 306, no. 5695, pp. 466–469, 2004.

[29] C. F. Hirjibehedin, C. P. Lutz, and A. J. Heinrich, "Spin coupling in engineered atomic structures," *Science*, vol. 312, no. 5776, pp. 1021–1024, 2006.

[30] C. F. Hirjibehedin, C.-Y. Lin, A. F. Otte, M. Ternes, C. P. Lutz, B. A. Jones, and A. J. Heinrich, "Large magnetic anisotropy of a single atomic spin embedded in a surface molecular network," *Science*, vol. 317, no. 5842, pp. 1199–1203, 2007.

[31] A. F. Otte, M. Ternes, K. Von Bergmann, S. Loth, H. Brune, C. P. Lutz, C. F. Hirjibehedin, and A. J. Heinrich, "The role of magnetic anisotropy in the Kondo effect," *Nature Physics*, vol. 4, no. 11, pp. 847–850, 2008.

[32] C. Iacovita, M. V. Rastei, B. W. Heinrich, T. Brumme, J. Kortus, L. Limot, and J. P. Bucher, "Visualizing the spin of individual cobalt-phthalocyanine molecules," *Physical Review Letters*, vol. 101, no. 11, p. 116602, 2008.

[33] A. F. Otte, M. Ternes, S. Loth, C. P. Lutz, C. F. Hirjibehedin, and A. J. Heinrich, "Spin excitations of a Kondo-screened atom coupled to a second magnetic atom," *Physical Review Letters*, vol. 103, no. 10, p. 107203, 2009.

[34] S. Loth, K. von Bergmann, M. Ternes, A. F. Otte, C. P. Lutz, and A. J. Heinrich, "Controlling the state of quantum spins with electric currents," *Nature Physics*, vol. 6, no. 5, pp. 340–344, 2010.

[35] S. Loth, M. Etzkorn, C. P. Lutz, D. M. Eigler, and A. J. Heinrich, "Measurement of fast electron spin relaxation times with atomic resolution," *Science*, vol. 329, no. 5999, pp. 1628–1630, 2010.

[36] L. Zhou, J. Wiebe, S. Lounis, E. Vedmedenko, F. Meier, S. Blügel, P. H. Dederichs, and R. Wiesendanger, "Strength and directionality of surface Ruderman–Kittel–Kasuya–Yosida interaction mapped on the atomic scale," *Nature Physics*, vol. 6, no. 3, pp. 187–191, 2010.

[37] N. Tsukahara, S. Shiraki, S. Itou, N. Ohta, N. Takagi, and M. Kawai, "Evolution of Kondo resonance from a single impurity molecule to the two-dimensional lattice," *Physical Review Letters*, vol. 106, no. 18, p. 187201, 2011.

[38] A. A. Khajetoorians, J. Wiebe, B. Chilian, and R. Wiesendanger, "Realizing all-spin–based logic operations atom by atom," *Science*, vol. 332, no. 6033, pp. 1062–1064, 2011.

[39] S. Loth, S. Baumann, C. P. Lutz, D. M. Eigler, and A. J. Heinrich, "Bistability in atomic-scale antiferromagnets," *Science*, vol. 335, no. 6065, pp. 196–199, 2012.

[40] J. Schwöbel, Y. Fu, J. Brede, A. Dilullo, G. Hoffmann, S. Klyatskaya, M. Ruben, and R. Wiesendanger, "Real-space observation of spin-split molecular orbitals of adsorbed single-molecule magnets," *Nature Communications*, vol. 3, p. 953, 2012.

[41] A. A. Khajetoorians, B. Baxevanis, C. Hübner, T. Schlenk, S. Krause, T. O. Wehling, S. Lounis, A. Lichtenstein, D. Pfannkuche, J. Wiebe, *et al.*, "Current-driven spin dynamics of artificially constructed quantum magnets," *Science*, vol. 339, no. 6115, pp. 55–59, 2013.

[42] A. A. Khajetoorians, J. Wiebe, B. Chilian, S. Lounis, S. Blügel, and R. Wiesendanger, "Atom-by-atom engineering and magnetometry of tailored nanomagnets," *Nature Physics*, vol. 8, no. 6, pp. 497–503, 2012.

[43] S. Yan, D.-J. Choi, J. A. J. Burgess, S. Rolf-Pissarczyk, and S. Loth, "Control of quantum magnets by atomic exchange bias," *Nature Nanotechnology*, vol. 10, no. 1, pp. 40–45, 2015.

[44] J. Brede, N. Atodiresei, V. Caciuc, M. Bazarnik, A. Al-Zubi, S. Blügel, and R. Wiesendanger, "Long-range magnetic coupling between nanoscale organic–metal hybrids mediated by a nanoskyrmion lattice," *Nature Nanotechnology*, vol. 9, no. 12, pp. 1018–1023, 2014.

[45] S. Müllegger, S. Tebi, A. K. Das, W. Schöfberger, F. Faschinger, and R. Koch, "Radio frequency scanning tunneling spectroscopy for single-molecule spin resonance," *Physical Review Letters*, vol. 113, no. 13, p. 133001, 2014.

[46] S. Baumann, W. Paul, T. Choi, C. P. Lutz, A. Ardavan, and A. J. Heinrich, "Electron paramagnetic resonance of individual atoms on a surface," *Science*, vol. 350, no. 6259, pp. 417–420, 2015.

[47] F. Donati, S. Rusponi, S. Stepanow, C. Wäckerlin, A. Singha, L. Persichetti, R. Baltic, K. Diller, F. Patthey, E. Fernandes, *et al.*, "Magnetic remanence in single atoms," *Science*, vol. 352, no. 6283, pp. 318–321, 2016.

[48] M. A. Ruderman and C. Kittel, "Indirect exchange coupling of nuclear magnetic moments by conduction electrons," *Physical Review*, vol. 96, no. 1, p. 99, 1954.

[49] T. Kasuya, "A theory of metallic ferro-and antiferromagnetism on Zener's model," *Progress of Theoretical physics*, vol. 16, no. 1, pp. 45–57, 1956.

[50] K. Yosida, "Magnetic properties of Cu-Mn alloys," *Physical Review*, vol. 106, no. 5, p. 893, 1957.

[51] I. Fernández-Torrente, K. J. Franke, and J. I. Pascual, "Vibrational Kondo effect in pure organic charge-transfer assemblies," *Physical Review Letters*, vol. 101, no. 21, p. 217203, 2008.

[52] R. Temirov, A. Lassise, F. B. Anders, and F. S. Tautz, "Kondo effect by controlled cleavage of a single-molecule contact," *Nanotechnology*, vol. 19, no. 6, p. 065401, 2008.

[53] T. Choi, S. Bedwani, A. Rochefort, C.-Y. Chen, A. J. Epstein, and J. A. Gupta, "A single molecule Kondo switch: multistability of tetracyanoethylene on Cu (111)," *Nano Letters*, vol. 10, no. 10, pp. 4175–4180, 2010.

[54] G. Binnig, H. Rohrer, C. Gerber, and E. Weibel, "Surface studies by scanning tunneling microscopy," *Physical Review Letters*, vol. 49, no. 1, p. 57, 1982.

[55] G. Binnig, H. Rohrer, C. Gerber, and E. Weibel, "Tunneling through a controllable vacuum gap," *Applied Physics Letters*, vol. 40, no. 2, pp. 178–180, 1982.

[56] D. M. Eigler and E. K. Schweizer, "Positioning single atoms with a scanning tunnelling microscope," *Nature*, vol. 344, no. 6266, pp. 524–526, 1990.

[57] M. F. B. Green, T. Esat, C. Wagner, P. Leinen, A. Grötsch, F. S. Tautz, and R. Temirov, "Patterning a hydrogen-bonded molecular monolayer with a hand-controlled scanning probe microscope," *Beilstein Journal of Nanotechnology*, vol. 5, no. 1, pp. 1926–1932, 2014.

[58] J. Bardeen, "Tunnelling from a many-particle point of view," *Physical Review Letters*, vol. 6, no. 2, p. 57, 1961.

[59] J. Tersoff and D. R. Hamann, "Theory and application for the scanning tunneling microscope," *Physical Review Letters*, vol. 50, no. 25, p. 1998, 1983.

[60] J. Tersoff and D. R. Hamann, "Theory of the scanning tunneling microscope," in *Scanning Tunneling Microscopy*, pp. 59–67, Springer, 1985.

[61] N. D. Lang, "Spectroscopy of single atoms in the scanning tunneling microscope," *Physical Review B*, vol. 34, no. 8, p. 5947, 1986.

[62] V. A. Ukraintsev, "Data evaluation technique for electron-tunneling spectroscopy," *Physical Review B*, vol. 53, no. 16, p. 11176, 1996.

[63] J. C. Slonczewski, "Conductance and exchange coupling of two ferromagnets separated by a tunneling barrier," *Physical Review B*, vol. 39, no. 10, p. 6995, 1989.

[64] D. Wortmann, S. Heinze, P. Kurz, G. Bihlmayer, and S. Blügel, "Resolving complex atomic-scale spin structures by spin-polarized scanning tunneling microscopy," *Physical Review Letters*, vol. 86, no. 18, p. 4132, 2001.

[65] W. J. De Haas, J. De Boer, and G. J. Van den Berg, "The electrical resistance of gold, copper and lead at low temperatures," *Physica*, vol. 1, no. 7-12, pp. 1115–1124, 1934.

[66] A. A. Abrikosov, "On the Anomalous Temperature Dependence of the Resistivity of Non-magnetic Metals with a Weak Concentration of Magnetic Impurities," *Soviet Journal of Experimental and Theoretical Physics*, vol. 21, p. 660, 1965.

[67] H. Suhl, "Dispersion theory of the Kondo effect," *Physical Review*, vol. 138, no. 2A, p. A515, 1965.

[68] Y. Nagaoka, "Self-consistent treatment of Kondo's effect in dilute alloys," *Physical Review*, vol. 138, no. 4A, p. A1112, 1965.

[69] J. Kondo, "sd Scattering at Low Temperatures," *Progress of Theoretical Physics*, vol. 34, no. 2, pp. 204–209, 1965.

[70] A. A. Abrikosov and A. A. Migdal, "On the theory of the Kondo effect," *Journal of Low Temperature Physics*, vol. 3, no. 5, pp. 519–536, 1970.

[71] P. W. Anderson, "A poor man's derivation of scaling laws for the Kondo problem," *Journal of Physics C: Solid State Physics*, vol. 3, no. 12, p. 2436, 1970.

[72] P. Nozieres, "A ŞFermi-liquidŤ description of the Kondo problem at low temperatures," *Journal of Low Temperature Physics*, vol. 17, no. 1-2, pp. 31–42, 1974.

[73] K. G. Wilson, "The renormalization group: Critical phenomena and the Kondo problem," *Reviews of Modern Physics*, vol. 47, no. 4, p. 773, 1975.

[74] P. W. Anderson, "Localized magnetic states in metals," *Physical Review*, vol. 124, no. 1, p. 41, 1961.

[75] H. R. Krishna-Murthy, J. W. Wilkins, and K. G. Wilson, "Renormalization-group approach to the Anderson model of dilute magnetic alloys. I. Static properties for the symmetric case," *Physical Review B*, vol. 21, no. 3, p. 1003, 1980.

[76] H. R. Krishna-Murthy, J. W. Wilkins, and K. G. Wilson, "Renormalization-group approach to the Anderson model of dilute magnetic alloys. II. Static properties for the asymmetric case," *Physical Review B*, vol. 21, no. 3, p. 1044, 1980.

[77] J. R. Schrieffer and P. A. Wolff, "Relation between the anderson and kondo hamiltonians," *Physical Review*, vol. 149, no. 2, p. 491, 1966.

[78] K. Nagaoka, T. Jamneala, M. Grobis, and M. F. Crommie, "Temperature dependence of a single Kondo impurity," *Physical Review Letters*, vol. 88, no. 7, p. 077205, 2002.

[79] T. A. Costi, A. C. Hewson, and V. Zlatic, "Transport coefficients of the Anderson model via the numerical renormalization group," *Journal of Physics: Condensed Matter*, vol. 6, no. 13, p. 2519, 1994.

[80] D. Goldhaber-Gordon, J. Göres, M. A. Kastner, H. Shtrikman, D. Mahalu, and U. Meirav, "From the Kondo regime to the mixed-valence regime in a single-electron transistor," *Physical Review Letters*, vol. 81, no. 23, p. 5225, 1998.

[81] M. Plihal and J. W. Gadzuk, "Nonequilibrium theory of scanning tunneling spectroscopy via adsorbate resonances: Nonmagnetic and Kondo impurities," *Physical Review B*, vol. 63, no. 8, p. 085404, 2001.

[82] U. Fano, "Effects of configuration interaction on intensities and phase shifts," *Physical Review*, vol. 124, no. 6, p. 1866, 1961.

[83] A. Schiller and S. Hershfield, "Theory of scanning tunneling spectroscopy of a magnetic adatom on a metallic surface," *Physical Review B*, vol. 61, no. 13, p. 9036, 2000.

[84] R. Bulla, T. A. Costi, and T. Pruschke, "Numerical renormalization group method for quantum impurity systems," *Reviews of Modern Physics*, vol. 80, no. 2, p. 395, 2008.

[85] R. Bulla, T. Pruschke, and A. C. Hewson, "Anderson impurity in pseudo-gap Fermi systems," *Journal of Physics: Condensed Matter*, vol. 9, no. 47, p. 10463, 1997.

[86] B. A. Jones and C. M. Varma, "Study of two magnetic impurities in a Fermi gas," *Physical Review Letters*, vol. 58, no. 9, p. 843, 1987.

[87] B. A. Jones, C. M. Varma, and J. W. Wilkins, "Low-temperature properties of the two-impurity Kondo Hamiltonian," *Physical Review Letters*, vol. 61, no. 1, p. 125, 1988.

[88] B. A. Jones and C. M. Varma, "Critical point in the solution of the two magnetic impurity problem," *Physical Review B*, vol. 40, no. 1, p. 324, 1989.

[89] I. Affleck, A. W. W. Ludwig, and B. A. Jones, "Conformal-field-theory approach to the two-impurity Kondo problem: Comparison with numerical renormalization-group results," *Physical Review B*, vol. 52, no. 13, p. 9528, 1995.

[90] J. Gan, "Solution of the two-impurity Kondo model: Critical point, Fermi-liquid phase, and crossover," *Physical Review B*, vol. 51, no. 13, p. 8287, 1995.

[91] R. M. Fye, J. E. Hirsch, and D. J. Scalapino, "Kondo effect versus indirect exchange in the two-impurity Anderson model: A Monte Carlo study," *Physical Review B*, vol. 35, no. 10, p. 4901, 1987.

[92] R. M. Fye and J. E. Hirsch, "Quantum Monte Carlo study of the two-impurity Kondo Hamiltonian," *Physical Review B*, vol. 40, no. 7, p. 4780, 1989.

[93] R. M. Fye, ""Anomalous fixed point behavior"of two Kondo impurities: A reexamination," *Physical Review Letters*, vol. 72, no. 6, p. 916, 1994.

[94] J. B. Silva, W. L. C. Lima, W. C. Oliveira, J. L. N. Mello, L. N. Oliveira, and J. W. Wilkins, "Particle-hole asymmetry in the two-impurity Kondo model," *Physical Review Letters*, vol. 76, no. 2, p. 275, 1996.

[95] C. Jayaprakash, H. R. Krishna-Murthy, and J. W. Wilkins, "Two-impurity Kondo problem," *Physical Review Letters*, vol. 47, no. 10, p. 737, 1981.

[96] O. Sakai, Y. Shimizu, and T. Kasuya, "Excitation spectra of two impurity Anderson model," *Solid State Communications*, vol. 75, no. 2, pp. 81–87, 1990.

[97] C. A. Paula, M. F. Silva, and L. N. Oliveira, "Low-energy spectral density for the Alexander-Anderson model," *Physical Review B*, vol. 59, no. 1, p. 85, 1999.

[98] O. Sakai, Y. Shimizu, and N. Kaneko, "Excitation spectra of two-impurity and multi-channel Kondo systems by the numerical renormalization group method," *Physica B: Condensed Matter*, vol. 186, pp. 323–327, 1993.

[99] S. Nishimoto, T. Pruschke, and R. M. Noack, "Spectral density of the two-impurity Anderson model," *Journal of Physics: Condensed Matter*, vol. 18, no. 3, p. 981, 2006.

[100] K. Hattori and K. Miyake, "Charge anomaly at critical point of two-impurity Anderson model," *Journal of Magnetism and Magnetic Materials*, vol. 310, no. 2, pp. 452–453, 2007.

[101] D. F. Mross and H. Johannesson, "Two-impurity Anderson model at quantum criticality," *Physical Review B*, vol. 78, no. 3, p. 035449, 2008.

[102] L. Zhu and J.-X. Zhu, "Coherence scale of coupled Anderson impurities," *Physical Review B*, vol. 83, no. 19, p. 195103, 2011.

[103] T. Jabben, N. Grewe, and S. Schmitt, "Spectral properties of the two-impurity Anderson model with varying distance and various interactions," *Physical Review B*, vol. 85, no. 4, p. 045133, 2012.

[104] T. Pruschke and R. Bulla, "Hund's coupling and the metal-insulator transition in the two-band Hubbard model," *The European Physical Journal B-Condensed Matter and Complex Systems*, vol. 44, no. 2, pp. 217–224, 2005.

[105] A. H. Nevidomskyy and P. Coleman, "Kondo resonance narrowing in d-and f-electron systems," *Physical Review Letters*, vol. 103, no. 14, p. 147205, 2009.

[106] S. Sachdev, *Quantum phase transitions*. Wiley Online Library, 2007.

[107] M. Vojta, "Quantum phase transitions," *Reports on Progress in Physics*, vol. 66, no. 12, p. 2069, 2003.

[108] M. Vojta, "Impurity quantum phase transitions," *Philosophical Magazine*, vol. 86, no. 13-14, pp. 1807–1846, 2006.

[109] W. Hofstetter and H. Schoeller, "Quantum phase transition in a multilevel dot," *Physical Review Letters*, vol. 88, no. 1, p. 016803, 2001.

[110] N. Roch, S. Florens, V. Bouchiat, W. Wernsdorfer, and F. Balestro, "Quantum phase transition in a single-molecule quantum dot," *Nature*, vol. 453, no. 7195, pp. 633–637, 2008.

[111] S. Doniach, "The Kondo lattice and weak antiferromagnetism," *Physica B+ C*, vol. 91, pp. 231–234, 1977.

[112] H. Tsunetsugu, M. Sigrist, and K. Ueda, "The ground-state phase diagram of the one-dimensional Kondo lattice model," *Reviews of Modern Physics*, vol. 69, no. 3, p. 809, 1997.

[113] M. B. Maple, J. W. Chen, Y. Dalichaouch, T. Kohara, C. Rossel, M. S. Torikachvili, M. W. McElfresh, and J. D. Thompson, "Partially gapped Fermi surface in the heavy-electron superconductor URu 2 Si 2," *Physical Review Letters*, vol. 56, no. 2, p. 185, 1986.

[114] L. Kilian, U. Stahl, I. Kossev, M. Sokolowski, R. Fink, and E. Umbach, "The commensurate-to-incommensurate phase transition of an organic monolayer: A high resolution LEED analysis of the superstructures of NTCDA on Ag (111)," *Surface Science*, vol. 602, no. 14, pp. 2427–2434, 2008.

[115] J. Ziroff, S. Hame, M. Kochler, A. Bendounan, A. Schöll, and F. Reinert, "Low-energy scale excitations in the spectral function of organic monolayer systems," *Physical Review B*, vol. 85, no. 16, p. 161404, 2012.

[116] A. Bendounan, F. Forster, A. Schöll, D. Batchelor, J. Ziroff, E. Umbach, and F. Reinert, "Electronic structure of 1ML NTCDA/Ag (111) studied by photoemission spectroscopy," *Surface Science*, vol. 601, no. 18, pp. 4013–4017, 2007.

[117] U. Stahl, D. Gador, A. Soukopp, R. Fink, and E. Umbach, "Coverage-dependent superstructures in chemisorbed NTCDA monolayers: a combined LEED and STM study," *Surface Science*, vol. 414, no. 3, pp. 423–434, 1998.

[118] C. R. Braatz, T. Esat, C. Wagner, R. Temirov, F. S. Tautz, and P. Jakob, "Switching orientation of adsorbed molecules: Reverse domino on a metal surface," *Surface Science*, vol. 643, pp. 98–107, 2016.

[119] R. Temirov, S. Soubatch, A. Luican, and F. S. Tautz, "Free-electron-like dispersion in an organic monolayer film on a metal substrate," *Nature*, vol. 444, no. 7117, pp. 350–353, 2006.

[120] N. L. Zaitsev, I. A. Nechaev, P. M. Echenique, and E. V. Chulkov, "Transformation of the Ag (111) surface state due to molecule-surface interaction with ordered organic molecular monolayers," *Physical Review B*, vol. 85, no. 11, p. 115301, 2012.

[121] C. Toher, R. Temirov, A. Greuling, F. Pump, M. Kaczmarski, G. Cuniberti, M. Rohlfing, and F. S. Tautz, "Electrical transport through a mechanically gated molecular wire," *Physical Review B*, vol. 83, no. 15, p. 155402, 2011.

[122] A. Greuling, M. Rohlfing, R. Temirov, F. S. Tautz, and F. B. Anders, "Ab initio study of a mechanically gated molecule: From weak to strong correlation," *Physical Review B*, vol. 84, no. 12, p. 125413, 2011.

[123] A. Greuling, R. Temirov, B. Lechtenberg, F. B. Anders, M. Rohlfing, and F. S. Tautz, "Spectral properties of a molecular wire in the Kondo regime," *Physica Status Solidi (b)*, vol. 250, no. 11, pp. 2386–2393, 2013.

[124] T. A. Costi, "Kondo effect in a magnetic field and the magnetoresistivity of Kondo alloys," *Physical Review Letters*, vol. 85, no. 7, p. 1504, 2000.

[125] T. Esat, T. Deilmann, B. Lechtenberg, C. Wagner, P. Krüger, R. Temirov, F. B. Anders, M. Rohlfing, and F. S. Tautz, "Transfering spin into an extended π orbital of a large molecule," *Physical Review B*, vol. 91, no. 14, p. 144415, 2015.

[126] R. Temirov and P. Jelinek. private communication, 2016.

[127] J. Bork, Y.-h. Zhang, L. Diekhöner, L. Borda, P. Simon, J. Kroha, P. Wahl, and K. Kern, "A tunable two-impurity Kondo system in an atomic point contact," *Nature Physics*, vol. 7, no. 11, pp. 901–906, 2011.

[128] H. Prüser, P. E. Dargel, M. Bouhassoune, R. G. Ulbrich, T. Pruschke, S. Lounis, and M. Wenderoth, "Interplay between the Kondo effect

and the Ruderman–Kittel–Kasuya–Yosida interaction," *Nature Communications*, vol. 5, 2014.

[129] B. C. Stipe, M. A. Rezaei, and W. Ho, "Single-molecule vibrational spectroscopy and microscopy," *Science*, vol. 280, no. 5370, pp. 1732–1735, 1998.

[130] R. Temirov, S. Soubatch, A. Lassise, and F. S. Tautz, "Bonding and vibrational dynamics of a large π-conjugated molecule on a metal surface," *Journal of Physics: Condensed Matter*, vol. 20, no. 22, p. 224010, 2008.

[131] R. Tonner, P. Rosenow, and P. Jakob, "Molecular structure and vibrations of NTCDA monolayers on Ag (111) from density-functional theory and infrared absorption spectroscopy," *Physical Chemistry Chemical Physics*, vol. 18, no. 8, pp. 6316–6328, 2016.

[132] J. I. Pascual, N. Lorente, P. Grütter, W. Hofer, and F. Rosei, "Single-molecule vibrational spectroscopy and chemistry," *Properties of Single Organic Molecules on Crystal Surfaces*, p. 209, 2006.

[133] R. Temirov, *Studying complex metal-molecule interface with low temperature scanning tunneling microscope: from electronic structure to charge transport*. PhD thesis, Jacobs University Bremen, 2008.

[134] H. Wende, M. Bernien, J. Luo, C. Sorg, N. Ponpandian, J. Kurde, J. Miguel, M. Piantek, X. Xu, P. Eckhold, *et al.*, "Substrate-induced magnetic ordering and switching of iron porphyrin molecules," *Nature Materials*, vol. 6, no. 7, pp. 516–520, 2007.

[135] M. Bernien, J. Miguel, C. Weis, M. E. Ali, J. Kurde, B. Krumme, P. M. Panchmatia, B. Sanyal, M. Piantek, P. Srivastava, *et al.*, "Tailoring the nature of magnetic coupling of Fe-porphyrin molecules to ferromagnetic substrates," *Physical Review Letters*, vol. 102, no. 4, p. 047202, 2009.

[136] M. Callsen, V. Caciuc, N. Kiselev, N. Atodiresei, and S. Blügel, "Magnetic hardening induced by nonmagnetic organic molecules," *Physical Review Letters*, vol. 111, no. 10, p. 106805, 2013.

[137] M. Galbiati, S. Tatay, C. Barraud, A. V. Dediu, F. Petroff, R. Mattana, and P. Seneor, "Spinterface: Crafting spintronics at the molecular scale," *MRS Bulletin*, vol. 39, no. 07, pp. 602–607, 2014.

[138] R. Friedrich, V. Caciuc, N. S. Kiselev, N. Atodiresei, and S. Blügel, "Chemically functionalized magnetic exchange interactions of hybrid organic-ferromagnetic metal interfaces," *Physical Review B*, vol. 91, no. 11, p. 115432, 2015.

[139] R. Friedrich, V. Caciuc, N. Atodiresei, and S. Blügel, "Molecular induced skyhook effect for magnetic interlayer softening," *Physical Review B*, vol. 92, no. 19, p. 195407, 2015.

[140] T. Miyamachi, M. Gruber, V. Davesne, M. Bowen, S. Boukari, L. Joly, F. Scheurer, G. Rogez, T. K. Yamada, P. Ohresser, *et al.*, "Robust spin crossover and memristance across a single molecule," *Nature Communications*, vol. 3, p. 938, 2012.

[141] K. V. Raman, A. M. Kamerbeek, A. Mukherjee, N. Atodiresei, T. K. Sen, P. Lazić, V. Caciuc, R. Michel, D. Stalke, S. K. Mandal, *et al.*, "Interface-engineered templates for molecular spin memory devices," *Nature*, vol. 493, no. 7433, pp. 509–513, 2013.

[142] D. E. Bürgler, V. Heß, T. Esat, S. Fahrendorf, F. Matthes, C. M. Schneider, C. Besson, K. Y. Monakhov, P. Kögerler, A. Ghisolfi, *et al.*, "Spin-Hybrids: A Single-Molecule Approach to Spintronics," *e-Journal of Surface Science and Nanotechnology*, vol. 14, no. 0, pp. 17–22, 2016.

[143] J. Brede, N. Atodiresei, S. Kuck, P. Lazić, V. Caciuc, Y. Morikawa, G. Hoffmann, S. Blügel, and R. Wiesendanger, "Spin-and energy-dependent tunneling through a single molecule with intramolecular spatial resolution," *Physical Review Letters*, vol. 105, no. 4, p. 047204, 2010.

[144] N. Atodiresei, J. Brede, P. Lazić, V. Caciuc, G. Hoffmann, R. Wiesendanger, and S. Blügel, "Design of the local spin polarization at the organic-ferromagnetic interface," *Physical Review Letters*, vol. 105, no. 6, p. 066601, 2010.

[145] H. Oka, P. A. Ignatiev, S. Wedekind, G. Rodary, L. Niebergall, V. S. Stepanyuk, D. Sander, and J. Kirschner, "Spin-dependent quantum interference within a single magnetic nanostructure," *Science*, vol. 327, no. 5967, pp. 843–846, 2010.

[146] S. Braun, W. R. Salaneck, and M. Fahlman, "Energy-Level Alignment at Organic/Metal and Organic/Organic Interfaces," *Advanced Materials*, vol. 21, no. 14-15, pp. 1450–1472, 2009.

[147] C. Barraud, P. Seneor, R. Mattana, S. Fusil, K. Bouzehouane, C. Deranlot, P. Graziosi, L. Hueso, I. Bergenti, V. Dediu, *et al.*, "Unravelling the role of the interface for spin injection into organic semiconductors," *Nature Physics*, vol. 6, no. 8, pp. 615–620, 2010.

[148] J. De la Figuera, J. E. Prieto, C. Ocal, and R. Miranda, "Scanning-tunneling-microscopy study of the growth of cobalt on Cu (111)," *Physical Review B*, vol. 47, no. 19, p. 13043, 1993.

[149] N. N. Negulyaev, V. S. Stepanyuk, P. Bruno, L. Diekhöner, P. Wahl, and K. Kern, "Bilayer growth of nanoscale Co islands on Cu (111)," *Physical Review B*, vol. 77, no. 12, p. 125437, 2008.

[150] A. Rabe, N. Memmel, A. Steltenpohl, and T. Fauster, "Room-temperature instability of Co/Cu (111)," *Physical Review Letters*, vol. 73, no. 20, p. 2728, 1994.

[151] M. Cavallini and F. Biscarini, "Electrochemically etched nickel tips for spin polarized scanning tunneling microscopy," *Review of Scientific Instruments*, vol. 71, no. 12, pp. 4457–4460, 2000.

[152] R. Koltun, M. Herrmann, G. Güntherodt, and V. A. M. Brabers, "Enhanced atomic-scale contrast on Fe3O4 (100) observed with an Fe STM tip," *Applied Physics A*, vol. 73, no. 1, pp. 49–53, 2001.

[153] C. Albonetti, I. Bergenti, M. Cavallini, V. Dediu, M. Massi, J.-F. Moulin, and F. Biscarini, "Electrochemical preparation of cobalt tips for scanning tunneling microscopy," *Review of Scientific Instruments*, vol. 73, no. 12, pp. 4254–4256, 2002.

[154] A. L. Bassi, C. S. Casari, D. Cattaneo, F. Donati, S. Foglio, M. Passoni, C. E. Bottani, P. Biagioni, A. Brambilla, M. Finazzi, *et al.*, "Bulk Cr tips for scanning tunneling microscopy and spin-polarized scanning tunneling microscopy," *Applied Physics Letters*, vol. 91, no. 17, p. 173120, 2007.

[155] A. Schlenhoff, S. Krause, G. Herzog, and R. Wiesendanger, "Bulk Cr tips with full spatial magnetic sensitivity for spin-polarized scanning tunneling microscopy," *Applied Physics Letters*, vol. 97, no. 8, p. 083104, 2010.

[156] R. Wiesendanger, D. Bürgler, G. Tarrach, T. Schaub, U. Hartmann, H.-J. Güntherodt, I. V. Shvets, and J. M. D. Coey, "Recent advances in scanning tunneling microscopy involving magnetic probes and samples," *Applied Physics A*, vol. 53, no. 5, pp. 349–355, 1991.

[157] M. Bode, "Spin-polarized scanning tunnelling microscopy," *Reports on Progress in Physics*, vol. 66, no. 4, p. 523, 2003.

[158] A. Kubetzka, M. Bode, O. Pietzsch, and R. Wiesendanger, "Spin-polarized scanning tunneling microscopy with antiferromagnetic probe tips," *Physical Review Letters*, vol. 88, no. 5, p. 057201, 2002.

[159] G. Rodary, S. Wedekind, H. Oka, D. Sander, and J. Kirschner, "Characterization of tips for spin-polarized scanning tunneling microscopy," *Applied Physics Letters*, vol. 95, no. 15, p. 152513, 2009.

[160] O. Pietzsch, A. Kubetzka, M. Bode, and R. Wiesendanger, "Spin-polarized scanning tunneling spectroscopy of nanoscale cobalt islands on Cu (111)," *Physical Review Letters*, vol. 92, no. 5, p. 057202, 2004.

[161] O. Pietzsch, S. Okatov, A. Kubetzka, M. Bode, S. Heinze, A. Lichtenstein, and R. Wiesendanger, "Spin-resolved electronic structure of nanoscale cobalt islands on Cu (111)," *Physical Review Letters*, vol. 96, no. 23, p. 237203, 2006.

[162] G. Rodary, S. Wedekind, D. Sander, and J. Kirschner, "Magnetic hysteresis loop of single Co nano-islands," *Japanese Journal of Applied Physics*, vol. 47, no. 12R, p. 9013, 2008.

[163] L. Diekhöner, M. A. Schneider, A. N. Baranov, V. S. Stepanyuk, P. Bruno, and K. Kern, "Surface states of cobalt nanoislands on Cu (111)," *Physical Review Letters*, vol. 90, no. 23, p. 236801, 2003.

[164] M. V. Rastei, B. Heinrich, L. Limot, P. A. Ignatiev, V. S. Stepanyuk, P. Bruno, and J. P. Bucher, "Size-dependent surface states of strained cobalt nanoislands on Cu (111)," *Physical Review Letters*, vol. 99, no. 24, p. 246102, 2007.

[165] S. Wedekind, G. Rodary, J. Borme, S. Ouazi, Y. Nahas, M. Corbetta, H. Oka, D. Sander, and J. Kirschner, "Switching fields of individual Co nanoislands," *Magnetics, IEEE Transactions on*, vol. 47, no. 10, pp. 3351–3354, 2011.

[166] S. Ouazi, S. Wedekind, G. Rodary, H. Oka, D. Sander, and J. Kirschner, "Magnetization reversal of individual co nanoislands," *Physical Review Letters*, vol. 108, no. 10, p. 107206, 2012.

[167] D. Sander, H. Oka, M. Corbetta, V. Stepanyuk, and J. Kirschner, "New insights into nano-magnetism by spin-polarized scanning tunneling microscopy," *Journal of Electron Spectroscopy and Related Phenomena*, vol. 189, pp. 206–215, 2013.

[168] S. Wedekind, *A spin-polarized scanning tunneling microscopy and spectroscopy study of individual nanoscale particles grown on copper surfaces*. PhD thesis, Halle (Saale), Martin-Luther-Universität Halle-Wittenberg, Diss., 2010, 2009.

[169] J. Izquierdo, A. Vega, and L. C. Balbás, "Magnetism of Co nanoparticles supported on the Cu (111) substrate: Size and environment dependence," *Physical Review B*, vol. 55, no. 1, p. 445, 1997.

[170] L. Niebergall, V. S. Stepanyuk, J. Berakdar, and P. Bruno, "Controlling the spin polarization of nanostructures on magnetic substrates," *Physical Review Letters*, vol. 96, no. 12, p. 127204, 2006.

[171] R. Friedrich. private communication, 2016.

[172] R. Temirov, S. Soubatch, O. Neucheva, A. C. Lassise, and F. S. Tautz, "A novel method achieving ultra-high geometrical resolution in scanning tunnelling microscopy," *New Journal of Physics*, vol. 10, no. 5, p. 053012, 2008.

[173] C. Weiss, C. Wagner, R. Temirov, and F. S. Tautz, "Direct imaging of intermolecular bonds in scanning tunneling microscopy," *Journal of the American Chemical Society*, vol. 132, no. 34, pp. 11864–11865, 2010.

[174] C. Weiss, C. Wagner, C. Kleimann, M. Rohlfing, F. S. Tautz, and R. Temirov, "Imaging Pauli repulsion in scanning tunneling microscopy," *Physical Review Letters*, vol. 105, no. 8, p. 086103, 2010.

[175] G. Kichin, C. Weiss, C. Wagner, F. S. Tautz, and R. Temirov, "Single molecule and single atom sensors for atomic resolution imaging of chemically complex surfaces," *Journal of the American Chemical Society*, vol. 133, no. 42, pp. 16847–16851, 2011.

[176] P. Hapala, G. Kichin, C. Wagner, F. S. Tautz, R. Temirov, and P. Jelínek, "Mechanism of high-resolution STM/AFM imaging with functionalized tips," *Physical Review B*, vol. 90, no. 8, p. 085421, 2014.

[177] P. Hapala, R. Temirov, F. S. Tautz, and P. Jelínek, "Origin of high-resolution IETS-STM images of organic molecules with functionalized tips," *Physical Review Letters*, vol. 113, no. 22, p. 226101, 2014.

[178] L. Gross, F. Mohn, N. Moll, P. Liljeroth, and G. Meyer, "The chemical structure of a molecule resolved by atomic force microscopy," *Science*, vol. 325, no. 5944, pp. 1110–1114, 2009.

[179] R. Decker, J. Brede, N. Atodiresei, V. Caciuc, S. Blügel, and R. Wiesendanger, "Atomic-scale magnetism of cobalt-intercalated graphene," *Physical Review B*, vol. 87, no. 4, p. 041403, 2013.

[180] I. de P R Moreira, A. Roldán, F. Illas, *et al.*, "Electronic and magnetic structure of bulk cobalt: The α, β, and ε-phases from density functional theory calculations," *The Journal of chemical physics*, vol. 133, no. 2, p. 024701, 2010.

[181] M. Corbetta, S. Ouazi, J. Borme, Y. Nahas, F. Donati, H. Oka, S. Wedekind, D. Sander, and J. Kirschner, "Magnetic response and spin polarization of bulk Cr tips for in-field spin-polarized scanning tunneling microscopy," *Japanese Journal of Applied Physics*, vol. 51, no. 3R, p. 030208, 2012.

[182] M. Eltschka, B. Jäck, M. Assig, O. V. Kondrashov, M. A. Skvortsov, M. Etzkorn, C. R. Ast, and K. Kern, "Probing absolute spin polarization at the nanoscale," *Nano Letters*, vol. 14, no. 12, pp. 7171–7174, 2014.